

Ytterbium Silicate Environmental Barrier Coatings

---

A Dissertation

Presented to  
the faculty of the School of Engineering and Applied Science  
University of Virginia

---

in partial fulfillment  
of the requirements for the degree

Doctor of Philosophy

by

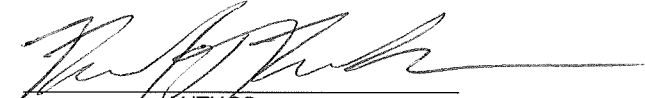
Bradley T. Richards

May

2015

APPROVAL SHEET

The dissertation  
is submitted in partial fulfillment of the requirements  
for the degree of  
Doctor of Philosophy

  
\_\_\_\_\_  
AUTHOR

The dissertation has been read and approved by the examining committee:

Haydn Wadley

\_\_\_\_\_  
Advisor

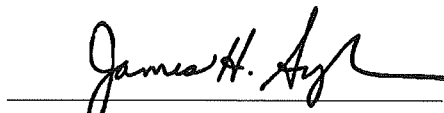
Elizabeth Opila, Chair

Sean Agnew

James Fitz-Gerald

Hilary Bart-Smith

Accepted for the School of Engineering and Applied Science:

  
\_\_\_\_\_

Dean, School of Engineering and Applied Science

May  
2015

## **Abstract**

Environmental Barrier Coatings (EBCs) are used as protective coatings for silicon carbide components in gas turbine engines to inhibit surface reactions with water vapor released by hydrocarbon combustion. In this high temperature environment, oxidizing species such as  $\text{H}_2\text{O}$  and  $\text{O}_2$  react with SiC to form gaseous CO and a solid  $\text{SiO}_2$  layer on the SiC surface. However, subsequent reaction of the normally protective silica layer with water vapor leads to the formation of gaseous  $\text{Si}(\text{OH})_4$ , and volatilization of the silica scale at a rate that increases with temperature, water vapor pressure and flow rate over the surface. All three of these parameters are high in modern gas turbine engines, leading to severe volatility issues for SiC-based ceramics. The primary objective of an environmental barrier coating (EBC) then is to impede access of oxidizing species to the underlying component while maintaining adherence over long durations (in the range of 5,000 hours). The target use temperature of current EBCs is 1316 °C (2400 °F) with repeated cycling between this and the ambient temperature. While several EBC concepts have been proposed, there has been no fundamental study of their response to thermocyclic loading in water vapor environments, and little is known about the mechanisms that govern their performance and durability. Materials property data is also

unavailable for many of the candidate materials in their bulk (fully dense) and coating structure forms, and little is known about the relationships between coating microstructure and the way in which the coating is applied.

One promising coating system with very low steam volatility is the ytterbium monosilicate/mullite/silicon ( $\text{Yb}_2\text{SiO}_5/\text{Al}_6\text{Si}_2\text{O}_{13}/\text{Si}$ ) tri-layer EBC. EBCs are generally applied by an air plasma spray (APS) deposition process in which particles of the coating material are melted in an atmospheric pressure, Ar-based plasma jet, and the molten droplets sprayed onto the component surface. In collaboration with the NASA Glenn Research Center, this coating system was deposited on  $\alpha$ -SiC substrates using a high power APS approach, and the relation between the coating structure and the process environment characterized. Some of the coatings delaminated from the substrate upon cooling, which was indicative of significant variation in the adherence between the SiC substrate and Si layer. The EBC coated  $\alpha$ -SiC substrates that did not delaminate were then tested in a steam-cycling furnace designed to reproduce some aspects of the thermocyclic and environmental conditions found during lean combustion engine operation. The thermal cycles consisted of a 60 min 1316 °C hold time in a flowing 90 %  $\text{H}_2\text{O}$  and 10 %  $\text{O}_2$  environment followed by cooling to 110 °C with a hold for 10 min. All of the coatings delaminated from their substrate with coating lifetimes ranging from less than one hundred to several hundred cycles.

The primary factor contributing to rapid steam cycling failure of the coatings was rapid penetration of oxidizing species through channel (mud) cracks in the  $\text{Yb}_2\text{SiO}_5$  and  $\text{Al}_6\text{Si}_2\text{O}_{13}$  layers that terminated at the Si bond coat. An analysis of the residual stresses

resulting from differences in the coefficients of thermal expansion (CTE) of the three materials used in the coating and that of the SiC substrate indicated that mud cracks were formed as a result of large in-plane biaxial tensile stress in the ytterbium monosilicate and (to a lesser extent) mullite layers. The mud cracks provided a fast transport path to the silicon layer that resulted in rapid formation of a thermally grown oxide (TGO) identified to be the cristobalite phase of SiO<sub>2</sub>. The TGO layer was then found to undergo severe microfracture as it underwent a  $\beta$  (high)  $\rightarrow$   $\alpha$  (low) cristobalite phase transformation on cooling through  $\sim 220$  °C that was accompanied by a 4.5 vol% contraction upon cooling. The repetition of this phase transformation with cracking led to rapid oxidation of the silicon layer and failure of the system by spallation of the Yb<sub>2</sub>SiO<sub>5</sub> and Al<sub>6</sub>Si<sub>2</sub>O<sub>13</sub> layers above it.

An improved APS system was designed and installed at the University to enable the deposition process to be studied carefully, and an optimized coating process to be developed. In this revised process, the Si layer was deposited onto the SiC at high temperature (1200 °C) under a reducing environment to improve its adherence with the substrate and ensure the layer had a high relative density (only a few isolated pores). This eliminated premature delamination issues experienced during cooling for some of the high power deposited coatings. The effect of spray parameter selection upon the microstructure of Yb<sub>2</sub>SiO<sub>5</sub> and its disilicate (Yb<sub>2</sub>Si<sub>2</sub>O<sub>7</sub>) counterpart (which has a CTE more closely matched to the substrate) was investigated. Secondary phases were identified and shown to result from SiO evaporation from the powder particles during plasma heating. Their volume fractions, as well as other microstructural and defect features of the layers were all investigated. Though mud cracking was again observed in

$\text{Yb}_2\text{SiO}_5$  layers, no such cracking was identified in  $\text{Yb}_2\text{Si}_2\text{O}_7$  layers. This difference in cracking behavior was consistent with differences in the residual stress developed during cooling of the two ytterbium silicates.

The (optimized) low power  $\text{Yb}_2\text{SiO}_5/\text{Al}_6\text{Si}_2\text{O}_{13}/\text{Si}$  EBCs were again tested in steam-cycling, but no statistically significant improvement in coating life was observed. The improved Si layer adherence and microstructure eliminated the primary delamination mode seen in the high power deposited coatings, but a new failure mechanism was observed in the optimized ytterbium monosilicate protected system. As opposed to mud crack termination at the Si bond coat, mud cracks in the low power tri-layer system bifurcated either within the  $\text{Al}_6\text{Si}_2\text{O}_{13}$  layer or at one of its interfaces. The bifurcated cracks continued to propagate towards the Si bond coat where the crack ligaments turned and propagated as horizontal delamination cracks through the mid-plane of the Si layer. Rapid oxidizing species access to the interior of the EBC still occurred through these mud cracks, but instead of oxidizing the  $\text{Al}_6\text{Si}_2\text{O}_{13}$  – Si interface, the faces of the delamination cracks within the Si layer were oxidized to form cristobalite. These cracks advanced sequentially during steam cycling until spallation occurred. In collaborations with researchers at UCSB, the thermomechanical competition between the single channel and bifurcated crack damage modes was investigated using Finite Element Analysis (FEA) combined with J-integral methods to calculate the stored elastic strain energy release rate (ERR) during fracture by the two crack propagation paths.

Simpler bi-layer  $\text{Yb}_2\text{Si}_2\text{O}_7/\text{Si}$  EBCs were also deposited on the same SiC substrates using the optimized, low power APS process. The ytterbium disilicate layer in these

coatings contained about 15 vol%  $\text{Yb}_2\text{SiO}_5$  but did not crack upon cooling. Neither spallation failure of the coatings nor cracking of the ytterbium silicate layer was observed during steam furnace testing for up to 2,000 cycles (2,000 hours at 1316 °C). A cristobalite TGO layer was found to form slowly at the  $\text{Yb}_2\text{Si}_2\text{O}_7$  – Si interface, and the thickness of this layer was measured by sectioning samples extracted from the furnace after 250, 500, 750, 1,000, and 2,000 steam cycles. The maximum TGO thickness reached only  $\sim 2.5$   $\mu\text{m}$  after 2,000 hours of exposure, even though it had begun to microcrack and therefore had lost its protective properties. The TGO layer thickness exhibited a linear dependence upon high temperature exposure time, consistent with growth being limited by diffusion of the oxidizing species through the ytterbium disilicate layer. The linear oxidation rate constant was used to calculate a monatomic oxygen flux and effective oxygen diffusion coefficient through the  $\text{Yb}_2\text{Si}_2\text{O}_7$  layer. Some volatilization of Si from the surface of the  $\text{Yb}_2\text{Si}_2\text{O}_7$  layer was also observed, and the coating edges suffered from preferential attack. However, the steam-cycling performance of this coating was deemed sufficient to merit further investigations of the system for stressed (rotating) environments.

Large stand-alone plates of  $\text{Yb}_2\text{Si}_2\text{O}_7$  and Si were deposited by APS. These plates were precision ground into mechanical test specimens through collaboration with technical staff at the NASA Glenn Research Center. The specimens were used to measure the elastic modulus, fracture toughness, flexure strength at low and high temperatures, and obtain estimates of the materials' creep resistance. The mechanical properties of the ytterbium disilicate material were significantly lower than values for fully dense materials. Reductions of 2-5x were observed across all quasi-static properties. The creep

rates of APS  $\text{Yb}_2\text{Si}_2\text{O}_7$  were found to be very rapid (1 % creep strain accumulated in only 25 h at 900 °C and 16MPa). The activation energy for creep in the 10 % porous APS material was in the 130-150 kJ/mol range. The creep rate of the APS Si samples was also high, but in this case similar to bulk polycrystalline silicon. The mechanical properties of the APS deposited ytterbium disilicate/Si system appear insufficient for future application on rotating components.

The implications of the various failure mechanisms observed and the material properties measured and calculated for these EBC systems are discussed. The materials selection, processing, and performance relationships are interpreted in the context of further EBC development, and several suggestions are proposed for future work to address the technical challenges of this evolving field.

## **Acknowledgements**

Many individuals contributed to this work in invaluable ways. I would first like to highlight these contributions for the 6 publications developed and represented in this dissertation. All of these works were co-written with my dissertation adviser, Haydn Wadley.

Chapter 2 was my first foray into EBCs, and I express my gratitude to Dennis Fox, Bryan Harder, and Michael Cuy at NASA Glenn who helped me to deposit the APS coatings described. I am also grateful to Elizabeth Opila (UVA) for advice on thermochemistry and Md Shamsujjoha (UVA) for aid in residual stress measurement. Some imaging in this work was performed at ICTAS NCFL. Rolls Royce (Indianapolis) supported some aspects of this work and we are grateful to Kang Lee of that organization for helpful discussions. The Office of Naval Research (ONR) also supported this study under grant N00014-11-1-0917 managed by Dr. David Shifler.

Chapter 3 was co-authored with Matthew Begley (UCSB). I would again like to acknowledge the contributions of Bryan Harder, Dennis Fox, and Michael Cuy of the NASA Glenn Research Center for their assistance in depositing the EBCs that were

tested. I also thank Elizabeth Opila (UVA), Dongming Zhu (NASA Glenn) and Kang Lee (RR) for numerous helpful discussions. Characterization advice from Richard White (UVA) was also greatly appreciated. This work was supported in part by Rolls Royce (Indianapolis) and the Office of Naval Research under grants N00014-11-1-0917 (BTR and HNGW) and N00014-13-1-0859 (MRB) managed by Dr. David Shifler.

The work of Chapter 5 was carried out with the aid of co-author Hengbei Zhao (UVA). Discussions with Elizabeth Opila (UVA) and Bryan Harder (NASA Glenn) were critical at several stages. I would also like to acknowledge Ryan Hinckley for his aid in initial formulation of spray parameters. This work was supported by the Office of Naval Research under grant N00014-11-1-0917 managed by Dr. David Shifler.

Chapter 6 was executed in collaboration with Foucault de Francqueville, Stephen Sehr, and Matthew Begley, all of UCSB. My thanks are extended to Bryan Harder and Dongming Zhu (NASA Glenn) as well as to Kang Lee (RR) for helpful consultations. This work was supported in part by Rolls Royce (Indianapolis) and the Office of Naval Research under grants N00014-11-1-0917 (BTR and HNGW) and N00014-13-1-0859 (FF, SS and MRB) managed by Dr. David Shifler.

The research of Chapter 7 was performed at UVA with the assistance of Kelly Young. Foucault de Francqueville, Stephen Sehr, and Matthew Begley of UCSB also performed mechanical analyses of the system. I would like to thank Elizabeth Opila of UVA for advice and many helpful discussions regarding various aspects of the work. The research was supported by the Office of Naval Research under grants N00014-11-1-0917

(BTR, KAY and HNGW) and N00014-13-1-0859 (FF, SS and MRB) managed by Dr. David Shifler.

The peer reviewed conference proceeding of Chapter 8 was performed largely at the NASA Glenn Research center under the guidance of Dongming Zhu with modeling support by Louis Ghosn, both of whom are co-authors. I would like to extend my thanks to Ralph Pawlik (NASA Glenn) for his expertise in mechanical testing of materials. Jeroen Djeikers and Hengbei Zhao (UVA) assisted me in the deposition and characterization of coating materials at the University. This work was supported under the NASA Fundamental Aeronautics Program. The Office of Naval Research supported work performed at UVA under grant N00014-11-1-0917 managed by Dr. David Shifler. I am also grateful to Mitch Dorfman of Oerlikon Metco for support in development of the HOSP ytterbium silicate powder for NASA research programs.

There are several personal thanks that I would like to extend to individuals who have made a great impact upon my journey. First, to my adviser, Haydn: it took a subtle, practiced, and brilliant hand to direct me successfully. There are innumerable ways in which this project could have failed spectacularly, and you managed to steer me clear of all of them while still allowing me to thoroughly enjoy my work and flourish as a scientist. I feel that I have learned as much under your guidance as I did in the rest of my education combined, and I will never forget my time working as your student. I am enormously grateful for the opportunities you have provided me and the freedom you have allowed me in my work. I simply cannot imagine having succeeded under the hand of anyone else, nor would I have wanted to.

To my committee chair, Beth: you have supported me as a teacher in the classroom, as a scientist in the lab, and in your role as my committee chair. Your continual willingness to aid me in my endeavors has had a tremendous influence on my development as a scientist. I also greatly appreciate your referral to the NASA co-op program which has been an incredible experience and also your continual suggestion to pursue the career I have always dreamed of regardless of what others suggest I do.

To my collaborators and friends at UCSB, Matt Begley, Stephen Sehr, and Foucault de Francqueville: As hard as I try, I cannot put words to how valuable your contributions and insights have been. I hope I have in some way helped to support your work in as much as you have supported mine. You are all brilliant and I wish you nothing but the greatest success in your careers.

To my NASA colleagues: Working at NASA has always been a dream. I hope that you all continue to inspire engineers and scientists throughout the world as you have over the last 50 years. Many of us would not be where we are without you. To my NASA mentor Dongming Zhu: it has been an honor to work with you. Never have I felt the need to double check myself so much. Your eagerness to get meaningful, impactful results and your tireless commitment to our field are truly inspiring. I also owe particular thanks to my friend and colleague Bryan Harder: I will never forget your support and your passion for science. I believe a long and well reputed career in academia looms in your future. You are simply too skilled of an educator to be permitted to do anything else. To the mechanical testing guru Ralph Pawlik: your help and insights are greatly appreciated and were very impactful in what I learned in this dissertation.

To the other members of my committee: your advisement in this work is greatly appreciated, and I thank you all for committing your time and effort.

To my co-workers in the group and the others at UVA who have shared in this experience: you all have made this journey exciting. We have shared much that I will never forget. My heartfelt thanks and highest hopes go to you all.

My family has always supported me in every venture of my education. It's hard to put into words what that means. I'm truly appreciative of everything you have done for me and thankful for your enduring support. Laura, I hope you don't feel any pressure as a result of this.

Finally, very little of this could have been done without the support of my wife, Kendall. She knows when to be kind and when to call me lazy. She kept my spirits up and my feet moving forward when I was feeling down, and made sure to use the emergency brake when I lost control. I am truly honored to have such a loving, caring spouse who has supported my dreams. I hope I can provide for you in the future what you have given me, and I look forward to the next part of our life together.

## **Table of Contents**

Abstract.....	i
Acknowledgements.....	vii
Table of Contents.....	xii
List of Figures.....	xix
List of Tables.....	xxxiv
1 Introduction.....	1
1.1 Evolution of the Gas Turbine Operating Temperature.....	1
1.2 SiC and Ceramic Matrix Composites (CMCs).....	4
1.3 First Generation Environmental Barrier Coatings (EBCs).....	6
1.4 Second Generation EBCs.....	7
1.5 Air Plasma Spray (APS) Deposition.....	10
1.6 Mechanical Properties of APS Materials.....	12
1.7 Dissertation Goals.....	14

1.8	Dissertation Outline.....	15
2	Plasma Spray Deposition of Tri-Layer Environmental Barrier Coatings.....	17
2.1	Introduction .....	18
2.2	Experimental .....	19
2.2.1	Coating Deposition .....	19
2.2.2	Characterization .....	22
2.2.3	Dilatometry .....	24
2.3	Results and Discussion.....	24
2.3.1	Yb <sub>2</sub> SiO <sub>5</sub> Thermal Expansion Coefficient .....	24
2.3.2	Tri-layer EBC Structure.....	25
2.3.3	Yb <sub>2</sub> SiO <sub>5</sub> Topcoat.....	27
2.3.4	Mullite Intermediate Layer .....	39
2.3.5	Silicon Bond Coat.....	46
2.4	Conclusions .....	49
3	Ytterbium Monosilicate/Mullite/Silicon Coating Failure during Steam-cycling .....	51
3.1	Introduction .....	52
3.2	Experimental .....	53
3.2.1	Coating Deposition .....	53
3.2.2	Steam Furnace Cycling.....	54
3.2.3	Coating Characterization .....	56

3.2.4	Thermomechanical Analysis.....	57
3.3	Results .....	57
3.3.1	Coating Structure .....	58
3.3.2	Steam-cycling Response .....	61
3.4	Calculated Stress States and Energy Release Rates .....	68
3.5	Discussion .....	71
3.6	Conclusions .....	77
4	Air Plasma Spray (APS) System at UVA.....	78
4.1	APS System Selection.....	78
4.2	APS Facility .....	81
4.3	Equipment and Process Modifications.....	82
4.4	APS Torch Control and Deposition .....	86
5	Structure, Composition and Defect Control of APS Ytterbium Silicates.....	90
5.1	Introduction .....	91
5.2	Experimental .....	92
5.2.1	Plasma Spray Process .....	92
5.2.2	Powder Materials .....	96
5.2.3	Coating Characterization .....	97
5.3	Results .....	99
5.3.1	Phase Content.....	100

5.3.2	Splat Aspect Ratio.....	109
5.3.3	Coating Composition .....	110
5.3.4	Channel Type and Equiaxed Microcracking.....	118
5.4	Discussion .....	120
5.5	Conclusions .....	125
5.6	Appendix A: Dilatometry of $\text{Yb}_2\text{Si}_2\text{O}_7$ .....	127
6	Delamination and Cracking of $\text{Yb}_2\text{SiO}_5/\text{Al}_6\text{Si}_2\text{O}_{13}/\text{Si}$ Coatings in Steam-cycling. ....	129
6.1	Introduction .....	130
6.2	Experimental .....	133
6.2.1	Coating Deposition .....	133
6.2.2	Coating Stabilization and Steam Furnace Cycling .....	134
6.2.3	Coating Characterization .....	135
6.2.4	Thermomechanical Analysis.....	136
6.3	Results .....	138
6.3.1	Coating Structure .....	140
6.3.2	Steam-cycling Response .....	146
6.4	Calculated Stress States, Strain Energy Release Rates and FEA of Cracking. ....	151
6.5	Discussion .....	157
6.6	Conclusions .....	165
7	Ytterbium Disilicate-Silicon Coating Performance in Steam-cycling.....	168

7.1	Introduction .....	169
7.2	Experimental .....	172
7.2.1	Coating Deposition .....	172
7.2.2	Steam-cycling .....	174
7.2.3	Coating Characterization .....	175
7.2.4	Energy Release Rates and Residual Stresses .....	177
7.3	Results .....	177
7.3.1	Thermally Grown Oxide (TGO) .....	179
7.3.2	YbDS Volatilization.....	183
7.3.3	Edge Delamination.....	189
7.4	Oxide Growth at the Silicon Surface.....	192
7.5	Fracture Mechanisms .....	198
7.6	Conclusions .....	201
8	Mechanical Properties of APS EBC Materials .....	204
8.1	Introduction .....	205
8.2	Experimental .....	206
8.3	Results .....	211
8.3.1	APS $\text{Yb}_2\text{Si}_2\text{O}_7$ .....	211
8.3.2	APS Si.....	216
8.3.3	Mixed-Mode Interface Toughness .....	219

8.4	Discussion .....	220
8.4.1	APS $\text{Yb}_2\text{Si}_2\text{O}_7$ .....	220
8.4.2	APS Si .....	227
8.4.3	Mixed-Mode Interface Toughness .....	229
8.5	Conclusions .....	231
9	Discussion .....	233
9.1	Air Plasma Spray of EBC Materials .....	235
9.2	Performance of the $\text{Yb}_2\text{SiO}_5/\text{Al}_6\text{Si}_2\text{O}_{13}/\text{Si}$ System .....	239
9.3	Environmental and Mechanical Behavior of the $\text{Yb}_2\text{Si}_2\text{O}_7/\text{Si}$ System .....	243
10	Conclusions .....	249
10.1	APS Deposition .....	250
10.2	$\text{Yb}_2\text{SiO}_5/\text{Al}_6\text{Si}_2\text{O}_{13}/\text{Si}$ Tri-layer EBC .....	251
10.3	$\text{Yb}_2\text{Si}_2\text{O}_7/\text{Si}$ Bi-layer EBC .....	254
10.4	Future Work .....	257
10.4.1	Bond Coat .....	258
10.4.2	Environmental Barrier Layer .....	258
10.4.3	Thermal Barrier Layer .....	259
10.4.4	Modeling .....	259
10.4.5	Advanced Systems .....	260
11	References .....	261

12	Appendix A: Experimental Methods .....	279
12.1	Scanning Electron Microscopy.....	279
12.2	Image Adjustments and Analyses.....	281
12.3	X-ray Diffraction (XRD).....	282
12.4	Mechanical Properties Testing .....	284

## **List of Figures**

Figure 1.1: The evolution of turbine blade materials, coatings, cooling concepts and turbine inlet $T_{4.1}$ gas temperature plotted against the year of entry. Current engines utilize internal and film cooled single crystal (SX) superalloy blades protected by thermal barrier coatings in the hottest regions of the engine (adapted from reference) <sup>23</sup> . .....	3
Figure 2.1: Schematic illustration of an APS deposited tri-layer EBC structure. ....	20
Figure 2.2: Schematic illustration of the APS and substrate heating system used to deposit the environmental barrier coatings.....	22
Figure 2.3: Thermal expansion and CTE data for hot-pressed $\text{Yb}_2\text{SiO}_5$ with a relative density of ~70%. .....	25
Figure 2.4: BSE micrographs of $\text{Yb}_2\text{SiO}_5/\text{Al}_6\text{Si}_2\text{O}_{13}/\text{Si}$ three layer EBC; (a) as-fabricated and (b) after a 20 hour stabilization anneal in air at 1300°C. Dashed boxes indicate regions where higher magnification micrographs are subsequently analyzed.....	26
Figure 2.5: High magnification micrographs of the $\text{Yb}_2\text{SiO}_5$ topcoats from; (a) region I in the as-deposited micrograph- Figure 2.4(a), and (b) region IV in the annealed condition micrograph- Figure 2.4(b).....	28

Figure 2.6: High magnification views of (a) region VII in the as-deposited coating shown in Figure 2.5(a), and (b) annealed topcoat near a splat boundary.....	29
Figure 2.7: EDS line scan of annealed ytterbium silicate topcoat. Dashed lines indicate atomic compositions for $\text{Yb}_2\text{SiO}_5$ . Note 40at% Yb- 60at% O is the composition of ytterbia. Location of scan line is indicated on accompanying micrograph.....	32
Figure 2.8: Calculated partial pressure versus temperature plot for primary gaseous species in the Yb-Si-O system. Curves are reported for an equilibrated system.....	33
Figure 2.9: Ytterbia-silica binary phase diagram (redrawn from reference) <sup>81</sup> .....	34
Figure 2.10: XRD patterns for the nominally ytterbium monosilicate topcoat; (a) as-deposited and (b) annealed. Peaks are indexed for $\text{Yb}_2\text{O}_3$ in (a) and $\text{Yb}_2\text{SiO}_5$ in (b). Reference peaks for both phases in (a) and calculated Rietveld refinement pattern in (b) are also shown.....	36
Figure 2.11: High magnification micrographs of the mullite intermediate layer from (a) region II in as-deposited Figure 2.4(a) and (b) region V in annealed Figure 2.4(b).....	40
Figure 2.12: EDS line scan of annealed mullite layer. The initial $3\text{Al}_2\text{O}_3:2\text{SiO}_2$ molar mullite composition is indicated by dashed lines. Note that 40at% Al- 60at% O is the composition of alumina. The location of the line scan is indicated on the micrograph. ..	42
Figure 2.13: High magnification view of phase decomposition into alumina plate separated by silicon rich material in the annealed mullite coat. ....	43
Figure 2.14: Calculated partial pressure vs. temperature plot for primary gaseous species in the Al-Si-O system. Data are reported for a fully equilibrated system.....	44
Figure 2.15: Alumina-Silica binary phase diagram. Dashed lines indicate the boundaries of metastable phases (modified and redrawn) <sup>85</sup> .....	45

Figure 2.16: High magnification micrographs of the silicon bond coat from (a) region III in as-deposited Figure 2.4(a), and (b) region VI after annealing in air (20 h at 1300 °C) from Figure 2.4(b).....	46
Figure 2.17: High magnification view corresponding to region VIII in Figure 2.4(b) showing a mud-crack penetrating the mullite coat and terminating in the upper few micrometers of the silicon bond coat. ....	48
Figure 3.1: Schematic illustration of the tri-layer EBC covered SiC samples showing the coating structure and side edge coverage of the substrate. ....	54
Figure 3.2: Schematic illustration of the steam-cycling furnace in the configuration that subjected the samples to the hot part of a steam cycle (60 min at 1316°C). The furnace was then translated vertically while maintaining the sample stationary, thereby removing the sample from the furnace hot zone and subjecting it to the cold part of a steam cycle (10 min at 110°C). ....	55
Figure 3.3: (a) Low magnification BSE mode SEM image of the 1300°C annealed EBC with mud cracks indicated by arrows. (b) Shows a higher magnification view of the coating in a region where a mud crack penetrated the ytterbium monosilicate and mullite layers. (c) A high magnification view of the dashed box area in (b) showing arrest of the mud crack at the mullite – silicon bond coat interface. ....	60
Figure 3.4: The Si – SiC interface of (a) an annealed sample in a region of relatively poor adherence with oxidized pore structures and poor interfacial bonding and (b) an interfacial region of higher quality in the same annealed specimen. ....	61
Figure 3.5: Images of an EBC covered sample. (a) Optical image of top surface after annealing. (b) Optical image of the top surface of the same sample after it had	

delaminated following 50 steam cycles at 1316°C. (c) SEM cross-section (in BSE mode) of the delaminated sample shown in (b). The red bar in (b) indicates the location of the cross section shown in (c). ..... 62

Figure 3.6: Cross sectional BSE micrographs of the same failed coating after 600 1-hour steam cycles at 1316°C with serial sections at (a) 1mm, (b) 3mm, and (c) 5mm from the coating edge. The dashed white line shows the TGO-mullite interface. The boxed section in (c) indicates the region subjected to compositional analysis. .... 64

Figure 3.7: (a) A SEM image taken in BSE mode of a mud-crack root intersection with an adherent silica TGO –  $\text{Al}_6\text{Si}_2\text{O}_{13}$  interface as identified in Figure 3.6(c). (b) An oxygen, (c) aluminum, and (d) silicon dot map of the same region. .... 65

Figure 3.8: Raman spectra from the thermally grown (silica) oxide at the Si-mullite interface as a function of distance from the edge of the coated sample. .... 67

Figure 3.9: High magnification BSE mode SEM images of (a) ytterbium monosilicate and (b) the mullite layers after a 200 steam cycle exposure. .... 68

Figure 3.10: SEM micrograph (in BSE mode) of the interface between the ytterbium monosilicate and mullite layers in a sample that delaminated after 600 steam cycles at 1316°C. Note the formation of an approximately 5 $\mu\text{m}$  thick reaction product between the two layers and interfacial pores created by the inter-diffusion reaction. .... 69

Figure 3.11: Raman spectra of the Yb-Si-Al-O reaction product formed at the  $\text{Yb}_2\text{SiO}_5$  –  $\text{Al}_6\text{Si}_2\text{O}_{13}$  interface in Figure 3.10 and a reference pattern for APS  $\text{Yb}_2\text{SiO}_5$ . .... 70

Figure 3.12: The elastic stored energy release rate for delamination at the various interfaces of a tri-layer EBC as a function of temperature cooling from 1316°C. (a) For an annealed coating assuming bulk (full) elastic moduli, and (b) the same coating after

growing a 20 $\mu$ m thick cristobalite TGO at the Al <sub>6</sub> Si <sub>2</sub> O <sub>13</sub> – Si interface. (c) and (d) repeat (a) and (b) but with the reduced elastic moduli assumed for the APS materials given in Table 3.1. ....	71
Figure 3.13: The damage mechanism sequence in an Yb <sub>2</sub> SiO <sub>5</sub> /Al <sub>6</sub> Si <sub>2</sub> O <sub>13</sub> /Si tri-layer EBC applied to an $\alpha$ -SiC substrate. (a) Shows the initial damage and stress states in the annealed EBC, (b) shows reaction at 1316°C and (c) details mechanical damage at low temperature. (d) Schematic of the edge localized damage and failure. ....	74
Figure 4.1: Schematic illustration of the configuration of UVA’s APS lab. ....	80
Figure 4.2: Photography of the process gas handling and primary controls of UVA’s APS system. ....	81
Figure 4.3: The four powder feeders that can be connected to the APS torch. ....	82
Figure 4.4: Schematic illustration of the effect of substrate heating upon crystallinity of splats deposited by APS. ....	84
Figure 4.5: Photograph of Brad Richards removing a deposition fixture with four coated samples from the high temperature deposition furnace. ....	85
Figure 4.6: Control pendant of the ABB IRB-140 robot that runs the APS system. ....	88
Figure 4.7: Live plasma spraying into the high temperature deposition furnace. ....	89
Figure 5.1: (a) Schematic illustration of the air plasma spray (APS) deposition approach used for high temperature environmental barrier coating (EBC) deposition. (b) Schematic illustration of the plasma torch design. (c) The spray pattern and definition of relevant deposition parameters. (d) Photograph taken during APS deposition into the box furnace. ....	93

- Figure 5.2: As-deposited tri-layer EBC systems deposited on a monolithic  $\alpha$ -SiC substrate. (a) Ytterbium monosilicate and (b) ytterbium disilicate topcoats both deposited on mullite using silicon bond coated substrates. The SEM images were collected in BSE mode and so the whitest contrast phases contained the highest concentration of the highest atomic number element (ytterbium). ..... 100
- Figure 5.3: X-ray diffraction patterns of as-deposited and annealed topcoats. (a) Ytterbium monosilicate and (b) ytterbium disilicate both deposited using the S combination of deposition parameters. .... 102
- Figure 5.4: BSE mode SEM micrographs of the ytterbium silicate layers deposited using the S combination of deposition parameters. (a) As-deposited, (b) annealed, and (c) high magnification annealed ytterbium monosilicate layer. (d), (e), and (f) correspond to as-deposited, annealed, and high magnification annealed ytterbium disilicate layers. .... 104
- Figure 5.5: (a) Bright field TEM image of the ytterbium monosilicate coating. (b) The [111] and (c) the [011] selected area electron diffraction (SAED) zone axis patterns from the monoclinic  $\text{Yb}_2\text{SiO}_5$  phase. (d) High magnification bright field image of the precipitated phase in the  $\text{Yb}_2\text{SiO}_5$  matrix. (e) Shows the cubic  $\text{Yb}_2\text{O}_3$  precipitate diffraction pattern along the [210] zone axis. .... 106
- Figure 5.6: (a) Bright field TEM image of the ytterbium disilicate coating and (b) high magnification bright field image of a precipitated  $\text{Yb}_2\text{SiO}_5$  particle. Crosses indicate the locations of EDS probes for characterizing the matrix and precipitate phases. (c) The [110] and (d) the [010] selected area electron diffraction patterns along zone axes of monoclinic  $\text{Yb}_2\text{Si}_2\text{O}_7$  from the region indicated by SAED circled in (a). .... 109

- Figure 5.7: Volume fraction of second phase precipitates in annealed coatings plotted against plasma spray power. (a)  $\text{Yb}_2\text{O}_3$  precipitated in ytterbium monosilicate coatings. (b)  $\text{Yb}_2\text{SiO}_5$  precipitated in ytterbium disilicate coatings. .... 111
- Figure 5.8: BSE mode SEM micrographs of as-deposited ytterbium monosilicate coatings deposited using different combinations of spray parameters. (a) 2C coating, (b) 5C coating, (c) 2H coating, and (d) 4H coating. .... 112
- Figure 5.9: BSE mode SEM micrographs of as-deposited ytterbium disilicate coatings deposited using different combinations of spray parameters. (a) 1C coating, (b) 5C coating, (c) 1H coating, and (d) 4H coating. .... 114
- Figure 5.10: Variations in average splat aspect ratio ( $l/t$ ) as a function of plasma spray power for (a) ytterbium monosilicate and (b) ytterbium disilicate coatings in the as deposited condition. .... 115
- Figure 5.11: (a) Yb:Si ratio dependence upon molar volumes of second phases. Average Yb to Si ratios and BSE contrast based estimates of the composition variation in a coating for (b) the ytterbium monosilicate and (c) the ytterbium disilicate layers. BSE derived distributions were scaled by aligning the lowest Yb:Si ratio (darkest BSE contrast) end of the distribution with the stoichiometric compound and enforcing the average of the distribution to match that deduced from the phase volume fractions. .... 116
- Figure 5.12: Partial pressure ratio of dominant vapor species to SiO as a function of temperature for the S spray parameter condition with (a)  $\text{Yb}_2\text{SiO}_5$  and (b)  $\text{Yb}_2\text{Si}_2\text{O}_7$  injected into the plume. (c) Calculated vapor partial pressures of dominant species. Partial pressures are calculated based on ideal thermochemical interactions. .... 117

- Figure 5.13: Crack areal density (CAD) of ytterbium silicate layers: micro-crack length (in  $\mu\text{m}$ ) per  $10,000\mu\text{m}^2$  of coating cross section. (a) Crack length of all orientations plotted as a function of plasma spray power for the ytterbium monosilicate layers. (b) Crack length as a function of angle of divergence from horizontal crack path in ytterbium monosilicate layers. A  $90^\circ$  angle indicates vertical (mud crack type) cracking. The plots in (c) and (d) are similar data for ytterbium disilicate layers..... 120
- Figure 5.14: Thermal strain and expansion coefficient of 100 hour annealed 95% dense spark plasma sintered (SPS) ytterbium disilicate ( $\text{Yb}_2\text{Si}_2\text{O}_7$ )..... 128
- Figure 6.1: BSE images of an annealed tri-layer EBC deposited using high power plasma spray parameters from Chapter 2. (a) The three layers on a SiC substrate with mud cracks indicated. (b) Higher magnification view showing penetration of a mud crack, and (c) zoom of boxed region in (b) showing a higher magnification view of the mud crack within the EBC..... 131
- Figure 6.2: Schematic illustration of the failure mechanism of high power deposited tri-layer EBCs on a SiC substrate (see Chapter 3)..... 132
- Figure 6.3: Schematic illustration of an as-deposited tri-layer coated  $\alpha$ -SiC substrate.. 134
- Figure 6.4: (a) Shows a schematic of the cracking configuration simulated with the relevant dimensions and scaling features indicated. (b) Part of the actual mesh simulated with (c) a higher magnification view of the putative crack in the  $\text{Al}_6\text{Si}_2\text{O}_{13}$  layer using 5x displacement magnification to show mesh behavior. (b) and (c) are for a normalized bifurcation position of 0.8 (parent crack length of  $140\mu\text{m}$ ) with  $\theta = 45^\circ$  and  $a = 1\mu\text{m}$ . . 139
- Figure 6.5: BSE images of an annealed tri-layer EBC deposited using optimized low power plasma spray parameters. (a) The three layers on a SiC substrate with mud cracks

indicated. (b) Higher magnification view showing two mud cracks and (c) zoom of boxed region in (b) showing the penetration of the two mud cracks into the  $\text{Al}_6\text{Si}_2\text{O}_{13}$  layer.. 141

Figure 6.6: (a) Shows a typical Si – SiC interface of the low power deposited EBC with a well-bonded interface and limited porosity. (b) The Si – SiC interface formed when using high power plasma spray deposition parameters and no reducing gas flow..... 142

Figure 6.7: BSE images of  $\text{Al}_6\text{Si}_2\text{O}_{13}$  – Si interfaces in the annealed tri-layer EBC system. High power deposited interfaces are shown in (a) and (b) whereas (c) and (d) show the same interface in low power EBCs where the Si layer was deposited using a reducing gas flow. .... 143

Figure 6.8: BSE micrographs of mud crack bifurcation in stabilization annealed low power  $\text{Yb}_2\text{SiO}_5/\text{Al}_6\text{Si}_2\text{O}_{13}/\text{Si}$  EBCs plasma sprayed onto  $\alpha$ -SiC. (a) Shows a bifurcation at the  $\text{Yb}_2\text{SiO}_5$  –  $\text{Al}_6\text{Si}_2\text{O}_{13}$  interface, (b) bifurcation within the  $\text{Al}_6\text{Si}_2\text{O}_{13}$  layer, and (c) bifurcation at the  $\text{Al}_6\text{Si}_2\text{O}_{13}$  – Si interface. In all three cases the resultant trajectory of the bifurcated crack ligaments was directed toward the silicon bond coat..... 145

Figure 6.9: Spallation failure probability of low power and high power<sup>95</sup> tri-layer coatings as a function of number of 60 min steam cycles at 1316°C. .... 146

Figure 6.10: (a) Shows an annealed tri-layer EBC deposited using low power plasma spray parameters. The same sample after 250 steam cycles at 1316°C is imaged optically in (b) and its cross section near an edge in (c) using BSE mode SEM imaging. The red bar in (b) indicates the location of the section shown in (c). .... 148

Figure 6.11: Cross sectional BSE micrographs of the same failed coating presented in Figure 8 after 250 1-hour steam cycles at 1316°C with cross-sections at (a) 1mm and (b)

3mm from the coating edge. Note the oxide layer that has formed on the bifurcated crack faces in the silicon bond coat. ....	149
Figure 6.12: (a) BSE mode image of mud-crack and bifurcated delamination cracks for the dashed box region in Figure 9. EDS dot maps are shown for (b) aluminum, (c) oxygen and (d) silicon signals for the same region. ....	151
Figure 6.13: The ERR for delamination at the various interfaces in the tri-layer EBC as a function of topcoat thickness prior to TGO growth. Results using bulk (left) and APS (right) estimated elastic moduli are shown. ....	153
Figure 6.14: FEA computed ERR maps for bifurcation cracking as a function of putative crack angle and bifurcation depth in low power deposited EBCs. Subplots (a) and (b) show the absolute and normalized ERR using the bulk material elastic moduli for coating layers given in Table 6.2. Subplots (c) and (d) show analogous ERR results for coating layers with 50% of the bulk elastic moduli, summarized in Table 6.2. The normalized ERR results were obtained by dividing the ERR for bifurcated crack extension by that for a vertically penetrating single crack. ....	154
Figure 6.15: FEA computed ERR maps for bifurcation cracking as a function of putative crack angle and bifurcation depth. Subplots (a) and (b) show the absolute ERR for 5 $\mu$ m and 10 $\mu$ m putative cracks in the low power EBC using the 50% reduced elastic moduli for coating layers given in Table 6.2. Subplots (c) and (d) show analogous ERR results for high power layers using the reduced elastic moduli given in Table 6.2. ....	156
Figure 6.16: Schematic illustration of the differences in failure mode for (a) high and (c) low power deposited tri-layer EBCs in the annealed condition. The fracture mechanisms	

that develop during steam-cycling are shown in (b) and (c) for high and low power deposition respectively.....	158
Figure 6.17: The ERR for delamination as a function of normalized penetration depth into the Si layer of the tri-layer EBC. ....	159
Figure 6.18: Damage mechanisms contributing to failure of the tri-layer EBC. (a) Shows the stresses in the post annealed coating system. (b) Illustrates the damage mechanisms active during high temperature exposure and (c) shows the mechanical damage that develops during cooling of the sample. ....	163
Figure 7.1: Schematic illustration of a bi-layer $\text{Yb}_2\text{Si}_2\text{O}_7/\text{Si}$ (YbDS/Si) coated $\alpha$ -SiC substrate. ....	173
Figure 7.2: BSE images of an annealed YbDS/Si bi-layer coating deposited onto $\alpha$ -SiC. (a) Low magnification image showing two phases in the YbDS topcoat. (b) High magnification view of the YbDS – Si interface showing interface structure and small $\text{Yb}_2\text{SiO}_5$ (YbMS) precipitates in the YbDS topcoat. ....	175
Figure 7.3: Schematic illustration of the testing configuration and environment local to the samples during the $1316^\circ\text{C}$ hot cycle of steam-cycling.....	176
Figure 7.4: Optical images of YbDS/Si coated SiC substrates. (a) As-deposited, (b) annealed, and (c) after 2,000 steam cycles at $1316^\circ\text{C}$ with the gas flow direction indicated.....	180
Figure 7.5: BSE mode SEM micrographs of YbDS/Si coated system before and after steam-cycling. (a) As-deposited, (b) annealed, (c) after 250 steam cycles, (d) 500 cycles, (e) 1,000 cycles, and (f) 2,000 cycles. ....	181

- Figure 7.6: BSE micrographs of the YbDS – Si interface after steam-cycling showing the development of a thermally grown oxide (TGO). (a) After 250, (b) 500, (c) 1,000, and (d) 2,000 cycles at 1316°C with 90% $H_2O$ /10% $O_2$  flowing at 44mm/s..... 182
- Figure 7.7: Plots of  $SiO_2$  TGO thickness as a function of accumulated exposure time at 1316°C for a bi-layer EBC. (a) Average thicknesses measured from multiple samples with varying YbDS layer thickness. (b) Average thicknesses normalized for thermally grown silica beneath a 100 $\mu m$  thick YbDS layer. .... 183
- Figure 7.8: BSE micrograph of the thermally grown cristobalite ( $SiO_2$ ) oxide at the YbDS – Si interface during steam-cycling. (a) TGO at the YbDS – Si interface after 2,000 steam cycles, (b) after 1,000 steam cycles. .... 184
- Figure 7.9: X-ray diffraction patterns of the annealed and 2,000 steam-cycle sample surfaces. All peaks of the patterns have been indexed using equilibrium YbDS (C2/m) and equilibrium I2/a and metastable P21/c YbMS peaks. The slightly raised background of the 2,000 cycle pattern results from a very thin layer of epoxy on the surface that was used to prevent spallation during handling. .... 186
- Figure 7.10: (a) BSE micrograph of a surface volatilized region of the topcoat. Dot map of (b) Yb and (c) Si from EDS analysis..... 188
- Figure 7.11: BSE cross-section micrographs showing  $SiO_2$  volatilization from the YbDS surface after 2,000 steam cycles at 1316°C. (a) Adherent area of YbMS with porosity and microcracking. (b) Spalled region of surface volatilized layer. (c) Delaminated region of coating containing steam-reduced YbMS and region of unaffected YbDS..... 190

- Figure 7.12: Schematic illustration of the volatility mechanism that results in a porous surface layer of YbMS on the surface of exposed YbDS after steam-cycling. (a) Initial phases of volatilization and (b) late in exposure..... 191
- Figure 7.13: BSE micrographs of coating edges showing edge attack during steam-cycling of the bi-layer EBCs. (a) Annealed coating with edge over-sprayed, (b) edge TGO growth after 500 steam cycles, (c) significant edge lifting after 1,000 steam cycles, and (d) example of edge delamination after 2,000 steam cycles. .... 193
- Figure 7.14: Schematic illustration of the SiO<sub>2</sub> wedging mechanism that lead to edge lifting during steam-cycling of YbDS/Si EBCs deposited on SiC. .... 194
- Figure 7.15: Predicted strain energy release rates of the interfaces in the YbDS – Si EBC system after cooling from 1316°C to 20°C. The calculations used (a) bulk elastic properties of YbDS with APS and bulk elastic modulus for Si layer and (b) APS modified elastic modulus for YbDS with APS and bulk elastic modulus for Si. All mechanical properties are listed in Table 7.2..... 199
- Figure 8.1: Photographs of (a) the 13 mm thick air plasma sprayed Yb<sub>2</sub>Si<sub>2</sub>O<sub>7</sub> stand-alone plate in the deposition fixture, (b) Si test bars after machining from a stand-alone APS silicon plate, and (c) APS Yb<sub>2</sub>Si<sub>2</sub>O<sub>7</sub> coated Si test bars. .... 207
- Figure 8.2: Schematic illustrations of (a) the 4-point bending apparatus used for isothermal flexure tests (toughness, strength, and creep), and (b) the 4-point bending apparatus used for laser thermal gradient creep flexure testing. The incident laser beam had a ~25 mm diameter uniform profile. To create the uniform incident heat flux, a rotated integrator lens was used to distribute the beam. Both fixtures are operated in lab air. .... 209

- Figure 8.3: Schematic illustration of the 4-point bending test configuration used for mixed-mode fracture testing. The inset shows the EDM notch used to establish a “T”-shaped pre-crack in the stiffener and APS coating. .... 210
- Figure 8.4: BSE mode SEM images of the as-deposited  $\text{Yb}_2\text{Si}_2\text{O}_7$  stand-alone plate at a series of magnifications illustrating features relevant to the mechanical response showing (a) low magnification image with intersplat porosity, (b) the presence of (lighter contrast) Si depleted splats, (c) partially melted HOSP particles bound in the matrix, and (d) isolated intersplat pores and poorly adhered splat boundaries..... 212
- Figure 8.5: Isothermal 4-point flexure creep data of air plasma sprayed  $\text{Yb}_2\text{Si}_2\text{O}_7$ . (a) Shows the effect of temperature on the surface strain versus time behavior for a calculated surface stress of 15.8 MPa. (b) The pseudo-strain versus time response during the primary creep regime of the tests shown in (a). .... 214
- Figure 8.6: Laser thermal gradient creep curves for APS  $\text{Yb}_2\text{Si}_2\text{O}_7$ . (a) Strain and load curves for the two-temperature test with front face, back face, and inverse T average (weighted) test temperatures. (b) Linear fit strain equations for the two different temperature regimes of the thermal gradient creep test. .... 215
- Figure 8.7: Determination of creep stress parameter “n” for APS  $\text{Yb}_2\text{Si}_2\text{O}_7$  through optimization of  $R^2$  in an Arrhenius-type creep activation energy ( $E_a$ ) determination plot. .... 216
- Figure 8.8: BSE SEM images of (a) the as-deposited stand-alone Si plate showing the uniform distribution of pores. (b) Higher magnification image showing intersplat boundary and pore structures. (c) Low magnification image of an APS  $\text{Yb}_2\text{Si}_2\text{O}_7$  coated silicon test specimen used to protect the sample from oxidation during laser thermal

gradient testing. (d) Higher magnification image of the $\text{Yb}_2\text{Si}_2\text{O}_7$ – Si coating interface showing good interface adherence.....	217
Figure 8.9: Laser thermal gradient creep curves for APS Si. (a) Strain and load curves for the four-temperature test with front face, back face, and Si test temperatures. (b) Linear fit strain equations for the four different temperature regimes of the thermal gradient creep test. ....	220
Figure 8.10: Creep activation energy ( $E_a$ ) determination for APS Si in an Arrhenius-type plot. ....	221
Figure 8.11: Load and displacement curves for a 4-point bending interfacial toughness test. ....	222

## **List of Tables**

Table 1.1: Thermal expansion coefficients of EBC materials, adapted from Lee. <sup>78</sup> .....	8
Table 2.1: Measured composition of received ytterbium monosilicate powder, and predictions for ytterbium silicates and ytterbia. Data is also shown from individual splats in an as-deposited coating. ....	21
Table 2.2: Atomic compositions for as-deposited ytterbium silicate topcoat calculated from EDS point probe spectra at 550 rectangular grid points distributed over six different collection areas.....	31
Table 2.3: Material parameters and calculated thermal stress at 20°C for coating layers assuming 1300°C stress free temperature and $\alpha$ -SiC substrate.....	38
Table 2.4: Atomic compositions for as-deposited mullite coat calculated from EDS point probe spectra at 550 rectangular grid points distributed over six different collection areas. All values are in at%. ....	41
Table 2.5: Atomic compositions reported by P/B-ZAF (non-standardized) analysis of point probe spectra in Figure 2.16(b).....	47
Table 3.1: Thermophysical properties of EBC system components. ....	58
Table 5.1: Plasma spray parameters for deposition of silicon and mullite layers.....	94

Table 5.2: Current and secondary hydrogen flows for the spray parameters used in this study to deposit the ytterbium silicate layers.....	96
Table 5.3: Chemical compositions of the precipitated particles and matrix in the annealed coatings. ....	107
Table 5.4: Lattice constants calculated from diffraction patterns and PDF cards. ....	108
Table 6.1: Deposition parameters for low power plasma spray parameter EBC layers.	133
Table 6.2: Thermomechanical properties and residual stress of the EBC system components. ....	137
Table 6.3: Properties of tri-layer $\text{Yb}_2\text{SiO}_5/\text{Al}_6\text{Si}_2\text{O}_{13}/\text{Si}$ EBCs.....	159
Table 7.1: Deposition parameters for air plasma sprayed YbDS/Si layers.....	174
Table 7.2: Thermophysical properties of EBC system components.....	178
Table 7.3: YbDS layer thicknesses of samples. Thicknesses range is $\pm 10\mu\text{m}$ .....	179
Table 8.1: Physical and mechanical properties of air plasma sprayed $\text{Yb}_2\text{Si}_2\text{O}_7$ . ....	213
Table 8.2: Physical and mechanical properties of air plasma sprayed Si. ....	218
Table 8.3: Interface toughness $K_c$ of Si – MI-CMC interface at $G_c$ calculated from finite element analysis solutions with phase load angle $\varphi = 29.1^\circ$ .....	222

# **1 Introduction**

The gas turbine engine has profoundly affected society since its initial development during WWII. It has enabled the cost of long distance travel to be dramatically reduced while also making it more reliable, greatly increasing safety, and reducing transit times. The gas turbine's impact upon global trade and other interactions between nations has been dramatic. It is also the power plant for many of the platforms used to ensure national defense including air, land and maritime applications. On top of this, it is used extensively worldwide for the efficient generation of electricity, particularly to meet peak energy demands. In spite of many years of development, the overall efficiency of gas turbine engines remains far from the thermodynamic limits for hydrocarbon combustion. All of the many uses of gas turbines can therefore be advanced by continued improvements to their fuel efficiency and power output.

## **1.1 Evolution of the Gas Turbine Operating Temperature**

Improvements to the fuel efficiency and specific thrust of *future* gas turbine engines will require advances in many areas including; (i) increasing the gas turbine inlet

temperature, (ii) higher overall pressure ratios of engines, (iii) increasing the by-pass ratio and (iv) incorporation of more efficient thermodynamic cycles into novel engine core designs.<sup>1-4</sup> Developments will be paced by the emergence of new propulsion materials, protective coatings, thermal management concepts, and manufacturing tools for economical component fabrication. Arguably, the most difficult materials challenge will be encountered in the engine's hot core section.<sup>2,4-6</sup> Here, severely stressed rotating components will be subjected to ever-increasing temperatures whose upper limit is set by stoichiometric combustion of the Jet-A fuel. At a combustor pressure of 1 MPa and an air charge temperature of 500 °C, the NASA CEA code<sup>7</sup> predicts this fuel burn temperature to be 2255 °C. However, the CEA code gives only an isentropic prediction of combustion. In a real combustion scenario, significant entropy production and thermal transfer occur such that the true limit is likely to be closer to 2,000 °C.

Recent increases to the turbine inlet temperature have been achieved by the use of internal air and surface film cooled superalloy components protected against oxidation and hot corrosion by thermal barrier coating (TBC) systems, Figure 1.1. This strategy is approaching its limit because: coating sintering leads to a loss of compliance and increased thermal conductivity,<sup>8-12</sup> the bond coat oxidation rate (and thus delamination risk) increases rapidly with temperature,<sup>8,13-15</sup> and calcium-magnesium-aluminum-silicate (CMAS) melting and infiltration cause premature coating failure<sup>16-18</sup>. Even if these issues were resolved, TBCs can be eroded by fine (dust) particles<sup>18-21</sup> or chipped away by larger foreign object damage (FOD)<sup>18,21,22</sup>.

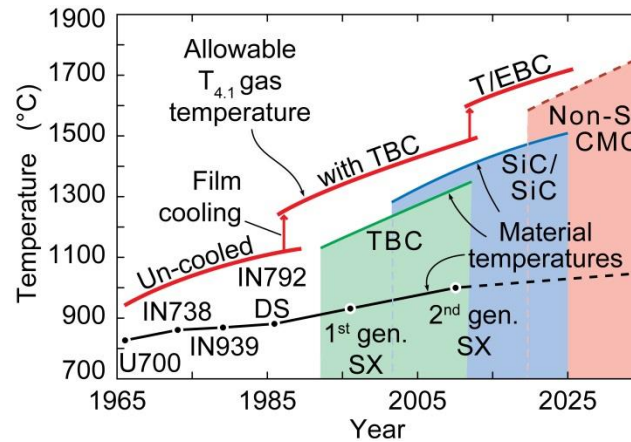


Figure 1.1: The evolution of turbine blade materials, coatings, cooling concepts and turbine inlet  $T_{4.1}$  gas temperature plotted against the year of entry. Current engines utilize internal and film cooled single crystal (SX) superalloy blades protected by thermal barrier coatings in the hottest regions of the engine (adapted from reference)<sup>23</sup>.

Gas path temperature increases might be extended with more aggressive cooling while maintaining current surface temperatures, but additional cooling airflow provided by the compressor would significantly reduce its efficiency. Therefore, as thermal protection concepts for superalloy components used in the most advanced gas turbine engines reach their limits, interest has grown in the development of components made from materials with much higher maximum use temperatures.<sup>24-32</sup> Implementation of such materials systems with significantly elevated use temperature could be beneficial throughout the hot section. First, in the high-pressure section of the turbine, the gas temperature (burn temperature) could be significantly increased keeping all other variables constant. This yields a small increase in propulsive efficiency and a large increase in specific power output of the engine. Second, in the intermediate pressure section of the turbine where temperatures are reduced, the increased temperature capability could allow similar components to be used with reduced cooling, improving

efficiency through a reduction of bleed air drawn from the compressor. Finally, in the low pressure section of the turbine where temperatures are much lower, bleed air could be eliminated. Again, this has the benefit of reducing bleed air consumption, but also greatly simplifies blade design and engine configuration by removing the bleed air system.

All of the considerations listed above are strong incentives for developing advanced materials systems with enhanced thermal capability. Based upon the very high use temperatures desired, ceramic systems are the most viable. Use of ceramics also carries the added benefit of considerably reduced density (technical ceramics are generally 30-50 % of the density of modern superalloys). High temperature technical ceramics would reduce the weight of the engine yielding further increases in aircraft efficiency.

## **1.2 SiC and Ceramic Matrix Composites (CMCs)**

Even “tough” monolithic ceramics such as  $\text{Si}_3\text{N}_4$  have insufficient fracture toughness for critical gas turbine applications. Therefore, materials development has focused upon damage tolerant fiber-reinforced ceramic matrix composites (CMCs) with weak fiber/matrix interfaces. The most promising composites use boron nitride coated SiC fibers (such as Hi-Nicalon S and Sylramic fibers) and SiC matrices incorporated by chemical vapor infiltration with residual pores filled by silicon slurry or melt infiltration followed by carburization.<sup>25,31-38</sup> The BN fiber coating creates a weak interface with the SiC matrix resulting in a highly desirable rising R curve (toughening) response upon micro-scale crack propagation. The composites also offer the high creep resistance needed for stressed rotating components.<sup>31-36,38</sup>

While their high temperature mechanical behavior offers much promise, CMCs are susceptible to fiber embrittling interactions and peeling at temperatures of 700 - 900 °C.<sup>39-45</sup> Also, the normally protective SiO<sub>2</sub> scale grown on SiC reacts with water vapor in hydrocarbon combustion environments to create gaseous silicon hydroxides (Si(OH)<sub>4</sub>) via several reaction pathways.<sup>46-51</sup> The temperature, pressure, incident water vapor flux, and local flow conditions during exposure determine the observed parabolic oxidation kinetics.<sup>47-49,51</sup> SiC recession rates significantly greater than 1 μm/hr have been observed in the 1300-1350 °C range.<sup>46</sup> This can severely impair the useful life and performance of SiC components due to shape change or net section thinning, which would render them unfit for turbine engine application. Consequently, CMC components must be protected by environmental barrier coatings (EBCs) to prevent component damage during operational lifetimes of thousands of hours.

The design of EBCs is therefore driven by a different combination of objectives to those governing the design of thermal barrier coating (TBC) systems, where the objective is to reduce a metal component's surface temperature while also protecting it from oxidation and various forms of hot corrosion.<sup>52-57</sup> Furthermore, unlike TBC systems, EBCs will eventually be used as a "prime-reliant" coating, since the life of unprotected SiC components under mechanical load in a combustion environment will be very short due to a combination of the damage mechanisms identified above.<sup>46,51,58-60</sup> However, they must still meet the demands of the engine environment shared with TBCs, including foreign object damage (FOD)<sup>18,21,22</sup> and reactions with molten calcium-magnesium-aluminum-silicates<sup>16-18,61,62</sup> (CMAS). Finally, when used on rotating components, EBCs will be required to sustain significant static and cyclic loads that can cause fracture and

creep.<sup>56,63-69</sup> The combination of these constraints with the high target use temperature leads to one of the most severe environments ever envisioned for the use of an advanced materials system. Therefore, the design of robust EBCs is likely to pace the implementation of CMCs in gas turbines.

### 1.3 First Generation Environmental Barrier Coatings (EBCs)

The first EBCs were proposed in the 1990's and consisted of a 3:2 mullite ( $3\text{Al}_2\text{O}_3 \cdot 2\text{SiO}_2$  or  $\text{Al}_6\text{Si}_2\text{O}_{13}$ ) coating applied directly to the SiC substrate.<sup>70</sup> During prolonged high temperature exposure, silica was volatilized from the mullite leaving an alumina scale that spalled readily, offering only short protection times.<sup>60</sup> Mullite was also found to suffer from severe cracking upon annealing when deposited onto ambient temperature substrates by air plasma spray (APS). This cracking was linked to high volume fractions of amorphous material and was remedied by performing APS depositions into a box furnace held above the crystallization point of mullite ( $\sim 1,000$  °C).<sup>70</sup> Deposition onto heated substrates was found to result in crystalline mullite with significantly improved adherence and reduced cracking after annealing. However, the improved coatings still did not provide adequate protection times as  $\text{SiO}_2$  was volatilized from the mullite surface and preferential attack through mud cracks was observed.<sup>59</sup>

The next EBC development focused on bi-layer concepts in which an yttria-stabilized zirconia (YSZ) topcoat was used to prevent volatilization (chemical attack) of the underlying mullite.<sup>71</sup> Thermal cycling tests in water vapor revealed that the coating quickly cracked and delaminated at either the YSZ –  $\text{Al}_6\text{Si}_2\text{O}_{13}$  or the  $\text{Al}_6\text{Si}_2\text{O}_{13}$  – SiC

interfaces. The rapid failure was attributed to the substantial CTE mismatch between YSZ, the underlying mullite layer and the substrate.<sup>60,72-75</sup> One additional drawback of such coating schemes with mullite applied directly to the substrate was the formation of a porous, low viscosity SiO<sub>2</sub> scale at the mullite – SiC interface.<sup>59</sup> This was linked to both chemical contamination of the SiO<sub>2</sub> scale and the bubbling of gaseous species (resulting from oxidation of SiC) through the scale. The end result was poor adhesion and premature spallation of the coating at the mullite – SiC interface.<sup>71,76</sup> Improved adherence of the coating was determined to be a critical priority for enhanced durability.

#### **1.4 Second Generation EBCs**

Several alkaline earth and rare earth silicates were identified with well-matched CTEs in the late 1990's and early 2,000's that exhibited little weight change during high temperature, high water vapor pressure environmental exposure,<sup>77,78</sup> Table 1.1. Barium-strontium aluminosilicate (BSAS) has a low silica activity and a CTE that is well matched with substrates. However, BSAS reacts with thermally grown silica, necessitating an intermediate Al<sub>6</sub>Si<sub>2</sub>O<sub>13</sub> layer architecture<sup>79</sup> to eliminate failure at the coating/substrate interface and increase EBC life.<sup>59</sup> It was also identified that applying a layer of Si in between the Al<sub>6</sub>Si<sub>2</sub>O<sub>13</sub> layer and the substrate considerably improved the adherence of the coating.<sup>80</sup> This was due to the pre-reaction of oxidizer with pure Si, which unlike SiC does not emit CO and therefore forms a dense scale.<sup>59,79</sup> Though this EBC had lifetimes over 1,000 hours below 1300 °C, low melting eutectics from above this temperature and limit the useful lifetime to under 1,000 hours.<sup>79</sup> This discovery

indicated the need for EBC topcoats to have reasonably matched CTE, low volatility, and high temperature phase stability over extended durations.

*Table 1.1: Thermal expansion coefficients of EBC materials, adapted from Lee.<sup>78</sup>*

Material	CTE ( $\times 10^{-6} \text{ }^\circ\text{C}^{-1}$ )	Melting Point ( $^\circ\text{C}$ )	Application
$\text{Y}_2\text{SiO}_5$	5–6	1980 <sup>81</sup>	
$\text{Er}_2\text{SiO}_5$	5–7, 7–8 <sup>a</sup>	1980 <sup>81</sup>	
$\text{Yb}_2\text{SiO}_5$	3.5–4.5, 7–8 <sup>a</sup>	1950 <sup>81</sup>	
$\text{Lu}_2\text{Si}_2\text{O}_7$	3.8 <sup>82</sup>	unknown	
$\text{Sc}_2\text{Si}_2\text{O}_7 + \text{Sc}_2\text{O}_3$	5–6	1860 <sup>b</sup>	Topcoat
$\text{Yb}_2\text{Si}_2\text{O}_7$	4–6 <sup>83</sup>	1850 <sup>81</sup>	
$\text{Yb}_2\text{O}_3$	6.8–8.4 <sup>84</sup>	2415 <sup>c</sup>	
BSAS (monoclinic)	4–5	1300 <sup>79</sup>	
BSAS (hexagonal)	7–8	1300 <sup>79</sup>	
Mullite	5–6	1800 <sup>85</sup>	Intermediate coat
Alumina	6.0–8.4 <sup>86</sup>	2072 <sup>87</sup>	coat
Si	3.5–4.5	1400 <sup>88</sup>	Bond coat
SiC, SiC/SiC	4.5–5.5	2545 <sup>89</sup>	
$\text{Si}_3\text{N}_4$	3–4	1875 <sup>90</sup>	Substrate

<sup>a</sup> more recent value reported.<sup>77</sup>

<sup>b</sup> Lower-melting eutectic at 1770  $^\circ\text{C}$  on  $\text{Sc}_2\text{O}_3$ -rich side and 1660  $^\circ\text{C}$  on  $\text{SiO}_2$ -rich side.<sup>91</sup>

<sup>c</sup> Undergoes pre-melt phase transformation at 2360  $^\circ\text{C}$ .<sup>92</sup>

Ytterbium and lutetium silicates exhibit some of the lowest volatilities in steam, and are monomorphic. Ytterbium has reported properties for both monosilicate ( $\text{Yb}_2\text{SiO}_5$ ) and disilicate ( $\text{Yb}_2\text{Si}_2\text{O}_7$ ) variants whereas lutetium disilicate ( $\text{Lu}_2\text{Si}_2\text{O}_7$ ) has only reported thermal expansion data. The CTE of these and other candidate materials are summarized in Table 1.1. Like BSAS, the RE-silicates are reportedly unstable as single layer coatings applied to SiC substrates, and so a tri-layer RE-silicate/mullite/silicon coating approach analogous to the BSAS topcoat EBC has been proposed.<sup>78</sup>

These tri-layer RE-silicate based EBCs reportedly have lifetimes of several hundred hours during steam-cycling at 1316 °C in slowly flowing 90 % H<sub>2</sub>O/10 % O<sub>2</sub>.<sup>77,78</sup> Despite the range of reported life, no lifetime data has been published. Additionally, though thermochemistry has been considered extensively, the thermomechanical behavior of EBCs has not been addressed in the open literature. This leaves a serious fundamental gap in the knowledgebase of environmental barrier coating performance. Particularly for the target “prime-reliant” application, understanding of the mechanical damage experienced by EBCs during thermal cycling and how this damage interacts with the environment is crucial.

In summary, for applications up to 1316 °C (2400 °F) research has focused on EBC systems consisting of a Si “bond coat” applied to the SiC, which is then covered by materials that impede the diffusion of oxygen and water vapor and that are resistant to steam volatilization.<sup>59,63,64,66,77-79,93-98</sup> The design objective for the bond coat is similar to that of the aluminum-rich metallic layer used in TBC systems. It serves as a sacrificial layer forming a protective oxide (SiO<sub>2</sub>) upon exposure to oxidizers, thereby inhibiting oxidizing species’ access to the SiC-based component surface. The objective of the upper EBC layers is to reduce the Si layer’s outer surface exposure to oxygen and steam, while also being highly resistant to steam volatilization itself.<sup>77,78</sup> Though several candidate systems have been proposed, the coating lifetime and the mechanisms by which these coatings are damaged in steam-cycling or true exposure have yet to be documented in open literature.

## 1.5 Air Plasma Spray (APS) Deposition

Plasma spray deposition methods have been developed in various forms for nearly 70 years, and are widely used to deposit a variety of surface protective coatings.<sup>99-102</sup> The air plasma spray (APS) process is an economic and often reliable method for the deposition of such coatings, and has attracted attention for the deposition of EBCs on SiC components.<sup>59,60,63-67,70,71,76-79,93-95,97,98,103-109</sup> This is a logical extension to the already widespread use of APS for deposition of the TBC systems used to protect superalloy components in current gas turbine engines.<sup>68,98,100,110-125</sup> Interest is therefore growing in the relationships between plasma spray deposition conditions and the composition, structure, and defect populations of coating layers deposited from EBC materials.

The fundamental interactions of interest in APS processing are those between the plasma spray parameters, the thermal and jet flow characteristics of the plasma plume, the composition and size distribution of the injected particles, chemical and flow interactions with the surrounding atmosphere, and the substrate surface roughness and temperature during deposition. These interactions have been studied for APS deposition via both simulation and experiment.<sup>72,126-147</sup> Increases of the direct arc current and secondary gas concentration (such as H<sub>2</sub>) have been demonstrated to increase the peak temperature within the plasma plume and thus that experienced by powder particles. They also increase the plasma plume's velocity, which results in a decreased particle residence time in the plasma, moderating the effect of the higher heating rate on particle temperature. Changes to the standoff distance between the exit of the torch and the substrate also change a particle's residence time, and its velocity and temperature upon impingement with the substrate.

The particle temperature history is primarily controlled by the powder size distribution and the precise trajectory a particle takes through the plasma flow.<sup>99,127-129,131,133-137,147-149</sup> The APS process therefore exhibits substantial stochastic character: small diameter particles that take trajectories through high temperature regions of the plasma jet may be super-heated and change composition by evaporative losses while larger particles traveling through comparably cool regions of the plasma may barely melt. The result is a coating containing a variety of droplet (splat) shapes and compositions after substrate impact, generally with the intentional incorporation of substantial porosity. Consequently, all of the plasma spray variables above can affect the composition, microstructure and defect populations within a coating.

Despite the application of EBCs to SiC components by APS techniques for over 20 years, no studies have been published detailing the relationships between the processing parameters and microstructure of EBCs. Great interest and opportunity therefore exists to study APS deposition of the unusual RE and heavy metal silicate compounds desired for topcoat applications. Furthermore, since the design constraints are different from TBCs (as indicated in Section 1.2), different microstructures are desirable. Therefore, different and previously unused combinations of spray parameters may be necessary for deposition of low porosity EBC microstructures. These issues have yet to be addressed, but will be of great interest as EBC concepts mature.

## 1.6 Mechanical Properties of APS Materials

As candidate EBC coating concepts begin to be identified for turbine engine applications, a more comprehensive understanding of their thermomechanical properties is needed to assess their response during exposure in future gas turbines, in particular for utilizing ceramic rotating components that are internally cooled. EBC research appears to be following the pattern of thermal barrier coating (TBC) systems, where thermochemistry, environmental stability and thermal cyclic durability of TBCs were studied for many years before the mechanical properties of TBCs were examined rigorously.<sup>57,114,120-124,150-153</sup> At this point the thermochemistry and environmental stability of several early generation EBCs applied to ceramic matrix composites (CMCs) have been assessed. Several studies have even been performed using advanced testing equipment that more accurately represents the turbine environment than steam-cycling testing,<sup>63-67</sup> but studies of the mechanical properties of current baseline and candidate EBC materials remain unpublished.

Characterization of both quasi-static and time-dependent mechanical properties of EBCs is particularly important for understanding failure modes and modeling the long duration response of coating systems. If the time dependent deformation of EBC materials can be approximated by the general creep constitutive equations of ceramics, their primary creep strain rate can be written as:

$$\frac{d\varepsilon}{dt} = e^{-Ea/RT} * \sigma^n * t^{-s} \quad 1.1$$

where  $\sigma$  is the applied stress,  $t$  is time,  $T$  is absolute temperature,  $R$  is the gas constant, and the relevant creep parameters are the activation energy  $E_a$ , the creep stress exponent  $n$ , and the primary creep time dependence  $s$ .<sup>154</sup>

Their secondary (steady state) creep strain rate also depends upon the same parameters:

$$\frac{d\varepsilon}{dt} = e^{-E_a/RT} * \sigma^n \quad 1.2$$

In TBC systems, these properties have been studied comprehensively by Choi, Zhu, and Miller<sup>120</sup> for both quasi-static and time-dependent properties. Others have also performed considerable in-depth analysis for both APS and EB-PVD coating systems.<sup>122-125</sup> Measurement of such properties allows analysis of both the stored strain energy and stress states of the coating, as well as how these evolve over time. Consequently, the driving forces for both quasi-static and time-dependent mechanical failure can be addressed in these systems.

The previously mentioned creep studies of TBC materials have been performed using 4-point flexure creep.<sup>120,122-125</sup> The validity of flexure creep has been discussed at length for such applications.<sup>155,156</sup> Based on several literature sources that examined high temperature flexure creep of a variety of ceramic materials,<sup>157-173</sup> the general conclusion is that flexure creep is a useful quantitative method due to the simplicity and greatly reduced cost when compared to uniaxial creep. It may also be favored for more brittle specimens such as coatings due to the smaller volume of material placed under maximum stress. However, flexure creep should not be used for engineering design curves due to

uncertainties in calculations of stress and strain arising from shifts in the neutral axis, differences in tensile and compressive creep behavior, difficulty in analytical modeling of flexure creep, and uncertainty in achieving steady state secondary creep, among others.<sup>155,156</sup> For preliminary investigations of materials systems such as EBCs, however, the 4-point flexure creep technique remains quite appealing.

Despite the proliferation of mechanical properties testing and processing – microstructure – property analyses of TBC systems, EBC materials have yet to be evaluated and documented in such a manner. All of the same fabrication and testing methodologies apply so that direct transference of tests is straightforward. It has also been clearly demonstrated that the mechanical performance of EBCs is of great concern.<sup>65,67,77,78,94</sup> This knowledge gap is therefore another critical issue that must be addressed in EBC literature to allow continued investigation and increased understanding of EBC performance.

## 1.7 Dissertation Goals

This dissertation was performed with the aim of filling some of the knowledge gaps identified in the literature. This is addressed by developing an understanding of the fundamental intrinsic and extrinsic factors that affect the durability of model EBC systems. The first goal is to assess the performance of the previously proposed tri-layer  $\text{Yb}_2\text{SiO}_5/\text{Al}_6\text{Si}_2\text{O}_{13}/\text{Si}$  EBC in a steam-cycling environment. This will be achieved by depositing and thoroughly characterizing the structure of the coating and identifying the mechanisms by which the coating is damaged during isothermal cyclic exposure (steam

cycling). The second goal is to develop an APS capability that enables study of the relationships between deposition parameters and the resultant microstructure of deposited coating layers. The third goal is to use the knowledge gained in the preceding efforts to propose and test a revised EBC with substantially improved performance in steam cycling. Finally, the fourth goal assesses the viability of steam-cycling qualified EBC systems in the mechanically loaded environment experienced by a rotating turbine blade.

## **1.8 Dissertation Outline**

Chapter 1 has briefly reviewed the evolution of the gas turbine field and development of ceramic composite components, which require protective EBCs for use in this application. Chapter 2 analyzes the structure of a model tri-layer  $\text{Yb}_2\text{SiO}_5/\text{Al}_6\text{Si}_2\text{O}_{13}/\text{Si}$  EBC deposited using the original hardware and deposition parameters from which that EBC system was developed, and Chapter 3 analyzes the performance of that system in steam-cycling. There, the various effects of sample geometry, oxidizing/volatilizing environment, and cyclic exposure are first introduced and discussed. Chapter 4 addresses the selection, installation, and operation of an APS system at the University, which was executed as part of this dissertation. The unique qualities of this system and several modifications that allow for improved coatings are discussed. Chapter 5 describes studies of the processing-microstructure relationships developed using the APS system at UVA. This analysis focuses primarily on the development of EBC topcoats, which are found to suffer from preferential volatility issues during deposition.

Chapter 6 assesses the performance of a revised tri-layer  $\text{Yb}_2\text{SiO}_5/\text{Al}_6\text{Si}_2\text{O}_{13}/\text{Si}$  EBC deposited at UVA. This system was developed with the intention of remedying several of the issues that compromised the EBC tested in Chapter 3. The alternate microstructure and an associated new failure mode are discussed. Chapter 7 examines an alternate baseline bi-layer  $\text{Yb}_2\text{Si}_2\text{O}_7/\text{Si}$  EBC. The coating's greatly improved performance in steam cycling is discussed in the context of an environmental barrier layer, as well as several damage mechanisms that are observed to occur over long duration steam cycling. Chapter 8 details mechanical tests performed on APS  $\text{Yb}_2\text{Si}_2\text{O}_7$  and APS Si. Both quasi-static and time-dependent properties of these materials are examined. Their behavior is compared to bulk materials, and interpreted in the context of EBC applications for stressed (rotating) hardware such as turbine blades. A comprehensive discussion of the results of the various chapters is presented in Chapter 9, and Chapter 10 provides concluding remarks from the dissertation as well as suggestions for future research directions in the field of environmental barrier coatings.

## **2 Plasma Spray Deposition of Tri-Layer Environmental Barrier Coatings<sup>1</sup>**

**Synopsis:** An air plasma spray process has been used to deposit tri-layer environmental barrier coatings consisting of a silicon bond coat, a mullite inter-diffusion barrier, and an  $\text{Yb}_2\text{SiO}_5$  topcoat on SiC substrates. Solidified droplets in as-deposited  $\text{Yb}_2\text{SiO}_5$  and mullite layers were discovered to be depleted in silicon. This led to the formation of an  $\text{Yb}_2\text{SiO}_5 + \text{Yb}_2\text{O}_3$  two-phase topcoat and 2:1 mullite ( $2\text{Al}_2\text{O}_3 \cdot \text{SiO}_2$ ) coat deposited from 3:2 mullite powder. The compositions were consistent with preferential silicon evaporation during transient plasma heating; a consequence of the high vapor pressure of silicon species at plasma temperatures. Annealing at 1300 °C resulted in internal bond coat oxidation of pore and splat surfaces, precipitation of  $\text{Yb}_2\text{O}_3$  in the topcoat, and transformation of 2:1 mullite to 3:2 mullite +  $\text{Al}_2\text{O}_3$ . Mud-cracks were found

---

<sup>1</sup> Based upon a peer reviewed technical article published in the *Journal of the European Ceramic Society*.<sup>97</sup>

in the  $\text{Yb}_2\text{SiO}_5$  layer and in precipitated  $\text{Al}_2\text{O}_3$  due to the thermal expansion mismatch between these coating phases and the substrate.

Several parts of this work were collaborative. Dennis Fox, Bryan Harder, and Michael Cuy of the NASA Glenn Research Center aided in deposition of the APS coatings described in this chapter. The depositions were performed using the original APS equipment upon which EBCs were developed at NASA. Md Shamsujjoha (UVA) helped in the residual stress measurements described and Elizabeth Opila (UVA) provided invaluable advice on thermochemistry and FactSage. Some imaging in this work was performed at VT's ICTAS NCFL.

## 2.1 Introduction

EBC concepts based upon barium-strontium aluminosilicate (BSAS), which has a low silica activity and a CTE that is well matched with substrates, Table 1.1, have attracted significant interest. However, BSAS EBCs have been found to react with thermally grown silica, necessitating a tri-layer BSAS/mullite/silicon EBC architecture<sup>79</sup> to eliminate failure at the coating/substrate interface and increase EBC life.<sup>59</sup> Unfortunately, low melting eutectics occur near 1300 °C and limit the useful lifetime to under 1,000 hours for higher temperatures,<sup>79</sup> indicating the need for topcoats with low volatility *and* high temperature phase stability. Ytterbium and lutetium silicates exhibit some of the lowest volatilities and are monomorphic. Ytterbium has monosilicate ( $\text{Yb}_2\text{SiO}_5$ ) and disilicate ( $\text{Yb}_2\text{Si}_2\text{O}_7$ ) variants with reported properties. The CTE of these and other candidate materials were also summarized in Table 1.1. The data for  $\text{Yb}_2\text{SiO}_5$  is

inconsistent. One report<sup>78</sup> gives a value of  $3.5\text{-}4.5 \times 10^{-6} \text{ }^\circ\text{C}^{-1}$  which is reasonably matched to SiC. However, a more recent report gives a higher value of  $7\text{-}8 \times 10^{-6} \text{ }^\circ\text{C}^{-1}$ .<sup>77</sup> Like BSAS, the RE-silicates are reported to be unstable as single layer coatings and so a tri-layer RE-silicate/mullite/silicon coating approach analogous to the BSAS topcoat EBC has been proposed.<sup>78</sup>

There have been few studies of the tri-layer EBC deposition process or investigations of the relationships between coating deposition conditions, coating structure, and thermo-cyclic durability. To gain insight into these relationships, an air plasma spray (APS) process is used to deposit tri-layer coatings on silicon carbide substrates with  $\text{Yb}_2\text{SiO}_5$  topcoats, and a wide variety of methods was used to characterize the coatings. The presence and formation mechanisms of previously unidentified phases in the  $\text{Yb}_2\text{SiO}_5$  and mullite layers described, and discussed in light of their propensity for inducing cracking.

## **2.2 Experimental**

### **2.2.1 Coating Deposition**

Three-layer  $\text{Yb}_2\text{SiO}_5$ /mullite/silicon EBCs were deposited onto SiC substrates using an APS approach. The general coating architecture is schematically illustrated in Figure 2.1. Coatings were deposited on 25.4 mm x 12.7 mm x 3.2 mm  $\alpha$ -SiC coupons obtained from Hexoloy<sup>TM</sup> (Saint Gobain Ceramics, Niagara Falls, NY). Prior to EBC deposition, the substrates were grit blasted using  $\sim 270 \text{ }\mu\text{m}$  diameter SiC grit (Black SiC, White Abrasives, Niagara Falls, ON CA) resulting in an average surface roughness  $R_a = 1 \text{ }\mu\text{m}$ , as

measured by surface profilometry using a 500  $\mu\text{m}$  sampling distance. The substrates were then ultrasonically cleaned in ethanol to remove surface contamination.

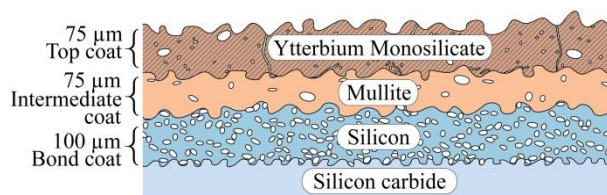


*Figure 2.1: Schematic illustration of an APS deposited tri-layer EBC structure.*

The silicon powder used for bond coat deposition was supplied by Micron Metals (Bergenfield, NJ) with a particle diameter range of 10 to 44  $\mu\text{m}$ . The mullite powder provided by Saint Gobain Ceramics (Worcester, MA) had a particle diameter of 16 to 53  $\mu\text{m}$ . The  $\text{Yb}_2\text{SiO}_5$  powder was supplied by Treibacher Industrie Inc. (Toronto, ON) with a particle diameter of 20 to 50  $\mu\text{m}$ . The composition certified powders were identified by their respective manufacturers as fully reacted and phase pure, and confirmed by XRD prior to deposition. The composition of the  $\text{Yb}_2\text{SiO}_5$  powder was also measured using EDS on polished cross sections. Using a P/B-ZAF algorithm (Bruker Corporation, Ewing, NJ; algorithm that relates the recorded spectrum to primary X-ray generation: Peak to Background modified – Z atomic number, Absorption, and secondary Fluorescence corrected), the composition was found to be very close to that of  $\text{Yb}_2\text{SiO}_5$  with variability of about  $\pm 0.5$  at%, Table 2.1.

The coatings were deposited using two air plasma spray systems at the NASA Glenn Research Center.<sup>70</sup> The silicon bond coat was deposited using an ambient substrate temperature APS system with a Sulzer Metco 9MB torch at a standoff distance of 100 mm. The two other coating layers were deposited at 1200  $^\circ\text{C}$  within a box furnace, using

a plasma torch originally designed by Electro-Plasma Inc. (EPI) with a standoff distance of 190 mm, Figure 2.2. Each spray system had a single Plasmatron Roto Feed Hopper (Model 1251) with standard powder feed wheel that was set to 2.2 RPM. Based on a similar powder feed system, we estimate the  $\text{Yb}_2\text{SiO}_5$  feed rate was  $\sim 27$  g/min and the mullite feed rate was  $\sim 13$  g/min. The fineness of the silicon powder led to difficulties with catch can experiments, but we project (based on differently sized Si powder) that the feed rate was  $\sim 10$  g/min.

*Table 2.1: Measured composition of received ytterbium monosilicate powder, and predictions for ytterbium silicates and ytterbia. Data is also shown from individual splats in an as-deposited coating.*

Spectrum Location	Yb (at%)	Si (at%)	O (at%)
Powder <sup>a</sup>	21.0-22.1	13.3-13.6	64.4-65.6
$\text{Yb}_2\text{SiO}_5$	25	12.5	62.5
$\text{Yb}_2\text{Si}_2\text{O}_7$	18.2	18.2	63.6
$\text{Yb}_2\text{O}_3$	40	0	60
Point 1	37.3	4.0	58.7
Point 2	32.9	7.0	60.1
Point 3	31.6	8.4	60
Point 4	29.6	9.9	60.4
Point 5	27.4	12.5	60.1
Point 6	26.5	12.4	61.1

<sup>a</sup> 95% confidence interval

The silicon bond coat was deposited onto unheated substrates using a torch power of 50 kW. The plasma forming gas was a 2:1 mixture of Ar and  $\text{N}_2$  with a flow rate of 3400 slm. The plasma plume was traversed 3 times across the sample at a speed of 1250 mm/s using six-axis robotic manipulation. For the mullite and  $\text{Yb}_2\text{SiO}_5$  topcoat deposition, the silicon coated substrates were heated to 1200 °C inside a box furnace containing a small aperture through which APS depositions were performed, Figure 2.2. The mullite layer was deposited using a plasma power of 56k W; the  $\text{Yb}_2\text{SiO}_5$  was deposited at a lower

power of 35 kW. Both coatings were deposited using a 2:1 mixture of Ar and He for the plasma forming gas and a flow rate of 763 slm. These coating layers were deposited by traversing the plasma plume twice across the samples at a speed of 950 mm/s. After fabrication, some samples were stabilization annealed in air at 1300 °C for 20 hours.

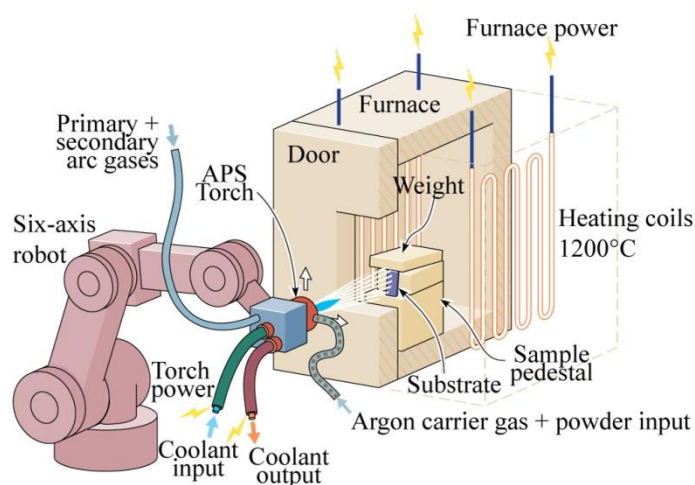


*Figure 2.2: Schematic illustration of the APS and substrate heating system used to deposit the environmental barrier coatings.*

### 2.2.2 Characterization

Both the as-fabricated and annealed samples were subjected to XRD analysis using a PANalytical X'Pert PRO MPD diffractometer (Westborough, MA) and Cu K $\alpha$  radiation to identify topcoat phases and volume fractions. Residual stress was calculated for the topcoat from XRD measurements using the  $\sin^2\psi$  technique<sup>174</sup> with  $\chi$  tilts of 0 °, 18.43 °, 26.56 °, 33.21 °, 39.23 °, and 45 ° for diffraction peaks ( $2\theta$ ) between 55 ° and 65 °. Diffraction peaks of this low angle reflection were used because neither Yb<sub>2</sub>O<sub>3</sub> nor Yb<sub>2</sub>SiO<sub>5</sub> had high angle peaks of measurable intensity. The low angle of the peaks prohibits precise measurements, but reported figures are semi-quantitative assessments of

the stress state. Peak center fitting was accomplished using a Gaussian fitting algorithm (Solver in Microsoft Excel) that included a slanting background fit. Additionally, both as-fabricated and annealed samples were sectioned and diamond polished to 0.25  $\mu\text{m}$  finish, and in some cases vibrapolished using 0.02  $\mu\text{m}$  silica colloid suspension. They were then examined by SEM in BSE mode, and with EDS.

The difference in electron backscattering coefficient  $\eta$  between regions of disparate composition was utilized during coating characterization. It relates the flux of backscattered electrons emitted from the sample to the flux of incident electrons in the probe. This factor can be calculated for a multicomponent mixture using a weighted sum:  $\eta_{mix} = \sum \eta_i C_i$  where  $\eta_i$  is the backscatter coefficient for the  $i$ -th element in pure form, and  $C_i$  the weight fraction for the  $i$ -th element in the compound.<sup>175</sup> The backscatter coefficient for each pure element may be estimated (for a broad range of accelerating voltages) using an empirical expression:<sup>176</sup>

$$\eta_i = -0.0254 + (0.016)Z_i - (1.86 \times 10^{-4})Z_i^2 + (8.3 \times 10^{-7})Z_i^3 \quad 2.1$$

where  $Z_i$  is the atomic number of the  $i$ -th element. Contrast in BSE images was adjusted using gamma-correction over multiple ranges of the 16-bit spectrum to preserve detail of compositional variation within each coating layer.

The EDS spectra were standardized (except where noted) using an aggregate spectrum from the respective powders for calibration. To form the calibration standard, spectra were collected from a minimum of 20 randomly selected particles of the as-received powder with greater than  $2.5 \times 10^5$  total counts for each spectrum. The net integrated intensity under the respective peaks was summed to attain a total standard

spectrum for the respective compound with greater than 5 million total counts. Crack and pore distributions were calculated by image analysis using an average from 3 different areas of the same sample where a 100  $\mu\text{m}$  length of the layer was examined.

### **2.2.3 Dilatometry**

We have measured the CTE of the ytterbium monosilicate using a Netzsch 402C Dilatometer (Burlington, MA) calibrated with high purity alumina. The  $\text{Yb}_2\text{SiO}_5$  sample was prepared by hot-pressing the as-received  $\text{Yb}_2\text{SiO}_5$  powder for 3 h at 1650  $^\circ\text{C}$  with  $\sim 40$  MPa load. The hot pressing resulted in a blank that was  $\sim 70$  % dense. Ignoring anisotropic mechanical effects, this low density should not alter the CTE. The  $\text{Yb}_2\text{SiO}_5$  dilatometry sample was cut from the blank with dimensions of 4 mm x 4 mm x 14 mm. The tests were performed between 20  $^\circ\text{C}$  and 1450  $^\circ\text{C}$  using heating and cooling rates of 3  $^\circ\text{C}/\text{min}$ . The expansion displacement data was recorded at 0.05  $^\circ\text{C}$  steps and used to compute the expansion strain and CTE. CTE curves have been smoothed whereas expansion curves have not.

## **2.3 Results and Discussion**

### **2.3.1 $\text{Yb}_2\text{SiO}_5$ Thermal Expansion Coefficient**

The thermal expansion strain versus temperature relationships during heating and cooling of hot pressed  $\text{Yb}_2\text{SiO}_5$  are shown in Figure 2.3. The hysteresis upon heating and cooling is similar to that previously reported for RE tungstate's of low crystal symmetry, attributed to anisotropic thermal expansion.<sup>177</sup> The CTE deduced from the strain data is

also shown in Figure 2.3. The CTE during heating ranged from  $5.7\text{-}9.1 \times 10^{-6} \text{ }^\circ\text{C}^{-1}$ , while during cooling it varied from  $2.8\text{-}10.9 \times 10^{-6} \text{ }^\circ\text{C}^{-1}$ . Standard convention is to report the CTE measured during the heating phase of the test, and we report an average CTE of  $7.4 \times 10^{-6} \text{ }^\circ\text{C}^{-1}$ , which supports the most recent value reported by Lee,<sup>77</sup> Table 1.1. While hysteresis of the thermal expansion strain was observed, no permanent change in length occurred ( $<0.02\%$  difference in length at  $200 \text{ }^\circ\text{C}$ ), indicating that sintering did not contribute to the measured CTE.

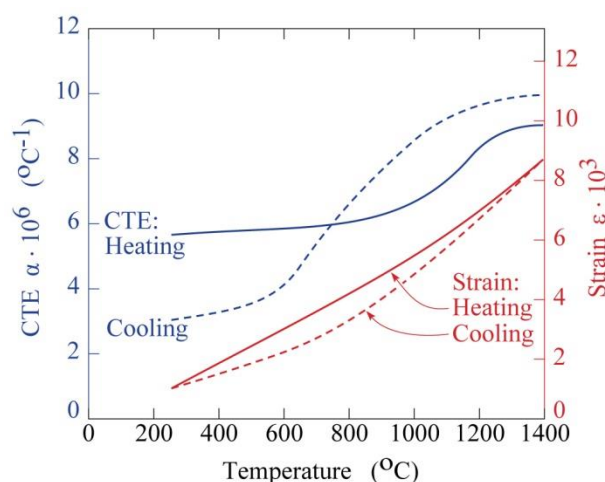


Figure 2.3: Thermal expansion and CTE data for hot-pressed  $\text{Yb}_2\text{SiO}_5$  with a relative density of  $\sim 70\%$ .

### 2.3.2 Tri-layer EBC Structure

A BSE image of an as-deposited tri-layered EBC system is shown in Figure 2.4(a). Detailed measurements over the  $12.7 \text{ mm}$  wide coating indicated a variation in silicon bond coat thickness of  $75$  to  $150 \text{ }\mu\text{m}$ , a mullite layer thickness variation of  $25$  to  $100 \text{ }\mu\text{m}$ , and an  $\text{Yb}_2\text{SiO}_5$  topcoat thickness between  $25$  and  $100 \text{ }\mu\text{m}$ . These variations resulted from fluctuations in the powder feed rate (“powder pulsing”, presumably due to low feed

RPM) and temperature variation of the particles which impacted the surface: those that had not sufficiently melted did not adhere to the sample, and those that were too hot may have “splashed” off. Mud-cracking of the topcoat was observed in the as-deposited coatings, Figure 2.4(a). These mud-cracks were spaced several hundred micrometers apart, and frequently extended into the mullite layer during the stabilization annealing treatment, Figure 2.4(b), but were arrested at the silicon bond coat confirming previous observations.<sup>78</sup> The average mud crack spacing was 276  $\mu\text{m}$  with a standard deviation of 103  $\mu\text{m}$ . The large variance is reflective of the variety of spacing captured by 2D analysis of the 3D structure. All three layers contained porosity in the as-deposited condition; it was not removed by stabilization annealing.

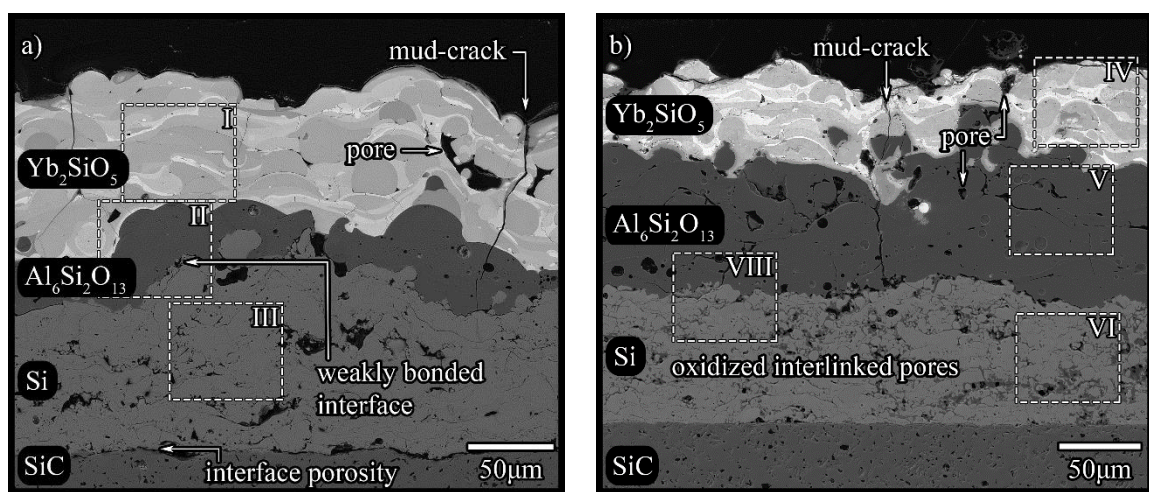


Figure 2.4: BSE micrographs of  $\text{Yb}_2\text{SiO}_5/\text{Al}_6\text{Si}_2\text{O}_{13}/\text{Si}$  three layer EBC; (a) as-fabricated and (b) after a 20 hour stabilization anneal in air at  $1300^\circ\text{C}$ . Dashed boxes indicate regions where higher magnification micrographs are subsequently analyzed.

Adhesion between the silicon bond coat and the SiC substrate appeared good, except in areas with high interfacial porosity, Figure 2.4(a). Though the pores on the interface were small, they were numerous with 5-10 pores of 3-5  $\mu\text{m}$  diameter intersecting each

100  $\mu\text{m}$  length of interface. The interface between the silicon bond coat and mullite also contained isolated regions of weak bonding that appeared to result from incomplete flow of the liquid mullite droplets over the rough silicon bond coat, Figure 2.4. The length of these regions ranged from a few to approximately 30  $\mu\text{m}$ . These more weakly bonded regions were generally spaced a few hundred micrometers apart. The interface between the mullite and the  $\text{Yb}_2\text{SiO}_5$  had very little porosity. The several micrometer long pores observed were typically located in areas where the radius of curvature of the underlying mullite coat was smallest.

### **2.3.3 *Yb<sub>2</sub>SiO<sub>5</sub> Topcoat***

Splat-to-splat adherence in the ytterbium monosilicate coat appeared very good, though some spherical pores (with pore diameter of  $<0.5 \mu\text{m}$ ) and more elongated porosity were seen at both splat-to-splat boundaries and within splats, Figure 2.5(a). The planar density of these pores in cross-section was approximately 50 pores per  $1,000 \mu\text{m}^2$  of coating. Pores of diameter  $<0.5 \mu\text{m}$  contributed about 0.2 % to the total porosity while the contribution from larger spherical pores was around 0.7 %. Filling defects (non-spherical/jagged pores) contributed roughly 0.6 % to the total porosity, resulting in a total void volume fraction of about 1.5 %.

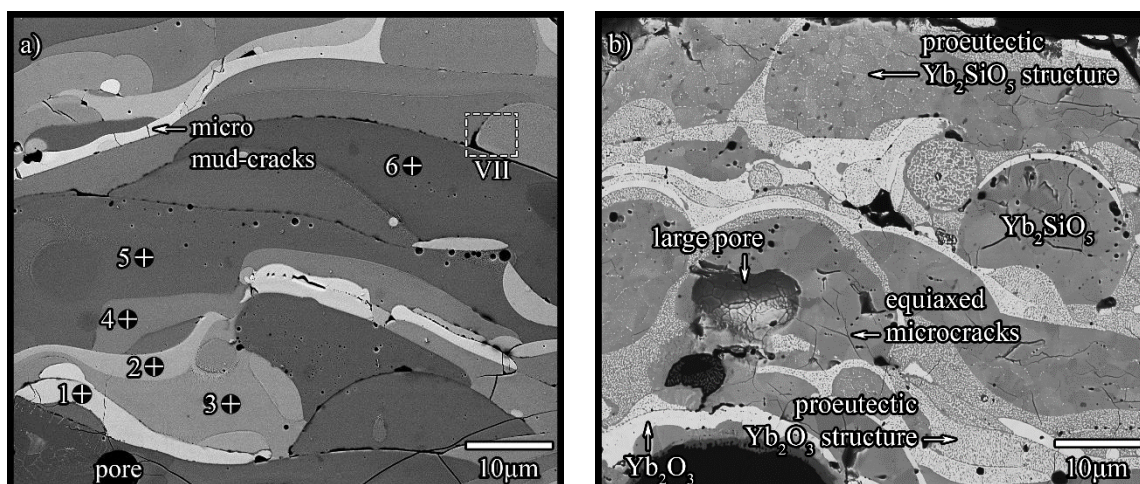


Figure 2.5: High magnification micrographs of the  $\text{Yb}_2\text{SiO}_5$  topcoats from; (a) region I in the as-deposited micrograph- Figure 2.4(a), and (b) region IV in the annealed condition micrograph- Figure 2.4(b).

Large vertical mud-cracks were present in as-deposited coatings, Figure 2.4(a). These mud-cracks were not deflected by splat boundaries or pores, and were oriented nearly normal to the coating's surface. The cracks in as-deposited coatings generally terminated at the  $\text{Yb}_2\text{SiO}_5$ /mullite interface and had crack face opening widths (at ambient temperature) greater than a micrometer. Additional 1-10  $\mu\text{m}$  long microcracks were also observed to originate at splat interfaces, Figure 2.5(a). Some of the cracks were confined to a single solidified droplet while others had penetrated several solidified droplets. The cross-section planar density of these microcracks was roughly 5 cracks per 1,000  $\mu\text{m}^2$  of topcoat examined. Most were oriented normal to the coating surface, and therefore appear to be a micro-scale form of mud-cracking. While this population of micro-mud-cracks did not extend during stabilization annealing at 1300  $^\circ\text{C}$ , Figure 2.5(b), a new population of equiaxed microcracks developed within many of the splats. These microcracks had lengths of 3-10  $\mu\text{m}$ , and the combined planar density of all the microcracks after

annealing had doubled to 10 cracks per 1,000  $\mu\text{m}^2$  of topcoat, Figure 2.5(b). No delamination cracks were found in either the as-deposited or annealed  $\text{Yb}_2\text{SiO}_5$  layer. When viewed at higher magnification, Figure 2.6(a), many of the splats appear to have deposited with fine dendritic structures with intermediate spacing around 100nm; these structures stabilized into a two-phase structure upon annealing similar to that expected for the slow cooling of proeutectic phase structures, Figure 2.6(b).

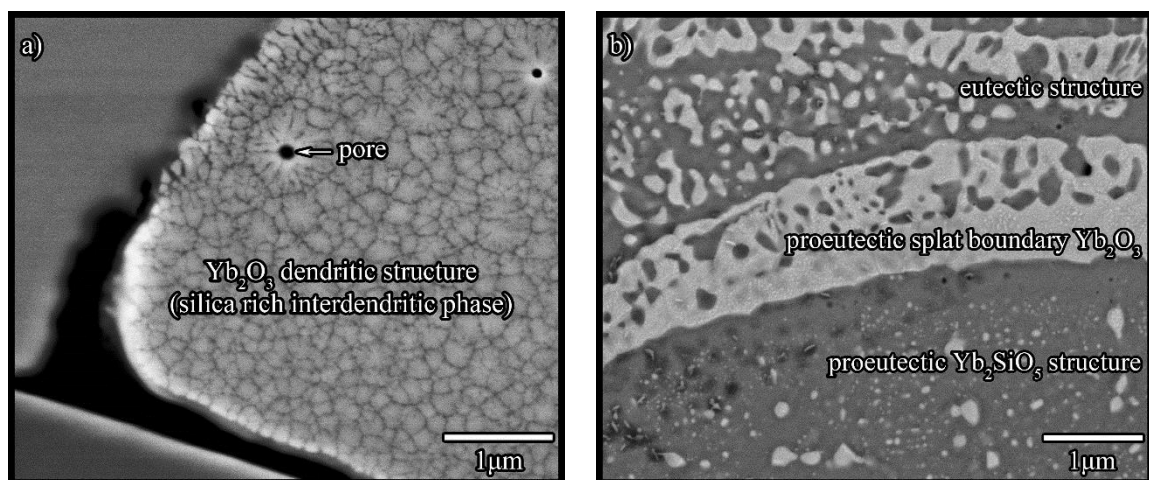


Figure 2.6: High magnification views of (a) region VII in the as-deposited coating shown in Figure 2.5(a), and (b) annealed topcoat near a splat boundary.

The presence of both circular (undeformed) and highly elongated splat shapes in the as-deposited coatings indicates both partially and fully melted particles were present during deposition of the layer, Figure 2.5. This variation is consistent with a substantial spread in particle trajectories (and therefore thermal profiles) through the plasma plume.<sup>128,134,135,178,179</sup> BSE contrast differences between individual splats in Figure 2.5(a) indicate compositional variations in the as deposited ytterbium silicate layer. The contrast

is directly related to the electron backscatter coefficient  $\eta$  of a composition. We calculate (using Equation (2.1)) that for  $\text{Yb}_2\text{O}_3$ ,  $\eta = 0.75$ . It is  $0.67$  for  $\text{Yb}_2\text{SiO}_5$ , and  $0.61$  for  $\text{Yb}_2\text{Si}_2\text{O}_7$ . The large differences in  $\eta$  between these three phases indicate that small compositional differences in the  $\text{Yb}_2\text{O}_3$ - $\text{SiO}_2$  pseudo-binary system are readily observed by BSE imaging, and the differences in contrast of the various splats in Figure 2.5(a) are due to variations of their composition.

To quantify the compositional differences of splats in the as-deposited coating, energy dispersive spectra were collected from the points indicated in Figure 2.5(a). A summary of the composition data as well as that of the as-received powder was given in Table 2.1. A summary of the EDS analysis, Table 2.2, shows some splats contained as little as 2 at% silicon. The deposited stoichiometry was on average 0.6 at% lower in Yb, 1.9 at% lower in Si and 2.5 at% higher in O than the starting powder, indicating loss of Si with respect to Yb. Similar preferential loss of silicon during APS processing has previously been suggested for  $\text{La}_9\text{SrSi}_6\text{O}_{26.5}$ .<sup>180</sup> When the as-deposited splats with significant silicon loss were examined at higher magnification, Figure 2.6(a), a sub-micrometer, two-phase dendritic structure could be identified. The fineness of this structure precluded EDS identification of the composition of each phase.

Upon stabilization annealing (1300 °C, 20 h, air), many of the solidified droplets appeared to have undergone a phase decomposition reaction with a light BSE contrast phase appearing on the grain boundaries. This can be clearly seen for the center top splat of Figure 2.5(b). After stabilization annealing, the dendritic structure of the splats in Figure 2.6(a) has been replaced with an equiaxed polycrystalline structure with extremely fine precipitates, Figure 2.6(b). Again, the precipitate structure was too fine to analyze

via EDS, but compositional fluctuations within the bulk structure after annealing were assessed using a line scan, Figure 2.7. The variations in Si, Yb and O are shown together with the reference concentrations of these elements in  $\text{Yb}_2\text{SiO}_5$ . The results indicate that the darker contrast droplets had compositions close to that of  $\text{Yb}_2\text{SiO}_5$  and precipitated a smaller volume fraction of the second phase than the silicon depleted droplets. The medium contrast splats had low silicon contents and decomposed into a two-phase mixture with approximately equal volume fractions of each phase. The lightest contrast splats precipitated small amounts of the grey phase in some instances (as can be seen in Figure 2.6(b)), but remained largely free of grey phase precipitates. The composition of the lightest regions approached that of ytterbia ( $\text{Yb}_2\text{O}_3$ ).

*Table 2.2: Atomic compositions for as-deposited ytterbium silicate topcoat calculated from EDS point probe spectra at 550 rectangular grid points distributed over six different collection areas.*

Parameter	Composition (at%)
Average Yb content	24.4±2.7
Yb max/min	36.1/17.4
Average Si content	10.6±2.3
Si max/min	14.3/1.6
Average O content	65.0±0.9
O max/min	68.9/59.1

The silicon content of the solidified droplets in the as-deposited ytterbium monosilicate layer showed considerable variability, Table 2.1, but was almost always less than that of the powder used for its fabrication. Examination of Figure 2.4 shows that while some of the larger diameter powder particles had retained a spherical shape, indicating they had barely melted in the plasma plume, others with much lighter BSE contrast (indicative of a higher fraction of high atomic number elements) had flowed

significantly upon impingement with the depositing coating. This suggests they had been heated well above the melting point of ytterbium monosilicate ( $T_M = 1950\text{ }^\circ\text{C}$ ). The lighter BSE contrast and the EDS compositional characterization is consistent with preferential silicon evaporation from the most heated particles during the plasma spray process.

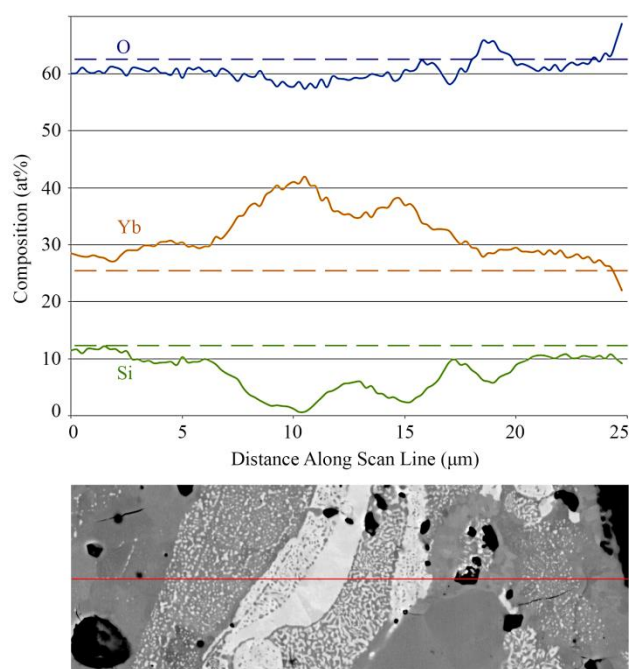


*Figure 2.7: EDS line scan of annealed ytterbium silicate topcoat. Dashed lines indicate atomic compositions for  $\text{Yb}_2\text{SiO}_5$ . Note 40at% Yb- 60at% O is the composition of ytterbia. Location of scan line is indicated on accompanying micrograph.*

The partial pressure of the highest vapor pressure species in equilibrium with a mixture of  $\text{Yb}_2\text{O}_3 + \text{SiO}_2$  and plasma forming gases at 1 MPa can be calculated using the FactSage software program.<sup>181</sup> Assuming ideal interactions between  $\text{Yb}_2\text{O}_3$  and  $\text{SiO}_2$ , and 80 g of  $\text{Yb}_2\text{SiO}_5$  in 761 standard liters of an inert gas mixture with an Ar:He gas volume ratio of 2:1 containing 10 ppm of  $\text{O}_2$ , it is possible to calculate the partial pressure of the

constituents as a function of temperature, Figure 2.8. Recent thermal models of plasma spray processes predict temperatures of powder particles in plasma spray plumes in the 2,000-3500 °C range for spray parameters similar to those used here.<sup>127,136,139-141</sup> Particles heated into this temperature range have SiO activities (vapor partial pressures) that are many orders of magnitude above those of Yb or any of its oxides. We therefore conclude that during super-heated molten particle transport through the plasma plume, the loss of SiO significantly exceeds that of Yb. This will be exacerbated for particles that are heated to the highest temperatures or for the longest times; i.e. smaller diameter particles or those entrained in the core of the plasma plume where temperatures are the highest.<sup>127,136,139-141</sup>

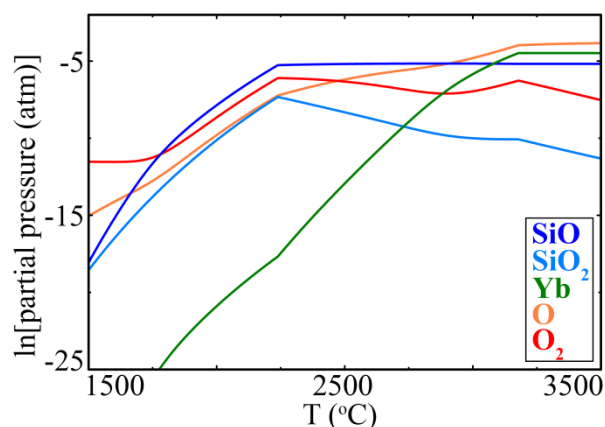


Figure 2.8: Calculated partial pressure versus temperature plot for primary gaseous species in the Yb-Si-O system. Curves are reported for an equilibrated system.

The phases that form during solidification of silicon depleted droplets can be understood with the aid of the ytterbia-silica pseudo-binary phase diagram, Figure 2.9.<sup>81</sup> Silicon loss from Yb<sub>2</sub>SiO<sub>5</sub> line compound shifts the composition into a two phase Yb<sub>2</sub>O<sub>3</sub> + Yb<sub>2</sub>SiO<sub>5</sub> region of the phase diagram. This region contains a eutectic point, and so the

as-solidified structure that forms will be dependent upon a droplet's composition. Examination of Table 2.2 shows that some particles contained only a tenth the silicon fraction of the original powder. Under equilibrium cooling conditions, these would nucleate solid proeutectic  $\text{Yb}_2\text{O}_3$  dendrites, and a eutectic  $\text{Yb}_2\text{SiO}_5 + \text{Yb}_2\text{O}_3$  interdendritic structure consistent with the result shown in Figure 2.6(a). Liquid droplets with hypereutectic compositions would precipitate proeutectic  $\text{Yb}_2\text{SiO}_5$  and an inter-dendritic eutectic structure. The rapid solidification rate of the droplets is likely to result in a very small dendrite spacing that would be difficult to resolve with the SEM; but on annealing, these two microstructures are expected to evolve to the two types of coarser structure seen in micrographs such as Figure 2.5(b) and Figure 2.6(b). The lightest contrast (most silicon depleted) regions consisted of a continuous  $\text{Yb}_2\text{O}_3$  phase containing particles of  $\text{Yb}_2\text{SiO}_5$ , Figure 2.6(b), whereas those with hyper-eutectic compositions consisted of equiaxed  $\text{Yb}_2\text{SiO}_5$  polycrystals with grain boundary  $\text{Yb}_2\text{O}_3$  particles as seen in the darker contrast splats in Figure 2.5(b).

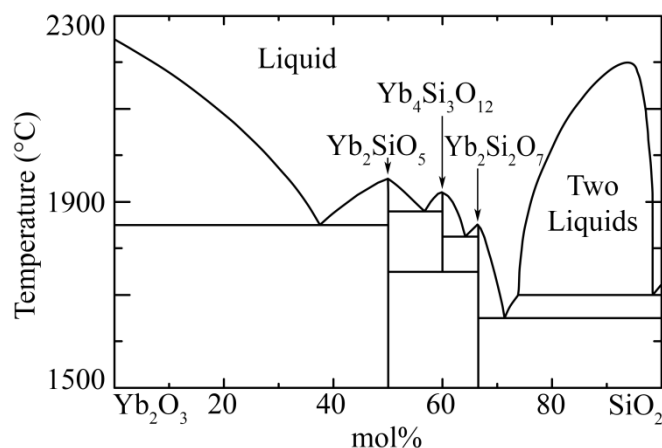


Figure 2.9: Ytterbia-silica binary phase diagram (redrawn from reference)<sup>81</sup>.

XRD patterns of both the as-deposited and annealed topcoat are shown in Figure 2.10. The reflection peaks in both patterns can be indexed using the diffraction patterns of monoclinic ytterbium monosilicate and cubic ytterbia. A hump in the diffraction pattern at low  $2\theta$  (below  $20^\circ$ , not shown) was present in the XRD patterns of as-deposited topcoats indicating the presence of amorphous material. After the annealing, the absence of a low  $2\theta$  hump in the patterns indicated the coating had fully crystallized. Rietveld analyses<sup>182</sup> of phase fractions were attempted, but disagreed with image analysis results, which indicated the coating to be  $\sim 60$  vol%  $\text{Yb}_2\text{SiO}_5$  and  $\sim 40$  vol%  $\text{Yb}_2\text{O}_3$ , Figure 2.10(b). The as-deposited ytterbia exhibited peak shifts with respect to the ytterbia reference pattern; for example the ytterbia {222} peak was shifted  $+0.5^\circ$ . This peak shift is not seen in annealed coatings and corresponds to a contraction in lattice parameter in the out-of-plane (coating normal) direction.

XRD residual stress measurement of the as-deposited topcoat was performed using the ytterbia {622} peaks, and indicated the ytterbia in the topcoat at room temperature to have a tensile residual stress of  $\sim 400$  MPa with a  $\sin^2\psi$  correlation coefficient of  $R^2 = 0.74$ . For the annealed topcoat only ytterbium monosilicate peaks had high enough intensities for stress measurements, but many of these were overlaid. Also, since  $\text{Yb}_2\text{SiO}_5$  is monoclinic,<sup>81</sup> the room temperature stress state between individual grains is expected to vary widely, and the  $\sin^2\psi$  measurement technique was inconclusive.

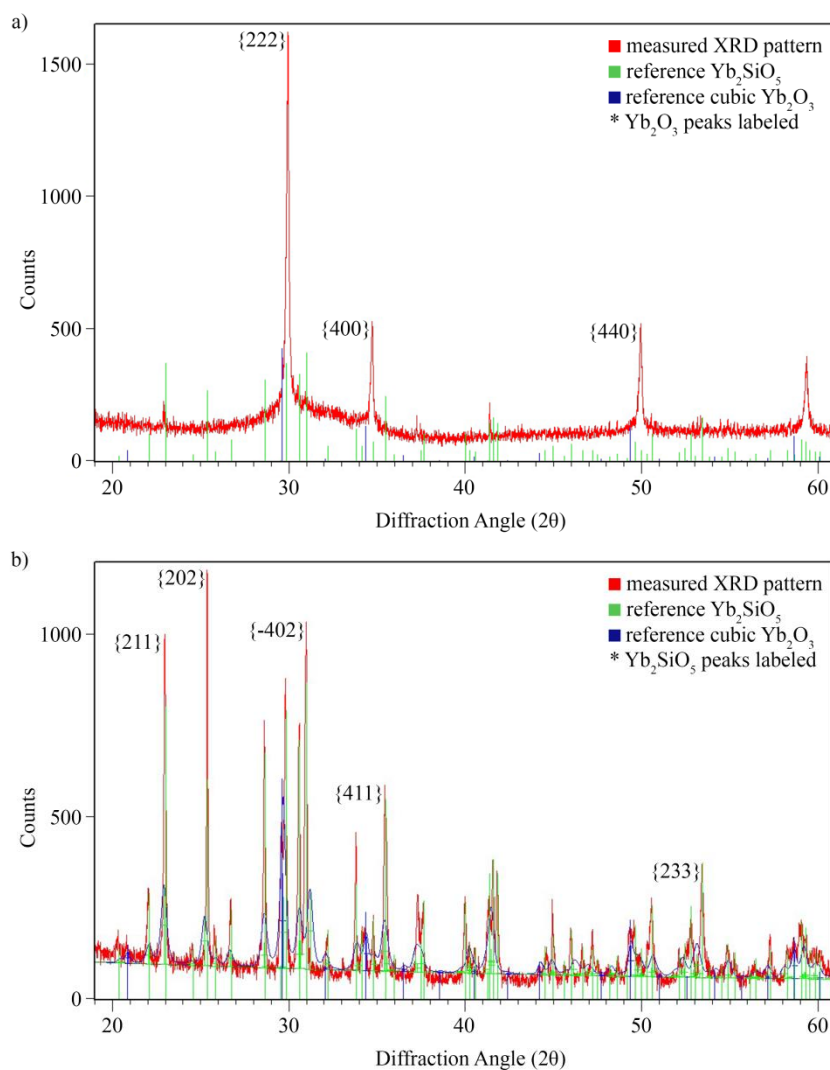


Figure 2.10: XRD patterns for the nominally ytterbium monosilicate topcoat; (a) as-deposited and (b) annealed. Peaks are indexed for  $\text{Yb}_2\text{O}_3$  in (a) and  $\text{Yb}_2\text{SiO}_5$  in (b). Reference peaks for both phases in (a) and calculated Rietveld refinement pattern in (b) are also shown.

The observed mud-cracking is consistent with the substantial CTE difference between the topcoat and the rest of the system, as suggested by a recently reported CTE measurement for  $\text{Yb}_2\text{SiO}_5$ <sup>77</sup> and confirmed by our dilatometry measurements in Section 3.1. To investigate the origin of cracking, we performed an elastic thermomechanical calculation of the stress state in the coating system by a previously described approach

that used a thin film approximation.<sup>183</sup> The thin film approximation assumes curvature of the composite system and a biaxial stress state in coating layers whose elastic moduli, Poisson's ratio and CTE are different. It is also assumed that the interactions between coating layers are small in comparison to the interaction with the substrate, and the stress in each coating layer is therefore independent of that in adjacent layers. This approach leads to a thermal residual stress in the  $i$ -th coating layer (prior to relaxation by cracking) given by:

$$\sigma_i = (E_i / (1 - \nu_i)) (\alpha_s - \alpha_i) \Delta T \quad 2.2$$

where  $\sigma_i$  is the thermal stress in the  $i$ -th layer,  $E_i$  is the elastic modulus of the  $i$ -th layer,  $\nu_i$  is its Poisson's ratio,  $\alpha_s$  and  $\alpha_i$  are the CTE of the substrate and  $i$ -th layer respectively, and  $\Delta T$  is the difference in temperature between the stress free (deposition) temperature of the  $i$ -th layer and the temperature of interest. We have verified the validity of this approach using a more accurate solution formulated by Hsueh<sup>184</sup> where the layer stresses are interdependent: the stresses calculated using the two methods were identical.

Residual thermal stresses have been calculated for all layers of the coating and secondary phases using the thermophysical properties of each layer and assuming the stress free temperature to be the annealing temperature (1300 °C), Table 2.3. If we assume the topcoat to be pure ytterbium monosilicate with a CTE of  $7.5 \times 10^{-6} \text{ }^\circ\text{C}^{-1}$  (as proposed by Lee<sup>77</sup> and consistent with our measurements), we calculate that the topcoat develops a biaxial *tensile* stress of 893 MPa upon cooling to ambient temperature. The stress calculated for an  $\text{Yb}_2\text{O}_3$  enriched  $\text{Yb}_2\text{SiO}_5/\text{Yb}_2\text{O}_3$  topcoat would be somewhere

between the values calculated for  $\text{Yb}_2\text{SiO}_5$  and  $\text{Yb}_2\text{O}_3$ : the stress will increase slightly with increasing  $\text{Yb}_2\text{O}_3$  content, Table 2.3.

The mud-cracking observed in as-deposited and annealed coatings is consistent with the high tensile stress calculated for the topcoat using Equation 2.2. If such a tensile stress exists upon cooling from deposition, the lattice parameter of all phases should be slightly larger in the in-plane directions due to the biaxial tensile stress state, and slightly contracted in the out-of-plane directions (due to the Poisson effect). This is consistent with analysis of the diffraction pattern of Figure 2.10(a). The measured residual tensile stress of  $\sim 400$  MPa in the  $\text{Yb}_2\text{O}_3$  phase of the as-deposited coating is about half that calculated in Table 2.3, presumably because mud-cracking had partially relaxed the strain in this layer.

*Table 2.3: Material parameters and calculated thermal stress at 20°C for coating layers assuming 1300°C stress free temperature and  $\alpha$ -SiC substrate.*

Coating Layer	Young's Modulus (GPa)	CTE ( $\alpha \times 10^6$ ) $^{\circ}\text{C}^{-1}$	Poisson Ratio $\nu$	Thermal Stress (MPa)
$\text{Yb}_2\text{SiO}_5$ (monoclinic)	172 <sup>a</sup>	7.5 <sup>b</sup>	0.27 <sup>c</sup>	893
$\text{Yb}_2\text{SiO}_5$ (monoclinic)	172 <sup>a</sup>	4.0 <sup>78</sup>	0.27 <sup>c</sup>	-211
$\text{Yb}_2\text{O}_3$ (cubic)	188 <sup>185</sup>	7.6 <sup>84</sup>	0.304 <sup>d</sup>	1,013
3:2 Mullite (orthorhombic)	220 <sup>186</sup>	5.3 <sup>70</sup>	0.28 <sup>187</sup>	246
Alumina ( $\alpha$ )	402 <sup>86</sup>	7.2 <sup>86</sup>	0.231 <sup>86</sup>	1,693
Silicon (dcc)	163 <sup>88</sup>	4.1 <sup>88</sup>	0.223 <sup>88</sup>	-153
Silicon Carbide ( $\alpha$ ) <sup>188</sup>	430	4.67	0.14	N/A

<sup>a</sup> Determined by nano-indentation.

<sup>b</sup> Value determined in Section 2.3.1.

<sup>c</sup> Value taken for  $\text{Y}_2\text{Si}_2\text{O}_7$  (94).

<sup>d</sup> Value taken for  $\text{Y}_2\text{O}_3$  (96).

Micro-mud-cracking was observed in the most silicon depleted droplets, Figure 2.5(a). If a rule of mixtures is assumed for the CTE and elastic modulus of such splats,

then the lightest contrast splats will have a slightly greater CTE and elastic modulus than dark contrast splats (Table 2.3). When the slightly higher CTE is combined with the increased elastic modulus of these predominantly ytterbia splats, the small, ytterbia rich splats will experience a state of triaxial tension (even in the mud-cracked coating) upon cooling due to their higher CTE. The strain energy may then be released by microcracking. We therefore conclude that in the most intensely heated, light contrast splats, evaporation of silicon in the molten state leads to the formation of  $\text{Yb}_2\text{O}_3$  which is susceptible to microcracking due to high macro and local tensile thermal residual stresses.

Upon annealing the topcoat, additional “equiaxed” microcracking was observed in the darker BSE contrast droplets, Figure 2.5(b). Increases in microcracking upon annealing have been observed previously in EBCs and have been linked to volume changes during phase transformation.<sup>70,79,93,104,105</sup> We note that the droplets where microcracking was most prevalent consisted primarily of  $\text{Yb}_2\text{SiO}_5$ . If a substantial difference in CTE with crystallographic orientation exists as in  $\text{Y}_2\text{SiO}_5$ <sup>189</sup> and other monoclinic structures,<sup>177</sup> anisotropic thermal stresses will occur upon cooling between  $\text{Yb}_2\text{SiO}_5$  crystals that may have contributed to the observed cracking.

#### **2.3.4 Mullite Intermediate Layer**

A higher magnification micrograph of region II from Figure 2.4(a) of the as-deposited mullite layer is shown in Figure 2.11(a). The as-deposited mullite layer contained a variety of pore structures. Some larger, rounded pores had diameters of several

micrometers while flattened pores existed at some inter-splat boundaries. Inter-splat pores have been reported to result from filling defects during plasma spray processing<sup>190</sup>. We calculate that rounded and flattened pores contributed roughly 1 % to total porosity of the coating layer. The majority of the mullite coat was nanoporous with a nanopore diameter of 10-100 nm and a cross-sectional pore density of approximately 7000 pores per 1,000  $\mu\text{m}^2$ , contributing 7 % to total porosity of the layer. The total mullite coat porosity was ~8 %. The as-deposited mullite structure was two-phase with a plate-like morphology second phase. After stabilization annealing, the number of plates had increased significantly and the spacing between plates decreased. Dense, recrystallized areas of the mullite matrix with columnar crystal growth were evident in the microstructure, Figure 2.11(b).

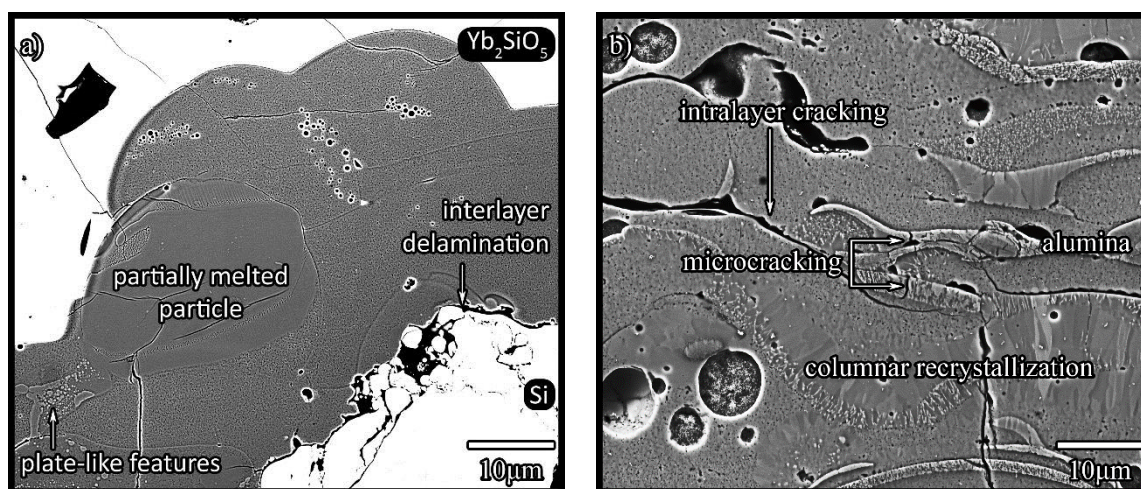


Figure 2.11: High magnification micrographs of the mullite intermediate layer from (a) region II in as-deposited Figure 2.4(a) and (b) region V in annealed Figure 2.4(b).

EDS analysis of the as-deposited mullite coats indicates they were oxygen and silicon deficient, Table 2.4. The average deposited composition of the layer was 6.3 at% higher

in Al, 1 at% higher in Si and 7.3 at% lower in O than the starting powder, indicating volatilization of Si and O. The deposited Al:Si ratio lies between 3:2 and 2:1 mullite, having a ratio of 3.5:1 (2:1 mullite is 4:1 Al:Si and 3:2 mullite is 3:1 Al:Si). The plate-like features seen in Figure 2.11(a) were slightly rich in aluminum, having aluminum contents 1-3 at% higher than the surrounding matrix. An EDS line scan analysis of the annealed mullite layer, Figure 2.12, indicates the stoichiometric difference between plate-like features and the surrounding matrix increased considerably during annealing. The EDS analysis indicated the plates to be composed of  $\text{Al}_2\text{O}_3$  containing 1-5 at% silicon, while the surrounding matrix composition approached 3Al:1Si corresponding to 3:2 mullite. Regions with no precipitated alumina yielded EDS compositions close to 3:2 mullite.

*Table 2.4: Atomic compositions for as-deposited mullite coat calculated from EDS point probe spectra at 550 rectangular grid points distributed over six different collection areas. All values are in at%.*

Parameter	Composition (at%)
Average Al content	34.9±1.6
Al max/min	39.9/27.1
Average Si content	10.5±1.6
Si max/min	19.2/5.2
Average O content	54.6±0.8
O max/min	56.9/51.4

The presence of alumina plates in APS mullite is consistent with previous XRD and SEM observations.<sup>70</sup> Higher resolution analysis showed the plates were composed of sub-plates of alumina with fine bands of a silicon-rich species interspersed, Figure 2.13. Analysis of a single area at high magnification indicated that the plate region was composed of 76 vol% alumina platelets, 22 vol% silicon-rich species, and 2 % porosity.

The silicon-rich bands were too small to analyze with EDS in the SEM, having widths ranging from several nanometers to roughly 100 nanometers, but BSE imaging contrast indicates that these bands may be similar in composition to the surrounding mullite matrix. Several plates in the annealed coating were microcracked, Figure 2.11(b) and Figure 2.12.

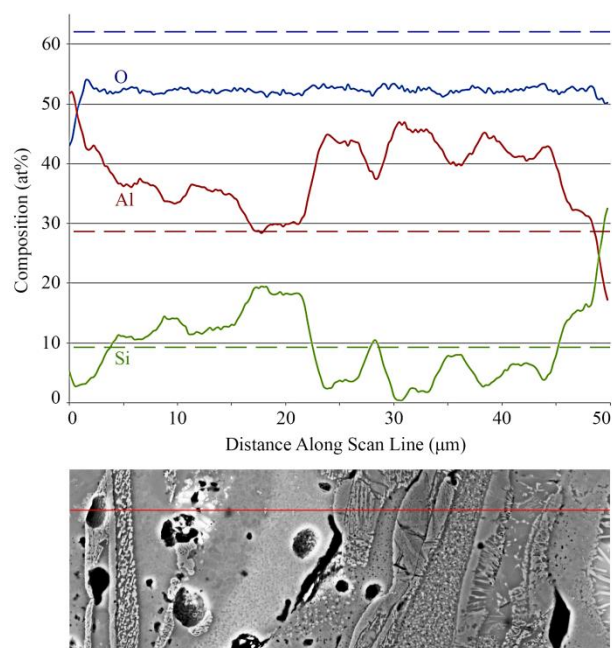
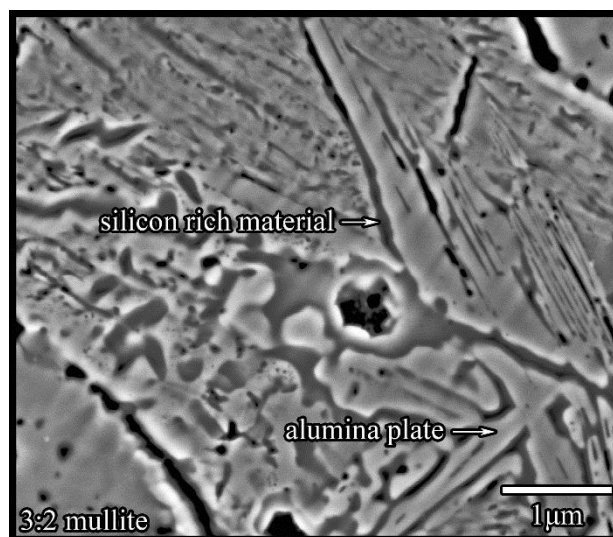


Figure 2.12: EDS line scan of annealed mullite layer. The initial  $3\text{Al}_2\text{O}_3:2\text{SiO}_2$  molar mullite composition is indicated by dashed lines. Note that 40at% Al- 60at% O is the composition of alumina. The location of the line scan is indicated on the micrograph.

We have observed that the APS melting and deposition of initially stoichiometric 3:2 mullite powder resulted in an alumina rich, near 2:1 mullite coating, Table 2.4. The composition deposited here is similar to that of previous studies on melt processed mullite,<sup>85,191</sup> but was less silicon deficient than the 3:1 stoichiometry coating previously reported for EBCs.<sup>70,192</sup> The FactSage software<sup>181</sup> can again be used to determine the equilibrium partial pressures of the gas species for a mixture of  $3\text{Al}_2\text{O}_3+2\text{SiO}_2$  and the

plasma forming gas assuming ideal interactions. Figure 2.14 shows the calculated vapor pressure versus temperature relations for the components of a system consisting of 35g of  $\text{Al}_2\text{O}_3$  and  $\text{SiO}_2$  (with a stoichiometry of  $\text{Al}_6\text{Si}_2\text{O}_{13}$ ) and 761 standard liters of 2:1 Ar:He volume fraction ratio gas containing 10 ppm  $\text{O}_2$ . The particle temperatures during plasma deposition lie in the 2,000-3,500 °C range where the vapor pressure of SiO is several orders of magnitude higher than those of any aluminum containing vapor species. This vapor pressure difference therefore results in preferential evaporation of SiO and formation of a compositionally modified mullite layer.



*Figure 2.13: High magnification view of phase decomposition into alumina plate separated by silicon rich material in the annealed mullite coat.*

A phase diagram for the  $\text{SiO}_2$ - $\text{Al}_2\text{O}_3$  system is shown in Figure 2.15.<sup>85</sup> Dashed lines for 2:1 and 3:1 mullite indicate compositional boundaries for the formation of metastable mullites. The silicon deficient 2:1 mullite we have deposited lies in the alumina + mullite two-phase field of the equilibrium phase diagram. Examination of Figure 2.11(a) indicates that a predominantly single-phase 2:1 composition mullite was deposited. This

then transformed upon annealing at 1300 °C into a two-phase structure consisting of  $\text{Al}_2\text{O}_3$  + mullite, consistent with the as-deposited composition and low temperature metastability of non-stoichiometric mullites.<sup>193</sup> After annealing, areas in the mullite coat also have dense, columnar recrystallized grains with similar BSE contrast to the surrounding matrix. High aspect ratio columnar mullite grains have been previously observed in fine-grained (recrystallized) 3:2 mullite with growth textured along the “c” axis.<sup>194</sup> These grains are interspersed with a very fine plate-morphology phase that appears similar in BSE contrast to alumina. The occurrence of such recrystallized regions is consistent with a phase transformation from metastable 2:1 mullite to equilibrium 3:2 mullite + alumina.

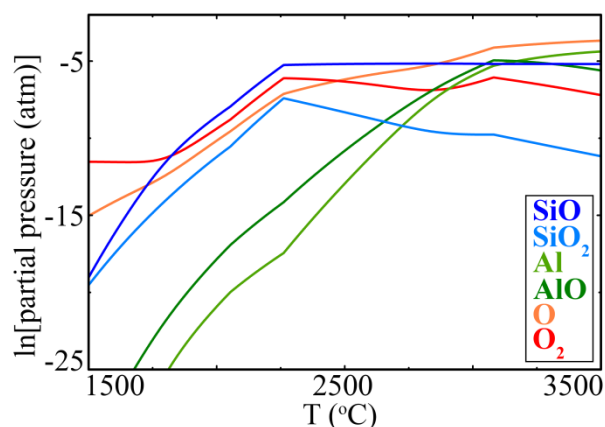


*Figure 2.14: Calculated partial pressure vs. temperature plot for primary gaseous species in the Al-Si-O system. Data are reported for a fully equilibrated system.*

The as-deposited mullite layer had not mud-cracked. However, some areas of delamination between this layer and the silicon bond coat were observed, Figure 2.11(a). During annealing 25-100  $\mu\text{m}$  long intra-layer microcracking between solidified droplets was observed, as well as mud-crack extension from the topcoat, Figure 2.11(b). These

observations are consistent with earlier findings of APS deposited mullite coatings.<sup>70,79</sup> The overall crack density was low with roughly 1 crack per 1,000  $\mu\text{m}^2$  of cross section examined. Previous work in APS deposited mullite has suggested that mullite layers can microcrack as a result of second phase alumina or silica precipitation.<sup>60</sup> The microcracking of the alumina plates after annealing, Figure 2.11(b) and Figure 2.12, appears to be a consequence of the CTE mismatch between alumina and mullite since  $\alpha$ -alumina has an average CTE of  $7.2 \times 10^{-6} \text{ }^\circ\text{C}^{-1}$ , which is substantially higher than that reported for surrounding mullite ( $5.5 \times 10^{-6} \text{ }^\circ\text{C}^{-1}$ , Table 1.1). Upon cooling to ambient temperature from the annealing temperature, this CTE difference would induce triaxial tensile stresses much higher than those experienced in the rest of the mullite coat (Table 2.3) that are conducive to alumina microcracking.

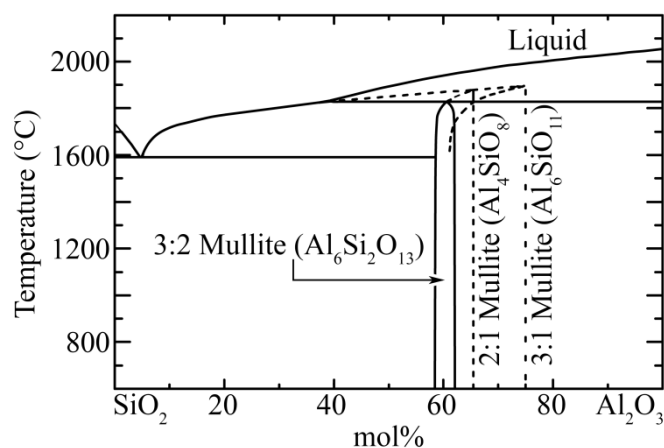


Figure 2.15: Alumina-Silica binary phase diagram. Dashed lines indicate the boundaries of metastable phases (modified and redrawn)<sup>85</sup>.

### 2.3.5 Silicon Bond Coat

The region marked as III in Figure 2.4(a) of the as-deposited bond coat is shown at higher magnification in Figure 2.16(a). The bond coat contained significant porosity located at splat boundaries. Typical pore diameter was 3-5  $\mu\text{m}$ . There were approximately 5-10 pores per 100  $\mu\text{m}$  of inter-splat interface. The many debonds and pores between the splats resulted in a network of interconnected pores and debonds within the bond coat. The porosity is estimated to be in the range of 20 %.

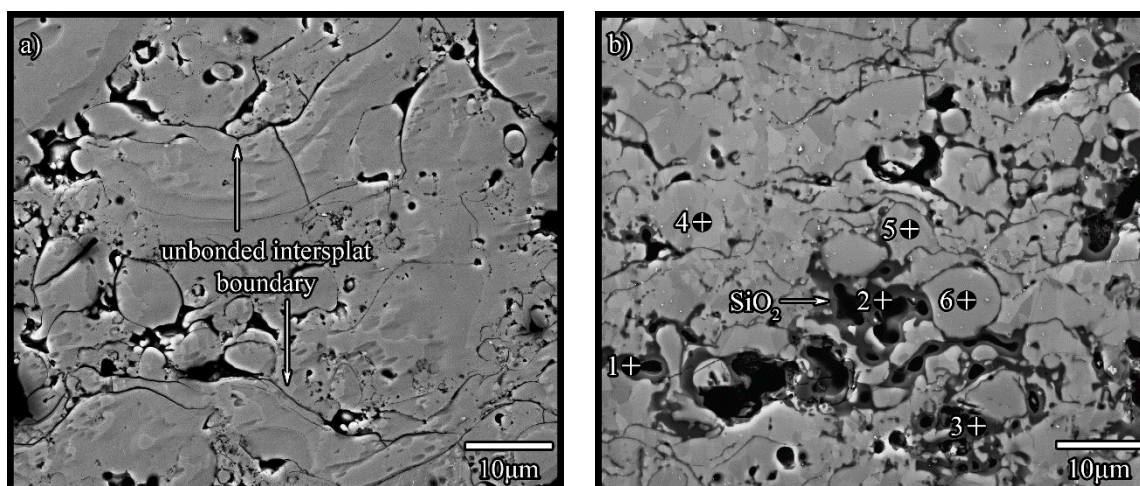


Figure 2.16: High magnification micrographs of the silicon bond coat from (a) region III in as-deposited Figure 2.4(a), and (b) region VI after annealing in air (20 h at 1300 °C) from Figure 2.4(b).

After the 20 h annealing treatment in air at 1300 °C, the interconnected pore-crack network became internally covered in a darker contrast phase. This appeared to be silica and was verified by EDS, Table 2.5. Oxidation of the pore surfaces resulted in an interconnected silica network throughout the bond coat, Figure 2.16(b). The measured silica thickness was ~500 nm throughout the majority of the bond coat, though greater thicknesses were observed near the coating edges. Mud-cracks that had extended from

the topcoat through the mullite layer had terminated at the silicon/mullite interface and did not show any sign of oxidation, Figure 2.17, indicating that these cracks formed upon cooling after the stabilization anneal.

The presence of porosity both within the Si coating and at the SiC/Si interface resulted from several causes. The presence of inter-splat voids, Figure 2.16(a), is consistent with both the temperature of some powder particles at impact being insufficient to allow complete liquid droplet flow over the coating surface and others being so hot that porous regions form due to droplet “splashing” that creates micrometer sized particles. Additionally, because the silicon bond coat was deposited in argon shrouded air, oxygen can be entrained in the plasma plume resulting in rapid formation of a native oxide on liquid particle surfaces that impedes inter-splat bonding.<sup>102</sup> The combination of these effects has resulted in a less than ideal bond coat structure.

*Table 2.5: Atomic compositions reported by P/B-ZAF (non-standardized) analysis of point probe spectra in Figure 2.16(b).*

Spectrum	Si (at%)	O (at%)
Point 1	27.0	73.0
Point 2	26.5	73.5
Point 3	27.3	72.7
Point 4	93.7	6.3 <sup>a</sup>
Point 5	94.2	5.8 <sup>a</sup>
Point 6	93.8	6.2 <sup>a</sup>
Silica (SiO <sub>2</sub> )	33.3	66.7

<sup>a</sup> Trace oxygen resulted from native oxide growth after sample preparation and oxygen detection inaccuracy in P/B-ZAF analysis.

After annealing, the appearance of a roughly 500 nm thick silica layer was observed on the interior surface of many voids and inter-splat debonds within the silicon bond coat, Figure 2.16(b). Regions closest to the edges of the sample coupon had silica scale

thicknesses exceeding 600 nm. The growth of such silica scales is well documented and accepted to follow the Deal and Groves model.<sup>195</sup> Using the Deal and Groves analysis, we have back-calculated the oxygen partial pressure during exposure to form a 500 nm silica scale in 20 h at 1300 °C. The oxygen partial pressure calculated is 0.13 atm, or 60 % of the oxygen partial pressure found in dry air at atmospheric pressure (101 kPa): this partial pressure is too great to result from bulk diffusion through the coating. An oxygen partial pressure lower than the surrounding environment implies that oxygen was forced to follow a gas diffusion route as opposed to a convective (physical gas flow) route to the bond coat; the relatively high partial pressure back-calculated is reflective of the rapid gas diffusion kinetics of oxygen at high temperatures. The necessity of molecular diffusion transport combined with the long diffusion path through silicon channels that are actively absorbing oxygen may have yielded lower O<sub>2</sub> partial pressures in pores located far from coating edges and close to the substrate.

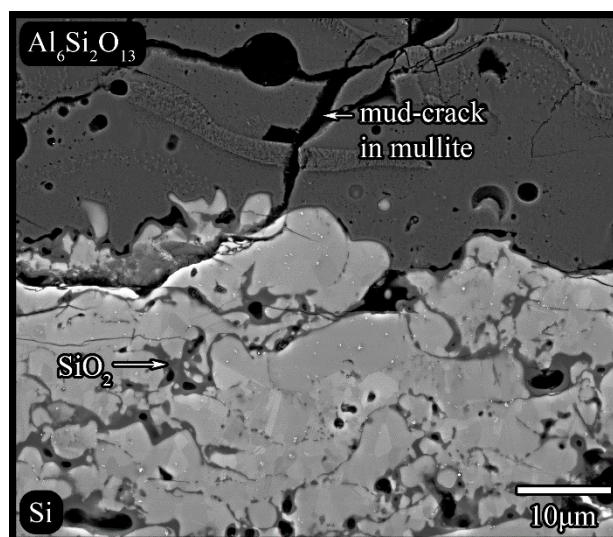


Figure 2.17: High magnification view corresponding to region VIII in Figure 2.4(b) showing a mud-crack penetrating the mullite coat and terminating in the upper few micrometers of the silicon bond coat.

## 2.4 Conclusions

An APS process was used to deposit a tri-layer environmental barrier coating system consisting of a silicon bond coat, a mullite interdiffusion barrier, and an  $\text{Yb}_2\text{SiO}_5$  topcoat on monolithic  $\alpha$  SiC substrates. It is found that:

- a) While the APS process is able to deposit tri-layer coatings, many defects are introduced during the process. These include micro and nanoscale porosity formed by incomplete molten droplet flow during splat impact, inter-splat delamination within the silicon bond coat forming an interconnected pore and crack network, and mud-crack formation in the  $\text{Yb}_2\text{SiO}_5$  topcoat resulting from in-plane biaxial thermal contraction during cooling.
- b) The majority of the solidified droplets in the as-deposited  $\text{Yb}_2\text{SiO}_5$  and mullite layers were depleted in silicon. This led to the formation of two-phase topcoats consisting of a mixture of  $\text{Yb}_2\text{SiO}_5$  and  $\text{Yb}_2\text{O}_3$  as well as 2:1 mullite layers deposited from 3:2 mullite powders. The loss of silicon was consistent with preferential silicon evaporation from superheated powder particles; a consequence of the higher vapor pressure of silicon bearing species at the temperatures experienced during transient plasma heating.
- c) Annealing in air at  $1300^\circ\text{C}$  resulted in mud-crack extension from the topcoat into the mullite layer and oxidation of the interconnected crack and pore network in the bond coat. The precipitation of  $\text{Yb}_2\text{O}_3$  combined with the anisotropic thermal expansion of  $\text{Yb}_2\text{SiO}_5$  in the topcoat resulted in microcracking.

- d) Upon annealing, the 2:1 as-deposited mullite transformed to a mixture of 3:2 mullite + alumina consistent with phase equilibria in this system. Additional microcracking occurred within the precipitated alumina plates due to significant CTE mismatch between alumina and the coating system.

### **3 Ytterbium Monosilicate/Mullite/Silicon Coating Failure during Steam-cycling<sup>2</sup>**

**Synopsis:** An air plasma spray process has been used to apply a model tri-layer  $\text{Yb}_2\text{SiO}_5/\text{Al}_6\text{Si}_2\text{O}_{13}/\text{Si}$  environmental barrier coating system on SiC test coupons. Significant differences in the thermal expansion of the component layers resulted in periodically spaced mud cracks in the  $\text{Yb}_2\text{SiO}_5$  and  $\text{Al}_6\text{Si}_2\text{O}_{13}$  layers. Upon thermal cycling in a 90 %  $\text{H}_2\text{O}/10$  %  $\text{O}_2$  environment between 1316 °C and 110 °C, it was found that partial delamination occurred with the fracture plane located within a thermally grown oxide (TGO) at the  $\text{Al}_6\text{Si}_2\text{O}_{13}$  – Si interface. Delamination initiated at test coupon edges where the gaseous environment preferentially oxidized the exposed Si bond coat to form  $\beta$ -cristobalite. Simultaneous ingress of the gaseous environment through mud cracks initiated local formation of  $\beta$ -cristobalite ( $\text{SiO}_2$ ), the thickness of which was greatest directly below mud cracks. Upon cooling, cristobalite transformed from the  $\beta$  to

---

<sup>2</sup> Based on a peer reviewed technical article submitted to the *Journal of the American Ceramic Society*.<sup>95</sup>

$\alpha$  phase with a large, constrained volume contraction that resulted in severe microfracture of the TGO. Continued thermal cycling eventually propagated delamination cracks and caused partial spallation of the coatings. Formation of the cristobalite TGO appears to be the delamination life-determining factor in protective coating systems utilizing a Si bond coat.

Matthew Begley (UCSB) contributed the thermal residual stress and strain energy release rate (ERR) calculations presented in this chapter. These were performed using LayerSlayer. Bryan Harder, Dennis Fox, and Michael Cuy of the NASA Glenn Research Center are acknowledged for their assistance in depositing the EBCs that were tested and their insights regarding processing. Consultations with Elizabeth Opila (UVA), Dongming Zhu (NASA Glenn) and Kang Lee (RR) were also very helpful. Characterization advice from Richard White (UVA) was greatly appreciated.

### 3.1 Introduction

The tri-layer RE coating architecture was first proposed in the mid 2,000's,<sup>78</sup> and a variant using a  $\text{Yb}_2\text{SiO}_5$  topcoat has been described in Chapter 2.<sup>97</sup> While  $\text{Yb}_2\text{SiO}_5$  has a very high silicon volatility resistance,<sup>196</sup> it has a relatively high coefficient of thermal expansion (CTE)<sup>77,97</sup> compared to that of the Si bond coat and SiC substrate. The difference in CTE causes mud cracking of the coating, with cracks terminating at the Si bond coat.<sup>77,79,97</sup> Nonetheless, the  $\text{Yb}_2\text{SiO}_5/\text{Al}_6\text{Si}_2\text{O}_{13}/\text{Si}$  system has been proposed as one of the most promising among the tri-layer RE silicate systems due to its thermochemical stability at high temperatures and the environmental stability of  $\text{Yb}_2\text{SiO}_5$ .<sup>77,78</sup>

There have been no published reports analyzing the thermomechanical damage mechanisms experienced during steam-cycling of the ytterbium monosilicate EBC systems. While a few tests of calcium-magnesium-aluminum-silicate (CMAS) attack of related RE silicates have been performed upon coupons,<sup>61,62,197,198</sup> no studies of the failure mechanisms of coating materials have been reported. Here a steam-cycling study has been performed for a tri-layer  $\text{Yb}_2\text{SiO}_5/\text{Al}_6\text{Si}_2\text{O}_{13}/\text{Si}$  (ytterbium monosilicate/mullite/silicon) system whose APS deposition and coating microstructure have been documented in Chapter 2,<sup>97</sup> and the evolution of damage and mechanisms of failure during steam-cycling are investigated.

## **3.2 Experimental**

### ***3.2.1 Coating Deposition***

Three-layer  $\text{Yb}_2\text{SiO}_5/\text{Al}_6\text{Si}_2\text{O}_{13}/\text{Si}$  coatings were deposited onto the (grit blast) roughened surface of 25.4 mm x 12.7 mm x 3.2 mm  $\alpha$ -SiC Hexoloy® (Saint Gobain Ceramics, Niagara Falls, NY) substrates using an APS deposition approach described by Richards and Wadley.<sup>18</sup> The Si layer was deposited with the substrate at ambient temperature. The  $\text{Al}_6\text{Si}_2\text{O}_{13}$  and then  $\text{Yb}_2\text{SiO}_5$  layers were deposited on the Si-coated substrates in a furnace held at 1200 °C. The structure of the coated samples is schematically illustrated in Figure 3.1. Only one surface of the substrate was coated, and the side edges were slightly over-sprayed to reduce edge attack during exposure. A 2 mm wide strip of the sample surface was left uncoated due to the fixture used for deposition. The nominal thickness of the  $\text{Yb}_2\text{SiO}_5$  and  $\text{Al}_6\text{Si}_2\text{O}_{13}$  layers was 75  $\mu\text{m}$  while that of the

Si bond coat was 100  $\mu\text{m}$ . However, considerable variability in layer thickness was observed within and between specimens due to an unsteady powder particle feed rate and large spread of the plasma plume over the long spray distance.<sup>97</sup>

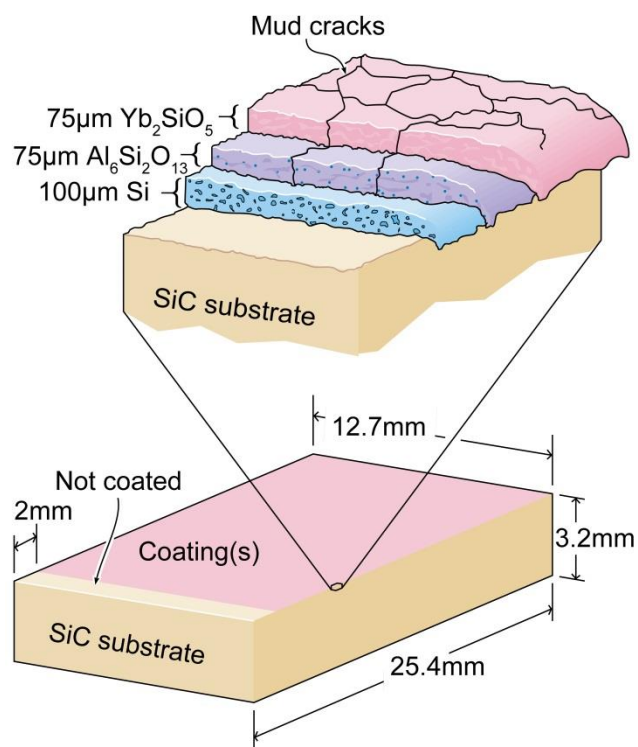
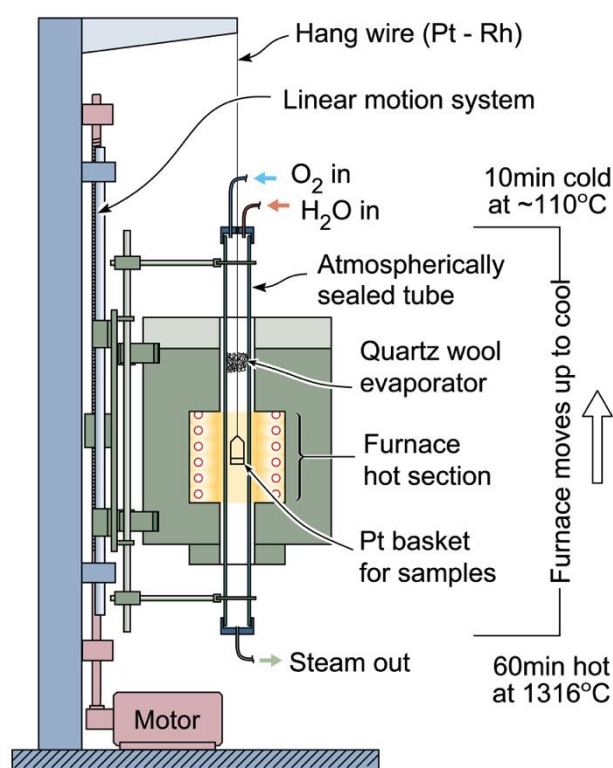


Figure 3.1: Schematic illustration of the tri-layer EBC covered SiC samples showing the coating structure and side edge coverage of the substrate.

### 3.2.2 Steam Furnace Cycling

After deposition, the coated samples were annealed at 1300 °C in lab air for 20 hours to stabilize the structure, consistent with prior EBC testing.<sup>77-79</sup> They were then thermally cycled in a steam-cycling furnace in a flowing, atmospheric pressure, 90 % H<sub>2</sub>O/10 % O<sub>2</sub> gas environment with a flow velocity of 44 mm/s (volumetric flow rate of 4.1 slm), Figure 3.2. When the steam furnace was in its raised (cold) configuration, the gas temperature at the sample location was 110 °C (sufficient to avoid steam condensation on

the sample). In the hot configuration, the sample temperature was measured to be 1316 °C in the flowing atmosphere by reference thermocouple. These testing conditions are similar to those used in prior EBC research,<sup>78</sup> and approximate the H<sub>2</sub>O partial pressure during lean combustion at a pressure of ~10 atm. The samples were examined visually before testing, after 50, 100 and then every 100 cycles thereafter to determine sample failure defined as coating spallation on any part of the test sample.



*Figure 3.2: Schematic illustration of the steam-cycling furnace in the configuration that subjected the samples to the hot part of a steam cycle (60 min at 1316°C). The furnace was then translated vertically while maintaining the sample stationary, thereby removing the sample from the furnace hot zone and subjecting it to the cold part of a steam cycle (10 min at 110°C).*

### ***3.2.3 Coating Characterization***

The steam cycled samples were sectioned and polished, and examined with a scanning electron microscope (Quanta 650 FE-SEM, FEI, Hillsboro, OR) operating in the back-scattered electron (BSE) mode. Images are collected under low-vacuum conditions for improved imaging of aged structures and sharp-edged features that experience severe charging issues even after coating. A gamma correction was applied to enable simultaneous visualization of Yb and non-Yb containing materials. Elemental mapping by Energy Dispersive Spectroscopy (X-Max<sup>N</sup> 150 SDD, Oxford Instruments, Concord, MA) was used to generate compositional maps. The EDS spectra were captured using a 20kV accelerating voltage so that elemental analysis of Yb could be performed more accurately using its L lines. The EDS spectra used for elemental mapping were not standardized.

Raman Spectroscopy was performed using an inVia (Renishaw, Hoffman Estates, IL) microscope to identify bond coat oxidation phases and reaction products in steam cycled coatings. The Raman analyses were performed using a 50x lens with a numerical aperture of 0.5. An argon-ion laser (wavelength of 488 nm) was used for incident illumination of the sample. Approximately 99 % of the Gaussian distributed incident light of the source resided within a 1 $\mu$ m diameter circle, resulting in a spatial resolution of approximately 1  $\mu$ m.

### **3.2.4 Thermomechanical Analysis**

Thermomechanical analyses of stress states and strain energy release rates (ERR) for debonding of the elastic coating layers were calculated using the LayerSlayer<sup>199</sup> software package. All strain energy release rate (ERR) calculations presented are for a system whose layers remained elastic throughout cooling, under the assumption that all layers are in their stress-free state at the annealing temperature of 1300 °C. The calculation ignores stress relief by mechanisms such as mud-cracking or creep. The thermophysical properties and residual stresses calculated for this elastic coating – substrate system after cooling from the stabilization (stress free) annealing temperature of 1300 °C are summarized in Table 3.1 and agree well with previous estimates.<sup>97</sup>

## **3.3 Results**

Eight substrates had coatings deposited upon them. One sample was used for as-deposited and annealed microstructural analysis, one sample delaminated upon cooling from deposition and a second delaminated upon cooling from annealing. Both delamination types were investigated by SEM and found to have occurred at the Si – SiC interface. The remaining five coated samples were thermally cycled in the steam-cycling apparatus shown in Figure 3.2. Spallation failure was observed in the cycled coatings at 50, 200, 400 (2), and 600 cycles.

Table 3.1: Thermophysical properties of EBC system components.

Material	CTE ( $\times 10^6$ $^{\circ}\text{C}^{-1}$ )	Young's Modulus (GPa)	Poisson Ratio $\nu$	Thermal Stress (MPa) <sup>a</sup>	Layer Thickness	Application
Yb <sub>2</sub> SiO <sub>5</sub> $E_{APS}^b$	7.5 <sup>97</sup>	172 <sup>97</sup> 86	0.27 <sup>c</sup>	840 425	75 $\mu\text{m}$	Topcoat
Mullite $E_{APS}^b$	5.3 <sup>70</sup>	220 <sup>186</sup> 110	0.28 <sup>187</sup>	215 110	75 $\mu\text{m}$	Diffusion barrier
Cristobalite- $\alpha$ Cristobalite- $\beta$	30 <sup>d</sup> 3.1 <sup>200</sup>	65 <sup>201</sup> 70 <sup>e</sup>	-0.164 <sup>202</sup> -0.042 <sup>203</sup>	4,350	0-150 $\mu\text{m}$	Oxidation product
Si $E_{APS}^b$	4.1 <sup>88</sup>	163 <sup>88</sup> 16	0.223 <sup>88</sup>	-180 -17	100 $\mu\text{m}$	Bond coat
SiC ( $\alpha$ )	4.67	430	0.14	-55 -34	3.2mm	Substrate

<sup>a</sup>Calculated at 20°C after cooling from stress free condition at 1300°C with LayerSlayer.

<sup>b</sup>Assumed 50% reduction in elastic modulus for APS material/cracking in Yb<sub>2</sub>SiO<sub>5</sub> and Al<sub>6</sub>Si<sub>2</sub>O<sub>13</sub> and 90% reduced elastic modulus for porous APS Si.

<sup>c</sup>Based on Y<sub>2</sub>Si<sub>2</sub>O<sub>7</sub>.<sup>204</sup>

<sup>d</sup>Average of values reported on the 20-200°C interval.<sup>201,205</sup>

<sup>e</sup>Based on Young's modulus ratio of  $\alpha$  and  $\beta$  quartz<sup>206</sup> and  $\alpha$  cristobalite.

### 3.3.1 Coating Structure

Figure 3.3 shows BSE mode SEM micrographs of a part of the coating – substrate system after stabilization annealing. The white arrows in Figure 3.3(a) indicate the locations of mud cracks in the Yb<sub>2</sub>SiO<sub>5</sub> layer. Many of these were observed to have also penetrated the Al<sub>6</sub>Si<sub>2</sub>O<sub>13</sub> layer, Figure 3.3(b) but were arrested near the Al<sub>6</sub>Si<sub>2</sub>O<sub>13</sub> – Si interface, Figure 3.3(c). Examination of the calculated residual stress states in the coated system, Table 3.1, indicates that the higher CTE of the Yb<sub>2</sub>SiO<sub>5</sub> layer (and to lesser extent the Al<sub>6</sub>Si<sub>2</sub>O<sub>13</sub> layer) resulted in tensile residual stresses in these layers. The residual stresses have been calculated for two sets of elastic moduli. The first is for full elastic moduli of the layers typical of dense material, and yields high tensile stresses in the Yb<sub>2</sub>SiO<sub>5</sub> and Al<sub>6</sub>Si<sub>2</sub>O<sub>13</sub> layers and a compressive stress in the Si bond coat. The

second is for 50 % elastic moduli of the low porosity  $\text{Yb}_2\text{SiO}_5$  and  $\text{Al}_6\text{Si}_2\text{O}_{13}$  layers and a 10 % elastic modulus for the highly porous Si bond coat (calculated to be in the range of 20 % porosity)<sup>97</sup>. These moduli are consistent with those observed for APS materials of comparable porosity,<sup>120,122-124,207-211</sup> and yield reduced tensile stresses in the  $\text{Yb}_2\text{SiO}_5$  and  $\text{Al}_6\text{Si}_2\text{O}_{13}$  layers and minimal compressive stress in the Si bond coat. In either case, the calculated stresses are consistent with the mud cracking observed. By analyzing the number of cracks in a 25 mm span of the coating, the average mud crack spacing was found to be  $\sim 280 \mu\text{m}$ .

The light and dark contrast features evident in the  $\text{Yb}_2\text{SiO}_5$  coating layer, Figure 3.3, are a manifestation of silicon evaporation from some of the (originally stoichiometric composition) powder particles during APS processing.<sup>97</sup> The lighter contrast regions correspond to solidified particles containing a lower silicon fraction. During their solidification, this resulted in the formation of a two-phase  $\text{Yb}_2\text{SiO}_5 + \text{Yb}_2\text{O}_3$  microstructure solidified droplet. It is worth noting that since the CTE and elastic modulus of  $\text{Yb}_2\text{SiO}_5$  and  $\text{Yb}_2\text{O}_3$  are similar<sup>97</sup> such silicon loss is not anticipated to significantly affect the thermomechanical response of the topcoat.

Figure 3.3(a) shows that significant variability in the thickness of the coating layers (especially the top two layers) resulted from the spray process implemented here. It can also be seen that the  $\text{Yb}_2\text{SiO}_5$  and  $\text{Al}_6\text{Si}_2\text{O}_{13}$  layers at the edge of the coating failed to fully cover the Si bond coat, even though considerable over-spray of the edge had been achieved. While this could have been resolved by changing the angle of deposition of these two layers during the spray process, this feature of the samples was retained since it provided insight into the failure modes at the edge during subsequent steam-cycling.

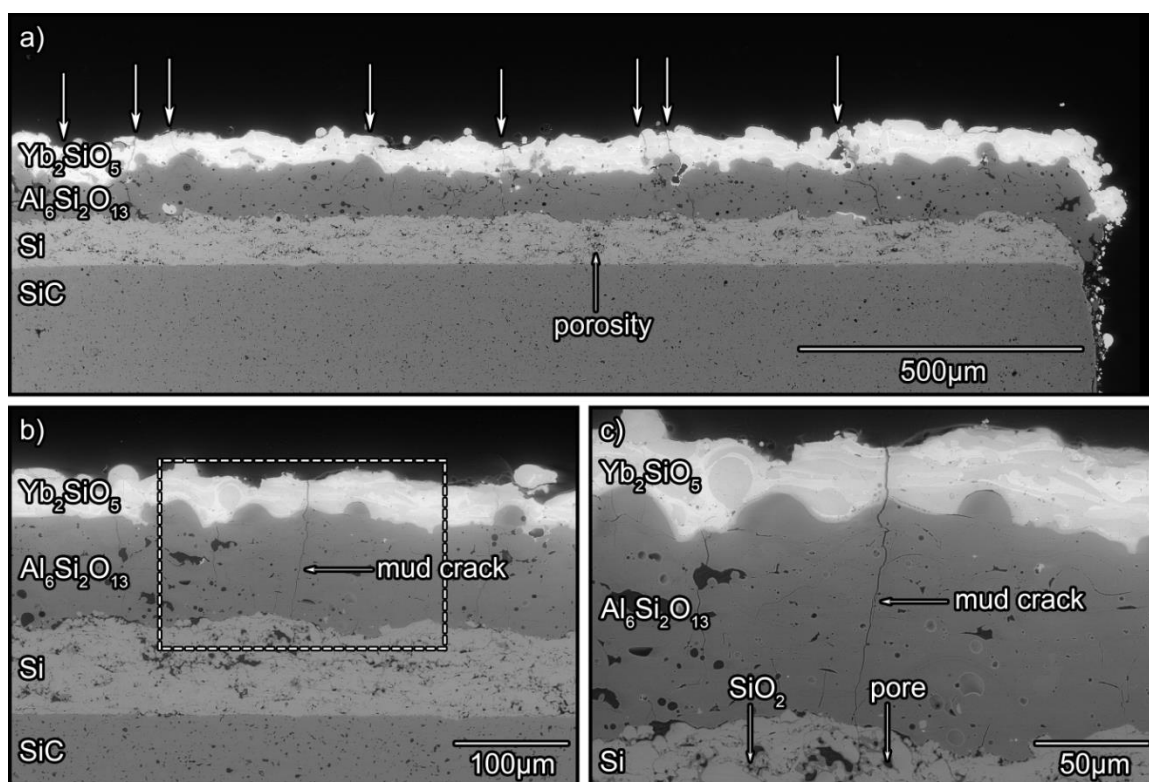
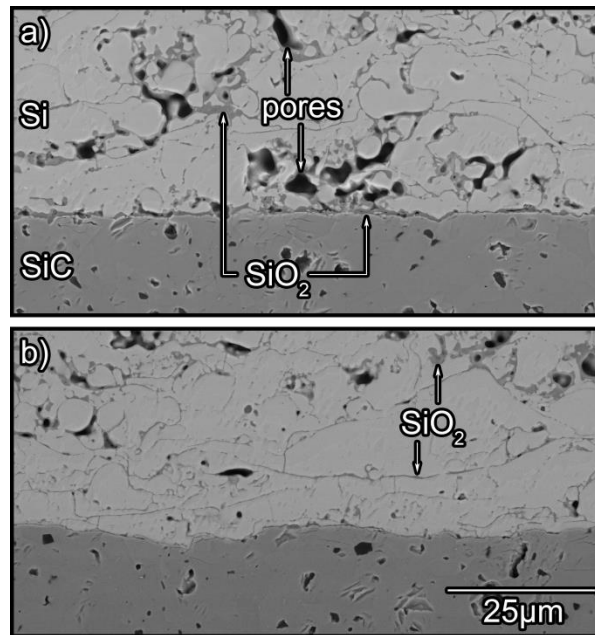


Figure 3.3: (a) Low magnification BSE mode SEM image of the 1300°C annealed EBC with mud cracks indicated by arrows. (b) Shows a higher magnification view of the coating in a region where a mud crack penetrated the ytterbium monosilicate and mullite layers. (c) A high magnification view of the dashed box area in (b) showing arrest of the mud crack at the mullite – silicon bond coat interface.

During the spray deposition process, the temperature of the silicon droplets that impacted the SiC substrate varied considerably. The exposure time of the SiC surface to the plasma plume also varied across its surface. This resulted in a porous Si bond coat and significant variability in the structure and strength of the interface between the grit blasted SiC and the Si bond coat. Figure 3.4 shows BSE micrographs of the Si bond coat – SiC interface at two different locations in an annealed sample. In some regions of the interface, Figure 3.4(a), some silica formation and substantial porosity were observed. The concentration of these defects varied considerably within specimens. Figure 3.4(b)

shows an interface from a region where these defects were much less prevalent. The Si bond coat contained ~20 % porosity and considerably splat boundary silica. Those specimens that spalled before steam-cycling were found to have spalled at the Si – SiC interface, presumably due to a saturation of those defects identified in Figure 3.4.



*Figure 3.4: The Si – SiC interface of (a) an annealed sample in a region of relatively poor adherence with oxidized pore structures and poor interfacial bonding and (b) an interfacial region of higher quality in the same annealed specimen.*

### 3.3.2 Steam-cycling Response

The samples that had very short delamination lifetimes (<200 steam cycles) all delaminated at the Si – SiC interface. Figure 3.5(a) shows a photograph of a coated substrate that had the shortest delamination lifetime (less than 50 steam cycles). A photograph taken after its delamination failure shows that delamination began at the left edge of this sample and progressed inward towards the center of the coating, Figure 3.5(b). Figure 3.5(c) shows a cross-sectional image taken at the coating edge location

marked by a red bar in Figure 3.5(b). The coating remained attached at this location, but delamination had already initiated at the Si – SiC interface. Since there had been insufficient time for oxidizer attack to occur, the crack opening displacement at the edge of the sample indicates the presence of a bending moment on the coating that is consistent with the increasing CTE of layers further from the substrate.

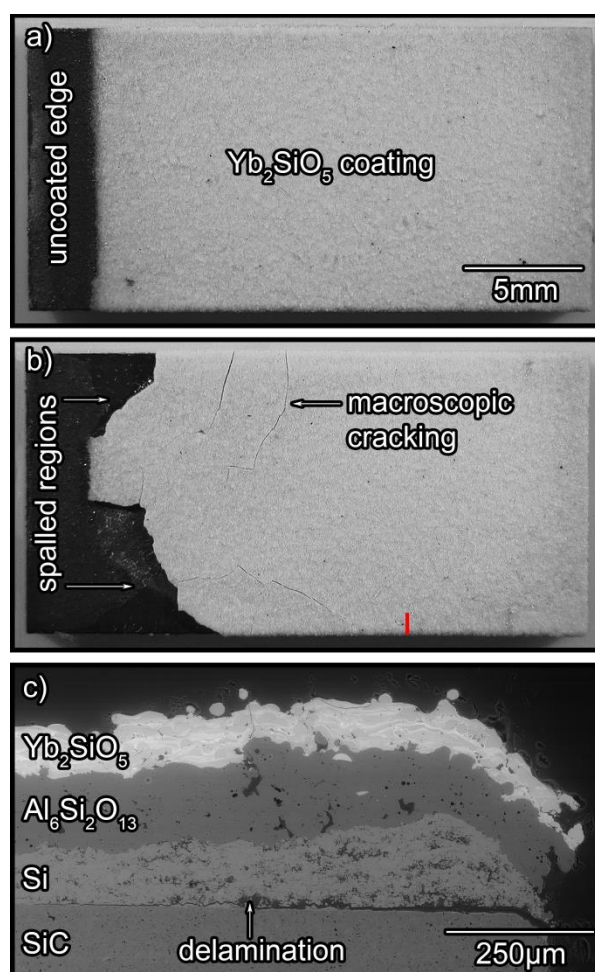


Figure 3.5: Images of an EBC covered sample. (a) Optical image of top surface after annealing. (b) Optical image of the top surface of the same sample after it had delaminated following 50 steam cycles at 1316°C. (c) SEM cross-section (in BSE mode) of the delaminated sample shown in (b). The red bar in (b) indicates the location of the cross section shown in (c).

Delamination after a few steam cycles (and those that occurred immediately after coating deposition and during cooling from the stabilization annealing treatment) appears to be a consequence of the large thermal residual stress in the coating system (as outlined in Table 3.1) acting in combination with insufficient Si – SiC interfacial adhesion. This is consistent with deposition conditions for these samples that resulted in interface sections such as that shown in Figure 3.4(a). No delamination of this character was evident in coatings with a steam-cycling lifetime in excess of 200 steam cycles.

An example of the failure mode of the sample that was most delamination resistant (600 steam cycles) is shown in Figure 3.6. This figure shows BSE images of the coating from cross-sections taken at various distances from the edge of the sample. Examination of these serial coating sections indicates that coating damage occurred at the  $\text{Al}_6\text{Si}_2\text{O}_{13}$  – Si interface and was greatest near the coating edges, Figure 3.6(a). A thick (up to 150  $\mu\text{m}$ , porous and cracked) TGO layer had formed on the Si bond coat. The TGO layer thickness increased towards the edges of the sample, and had microcracked and suffered from some combination of steam volatilization and mechanical damage leaving very large, frequently interconnected voids at the  $\text{Al}_6\text{Si}_2\text{O}_{13}$  – Si interface. This damage decreased towards the interior of the sample, Figure 3.6(b) and Figure 3.6(c). Figure 3.6(c), near the center of the coating, shows that cavities had been created in the TGO at the base of mud cracks; the TGO was thickest in these areas. Analysis of many sample sections indicated that such cavities were present at the bottom of all mud cracks, and were extended horizontally along the  $\text{Al}_6\text{Si}_2\text{O}_{13}$  – TGO interface. Their edges appeared sharp and connected with some of the many cracks in the TGO layer.

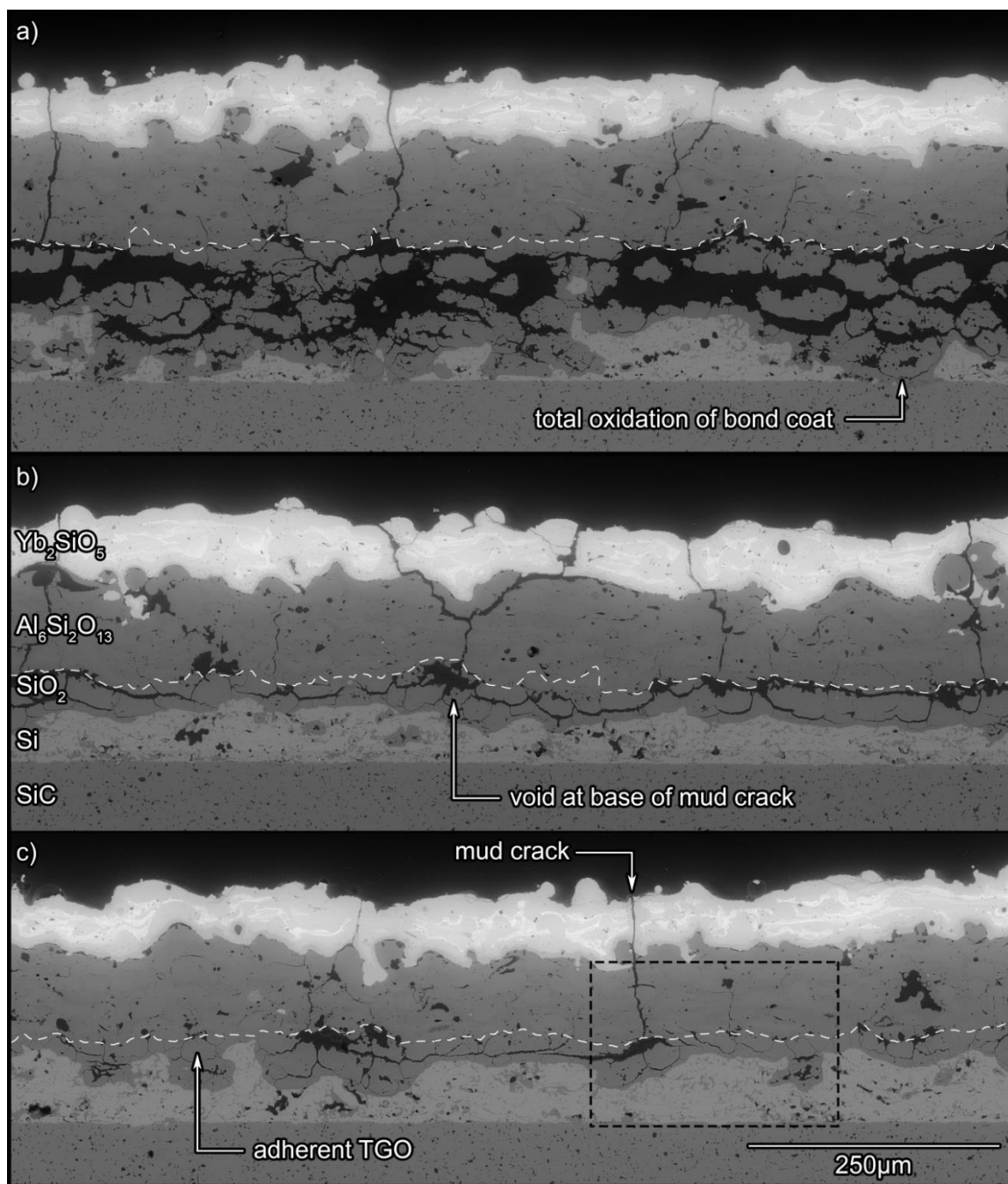


Figure 3.6: Cross sectional BSE micrographs of the same failed coating after 600 1-hour steam cycles at 1316°C with serial sections at (a) 1mm, (b) 3mm, and (c) 5mm from the coating edge. The dashed white line shows the TGO-mullite interface. The boxed section in (c) indicates the region subjected to compositional analysis.

A higher magnification image of the TGO region is compared with EDS mapping in Figure 3.7. It is apparent that the micro-fracture is contained within the TGO scale that grew on the Si bond coat at the original  $\text{Al}_6\text{Si}_2\text{O}_{13}$  – Si interface. The cracking within the TGO did not penetrate the adjoining  $\text{Al}_6\text{Si}_2\text{O}_{13}$  layer or the Si layer on which it had grown. Semi-quantitative EDS point analyses of the TGO indicated that it contained only Si and O with a composition consistent with  $\text{SiO}_2$ . In addition to the formation of the TGO, considerable internal oxidation of the Si bond coat is evident. This is consistent with an interconnected void structure whose interior surfaces were oxidized during annealing and subsequent steam-cycling.

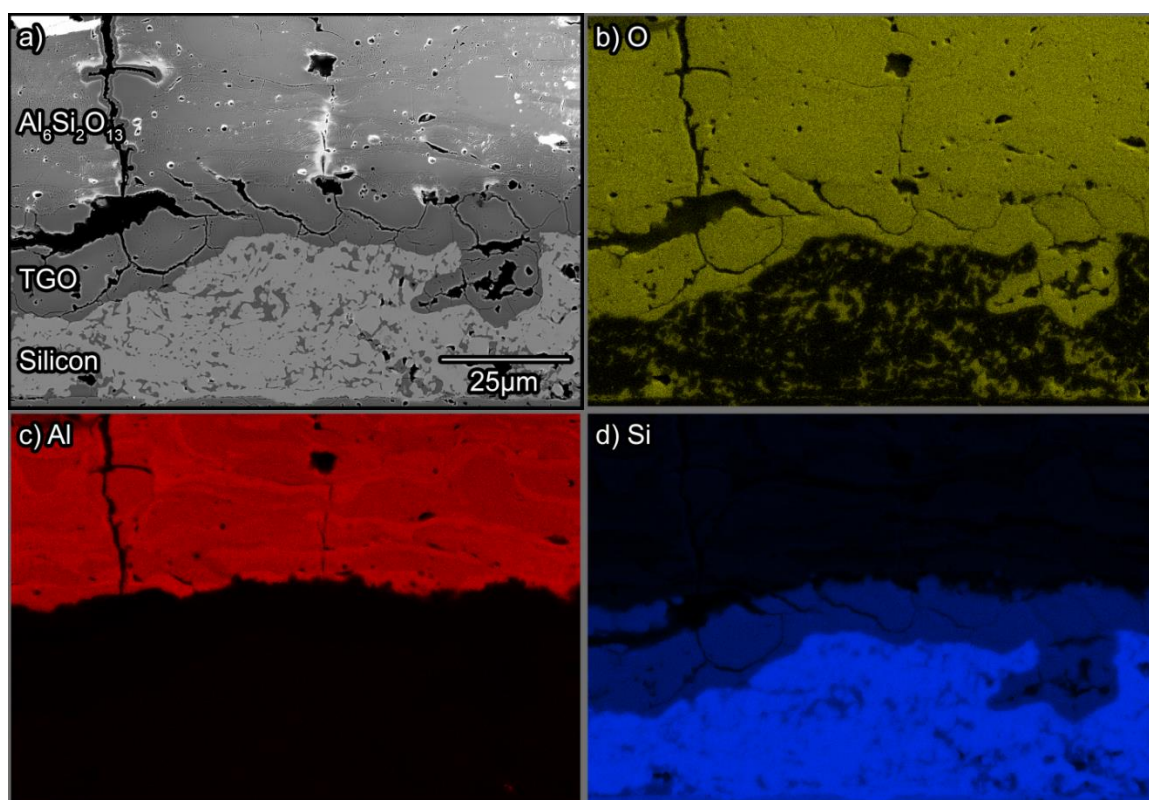


Figure 3.7: (a) A SEM image taken in BSE mode of a mud-crack root intersection with an adherent silica TGO –  $\text{Al}_6\text{Si}_2\text{O}_{13}$  interface as identified in Figure 3.6(c). (b) An oxygen, (c) aluminum, and (d) silicon dot map of the same region.

The TGO has been analyzed using Raman spectroscopy, and the ambient temperature phase identified to be  $\alpha$  (low) cristobalite based on the presence of spectral peaks with wavenumbers at  $230\text{ cm}^{-1}$  and  $416\text{ cm}^{-1}$ ,<sup>212-214</sup> Figure 3.8. The presence of the silicon peak at a wavenumber of  $520\text{ cm}^{-1}$  indicates that Si – Si bonding was sampled by the probe. The observed intensity of this peak is very low compared to the intensity for pure silicon, and may be due to retained silicon in the oxide. Raman analyses have been performed at multiple points across the width of the coating (Figure 3.8) and all measurements indicated the TGO to be  $\alpha$  cristobalite; no vitreous  $\text{SiO}_2$  was detected. While this did not preclude the presence of vitreous silica, it indicates that if a vitreous phase existed, its thickness was considerably less than the  $\sim 1\text{ }\mu\text{m}$  diameter laser probe used for the Raman analysis. The presence of  $\alpha$  (low) cristobalite at ambient temperature implies that  $\beta$  (high) cristobalite was formed during high temperature  $\text{H}_2\text{O}/\text{O}_2$  exposure, and that the  $\beta$  (high) cristobalite then underwent a phase transformation to the  $\alpha$  phase during cooling. Such a phase change typically commences at  $\sim 220\text{ }^\circ\text{C}$  during the cooling of  $\beta$ -cristobalite.<sup>201,214-216</sup> The variation in the Raman background signal may be an indication of the incorporation of hydroxyl groups within the silica, which are known to result in this phenomenon.<sup>217</sup>

Modest microstructural changes occurred within the  $\text{Yb}_2\text{SiO}_5$  and  $\text{Al}_6\text{Si}_2\text{O}_{13}$  layers during steam-cycling, Figure 3.9. After 200 steam cycles, equiaxed microcracking of the  $\text{Yb}_2\text{SiO}_5$  phase in the topcoat was observed, Figure 3.9(a). In the  $\text{Al}_6\text{Si}_2\text{O}_{13}$  layer, aggregation of  $\text{Al}_2\text{O}_3$  and coarsening into larger plates was observed, Figure 3.9(b). The presence of such plates has been previously identified in this system.<sup>97</sup> No evidence of volatilization of silica was observed in either layer. Steam-cycling of the coating system

resulted in the formation of a reaction product between the  $\text{Yb}_2\text{SiO}_5$  and  $\text{Al}_6\text{Si}_2\text{O}_{13}$  layers, Figure 3.10. The EDS-measured composition of this reaction product ranged between 11-12 at% Yb, 11-20 at% Al, 14-20 at% Si, and 56-57 at% O. Its thickness varied considerably and exceeded 5  $\mu\text{m}$  in some locations. The varying Al and Si contents indicate that the compound has a broad phase field. No cracking of the reaction product was observed, but porosity was present below the interface between the Yb-Al-Si-O reaction product and  $\text{Al}_6\text{Si}_2\text{O}_{13}$  layer. Raman analyses of this reaction product, Figure 3.11, indicated that it was crystalline and shared many of the atomic bonding configurations present in  $\text{Yb}_2\text{SiO}_5$ , though several additional peaks were also present in the spectra. Raman spectra for the phases of the Yb-Al-Si-O system have not been published and so this reaction product could not be identified.

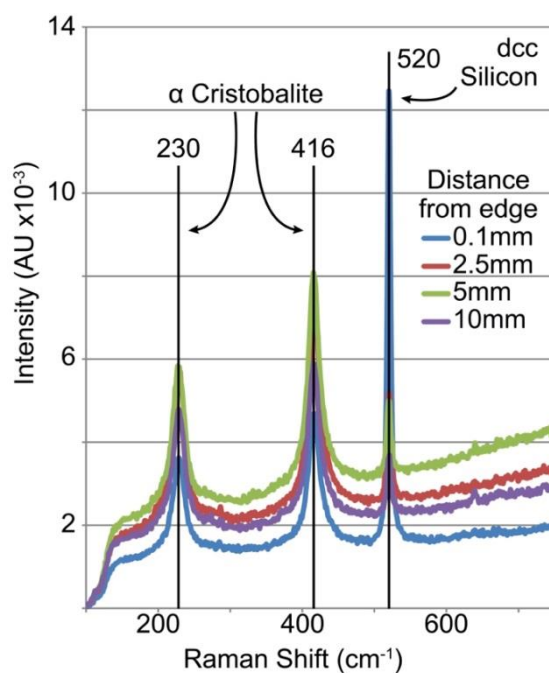


Figure 3.8: Raman spectra from the thermally grown (silica) oxide at the Si-mullite interface as a function of distance from the edge of the coated sample.

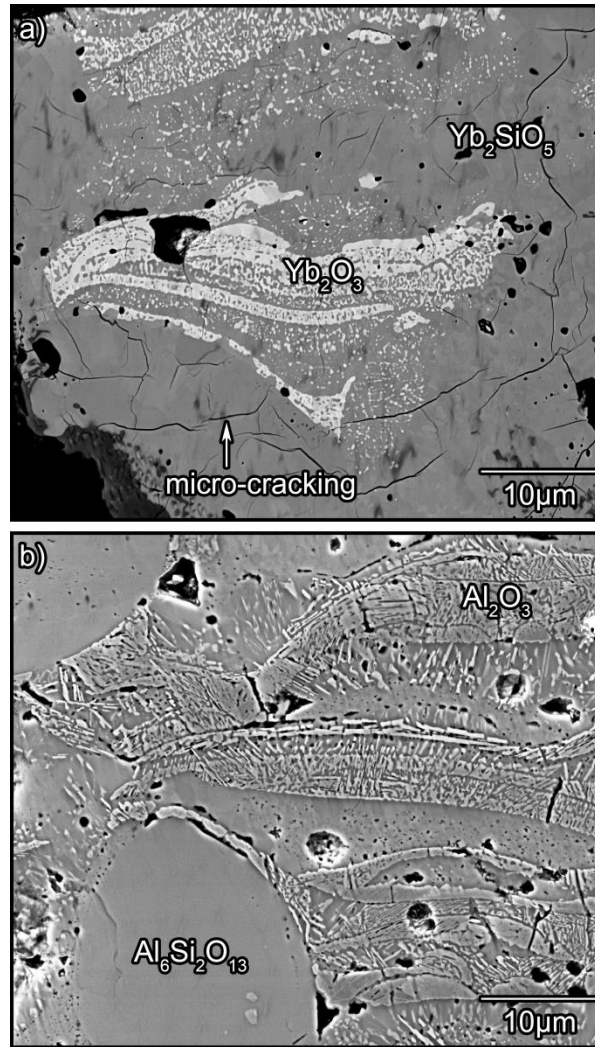
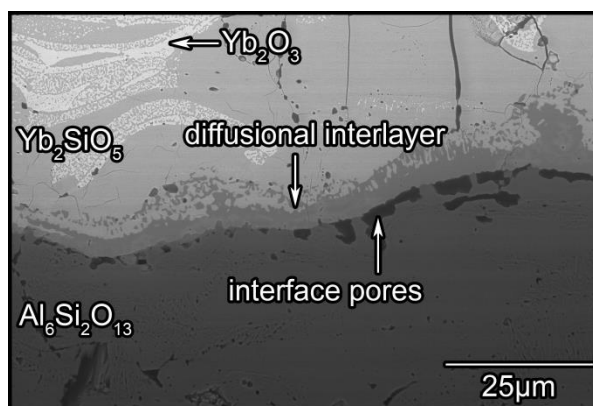


Figure 3.9: High magnification BSE mode SEM images of (a) ytterbium monosilicate and (b) the mullite layers after a 200 steam cycle exposure.

### 3.4 Calculated Stress States and Energy Release Rates

The mechanical properties and calculated thermal residual stresses for the EBC system of Figure 3.1 are presented in Table 3.1. Some explanation is merited for the stress states and energy release rates (ERRs) calculated for systems including cristobalite, which undergoes a phase transformation. It was assumed that oxidation grows a pure  $\beta$  cristobalite scale under stress free conditions at the steam-cycling temperature of 1316

°C. Upon cooling, strain is generated by the thermal contraction of  $\beta$  cristobalite. Plastic flow during cooling is neglected; creep is also neglected, but the contribution can be expected to be small due to the fast cooling rate. At 220 °C an inversion-type phase transformation occurs in cristobalite (i.e.  $\beta$  (high) to  $\alpha$  (low)), with a volume reduction of 4.5 % (an average of previously reported experimental values)<sup>201,216</sup>. The system is then further cooled with additional strain generated according to the CTE of  $\alpha$  cristobalite and the other layers of the system. The cristobalite is assumed to be constrained in the plane of the coating by the surrounding layers, and stresses are calculated based upon the thermal and transformation elastic strain mismatch. The resulting thermal residual stress at 20 °C within the cristobalite layer was greater than 4 GPa, assuming no cracking or strain relaxation occurred. Clearly, the large elastic strain energy generated by this phase transformation is a potent driving force for permanent deformation. It is noted that the stress calculation places only an upper bound on the attainable driving force.



*Figure 3.10: SEM micrograph (in BSE mode) of the interface between the ytterbium monosilicate and mullite layers in a sample that delaminated after 600 steam cycles at 1316°C. Note the formation of an approximately 5 $\mu$ m thick reaction product between the two layers and interfacial pores created by the inter-diffusion reaction.*

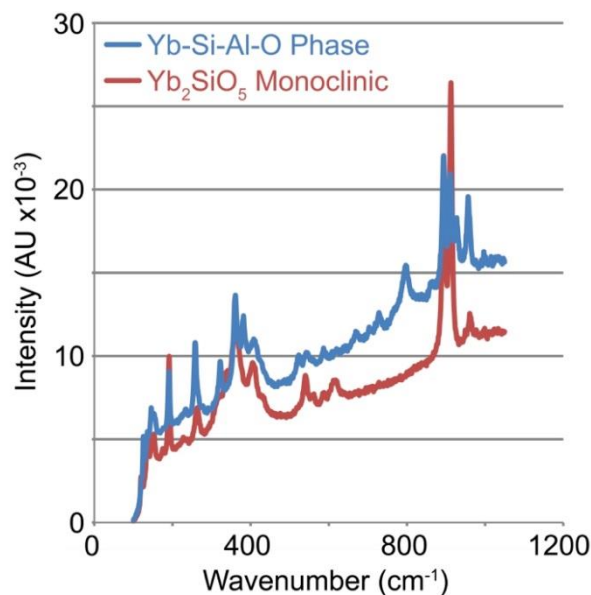


Figure 3.11: Raman spectra of the Yb-Si-Al-O reaction product formed at the  $\text{Yb}_2\text{SiO}_5 - \text{Al}_6\text{Si}_2\text{O}_{13}$  interface in Figure 3.10 and a reference pattern for APS  $\text{Yb}_2\text{SiO}_5$ .

The energy release rates for delamination at the various interfaces in the system both before and after a 20  $\mu\text{m}$  thick thermally grown  $\text{SiO}_2$  scale had formed at the  $\text{Al}_6\text{Si}_2\text{O}_{13} - \text{Si}$  interface have been calculated as a function of temperature assuming plane-strain constraint, and are shown in Figure 3.12. The conversion of pure Si to  $\text{SiO}_2$  is theoretically accompanied by a 110-120 % increase in volume on a molar basis (depending upon the molar volumes used), but for the case considered here it is assumed that some volatility occurred such that the actual volume increase was 100 %, corresponding to a molar volume ratio of 2. Figure 3.12(a) shows that when no TGO was present the ERRs of all three interfaces were very similar in magnitude. However, the energy release rates at interfaces below the TGO were increased considerably when the  $\alpha$ -cristobalite TGO was present, Figure 3.12(b). These trends also apply for computations that assume reduced APS elastic moduli of the layers, Figure 3.12(c) and (d).

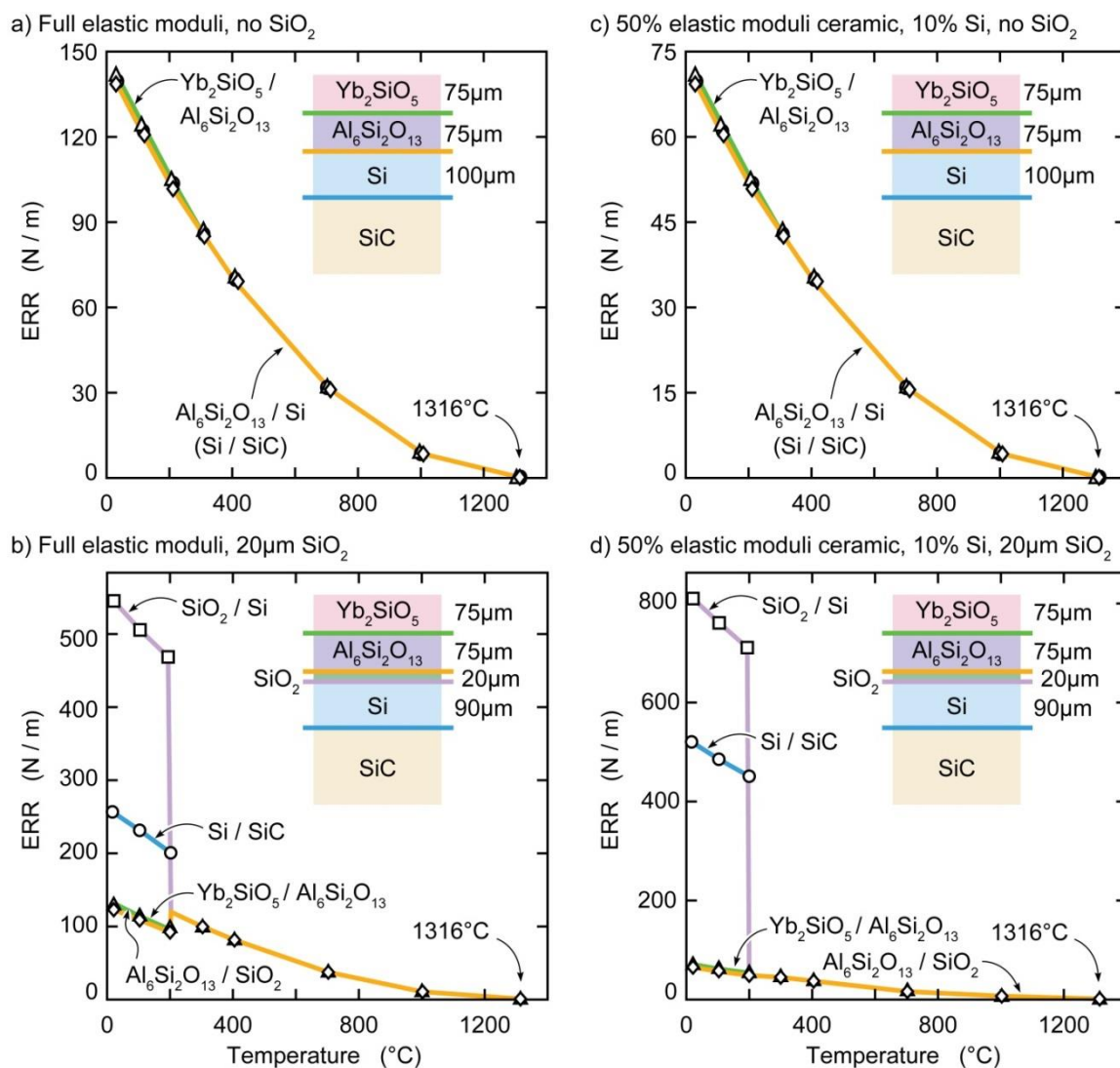


Figure 3.12: The elastic stored energy release rate for delamination at the various interfaces of a tri-layer EBC as a function of temperature cooling from 1316°C. (a) For an annealed coating assuming bulk (full) elastic moduli, and (b) the same coating after growing a 20µm thick cristobalite TGO at the  $\text{Al}_6\text{Si}_2\text{O}_{13}$  – Si interface. (c) and (d) repeat (a) and (b) but with the reduced elastic moduli assumed for the APS materials given in Table 3.1.

### 3.5 Discussion

The APS deposition of a tri-layer of the  $\text{Yb}_2\text{SiO}_5/\text{Al}_6\text{Si}_2\text{O}_{13}/\text{Si}$  EBC on a SiC substrate results in the development of a substantial stored elastic strain energy in the

coating system after cooling from either the deposition process, the stabilization annealing treatment, or the steam-cycling process, Figure 3.12(a) and (c). The resulting ERR is very high: for comparison the toughness of oxide ceramics lies in the range of 1-50 N/m (roughly equivalent to 0.1-10 MPa m<sup>1/2</sup>).<sup>218</sup> The ERR for an interface also rises considerably if cristobalite is formed above it in the coating, Figure 3.12(b) and (d). The delamination failures of coatings upon cooling from deposition, after annealing and after <200 steam cycles are all consistent with a thermomechanical stress-driven failure mechanism at the Si – SiC interface, initiated at the stress concentration present at the coating edge<sup>219</sup> in conjunction with insufficient adhesion at the Si – SiC interface.

It is worth noting again that the neglect of plastic flow during cooling implies that the ERR estimates are upper bounds. In addition, deformation mechanisms such as the observed channel (mud) cracking, microcracking of the TGO, and other microcracking would all considerably reduce the amount of strain energy available to drive cracking in the cooled state. Analysis of these competing effects is complicated, and the exact effect of these alternate energy release mechanisms has not been studied. As shown in Figure 3.12(c) and (d), the effect of reduced APS moduli on the ERR behavior has been studied and has a significant effect on the magnitude of the ERR (approximate factor of 2), but only a minor effect on the shape of the ERR curves and relative magnitude of ERR between the various interfaces. Based upon these limitations, the trends of Figure 3.12 are used as guides in explaining the damage observed and the tendency of the coating to incur damage at particular locations as opposed to direct measures of the true ERR.

In those coatings where the Si – SiC interface adhesion was sufficient to avoid early failure, coating delamination occurred by a combination of thermomechanical and

environmental effects. A schematic illustration of the damage mechanisms is shown in Figure 3.13. After the stabilization annealing treatment, the CTE mismatch between the coating layers and the substrate resulted in a large tensile residual stress in the  $\text{Yb}_2\text{SiO}_5$  layer. A smaller tensile stress was also formed in the  $\text{Al}_6\text{Si}_2\text{O}_{13}$  layer, Table 3.1 and Figure 3.13(a). These stresses varied considerably based upon the elastic moduli used for their calculation, but were substantial in either case. The tensile stresses resulted in the formation of mud cracks, which were arrested upon encountering the Si bond coat, presumably due to the compressive stress in that layer. At ambient temperature, the faces of these mud cracks were quite widely separated, especially in the  $\text{Yb}_2\text{SiO}_5$  layer.

Upon heating to 1316 °C in the steam-cycling furnace, the primary damage mechanism became environmental: even though the mud crack opening displacement was greatly reduced by thermal expansion, the gaseous environment permeated the mud crack network and began to oxidize the Si bond coat, forming a  $\beta$ -cristobalite TGO at the root of the mud cracks, Figure 3.13(b). Cristobalite has previously been observed in silica scales formed above 1200 °C during exposure to either water vapor or oxygen, with a prevalence that increases with temperature.<sup>51</sup> Some volatilization may occur through the reaction of solid silica with water vapor to form gaseous silicon hydroxides.<sup>46,47,51</sup> However, this is likely to be inhibited by the need for diffusive transport of  $\text{H}_2\text{O}$  and  $\text{Si}(\text{OH})_4$  through the crack network between the TGO and the external environment. The voids at the root of mud cracks are therefore likely a combination of mechanical damage and environmental effects.

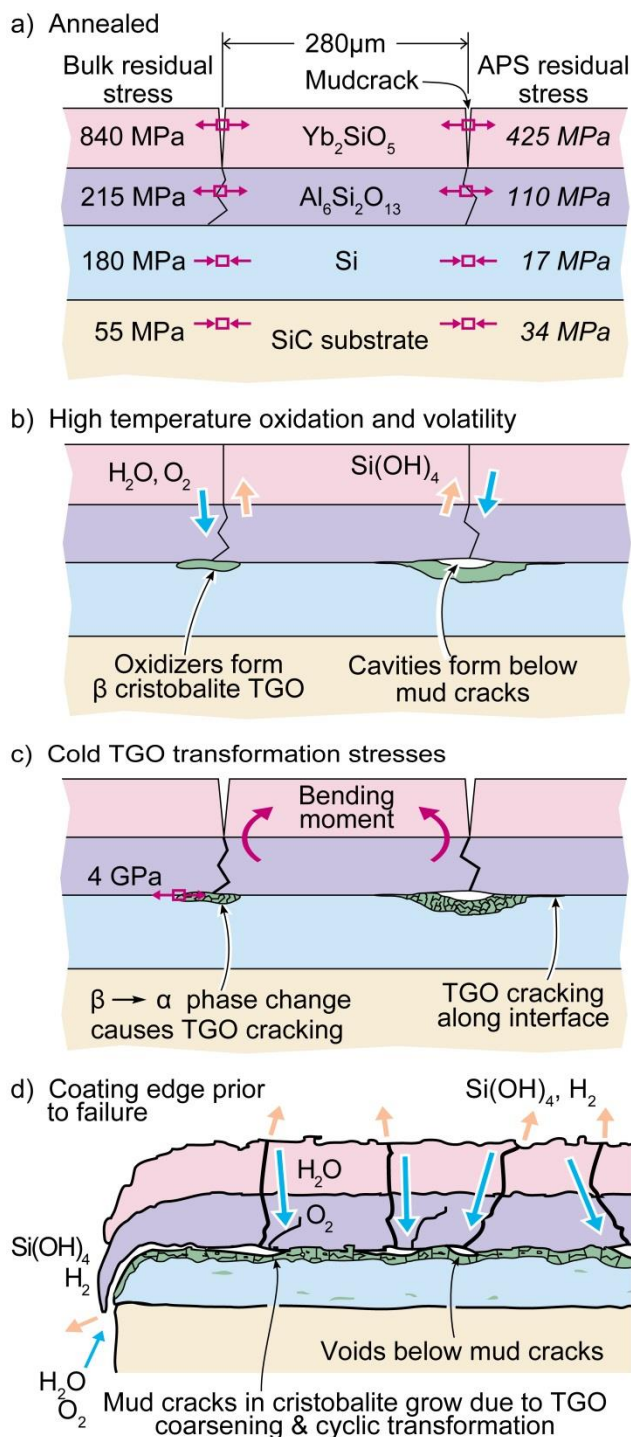


Figure 3.13: The damage mechanism sequence in an  $\text{Yb}_2\text{SiO}_5/\text{Al}_6\text{Si}_2\text{O}_{13}/\text{Si}$  tri-layer EBC applied to an  $\alpha$ -SiC substrate. (a) Shows the initial damage and stress states in the annealed EBC, (b) shows reaction at  $1316^\circ\text{C}$  and (c) details mechanical damage at low temperature. (d) Schematic of the edge localized damage and failure.

Upon cooling, Figure 3.13(c), the CTE mismatch-derived residual stresses began to develop and the mud cracks began to re-open. Significant bending moments are expected (based on elastic analyses) because the outermost coating layer had a higher CTE than the others. As the TGO grown on the bond coat thickened with increasing high temperature exposure time, the driving force for delamination rapidly became dominated by the release of strain energy in the TGO, as indicated in Figure 3.12(b) and (d). During the cooling of coatings with a thick TGO, the thermally grown  $\beta$  cristobalite transformed to the  $\alpha$ -phase at around 220 °C with a volume reduction of ~4.5 %. This volume change was constrained by adhesion to the surrounding Si and  $\text{Al}_6\text{Si}_2\text{O}_{13}$ , resulting in equiaxed microcracking of the TGO. During the next heating cycle, the TGO microcrack network provided a fast diffusion path for  $\text{O}_2$  and  $\text{H}_2\text{O}$  to reach un-oxidized Si, and thereby increased the oxidation and volatilization rate (due to the very high specific surface area of the microcracked silica). Repeated thermal cycling resulted in growth of the TGO and eventual linkage of the TGO regions emanated from each mud crack. At some point in this process, a delamination crack was formed by linkage of the TGO microcracks.

Delamination for the tested coating geometry initiated at the edge of the coatings, where the severity of the damage mechanisms shown in Figure 3.13(a)-(c) was increased due to additional environmental attack from the coating edge, Figure 3.13(d). The Si bond coat was left unprotected by the  $\text{Yb}_2\text{SiO}_5$  and  $\text{Al}_6\text{Si}_2\text{O}_{13}$  layers at the sample edge even though attempts were made to wrap the coating around the edge of the substrate. Upon heating in the steam-cycling furnace, this resulted in rapid oxide growth on and within the bond coat due to the presence of an interconnected pore network. Upon cooling, TGO microcracking commenced and this enabled more rapid oxidizer

penetration and TGO formation during the subsequent hot cycle. The large bending moment and substantial ERR that was developed upon cooling resulted in delamination and release of the coating between the edge and the first mud crack. Further cycling then resulted in the progressive delamination of the coating.

It is evident that the rapid delamination failure of the tri-layer coating system was controlled by the high diffusivity pathways for oxidizer access at either the coating edges or the mud cracked  $\text{Yb}_2\text{SiO}_5$  and  $\text{Al}_6\text{Si}_2\text{O}_{13}$  layers. Future coating developments should be focused upon systems where exposed edges are avoided and where the CTE mismatch between the layers of the coating and the substrate is sufficiently small to avoid mud crack formation. This CTE matching constraint in combination with the need for low silica activity will significantly reduce the number of candidate coating materials. The study has also identified two vulnerabilities of the Si bond coat. First, it is essential to identify optimized deposition conditions that result in tough interfaces between the bond coat and SiC and to produce a denser Si coating that does not contain surface connected pores. Second, the formation of a *cristobalite* TGO and its high stored elastic strain energy upon cooling will be problematic for practical EBC systems. Oxidizing species will eventually diffuse through the outer layers of the EBC system and lead to the formation of a TGO at the silicon surface. If the formation of cristobalite can be slowed or avoided, the driving force for delamination could be reduced and the coating lifetime might be considerably extended.

### 3.6 Conclusions

Three-layer  $\text{Yb}_2\text{SiO}_5/\text{Al}_6\text{Si}_2\text{O}_{13}/\text{Si}$  EBCs have been deposited onto SiC substrates using an APS approach. These coatings have been steam cycled to failure (defined as any observed spallation) in an atmospheric pressure, slowly flowing 90 %  $\text{H}_2\text{O}/10$  %  $\text{O}_2$  environment using 60 min hot (1316 °C) and 10 min cool (110 °C) cycles. The coating lifetime was controlled by interactions between environmental degradation and mechanical damage resulting from thermal residual stresses and phase transformation. Specifically, it is found that:

- a) Mud cracking of the as-deposited and annealed EBC was indicative of a thermomechanical incompatibility in the system. This led to the development of short circuit gas transport paths through the water vapor protective layers of the EBC.
- b) Oxygen and steam penetrate through the upper layers of the EBC and oxidize the Si bond coat. The dominant oxidizer access route appears to be through mud cracks and eroded channels in the TGO. The high testing temperature of 1316 °C resulted in the formation of  $\beta$  (high) cristobalite as opposed to vitreous  $\text{SiO}_2$ .
- c) Thermally grown cristobalite experiences a phase transformation upon cooling at around 220 °C that is accompanied by considerable volumetric contraction. This caused severe fracturing of the TGO, and ultimately led to coating delamination. *The formation of a cristobalite TGO was a major contributing factor to the poor steam-cycling durability of this tri-layer EBC system.*

## **4 Air Plasma Spray (APS) System at UVA**

A considerable amount of time was invested in the selection, installation, commissioning, and initial spray parameter development of a Praxair-TAFA APS system at UVA. The process took almost 18 months of dedicated work and coordination between the ONR funded project team, Praxair-TAFA, UVA Environmental Health and Safety (EHS), the Office of the University Building Official (UBO), the project engineers of Vansant & Gusler, inc., UVA Facilities Management, UVA Mechanical Trades, and the renovation and installation teams. All of these entities are in part responsible for the timely delivery of a fully functioning APS lab.

### **4.1 APS System Selection**

Several APS vendors were queried for information regarding APS systems. The two main providers of APS technologies (and most other thermal spray equipment) both domestically and internationally are Praxair-TAFA and Sulzer Metco. These two vendors also supply the overwhelming majority of (if not all) deposition equipment used by turbine hardware OEMs. Therefore, selection of a deposition system from one of these

two manufacturers was desirable. Of the available systems, Praxair-TAFA offered a cost effective unit with domestic service and the ability to use multiple deposition torches produced by both Praxair-TAFA and Sulzer Metco. Due to the flexibility of the system, the Praxair-TAFA UPC 7700 unit with a Praxair-TAFA SG-100 APS torch was selected for the University facility.

Four different plasma forming gases can be used to operate the APS torch (Ar, He, H<sub>2</sub>, and N<sub>2</sub>) over a wide range of flow rates and compositional ratios. This permits extreme flexibility in the range of operating environments attainable by the system, and allows for tailoring of the gas environment used to the particular material being deposited. The system also has a 100 kW power supply that can accurately control deposition power to ~100 W. Accordingly, a very wide range of plasma temperatures and flow velocities can be achieved with this single system. A schematic of the system is presented in Figure 4.1.

The deposition system was additionally outfitted with four rotary gravity-feed powder supply units- “powder feeders”. All four of these powder feeders can be individually or collectively operated allowing for very complex structures to be deposited. The availability of four feeders also greatly minimizes powder cross-contamination issues experienced when multiple powders must be fed through the same unit. If powder contamination is an issue for the coating application, the powder feeders must be disassembled, cleaned, and all consumables must be replaced. The process is both time consuming and costly, and greatly increases the time required to deposit multi-layer coatings. The presence of multiple powder feeders also carries the added benefit of allowing deposition of graded coatings from individual powder sources.

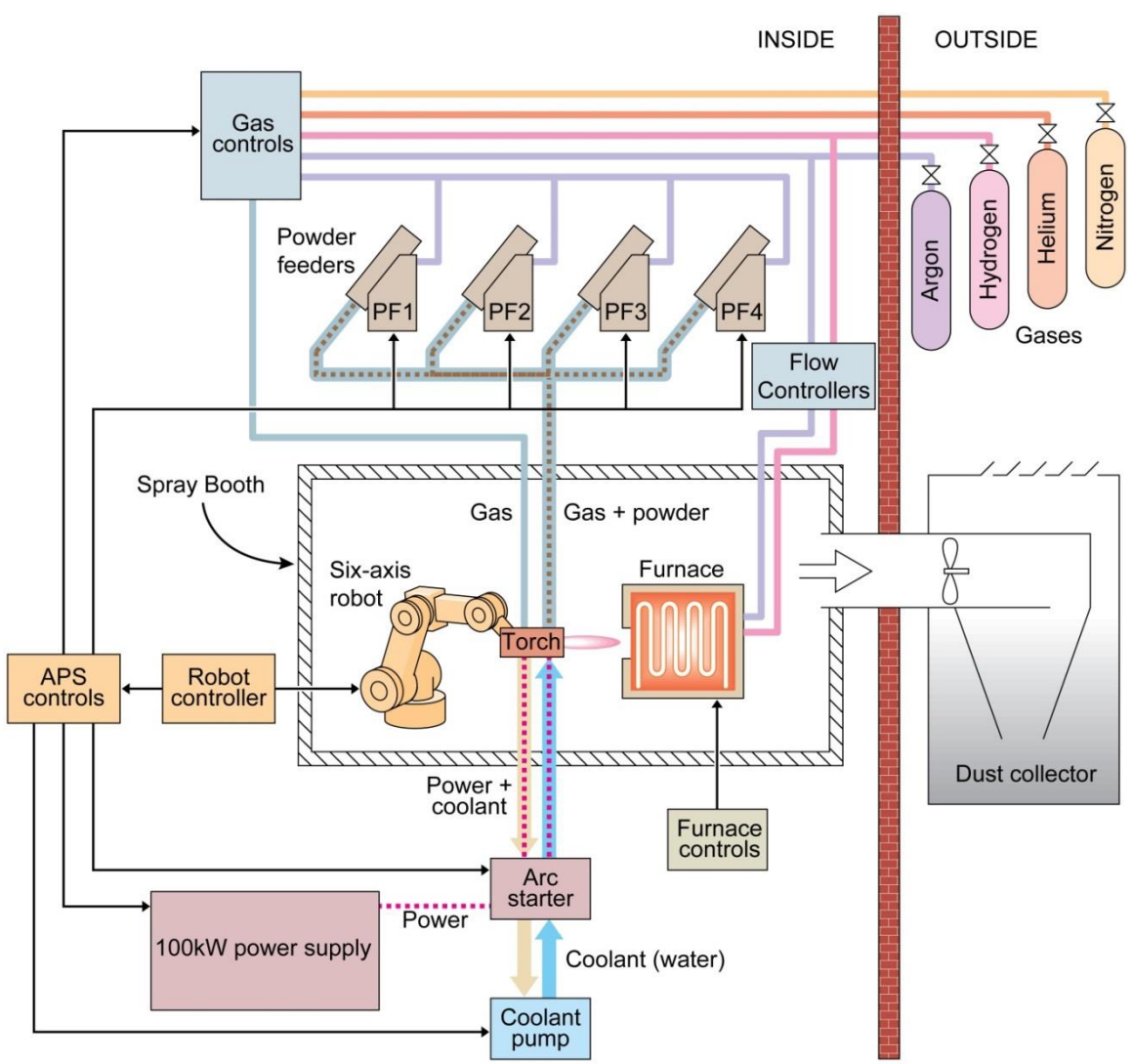


Figure 4.1: Schematic illustration of the configuration of UVA's APS lab.

The UVA system is ultimately controlled by a 6-axis ABB IRB-140 robot to which the APS torch is affixed. This allows for maximum flexibility by live manipulation of the torch during spraying. The desirability of this configuration and operation of the system will be discussed in Sections 4.3 and 4.4.

## 4.2 APS Facility

The APS lab is located in the Observatory Mountain Engineering Research Facility (OMERF). This location was determined to be the most suitable for a large deposition system due to its remoteness from central grounds, large laboratory space, and availability of the ~150 kW of power that can be drawn by the APS system and its ancillary equipment during peak operation. The control interfaces of the lab are set up in an open floor plan that promotes awareness of equipment operation and provides access to all equipment. The primary control system is shown in Figure 4.2.



*Figure 4.2: Photography of the process gas handling and primary controls of UVA's APS system.*

### 4.3 Equipment and Process Modifications

The APS system at UVA has four powder feeders, Figure 4.3. As described in Chapter 1 and evidenced in Chapters 2 and 3, the feed of powders is an incredibly important aspect of the APS deposition process. Inconsistent powder feed not only results in inconsistent thickness of deposited coatings, but also in an effective change in spray parameter due to the continuously varying density of powder particles in the APS plume (“powder load”); the phenomenon is termed “powder pulsing”. Either of these phenomena can very negatively affect control over the coating microstructure.



*Figure 4.3: The four powder feeders that can be connected to the APS torch.*

Powder pulsing was observed in initial studies of mullite, BSAS, and ytterbium silicate powders at UVA. These powders were all of fused-crushed manufacture, and

therefore had irregular shapes and relatively broad size distribution. When combined with the relatively low density and poor packing efficiency of these materials, this led to severe difficulties in powder feeding. Powder pulsing out of the powder feeder itself was remedied by fluidizing the system with 900 N air-powered rotary vibrators operating in the 100 Hz range. This effectively eliminated powder pulsing directly out of the feeders.

However, powder flow issues were still observed through the feed hoses. Electrostatic charge issues with powder flow through the feed lines were observed in the winter and humidification of the feed system was found to be highly problematic in the summer. Electrostatic discharge issues were remedied by grounding the entire length of powder hose with electrical conductor. Humidification issues were resolved by continuously storing all powders in desiccators and implementing several minute Ar purges of powder lines before feeding powders.

APS deposition of ceramic materials onto heated substrates was also discussed in Chapter 1. The premise of this technique is to reduce the quench rate of deposited material such that crystalline phases can be formed immediately upon deposition.<sup>70</sup> This is desirable for a number of reasons and is particularly applicable to APS ceramic materials. The difference between deposition of injected particles upon ambient temperature and heated substrates is schematically illustrated in terms of the crystallinity of deposits in Figure 4.4. Even if no crystalline core remains in the powder particles after traversing the plasma, the same concepts still apply. The slowed cooling rate extends the time permitted for nucleation, and therefore allows for crystalline phases with slower nucleation rates to form and grow.

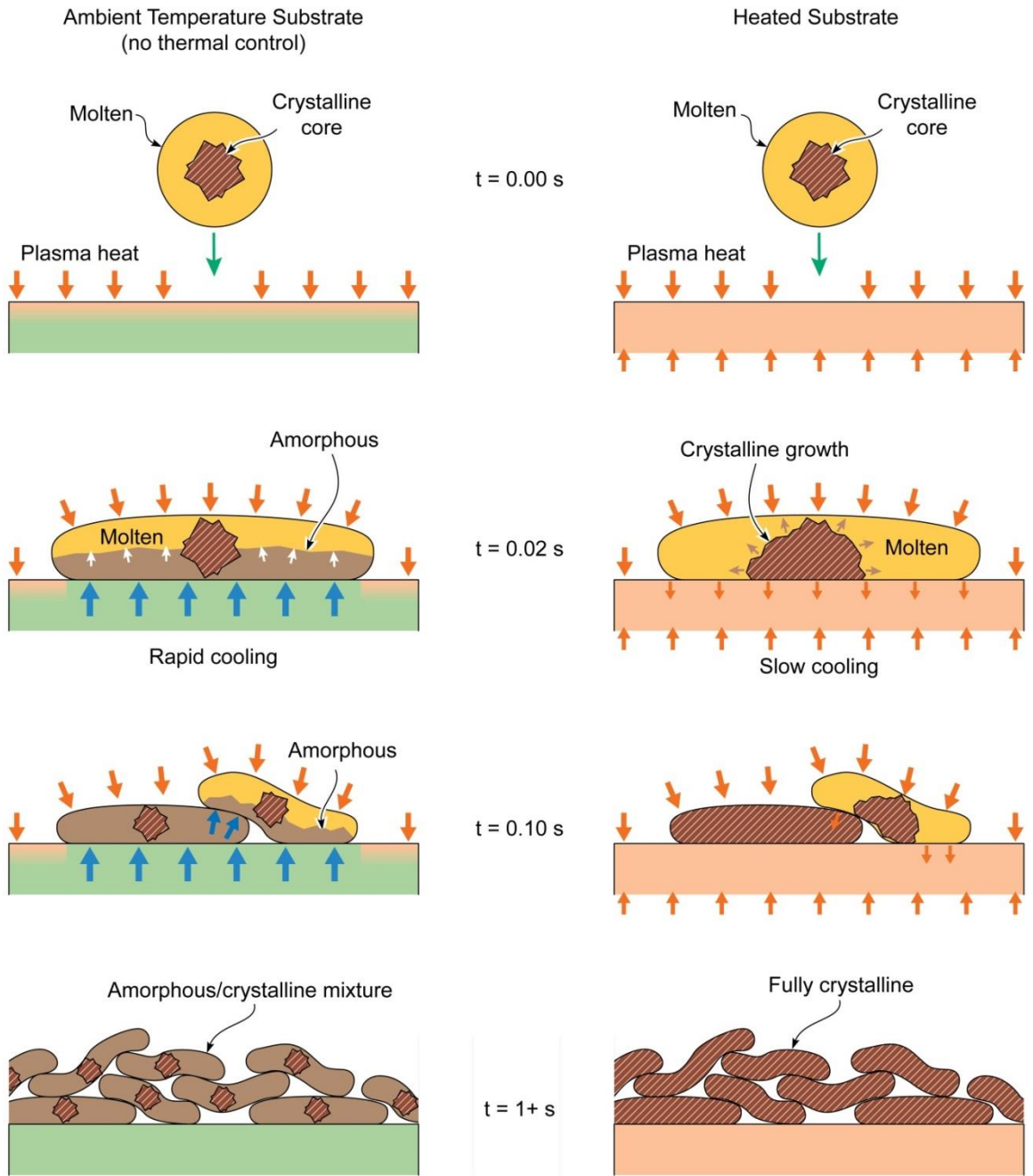


Figure 4.4: Schematic illustration of the effect of substrate heating upon crystallinity of splats deposited by APS.

Due to crystallization issues with APS deposition of mullite onto ambient temperature substrates,<sup>70</sup> the APS system at UVA was equipped with a high temperature deposition

furnace. This furnace is capable of holding a 1500 °C internal temperature with the deposition window open, as pictured in Figure 4.5. Though elevated temperature deposition resolves issues with deposition of amorphous materials, it also introduces a host of other logistical issues with fixturing samples for deposition. Superalloy fixtures were tested but were found to be insufficient for the extreme oxidizing environment. Aluminosilicate insulation fixtures comparable to those used at NASA Glenn were tested, but these had the disadvantage of overlapping the front of the sample, and their light weight often lead to movement inside the deposition furnace during APS processing.



*Figure 4.5: Photograph of Brad Richards removing a deposition fixture with four coated samples from the high temperature deposition furnace.*

Instead, SiC fixtures were custom designed and fabricated to hold the SiC substrates during deposition. One of these fixtures is shown being removed from the furnace in Figure 4.5. The fixtures had sufficient weight to remain stationary during the deposition, and their rigidity allows for gripping of substrates by grooves cut into their edges, thereby allowing one entire surface of the substrate to be coated inside the furnace. The fixture therefore solves an issue identified in Chapter 3 associated with exposed edges resulting from uncoated parts of the sample face. Due to the extreme thermal shock associated with loading and unloading the fixtures from a 1200 °C operating environment to ambient conditions, the sample fixtures were made out of stacks of 6 mm SiC plates machined to the desired shape.

The high temperature deposition furnace was also configured for continuous purging by mixtures of Ar and H<sub>2</sub> gases fed into the furnace. The Ar/H<sub>2</sub> purge allowed for a strongly reducing environment to be established within the furnace, the necessity of which will be discussed in Chapters 5 and 6. The reducing gas flow could be pumped into the furnace at rates exceeding 20 slm and was moderated by individual mass flow controllers for the Ar and H<sub>2</sub> lines.

#### **4.4 APS Torch Control and Deposition**

In the configuration installed at UVA, the entire APS system is controlled by the 6-axis robot. This allows for an operational mode to be implemented that is similar in many ways to spray painting. There, a human operator physically controls the flow of the paint source and traverses the paint cloud emanating from the spray can across the surface to

be painted. In the APS system, the robot physically activates the plasma spray plume and then traverses the APS torch (and plume) across the sample to be coated in a pattern that optimizes surface coverage. A variety of spray patterns have been programmed into the robot that permit deposition onto several different geometries of sample.

The entire control sequence is activated and operated from the control pendant of the robot, pictured in Figure 4.6. A software framework was provided for this system by Praxair-TAFA with basic capabilities and routines. This software has been greatly expanded upon throughout the dissertation to handle several relevant specimens. The interface is intuitive and prompts the operator with a series of questions that determine which coating layers to deposit, what sequence to deposit them in, and what sample and sample fixture are being used for deposition. The control software also allows for termination of the deposition routine at any point.

During operation, little of the actual deposition process is visible aside from the plasma flame and movement of the robotic arm. A photograph taken during deposition is shown in Figure 4.7. This photograph indicates the relative scale of the deposition furnace, the robot, and the APS torch. The photograph was taken through ANSI shade 8 weld screening. The distance between the face of the APS torch and the front face of the deposition furnace is ~25 mm.



*Figure 4.6: Control pendant of the ABB IRB-140 robot that runs the APS system.*

At peak production, the APS system is capable of depositing well over 100 coated substrates per day when using the high temperature deposition fixture. This number is considerably greater if low temperature depositions are performed. The production rate is such that the time required for deposition is unlikely to ever pose a problem even if numerous APS projects were active at the University. This lab adds a deposition capability to the School of Engineering and Applied Science that can be found at only a few other universities in the United States and internationally.



*Figure 4.7: Live plasma spraying into the high temperature deposition furnace.*

## **5 Structure, Composition and Defect Control of APS Ytterbium Silicates**<sup>3</sup>

**Synopsis:** Environmental barrier coatings (EBCs) are needed to protect SiC structures exposed to high temperatures in water vapor rich environments. A tri-layer EBC system consisting of a silicon layer attached to the SiC, a mullite diffusion barrier and a low steam volatility ytterbium silicate topcoat has shown some promise for use at temperatures up to 1316 °C. However, the performance of the coating system appears to be dependent upon the manner of its deposition. Here, an air plasma spray method has been used to deposit this tri-layer EBC on  $\alpha$ -SiC substrates and the effects of the plasma arc current and hydrogen content upon ytterbium monosilicate ( $\text{Yb}_2\text{SiO}_5$ ) and disilicate ( $\text{Yb}_2\text{Si}_2\text{O}_7$ ) topcoats' structure, composition and defects are investigated. Modification of spray parameters enabled the loss of Si from the injected powder to be reduced, leading to partial control of coating stoichiometry and phase content. It also enabled significant control of the morphology of solidified droplets, the porosity and the microcracking

---

<sup>3</sup> A technical article submitted to the *Journal of Materials Science*.<sup>220</sup>

behavior within the coatings. Differences between the  $\text{Yb}_2\text{SiO}_5$  and  $\text{Yb}_2\text{Si}_2\text{O}_7$  are discussed in the context of their EBC application.

The work in this Chapter of the dissertation was carried out with the aid of Hengbei Zhao (UVA) who performed the TEM analyses. Discussions with Bryan Harder (NASA Glenn) and Elizabeth Opila (UVA) were critical at several stages. Ryan Hinckley (GE Fuel Cells, formerly Praxair-TAFA) also aided the initial formulation of the recipes that were developed into the spray parameters used here.

## 5.1 Introduction

The design of second generation tri-layer EBCs has already been reviewed in Chapter 1 of this dissertation. Among these, ytterbium monosilicate ( $\text{Yb}_2\text{SiO}_5$ ) and ytterbium disilicate ( $\text{Yb}_2\text{Si}_2\text{O}_7$ ) topcoat based EBCs appear promising due to their monomorphic nature<sup>81</sup>, substantial prior investigations<sup>77,78,95,97</sup> (Chapters 2 and 3), and the availability of the powdered forms of both materials which facilitates deposition by plasma spray methods.

APS deposition methods have also been reviewed in Chapter 1, and their applicability to EBCs is clearly established. However, studies of the microstructure and performance of tri-layer ytterbium monosilicate/mullite/silicon EBCs in Chapter 2 and Chapter 3 have shown a significant sensitivity of the coating's steam-cycling durability to the composition, structure and various defects incorporated into the layers during APS deposition.<sup>95,97</sup> Interest therefore exists in the relationships between plasma spray

deposition conditions and the composition, structure, and defect populations of the coating layers.

Here we experimentally investigate the effects of varying some of the air plasma spray deposition parameters upon the resultant compositions, microstructures and defects of the deposited ytterbium silicate topcoat of a tri-layer ytterbium silicate/mullite/silicon EBC system applied to SiC substrates. Studies are conducted on both ytterbium monosilicate, which has a very low recession rate in steam environments<sup>196</sup> and upon its disilicate counterpart, which has been confirmed here to have a much closer thermal expansion coefficient to that of the  $\alpha$ -SiC substrates. The deposition studies are performed using the University's APS system, detailed in Chapter 4.

## 5.2 Experimental

### 5.2.1 Plasma Spray Process

Tri-layer Yb-silicate/ $\text{Al}_6\text{Si}_2\text{O}_{13}$ /Si EBCs were air plasma sprayed onto 25.4 mm x 12.7 mm x 4.8 mm Hexoloy<sup>TM</sup>  $\alpha$ -SiC substrates (Saint Gobain Ceramics, Niagara Falls, NY) using the process schematically illustrated in Figure 5.1(a). Substrates were prepared by lightly grit blasting one surface with SiC to achieve an approximately 1  $\mu\text{m}$  amplitude surface roughness ( $R_a$ ). The substrates were ultrasonically cleaned in ethanol and inserted into a deposition fixture. The substrate-loaded fixture was then placed in a furnace set at a temperature of 1200 °C. To inhibit sample oxidation, a reducing gas composed (by volume) of 21 parts Argon to 1 part  $\text{H}_2$  was flowed through the furnace at a rate of 20 slm.

The substrates were allowed to heat for 3 minutes within the furnace with the reducing gas flowing before a front plug was removed to allow deposition to commence.

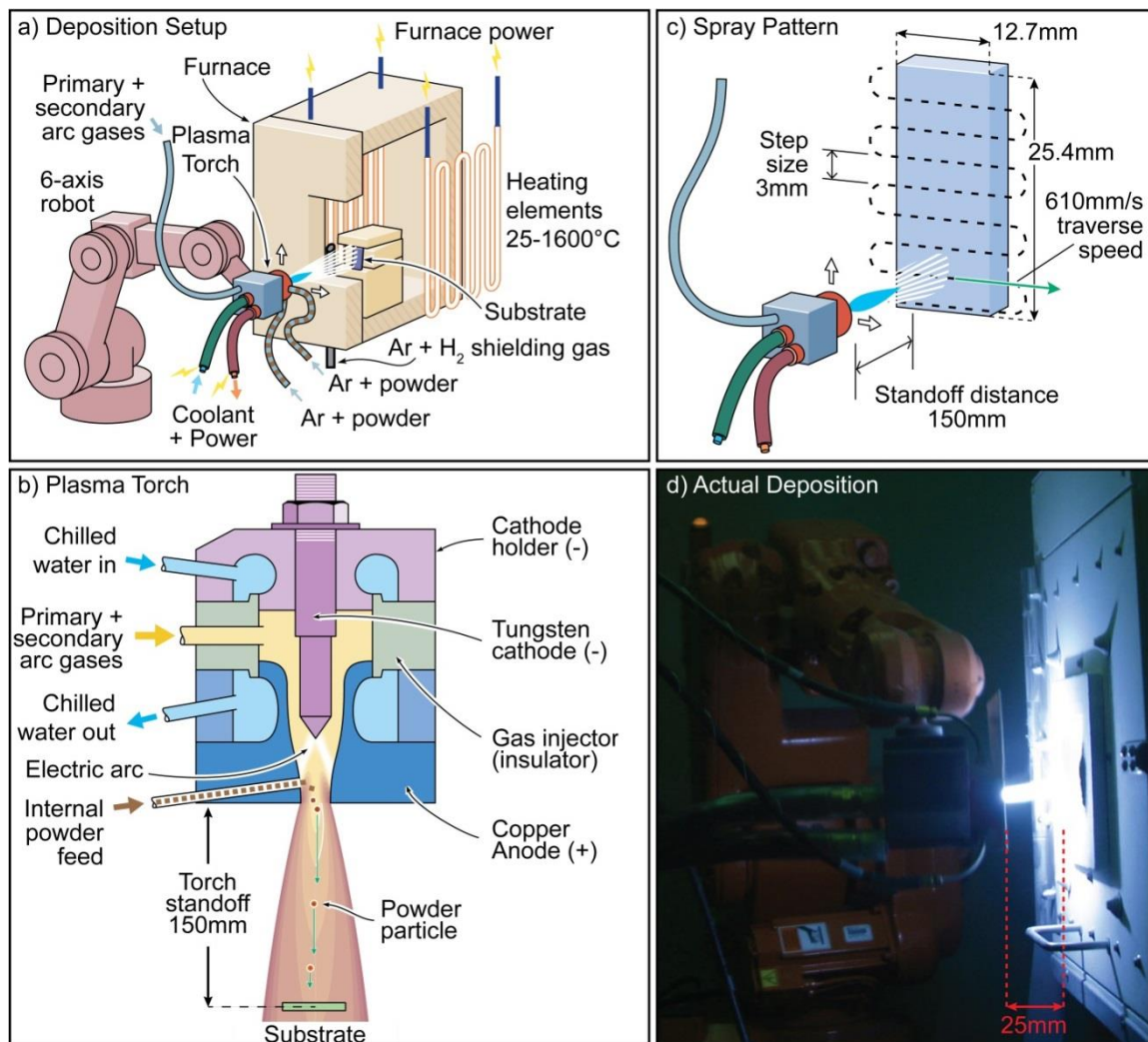


Figure 5.1: (a) Schematic illustration of the air plasma spray (APS) deposition approach used for high temperature environmental barrier coating (EBC) deposition. (b) Schematic illustration of the plasma torch design. (c) The spray pattern and definition of relevant deposition parameters. (d) Photograph taken during APS deposition into the box furnace.

A Praxair-TAFA Model SG-100 torch with a Model 02083-175 anode configuration was used for deposition of all of the coating layers. This torch, Figure 5.1(b), utilized

internal powder injection at a slight reverse injection angle. It was equipped with a Model 02083-120 cathode, a Model 03083-112 gas injector, and was cooled using 10 °C chilled water with a flow rate of 30 slm. The spray raster pattern shown in Figure 5.1(c) involving 2 passes of 12 steps was used to deposit all three coating layers. A photograph taken during deposition of an  $\text{Yb}_2\text{SiO}_5$  coating layer using this system is presented in Figure 5.1(d). All the depositions utilized a torch nozzle exit to the substrate surface standoff distance of ~150 mm while the distance from the torch to the outer front face of the furnace was ~25 mm.

Deposition of the Si layer was performed in the Ar/H<sub>2</sub> reducing gas environment furnace. Immediately after deposition of the Si layer, the reducing gas flow to the furnace was terminated and subsequent layers were then deposited. The deposition of each layer was completed in approximately 10 s (5 s per pass) and layer depositions were separated in time by only that required for the torch to change spray parameters, purge powder feed lines, and stabilize conditions for the next material (typically ~20 s). The spray parameters for deposition of the Si and  $\text{Al}_6\text{Si}_2\text{O}_{13}$  layers are provided in Table 5.1.

*Table 5.1: Plasma spray parameters for deposition of silicon and mullite layers.*

APS Layer	Si	$\text{Al}_6\text{Si}_2\text{O}_{13}$
Arc Current (A)	350	375
Primary Ar Flow (slm)	77.87	77.87
Secondary H <sub>2</sub> Flow (slm)	0.94	0.94
Carrier Ar Flow (slm)	5.90	5.43
Powder Flow (g/min, port)	31.0, upper	18.9, upper
Deposition Power (kW)	14.0	15.2

The ytterbium silicate layers were deposited using systematically varied sets of spray parameters that had been down-selected from an initially much wider range of parameters by selecting only those that resulted in fully dense coatings. Four primary spray variables controlled coating composition and microstructure: (i) powder size distribution and morphology, (ii) torch standoff distance, (iii) the plasma arc current, and (iv) the secondary gas ( $H_2$ ) concentration. Of these, the powder size distribution was fixed by the need to select from a commercially available ytterbium silicate powder source. Preliminary studies indicated that reducing the torch to substrate standoff distance beneficially affected the coating composition. However, reduction of the plasma torch standoff distance below 150 mm was physically constrained by the need for deposition onto heated substrates that resided in a thick walled high temperature furnace. Increasing the torch standoff distance beyond 150 mm was also discovered to increase coating porosity, and so this variable was therefore not varied. As a result, only variation of the plasma forming arc current and secondary ( $H_2$ ) gas concentration was systematically investigated in the present study.

A standard “S” set of parameters was first developed that produced low pore content ytterbium silicate coatings. Subsequent coatings were then deposited using variations of parameters about this “S” spray parameter center point. The parameter combinations are listed in Table 5.2 with their appropriate identifying labels. Combinations of the arc current while holding all other spray parameters fixed were identified as 1C, 2C and so on, as the current increased. Variations of the secondary  $H_2$  gas concentration while holding all other spray parameters fixed were designated 1H, 2H etc. The other spray parameters held constant across all depositions included the primary Ar gas flow of 84.95

slm as well as the powder carrier Ar flow of 5.90 slm for  $\text{Yb}_2\text{SiO}_5$  and 4.72 slm for  $\text{Yb}_2\text{Si}_2\text{O}_7$ . The injected powder mass flow rate was measured using catch-can experiments. The mass flow rate for  $\text{Yb}_2\text{SiO}_5$  was 41.5 g/min while that of  $\text{Yb}_2\text{Si}_2\text{O}_7$  was 35.2 g/min. Powder feed was assisted by 900N pneumatic vibrators to ensure feed consistency. No powder pulsing was observed during deposition of the coating layers.

*Table 5.2: Current and secondary hydrogen flows for the spray parameters used in this study to deposit the ytterbium silicate layers.*

Spray Parameter	Current (A)	Secondary $\text{H}_2$ (slm)	Power (kW) <sup>a</sup>	$\text{Yb}_2\text{SiO}_5$ Thickness	$\text{Yb}_2\text{Si}_2\text{O}_7$ Thickness
1C	225	0.94	9.3	N/A	80±5
2C	250	0.94	10.3	80±5	80±5
S	275	0.94	11.3	80±5	80±5
4C	300	0.94	12.3	110±5	80±5
5C	325	0.94	13.3	110±5	80±5
1H	275	0.57	10.6	N/A	100±5
2H	275	0.71	10.9	80±5	80±5
4H	275	1.18	11.7	80±5	120±5

<sup>a</sup> Minor deviations of +/-0.2kW in spray power were observed over the course of the due to wear of torch hardware.

### 5.2.2 Powder Materials

The silicon powder used for bond coat deposition was SI-122 electronics grade powder supplied by Micron Metals (Bergenfield, NJ) with a particle diameter range of 28 to 129  $\mu\text{m}$ . The mullite ( $\text{Al}_6\text{Si}_2\text{O}_{13}$ ) powder provided by Saint Gobain Ceramics (Worcester, MA) had a particle diameter of 16 to 53  $\mu\text{m}$ . Both of the ytterbium silicate powders ( $\text{Yb}_2\text{SiO}_5$  and  $\text{Yb}_2\text{Si}_2\text{O}_7$ ) were procured from Treibacher Industrie Inc. (Toronto, ON) in fused-crushed form with irregular/angular morphology and a particle diameter of 20 to 50  $\mu\text{m}$ . The ytterbium silicate powders had been previously characterized and

identified to be phase pure and within 2 at% of the target stoichiometry (25 at% Yb – 12.5 at% Si – 62.5 at% O for  $\text{Yb}_2\text{SiO}_5$  and 18.2 at% Yb – 18.2 at% Si – 63.6 at% O for  $\text{Yb}_2\text{Si}_2\text{O}_7$ ). Both contained only minor quantities of  $\text{SiO}_2$  and  $\text{Yb}_2\text{O}_3$  particulates (<1 % of all particles by number, estimated to be <0.25 vol% of particulates).<sup>97</sup>

### 5.2.3 Coating Characterization

As-deposited and annealed topcoats were subjected to X-ray diffraction (XRD) measurements (X'Pert Pro MPD, PANalytical, Westborough, MA) with patterns analyzed by Rietveld refinement (HighScore Plus, PANalytical, Westborough, MA). The samples were subsequently sectioned, polished, and examined with a scanning electron microscope (Quanta 650 FE-SEM, FEI, Hillsboro, OR) operating in the back-scattered electron (BSE) mode. All images were collected under low-vacuum imaging conditions. A gamma correction was applied to images to enable visualization of the Yb and non-Yb containing materials to be simultaneously observed on all the images, and to be comparable with images in earlier works.<sup>95,220</sup>

Quantitative image analysis was conducted using data collected from five randomly selected 200  $\mu\text{m}$  width by 150  $\mu\text{m}$  height cross-section images; the image size was sufficient to capture the full thickness of the topcoat in all spray parameter combinations. Average layer thicknesses were calculated from 50 equally spaced thickness measurements. The data from all five images was combined for quantitative metrics and taken to be a representative sample of the entire coating (having sampled a total coating layer length of approximately 10 times the coating thickness). The solidified droplet

(splat) length,  $l$  to thickness,  $t$  ratio was measured for over 1,000 splats for each spray parameter combination. EDS measurements of the as-deposited structures were attempted, but anomalous results were observed, leading to an inability to calculate compositions accurately by this technique. These discrepancies may have resulted from X-ray absorption and fluorescence in the Yb-Si-O system previously identified by other studies.<sup>221-227</sup> Average as-deposited compositions of ytterbium silicate layers were instead calculated from the measured volume fractions, and known compositions of the phases in each of the annealed layers. The volume fractions of the phases in annealed coatings were obtained using a simple contrast threshold-crossing criterion for BSE mode images. Volume fractions were measured over 1mm by 150  $\mu\text{m}$  areas for each coating and calculated as the number of pixels of each phase divided by the total number of pixels of coating material. The analysis of phase fractions was therefore insensitive to variations in the layer thickness, porosity, and cracking.

The combination of calculated as-deposited coating stoichiometry and the BSE images of as-deposited layers allowed BSE histogram overlays on as-deposited compositional measurements. For each layer, it was assumed that the average value of the BSE histogram corresponded to the average composition of the as-deposited layer from which the image was gathered. Further, it was assumed that in each image some area of very near stoichiometric material existed, such that the lower contrast bound of the histogram could be fixed to stoichiometric (precursor) material for all BSE images. This provides two points by which to scale the histogram in compositional space (only two points are required for linear scaling of any shape). Such compositionally paired histograms semi-quantitatively determine the compositional *variations* between as-

deposited materials. It is noted that the BSE contrast versus ytterbium concentration curve has been calculated to be linear over most of the composition space of interest<sup>97</sup>.

Microcrack density and orientation assessments were also performed on as-deposited 1 mm by 150  $\mu\text{m}$  wide regions of the coatings. Since the cracks had zig-zag shapes, the length and orientation of each individual linear segment of a microcrack was measured and then statistically summarized. Over 1,000 individual linear crack segments were measured for each spray parameter. The data reported for microcracking are in the form of a crack areal density (CAD), defined as the length of microcrack per unit of cross-sectional area. In the present study, the CAD data is reported as length of crack (in  $\mu\text{m}$ ) per 10,000  $\mu\text{m}^2$  of coating cross-section. The CAD has also been analyzed as a function of angle of divergence from horizontal (the plane of the coating) for all spray parameters. From symmetry considerations, the inclination angle was reported for a single angular quadrant (0-90  $^\circ$  angular range), by binning in nine 10  $^\circ$  wide increments.

### 5.3 Results

Tri-layer EBCs with  $\text{Yb}_2\text{SiO}_5/\text{Al}_6\text{Si}_2\text{O}_{13}/\text{Si}$  and  $\text{Yb}_2\text{Si}_2\text{O}_7/\text{Al}_6\text{Si}_2\text{O}_{13}/\text{Si}$  structure were deposited using an air plasma spray approach. Representative structures of the as-deposited tri-layer baseline (S parameter) coatings with ytterbium monosilicate and disilicate topcoats are shown in Figure 5.2. All deposited coatings were adherent through annealing. The thickness of the various deposited layers is presented along with the spray parameters used for deposition in Table 5.2. All the topcoat layers were almost fully dense, with only a very small number of pores with a diameter  $>10 \mu\text{m}$  scattered

randomly throughout the coatings. Total porosity in all ytterbium silicate layers was <2%. The density of the coating layers deposited here was higher than that of recently reported coatings deposited under very different plasma spray conditions<sup>95</sup>.

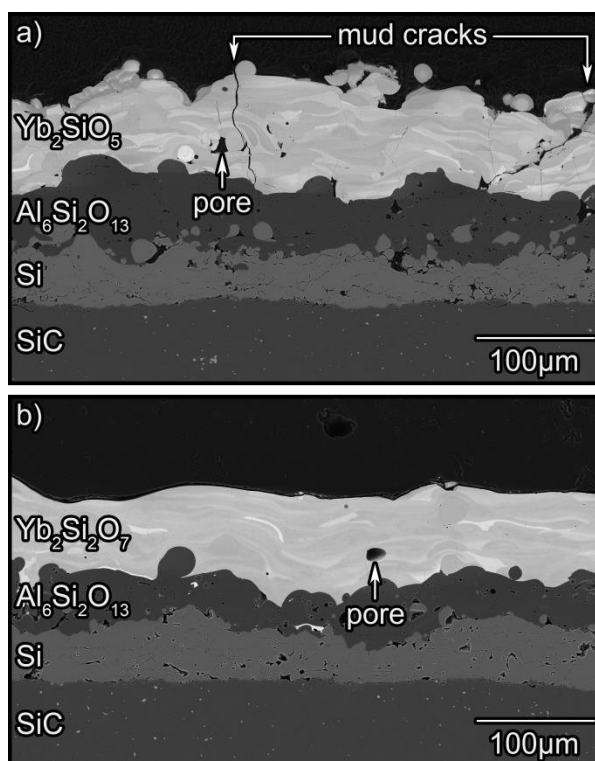


Figure 5.2: As-deposited tri-layer EBC systems deposited on a monolithic  $\alpha$ -SiC substrate. (a) Ytterbium monosilicate and (b) ytterbium disilicate topcoats both deposited on mullite using silicon bond coated substrates. The SEM images were collected in BSE mode and so the whitest contrast phases contained the highest concentration of the highest atomic number element (ytterbium).

### 5.3.1 Phase Content

The XRD pattern of the as-deposited ytterbium monosilicate coating deposited using the S combination of process parameters is shown in Figure 5.3(a). Analysis of this data indicated the layer contained two monoclinic  $\text{Yb}_2\text{SiO}_5$  phases indexed as an I2/a phase (PDF 00-040-0386) and a P21/c phase (PDF 00-052-1187), and a cubic  $\text{Yb}_2\text{O}_3$  phase

indexed as Ia-3 (PDF 00-041-1106). After annealing, the P21/c phase almost completely disappeared, and the coating then consisted of the I2/a monoclinic phase of  $\text{Yb}_2\text{SiO}_5$  and the cubic (Ia-3) phase of  $\text{Yb}_2\text{O}_3$ . Rietveld analysis was unable to resolve the volume fractions of the various phases accurately due to the large number of overlapping diffraction peaks and the varying background present after APS processing, presumably resulting from the fluorescence issues indicated in Section 5.2.3. Qualitatively, all of the as-deposited ytterbium monosilicate layers had P21/c to I2/a phase volume fraction ratio of ~2:1. The annealed ytterbium monosilicate coatings contained only trace amounts of the P21/c phase, Figure 5.3(a). The relative peak intensities of peaks belonging to the cubic ytterbia phase increased with increasing deposition power indicating an increase in volume fraction of ytterbia. However, they could not be used to determine quantitatively the volume fractions of the respective phases in the plasma sprayed material.

The diffraction patterns of as-deposited and annealed ytterbium disilicate layers deposited using the S combination of processing parameters are shown in Figure 5.3(b). The XRD pattern of the as-deposited layer could be indexed as a mixture of C2/m monoclinic  $\text{Yb}_2\text{Si}_2\text{O}_7$  (PDF 04-007-4857) and the same two phases of monoclinic  $\text{Yb}_2\text{SiO}_5$  observed in the as-deposited ytterbium monosilicate layers (I2/a and P21/c). After annealing, only the C2/m  $\text{Yb}_2\text{Si}_2\text{O}_7$  phase and I2/a  $\text{Yb}_2\text{SiO}_5$  phase were observed in the coating, Figure 5.3(b). Again, Rietveld analyses could not be used for quantitative phase determination due to the issues mentioned above. Qualitatively they indicated a monotonic increase in the P21/c to I2/a  $\text{Yb}_2\text{SiO}_5$  phase ratio with plasma spray power (from a ratio of 7:2 at low powers to 13:2 at the highest deposition power). After annealing, the metastable P21/c  $\text{Yb}_2\text{SiO}_5$  phase had again transformed in all the layers.

Similar to the monosilicate system, an increase in relative peak intensity of those peaks from the  $\text{Yb}_2\text{SiO}_5$  I2/a phase was observed with increasing deposition power in annealed coatings, indicating increased volume fraction of the monosilicate, but quantitative phase fraction measurement would have required comparisons with calibration curves derived from experiments with varied volume fractions of the phases (spike experiments)<sup>228</sup>.

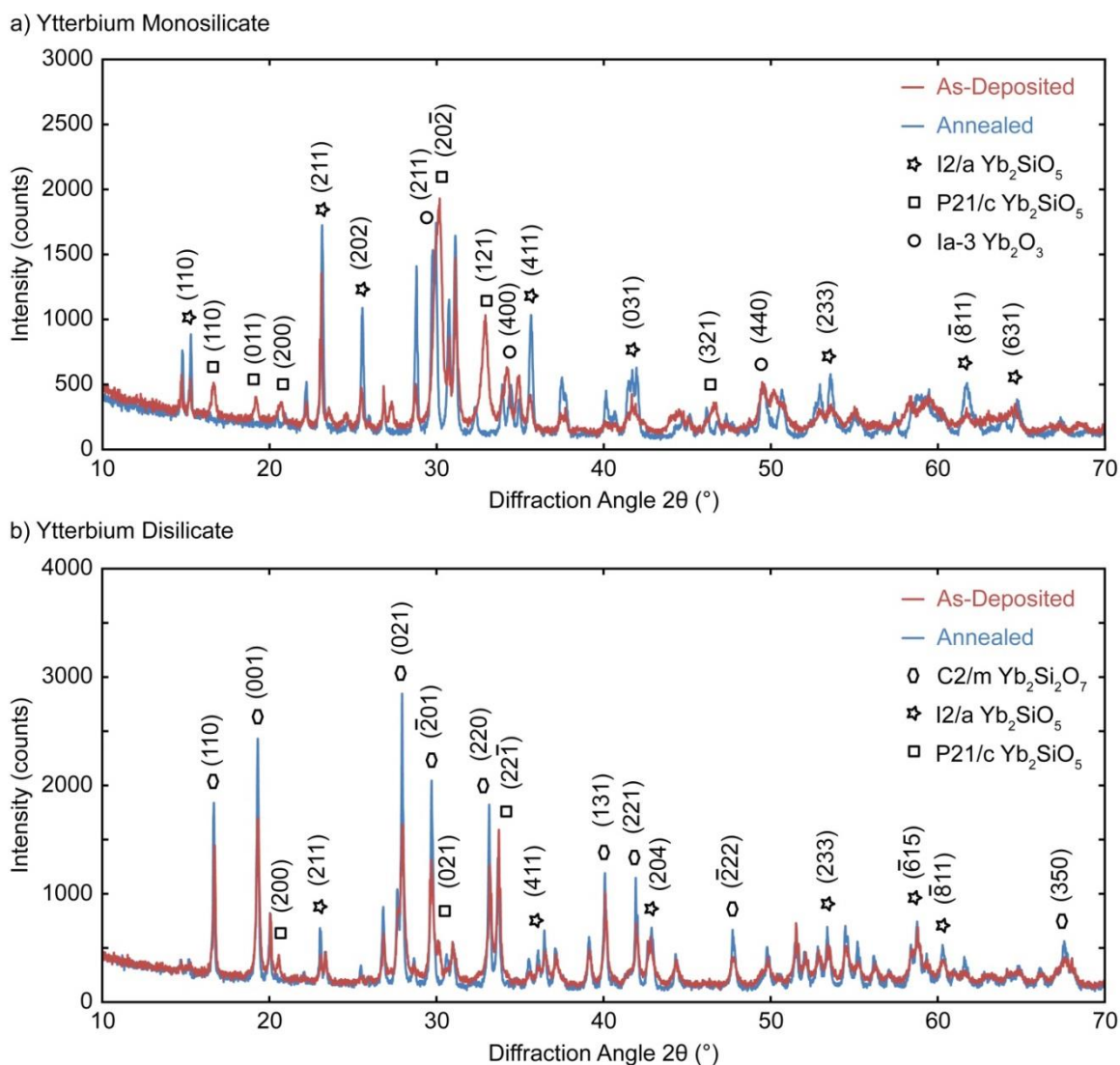


Figure 5.3: X-ray diffraction patterns of as-deposited and annealed topcoats. (a) Ytterbium monosilicate and (b) ytterbium disilicate both deposited using the *S* combination of deposition parameters.

Observations of the ytterbium silicate layers using BSE mode SEM imaging revealed regions of light and dark contrast in the ytterbium silicate layers, Figure 5.2. The light regions have been previously shown to correspond to solidified particle droplets that are ytterbium rich (Si-depleted) compared to the stoichiometric powder material<sup>95,97</sup>. Only the darkest grey regions in the images had a Si content close that of the stoichiometric powder. Examinations of the two topcoats at higher magnifications revealed the compositional variations to be quite severe, Figure 5.4.

In as-deposited layers observed in the SEM at relatively low magnification, Figure 5.4(a) and (d), a broad spectrum of contrast was observed indicative of a continuous range of compositions. However, there are only four equilibrium phases (including the two terminal compounds) in the  $\text{Yb}_2\text{O}_3 - \text{SiO}_2$  pseudo-binary phase diagram at temperatures up to 1750 °C: the two pure terminal oxides,  $\text{Yb}_2\text{SiO}_5$ , and  $\text{Yb}_2\text{Si}_2\text{O}_7$ .<sup>81,229</sup> The continuous variation of contrast in the two topcoats was found to not correspond to multiple intermediate phases, but rather from variations in the fractions of the extremely fine grained  $\text{Yb}_2\text{O}_3$ ,  $\text{Yb}_2\text{SiO}_5$ , and  $\text{Yb}_2\text{Si}_2\text{O}_7$  line compound phases simultaneously sampled by the electron beam.<sup>97</sup> This is supported by XRD analyses indicating the presence of only these three compounds in both as-deposited and annealed materials. The very fine crystal size in the as-deposited structure is consistent with the rapid quench rate of the APS process and slow crystallization kinetics of compounds with large unit cells.

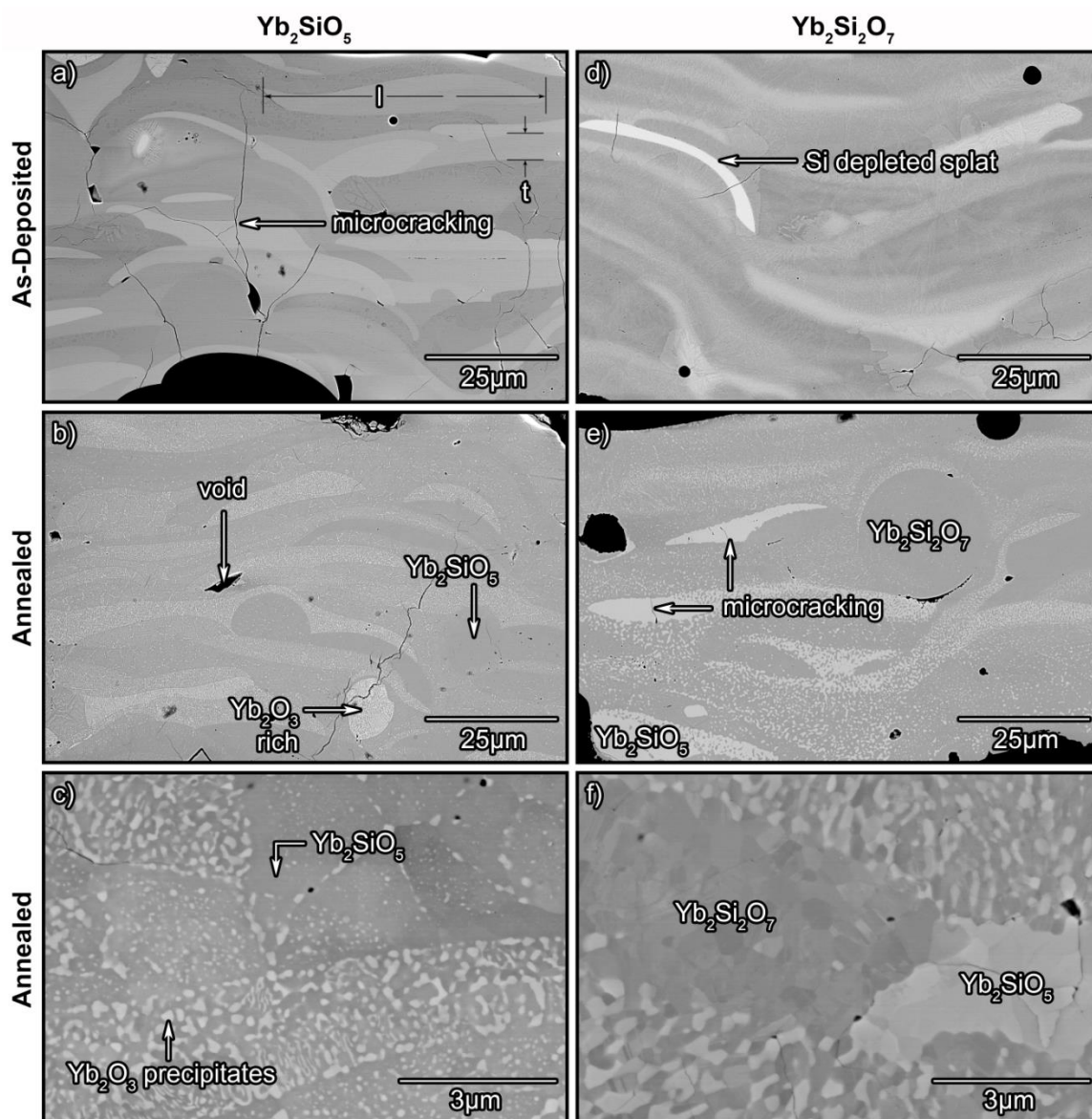


Figure 5.4: BSE mode SEM micrographs of the ytterbium silicate layers deposited using the S combination of deposition parameters. (a) As-deposited, (b) annealed, and (c) high magnification annealed ytterbium monosilicate layer. (d), (e), and (f) correspond to as-deposited, annealed, and high magnification annealed ytterbium disilicate layers.

After stabilization annealing, only two different contrast phases were observed in BSE micrographs, Figure 5.4 (annealed micrographs (b) and (e)). These phases correspond to those observed in X-ray diffraction: I2/a  $\text{Yb}_2\text{SiO}_5$  and Ia-3  $\text{Yb}_2\text{O}_3$  in the

ytterbium monosilicate layers, and C2/m  $\text{Yb}_2\text{Si}_2\text{O}_7$  and I2/a  $\text{Yb}_2\text{SiO}_5$  in the ytterbium disilicate layers. The volume fraction of a second phase that formed in an individual splat upon annealing varied in accordance with the stoichiometry of the splat during deposition, Figure 5.4(b) and (e). As a result, prior splat boundaries were “visible” in many images based upon differences in the volume fraction of their phases despite the lack of an actual physical boundary, Figure 5.4(c) and (f). High magnification imaging indicated a heterogeneous distribution of second phase precipitates on a fine scale and revealed the grain structure of the layer, Figure 5.4(c) and (f). The slight grain-to-grain variations in contrasts within the two phases in Figure 5.4(c) and (f) may be a result of variations in electron channeling with orientation (“band contrast”), not of compositional variation.

FIB lift-outs from annealed S spray parameter ytterbium monosilicate and disilicate layers were analyzed using transmission electron microscopy to verify the phases observed in XRD, Figure 5.5 and Figure 5.6. In bright field imaging, the contrast of the phases are reversed from SEM BSE imaging since they are transmission and not backscattered electron images. Thus, Yb-rich regions appear darker in contrast than Si-rich material in TEM micrographs. Imaging of the ytterbium monosilicate layer, Figure 5.5(a), revealed a structure reflective of that in Figure 5.4(c). EDS measurements of the composition of the two phases (probe locations indicated by crosses in Figure 5.5(d)) revealed compositions very close to  $\text{Yb}_2\text{O}_3$  for the precipitated phase and  $\text{Yb}_2\text{SiO}_5$  for the matrix, Table 5.3. Selected Area Electron Diffraction (SAED) was used in the area indicated in Figure 5.5(a) to capture diffraction patterns of the matrix phase on two different zone axes, Figure 5.5(b) and (c). Indexing of these diffraction patterns identified

the structure as monoclinic  $I2/a$   $Yb_2SiO_5$ , Table 5.4. The shape and structure of the precipitates was generally equiaxed, Figure 5.5(a) and (d). The SAED pattern of the precipitate from Figure 5.5(d) was indexed as cubic  $Yb_2O_3$ , Figure 5.5(e). Low intensity diffraction spots in Figure 5.5(e) resulted from beam overlap with neighboring  $Yb_2SiO_5$ .

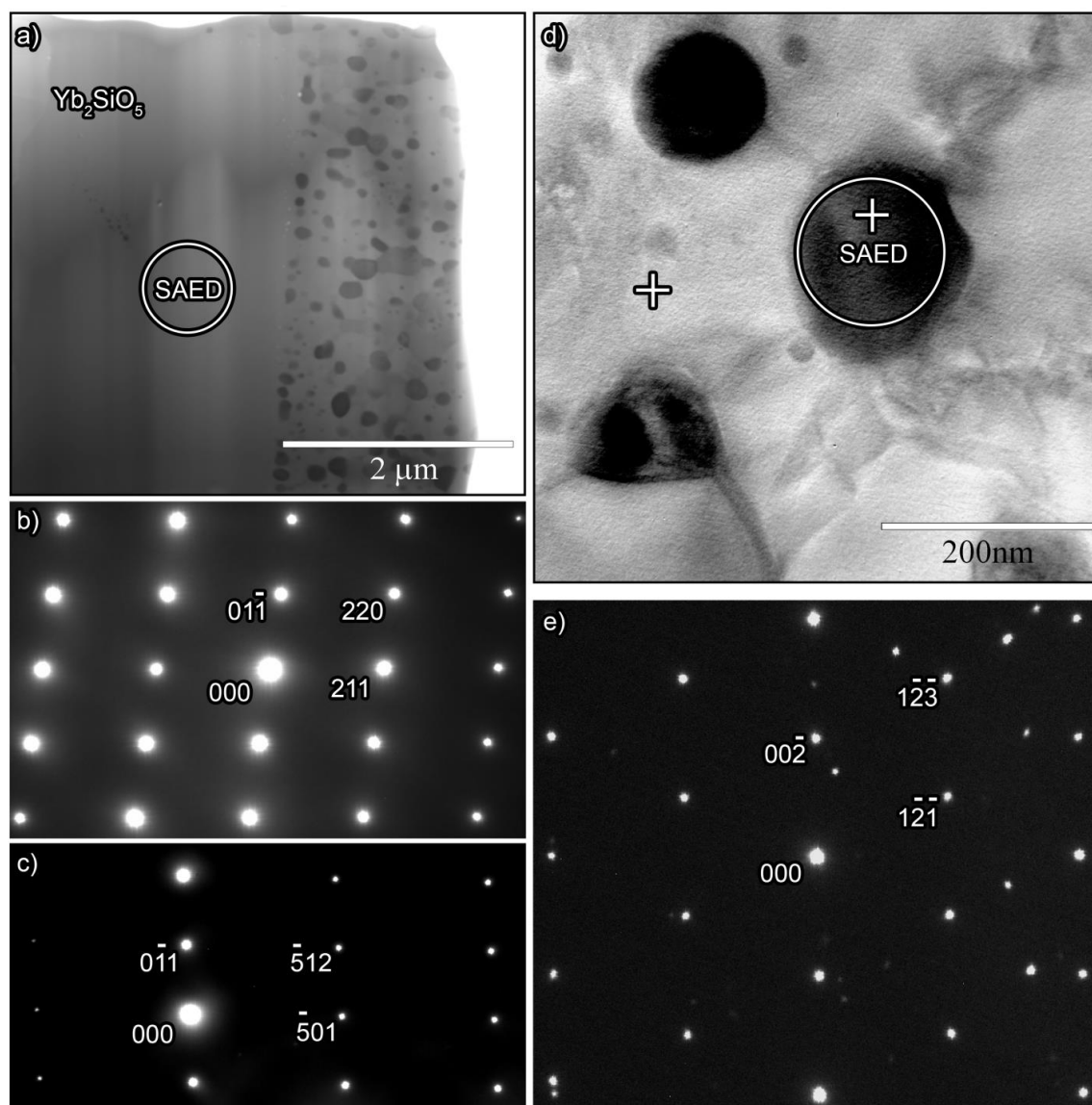


Figure 5.5: (a) Bright field TEM image of the ytterbium monosilicate coating. (b) The  $[\bar{1}11]$  and (c) the  $[0\bar{1}1]$  selected area electron diffraction (SAED) zone axis patterns from the monoclinic  $Yb_2SiO_5$  phase. (d) High magnification bright field image of the precipitated phase in the  $Yb_2SiO_5$  matrix. (e) Shows the cubic  $Yb_2O_3$  precipitate diffraction pattern along the  $[210]$  zone axis.

Analogous analyses were performed on an ytterbium disilicate coating deposited using the S-parameter combination, Figure 5.6. Bright field imaging indicated the layer to be multiphase (as in Figure 5.4(d)-(f)) with several large matrix-phase grains suitable for analysis in a FIB lift-out sample, Figure 5.6. Again, high magnification bright field imaging was used to capture the physical structure of precipitated particles and the matrix-precipitate interface, Figure 5.6(b). The EDS compositions measured at the probe points marked by crosses in Figure 5.6(b) aligned closely with the compositions of  $\text{Yb}_2\text{Si}_2\text{O}_7$  and  $\text{Yb}_2\text{SiO}_5$ , Table 5.3. SAED patterns from the spot in Figure 5.6(a) were analyzed for two different zone axes, Figure 5.6(c) and (d), and indexed as monoclinic C2/m  $\text{Yb}_2\text{Si}_2\text{O}_7$ , Table 4. SAED analyses were also performed upon the precipitates, and indexed diffraction patterns conform to those given in Table 5.4 for  $\text{Yb}_2\text{SiO}_5$ . These analyses indicate that air plasma spray deposition from stoichiometric composition powder has resulted in Si-depleted, mixed-phase coating layers.

*Table 5.3: Chemical compositions of the precipitated particles and matrix in the annealed coatings.*

Composition (at%)	O	Yb	Si
Precipitate in $\text{Yb}_2\text{SiO}_5$	60.0	38.1	1.9
Matrix of $\text{Yb}_2\text{SiO}_5$	62.8	24.3	12.9
Stoichiometric $\text{Yb}_2\text{SiO}_5$	62.5	25.0	12.5
Precipitate in $\text{Yb}_2\text{Si}_2\text{O}_7$	63.2	23.0	13.8
Matrix of $\text{Yb}_2\text{Si}_2\text{O}_7$	62.6	17.6	19.8
Stoichiometric $\text{Yb}_2\text{Si}_2\text{O}_7$	63.6	18.2	18.2

The average volume of precipitated phase in annealed coatings was calculated as a function of deposition parameter for all ytterbium silicate layers, Figure 5.7. The trends and relative magnitudes of Figure 5.7 were found to agree with the semi-quantitative data calculated by Rietveld refinement from diffraction patterns of the annealed layers, corroborating the validity of the image analysis measurements. In ytterbium monosilicate layers, Figure 5.7(a), the volume fraction of precipitated  $\text{Yb}_2\text{O}_3$  followed a monotonically increasing trend with deposition power as either the plasma current or  $\text{H}_2$  concentration were varied (while holding other deposition parameters constant). The minimum volume fraction of precipitated  $\text{Yb}_2\text{O}_3$  was  $\sim 8$  vol% in the 2H coating and the maximum was  $\sim 16$  vol% in the 5C coating as the plasma spray power was varied over a range of only 3.0 kW. In ytterbium disilicate coatings, the volume fraction of  $\text{Yb}_2\text{SiO}_5$  also followed a monotonically increasing trend with plasma current, Figure 5.7(b). The volume fraction of precipitated  $\text{Yb}_2\text{SiO}_5$  in ytterbium disilicate layers ranged from  $\sim 9$  vol% for the 1H coating to  $\sim 24$  vol% for the 5C coating. The volume fraction of the precipitated phase in ytterbium disilicate coatings could be changed by  $\sim 15$  vol% as the deposition power was varied over a range of 4.5 kW.

*Table 5.4: Lattice constants calculated from diffraction patterns and PDF cards.*

Lattice Source	a (Å)	b (Å)	c (Å)	$\beta$ (°)
$\text{Yb}_2\text{SiO}_5$ PDF <sup>a</sup>	12.38	6.67	10.29	102.54
$\text{Yb}_2\text{SiO}_5$ SAED	12.63	6.70	10.53	105.56
$\text{Yb}_2\text{Si}_2\text{O}_7$ PDF <sup>b</sup>	6.80	8.87	4.70	102.12
$\text{Yb}_2\text{Si}_2\text{O}_7$ SAED	6.78	8.42	4.73	100.48

<sup>a</sup>PDF card (00-040-0386)

<sup>b</sup>PDF card (04-007-4857)

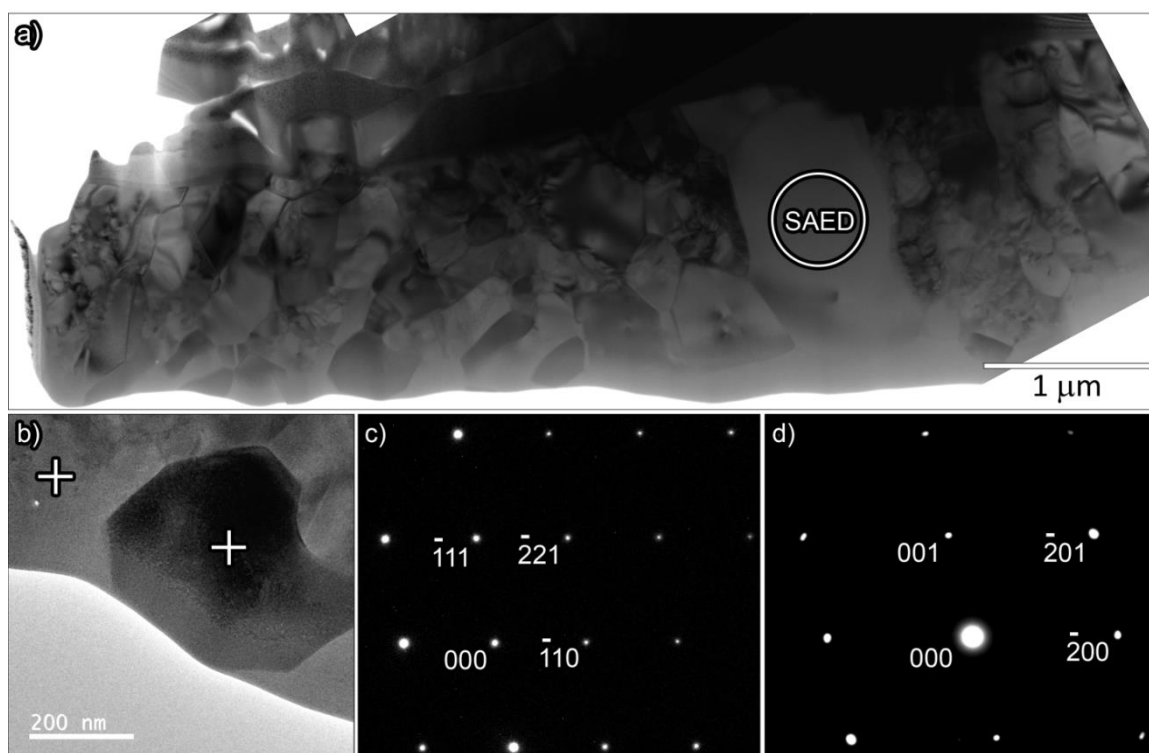


Figure 5.6: (a) Bright field TEM image of the ytterbium disilicate coating and (b) high magnification bright field image of a precipitated  $\text{Yb}_2\text{SiO}_5$  particle. Crosses indicate the locations of EDS probes for characterizing the matrix and precipitate phases. (c) The  $[110]$  and (d) the  $[010]$  selected area electron diffraction patterns along zone axes of monoclinic  $\text{Yb}_2\text{Si}_2\text{O}_7$  from the region indicated by SAED circled in (a).

### 5.3.2 Splat Aspect Ratio

Variation of the spray parameters resulted in changes to the solidified droplet structures of as-deposited ytterbium monosilicate coatings, Figure 5.8, and ytterbium disilicate coatings, Figure 5.9. In both Figure 5.8 and Figure 5.9, the spray deposition power increased from (a) to (c) to (d) to (b). Figure 5.8 and Figure 5.9 (a) and (b) correspond to the lowest and highest power used in the plasma direct arc current variation study whereas parts (c) and (d) corresponded to the lowest and highest power used in the  $\text{H}_2$  variation study. Very fine nano-grain structures were visible in all of the coatings. The

prevalence of large, round, unmelted particles also decreased with increasing deposition power in both materials. Variation of the process conditions caused changes to the splat length,  $l$ , its thickness,  $t$  and the aspect ratio ( $l/t$ ) of the splats. Increasing the plasma current or the plasma plume  $H_2$  concentration (while maintaining other spray parameters constant) resulted in an increase of splat  $l/t$  ratio, Figure 5.10. The splat  $l/t$  ratio ranged from  $\sim 4$  to  $\sim 17$  for ytterbium monosilicate layers and from  $\sim 7$  to  $\sim 14$  for the ytterbium disilicate layers. The data indicate that though variation of both plasma current and  $H_2$  concentration monotonically increase the splat aspect ratio, the effect was not simply governed by spray power alone. As suggested in Section 2.3, it is apparent in Figure 5.8 and Figure 5.9 that partially melted particles (of near stoichiometric composition) exist in all coating layers.

### 5.3.3 Coating Composition

Since EDS estimates of the coating composition were found to be unreliable, the average composition of as-deposited ytterbium silicate layers was calculated from volume fractions of the precipitated line compound phases and their stoichiometric compositions in annealed coatings. This relationship was calculated from molar volumes and densities of the  $Yb_2O_3$ ,  $Yb_2SiO_5$ , and  $Yb_2Si_2O_7$  phases and is shown for the ytterbium silicate systems in Figure 5.11(a). Since the volume fractions of the phases in each coating were known, Figure 5.7, it was then possible to estimate the effect of deposition conditions upon the average Yb:Si ratio of the two types of coating, Figure 5.11(b) and (c). There was a significant increase in the Yb:Si ratio of both types of coatings as the plasma spray power was increased.

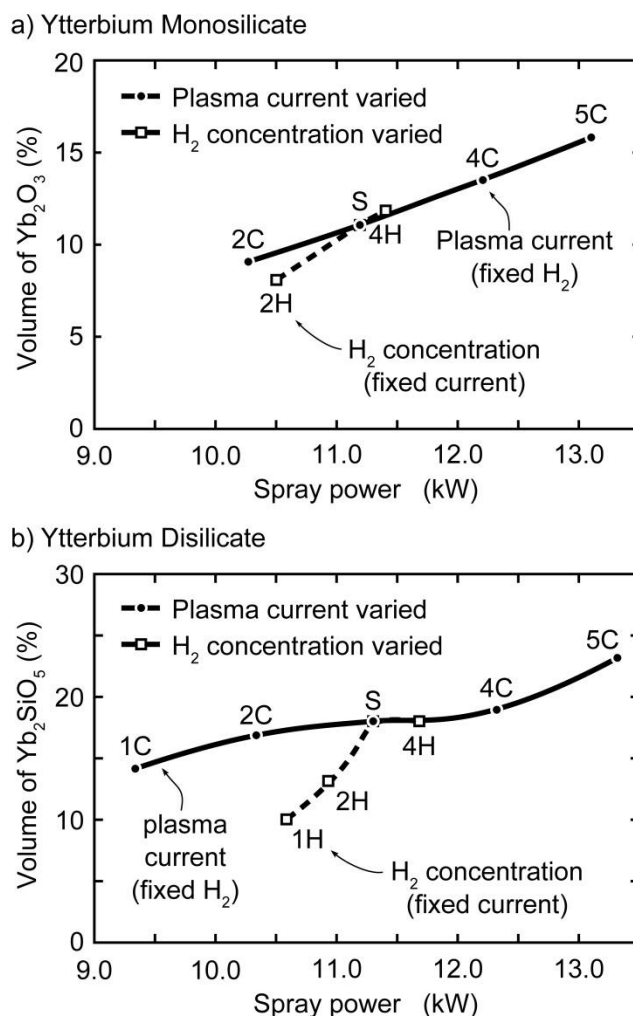


Figure 5.7: Volume fraction of second phase precipitates in annealed coatings plotted against plasma spray power. (a)  $\text{Yb}_2\text{O}_3$  precipitated in ytterbium monosilicate coatings. (b)  $\text{Yb}_2\text{SiO}_5$  precipitated in ytterbium disilicate coatings.

BSE mode imaging of annealed coatings indicated significant differences in grey scale contrast between the splats. The BSE grey scale was then mapped to the mole fraction of the elements in the as-deposited microstructures by rescaling the BSE histogram to known reference points (as described in Section 5.2.3) to obtain BSE-derived distributions of Yb:Si ratio. This was achieved by aligning the lowest Yb:Si ratio (darkest BSE contrast) end of the histogram with the stoichiometry of the lowest

equilibrium Yb:Si compound in the system<sup>4</sup> (corresponding to the starting powder composition- no Si loss), and the distributions average with that deduced from the phase volume fractions, Figure 5.11(b) and (c). Such a scaling assumed that some stoichiometric material remained in the coatings after deposition and that the BSE contrast scaled linearly with Yb:Si ratio. The BSE-derived distributions show that a significant increase in splat composition range accompanied an increase in the plasma spray power and plasma hydrogen content.

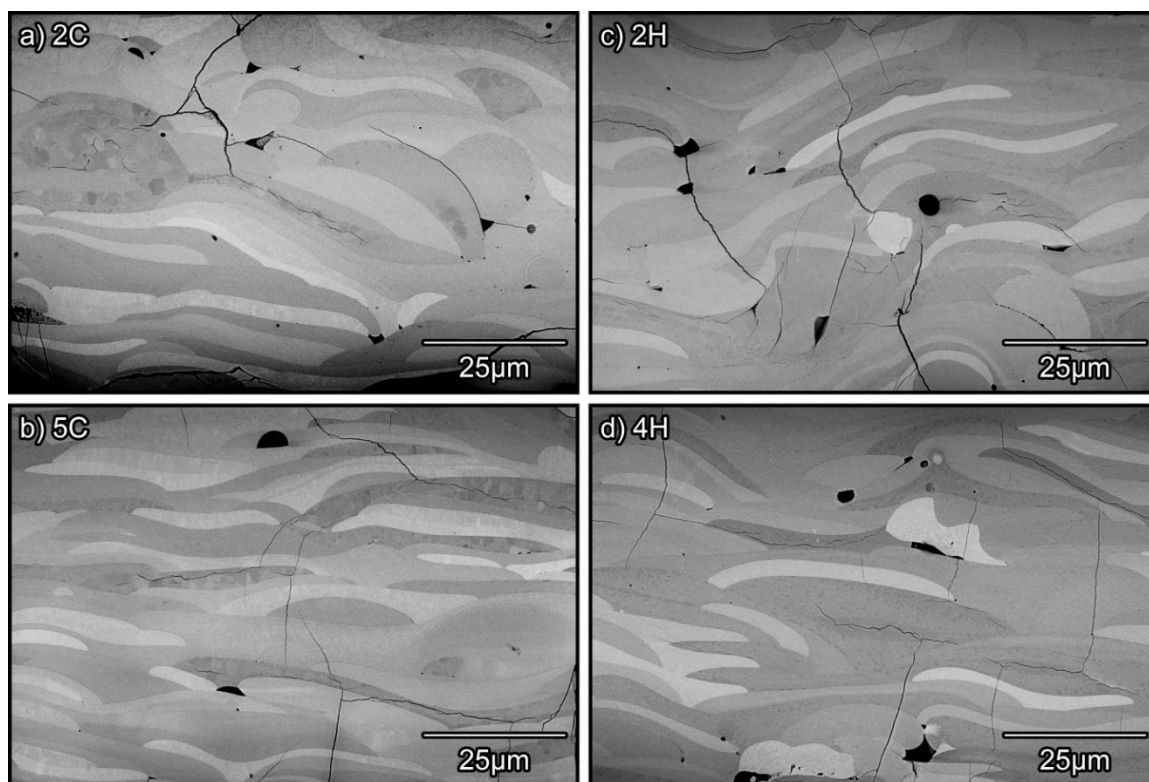


Figure 5.8: BSE mode SEM micrographs of as-deposited ytterbium monosilicate coatings deposited using different combinations of spray parameters. (a) 2C coating, (b) 5C coating, (c) 2H coating, and (d) 4H coating.

<sup>4</sup> For  $\text{Yb}_2\text{SiO}_5$  the stoichiometric Yb:Si ratio is 2 and for the  $\text{Yb}_2\text{Si}_2\text{O}_7$  this stoichiometric ratio is 1.

To understand the reasons for the loss of silicon in the coatings, equilibrium vapor pressure calculations were performed using FactSage<sup>181</sup> modeling software. All modeling of the Yb-Si-O system used ideal solution interaction calculations as insufficient published thermochemical data exists for this system to perform the desired calculations, despite determination of SiO<sub>2</sub> activity<sup>230</sup>. Vapor partial pressures and partial pressure ratios in the Yb-Si-O system were calculated over the temperature interval of 1,000-3000 °C that could be experienced by a powder particle during plasma spray deposition. Figure 5.12(a) shows the vapor pressures of the dominant vapor species (normalized by the vapor pressure of SiO) for a combination of Yb<sub>2</sub>SiO<sub>5</sub> (Yb<sub>2</sub>O<sub>3</sub> + SiO<sub>2</sub>), Ar, H<sub>2</sub>, and O<sub>2</sub> in the ratios corresponding to S spray parameter mass flows during ytterbium monosilicate deposition. Figure 5.12(b) shows recalculations for ratios of Yb<sub>2</sub>Si<sub>2</sub>O<sub>7</sub> (Yb<sub>2</sub>O<sub>3</sub> + 2SiO<sub>2</sub>), Ar, H<sub>2</sub>, and O<sub>2</sub> appropriate for the S spray parameter mass flows of the ytterbium disilicate coating depositions. Figure 5.12(c) plots the ideal solution predicted partial vapor pressures of the highest partial pressure Si-bearing and Yb-bearing vapor species of the S spray parameter for both Yb<sub>2</sub>SiO<sub>5</sub> and Yb<sub>2</sub>Si<sub>2</sub>O<sub>7</sub>. The inflections marked in all three plots of Figure 5.12 indicate the temperature above which all Si would be in vapor form in the equilibrium-modeled scenario.

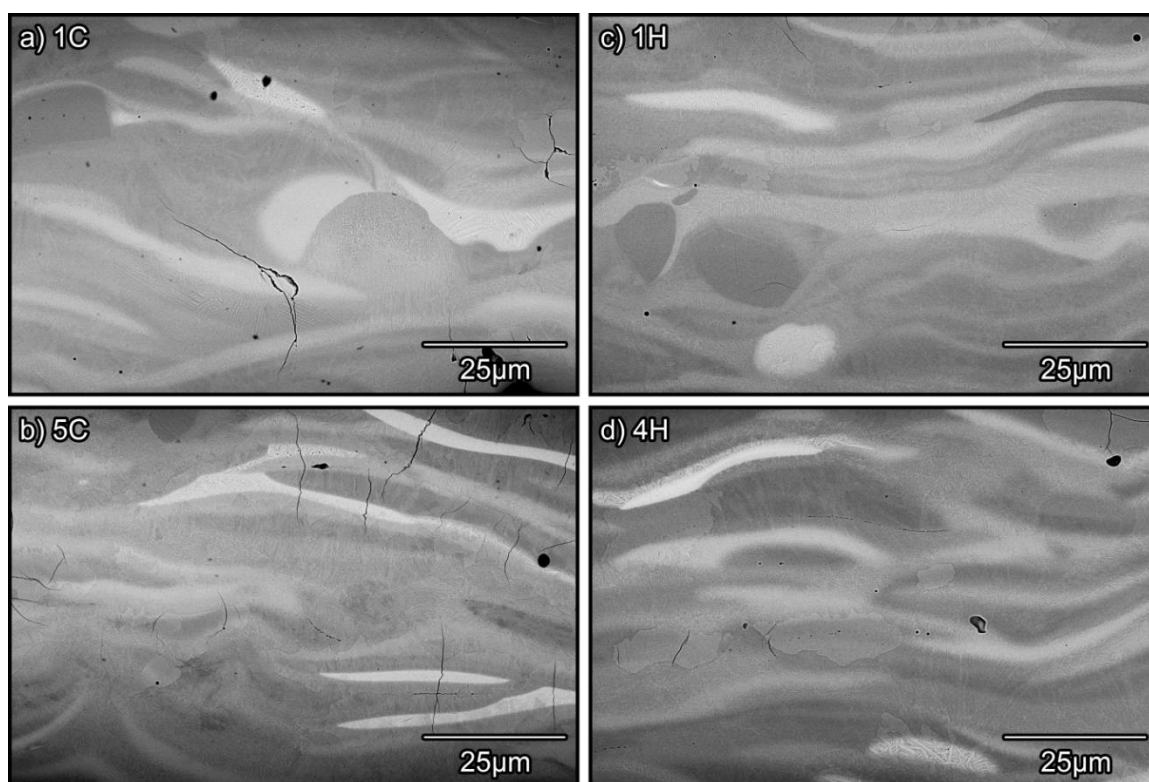


Figure 5.9: BSE mode SEM micrographs of as-deposited ytterbium disilicate coatings deposited using different combinations of spray parameters. (a) 1C coating, (b) 5C coating, (c) 1H coating, and (d) 4H coating.

In the  $\text{Yb}_2\text{SiO}_5$  system, Figure 5.12(a), the vapor pressure calculated for SiO was  $\sim 10^6$  times greater than that of Yb for temperatures below 2500 °C. At temperatures above 2500 °C, the ratio decreased, but was still roughly  $10^2$  times higher than that of Yb at 3000 °C.  $\text{SiO}_2$  vapor, the secondary Si-bearing species, had a vapor partial pressure ratio to SiO that varied from  $\sim 10^{-7}$  at 1,000 °C to  $\sim 10^{-1}$  at 2500 °C, decreasing to  $\sim 10^{-2}$  at 3000 °C. The partial pressure of oxidizers ( $\text{H}_2\text{O}$  and OH) was relatively high, with  $\text{H}_2\text{O}$  having partial pressure ratio with SiO equal to or greater than 1 until 2200 °C, where the partial pressure ratio began to gradually decline until reaching  $\sim 10^{-2}$  at 3000 °C. OH maintained a partial pressure ratio of  $\sim 10^{-2}$  to  $\sim 10^{-4}$  across the entire temperature range.

The  $\text{Yb}_2\text{Si}_2\text{O}_7$  system, Figure 5.12(b), was almost identical to that of  $\text{Yb}_2\text{SiO}_5$ . There was a slight difference in the Yb and  $\text{SiO}_2$  curves above 2500 °C, wherein the difference in partial pressures between SiO and Yb was slightly larger (by 10x) and the difference in partial pressures between SiO and  $\text{SiO}_2$  was slightly smaller (by 10x) when compared to the  $\text{Yb}_2\text{SiO}_5$  system.

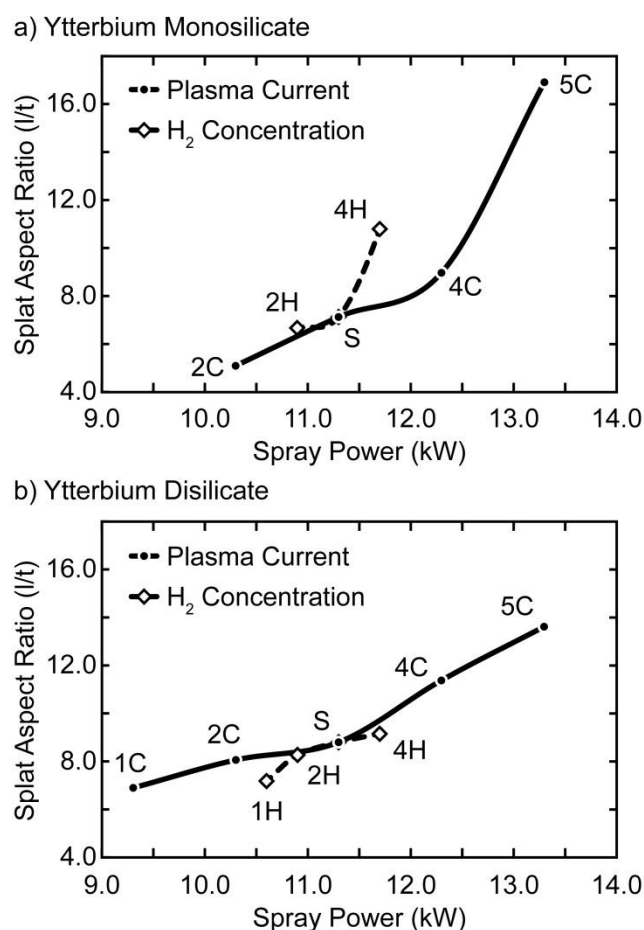


Figure 5.10: Variations in average splat aspect ratio ( $l/t$ ) as a function of plasma spray power for (a) ytterbium monosilicate and (b) ytterbium disilicate coatings in the as deposited condition.

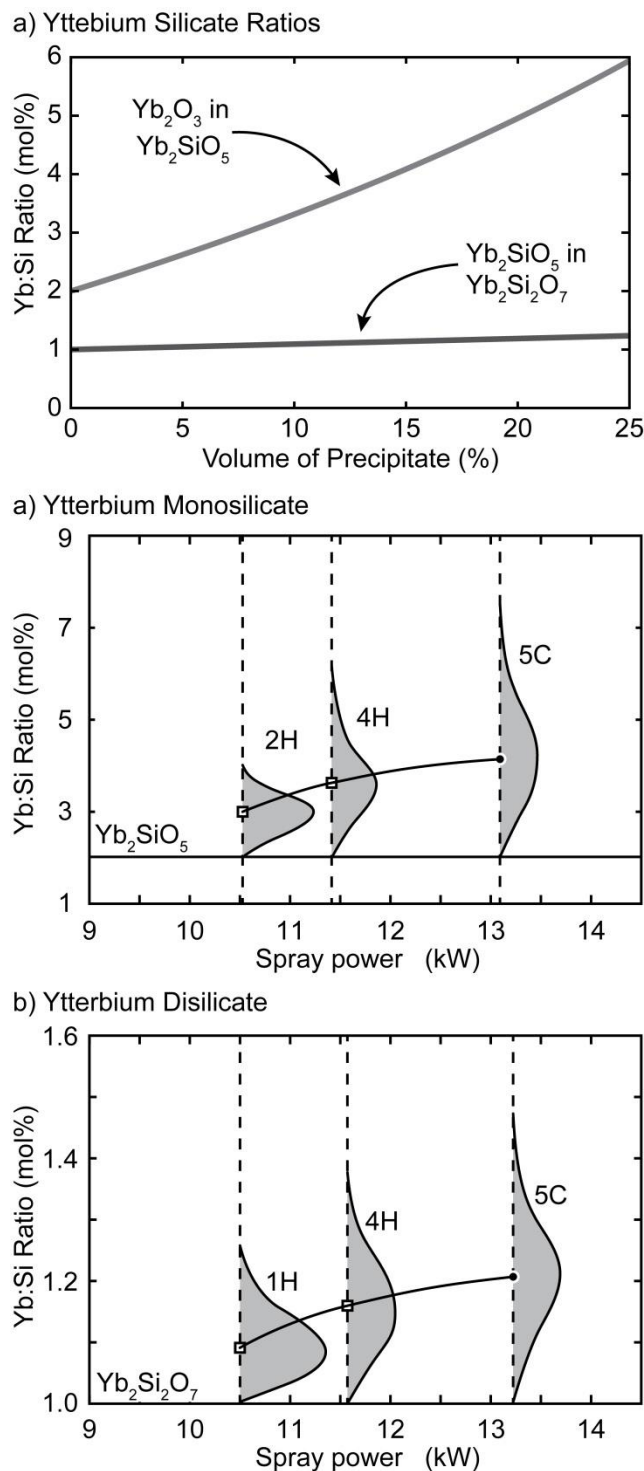


Figure 5.11: (a) Yb:Si ratio dependence upon molar volumes of second phases. Average Yb to Si ratios and BSE contrast based estimates of the composition variation in a coating for (b) the ytterbium monosilicate and (c) the ytterbium disilicate layers. BSE derived distributions were scaled by aligning the lowest Yb:Si ratio (darkest BSE contrast) end of the distribution with the stoichiometric compound and enforcing the average of the distribution to match that deduced from the phase volume fractions.

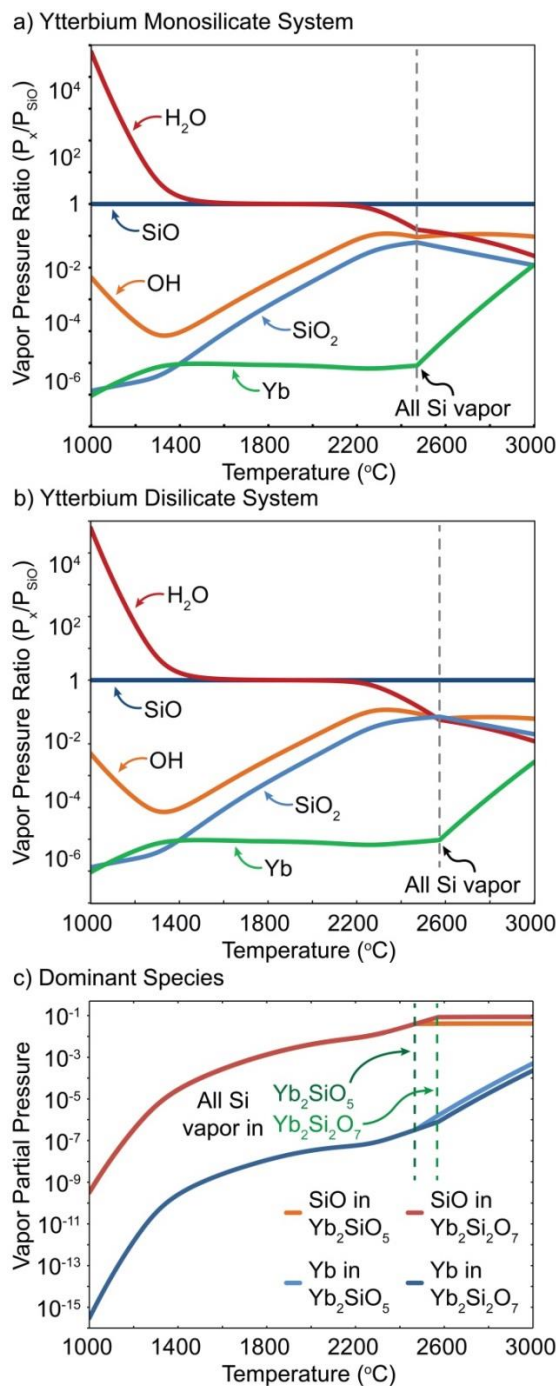


Figure 5.12: Partial pressure ratio of dominant vapor species to SiO as a function of temperature for the  $S$  spray parameter condition with (a)  $\text{Yb}_2\text{SiO}_5$  and (b)  $\text{Yb}_2\text{Si}_2\text{O}_7$  injected into the plume. (c) Calculated vapor partial pressures of dominant species. Partial pressures are calculated based on ideal thermochemical interactions.

The predicted values of vapor partial pressures for SiO and Yb for the two systems are shown in Figure 5.12(c). The calculated vapor pressures of both species exhibited a sharp increase over four orders of magnitude between 1,000 °C and 1400 °C. This increase was followed by a gradual rise of roughly two orders of magnitude between 1400 and 2500 °C. Above 2500 °C the vapor pressures of SiO in the two systems remained constant at  $\sim 10^{-1}$  (all Si was in vapor form as denoted) while those of Yb increased to  $\sim 10^{-4}$ . Over the 1,000-3000 °C temperature interval, the SiO partial pressure varied from  $\sim 10^{-10}$  to  $\sim 10^{-1}$  and the Yb partial pressure varied from  $\sim 10^{-16}$  to  $\sim 10^{-4}$ . It is emphasized that the results should be interpreted only qualitatively as the analysis was based upon ideal interactions. As such, the calculations are insensitive to differences in real thermochemical behavior of the system that would result in varying vapor pressures between  $\text{Yb}_2\text{SiO}_5$  and  $\text{Yb}_2\text{Si}_2\text{O}_7$  (such differences have been calculated in the Y-Si-O system using real thermochemical data<sup>231</sup>). In summary, the calculations demonstrate the existence of a significant driving force for preferential volatilization of Si from molten material.

#### ***5.3.4 Channel Type and Equiaxed Microcracking***

Significant channel (mud) type cracking was observed in ytterbium monosilicate coatings, Figure 5.2(a). The inter-crack spacing was  $\sim 240$   $\mu\text{m}$ , and resulted from the coating's substantially higher coefficient of thermal expansion (CTE) compared to that of the substrate<sup>77,97</sup>. These cracks fully penetrated the layer but their spacing did not vary with spray power. No mud cracking was observed in ytterbium disilicate layers. Dilatometry experiments with this material confirmed it had a similar CTE to the SiC

substrate (Appendix A). Both ytterbium silicate coatings also contained numerous microcracks. This microcracking was significantly affected by spray conditions used to deposit the ytterbium silicate layers, Figure 5.13. The total microcrack length per unit area generally decreased with increasing spray power used to deposit the ytterbium monosilicate layers, Figure 5.13(a). This trend was consistent with the increase in the coatings'  $\text{Yb}_2\text{O}_3$  fraction (decrease in  $\text{Yb}_2\text{SiO}_5$ ) with spray power, Figure 5.7. The variation in crack angle (defined from the plane of the coating) for the ytterbium monosilicate microcracks is shown in Figure 5.13(b) for each of the deposition conditions. The microcrack angle was almost random; only a very slight preference for high angle ( $90^\circ$ , i.e. micro-channel crack type) crack orientations was observed.

The microcrack length per unit area in the ytterbium disilicate layers was significantly less than that of ytterbium monosilicate layers, Figure 5.13(c). It generally tended to increase with spray power as the fraction of the high CTE  $\text{Yb}_2\text{SiO}_5$  phase increased, Figure 5.7. The crack length distribution as a function of angle from horizontal for the ytterbium disilicate layers is shown in Figure 5.13(d). Like the ytterbium monosilicate system, the orientation angle of ytterbium disilicate microcracks in most of the coatings was random. However, the coatings deposited at the highest spray powers (4C and 5C layers) had many more vertically oriented cracks, consistent with the presence of a higher fraction of the higher CTE  $\text{Yb}_2\text{SiO}_5$  phase.

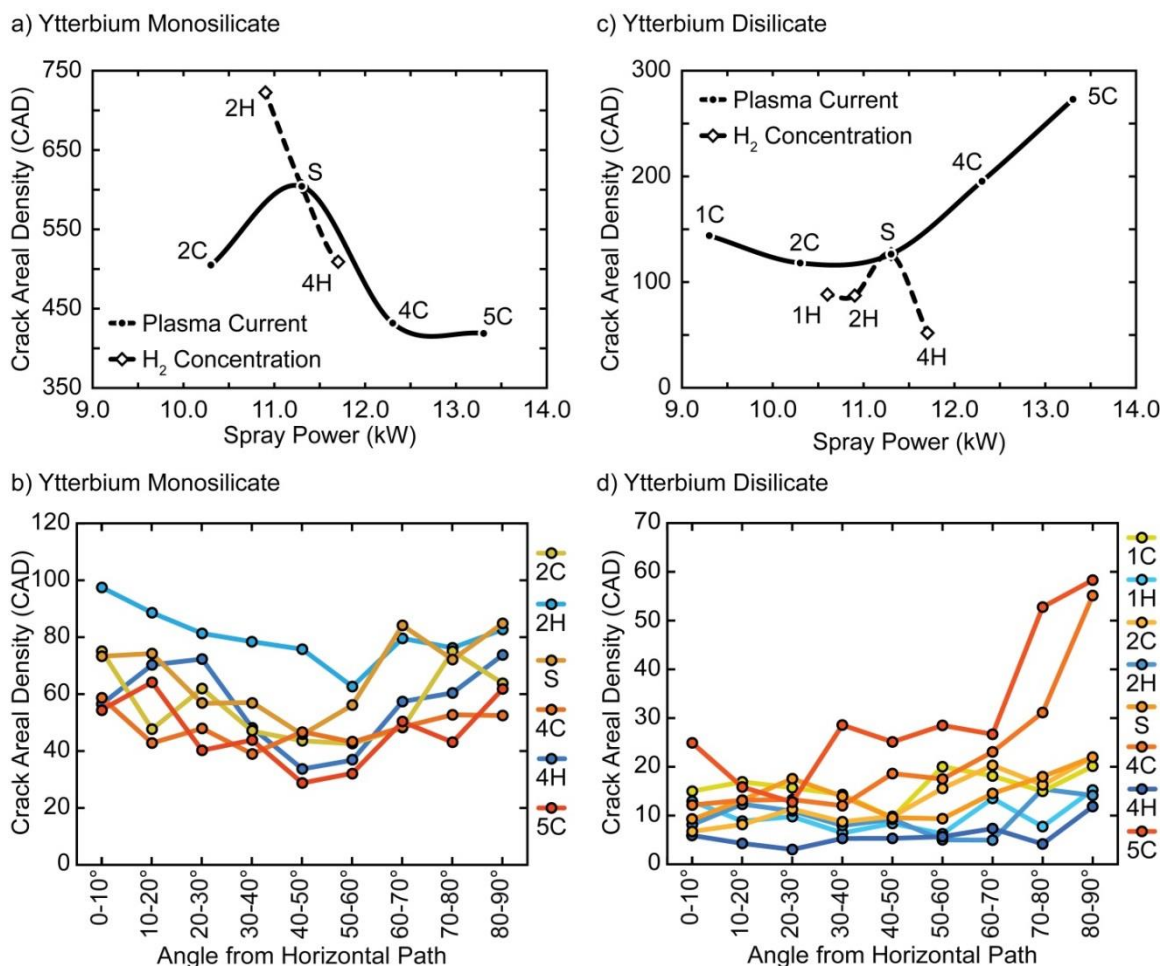


Figure 5.13: Crack areal density (CAD) of ytterbium silicate layers: micro-crack length (in  $\mu\text{m}$ ) per  $10,000\mu\text{m}^2$  of coating cross section. (a) Crack length of all orientations plotted as a function of plasma spray power for the ytterbium monosilicate layers. (b) Crack length as a function of angle of divergence from horizontal crack path in ytterbium monosilicate layers. A  $90^\circ$  angle indicates vertical (mud crack type) cracking. The plots in (c) and (d) are similar data for ytterbium disilicate layers.

## 5.4 Discussion

A combination of air plasma spray parameters have been identified that resulted in the deposition of low porosity ytterbium monosilicate and ytterbium disilicate layers on silicon and mullite coated  $\alpha$ -SiC substrates. However, the low porosity coatings were Si-depleted compared to the (near stoichiometric) composition of the starting powders. BSE

mode imaging indicated that the degree of Si depletion varied from solidified droplet to droplet in a given coating, Figures 5.2,4,8, and 9. This compositional variability increased with spray power. The average composition of the coatings was also increasingly depleted in Si with increase in the plasma spray arc current and the hydrogen content of the plasma plume, Figure 5.7 and Figure 5.11.

The loss of silicon was consistent with preferential volatilization of Si-bearing species from melted powder during transit through the plasma plume. Ideal solution thermochemical modeling indicated that Si-bearing species had vapor pressures that were  $\sim 10^6$  times higher than Yb-bearing species at the temperatures likely to have been reached during APS deposition of both the ytterbium monosilicate, Figure 5.12(a), and the ytterbium disilicate, Figure 5.12(b). This vapor pressure ratio difference also remained relatively constant across a temperature range from  $\sim 1300$ - $2600$  °C. Rapid Si depletion during powder particle transit through the plume was driven by the high Si-bearing species vapor pressure, Figure 5.12(c), which increased with increasing temperature in a manner consistent with the observed loss of Si with increasing deposition power, Figure 5.7 and Figure 5.11. Reducing the plasma temperature (by decreasing the plasma power and  $H_2$  concentration) and particle residence time in the plume (by shortening the standoff distance and increasing the particle velocity) provide a means for reducing the silicon loss, but at the risk of increased porosity.

While the powder particles used to deposit both ytterbium silicate layers were single phase and of stoichiometric composition, BSE imaging contrast of deposited microstructures revealed the presence of  $Yb_2O_3$  precipitate particles in  $Yb_2SiO_5$  coatings and  $Yb_2SiO_5$  particles in the  $Yb_2Si_2O_7$  coatings. Such precipitated phases have been

previously observed in plasma sprayed ytterbium silicates.<sup>77,78,95,97</sup> Both precipitates were Si-deficient in comparison to the matrix (and initial powder) phase. The crystal structures and compositions, Figures 5.3, 5 and 6 and Table 5.3 and Table 5.4 are consistent with the binary phase diagram predictions<sup>81</sup>. Despite appropriate stoichiometry and reported monomorphism,<sup>81</sup> a monoclinic P21/c  $\text{Yb}_2\text{SiO}_5$  phase was observed in both ytterbium monosilicate and ytterbium disilicate layers. This phase was not present in annealed coatings, as indicated in the diffraction patterns of Figure 5.3, indicating the P21/c  $\text{Yb}_2\text{SiO}_5$  phase to be metastable and transformable to the stable monoclinic I2/a phase of  $\text{Yb}_2\text{SiO}_5$ .

The volume fraction of precipitate in both ytterbium silicate layers increased with both increasing plasma current and  $\text{H}_2$  concentration, Figure 5.7. This occurs because increases in these spray parameters increased the temperatures of the plasma plume, and therefore the rate of silicon loss. This in turn increased precipitate fraction (by application of the lever rule to the  $\text{Yb}_2\text{O}_3 - \text{SiO}_2$  binary phase diagram). While increasing the plasma current and secondary gas ( $\text{H}_2$ ) concentration both increased the precipitate fraction, the effects of modifying these variables were not equal. This was clearly indicated by the difference in the slope of the precipitate phase volume fraction versus plasma current and  $\text{H}_2$  concentration curves in Figure 5.7.

The aspect ratio of the solidified droplets in both ytterbium silicate coatings, Figure 5.10, was also dependent upon the plasma current and  $\text{H}_2$  concentration in the plasma plume. Particles that had both high temperature and velocity during impingement with the substrate are expected to flatten the most and thus result in splats that had the highest aspect ratio. It is noted that both higher velocity and temperature result from increased

plasma current and/or secondary gas concentration,<sup>99,101,128,129,133-137,149,232,233</sup> but the entire temperature – time – velocity (T-t-V) history is important in determining splat microstructure. These process parameters have also affected the loss of silicon, Figure 5.11 (and accordingly the volume fraction of second phase precipitate, Figure 5.9), and the splat aspect ratio, Figure 5.10, in similar ways. Detailed plasma plume modeling and simulations are now necessary to understand these aspects of the study.

Channel type (mud) cracks were observed to fully penetrate the ytterbium monosilicate layers of the tri-layer coating system when deposited on a SiC substrate, Figure 5.2(a). However, no cracks of this type were found in the ytterbium disilicate coating system, Figure 5.2(b). Furthermore, the mud crack spacing in the ytterbium monosilicate layers was not found to depend upon the spray parameters (within statistical margins). The results are in agreement with previous studies which attributed the mud cracking to the development of tensile residual stress in the ytterbium monosilicate layer during cooling dictated by CTE<sup>77,78,95,97</sup>. Earlier studies used dilatometry and found that the CTE of ytterbium monosilicate was  $7.5 \times 10^{-6} \text{ }^\circ\text{C}^{-1}$ ,<sup>77,97</sup> approximately twice that of the SiC and sufficient to develop an in plane biaxial tensile stress approaching 1 GPa if dense material elastic moduli are assumed. A similar CTE measurement was conducted here for ytterbium disilicate (Appendix A), and confirmed that the disilicate layer has a CTE of  $\sim 4.1 \times 10^{-6} \text{ }^\circ\text{C}^{-1}$ , slightly less than that of SiC and consistent with the absence of mud cracking.

In addition to the mud cracks in the ytterbium monosilicate system, equiaxed microcracks were found in all the layers of both topcoat materials after the APS deposition process. In ytterbium monosilicate layers, the microcracking was severe and

varied considerably with deposition parameter, Figure 5.13(a). The angular distribution of microcracks in the ytterbium monosilicate layer was generally random and was unaffected by spray parameter, Figure 5.13(b). The equiaxed microcracking was associated with regions of highest ytterbia content which had a higher elastic modulus (and slightly higher CTE) than the surrounding ytterbium monosilicate phase<sup>97</sup>.

In ytterbium disilicate, the extent of microcracking was greatly reduced, Figure 5.13(c). The most severely cracked ytterbium disilicate layer had ~40 % lower crack density than the least severely cracked ytterbium monosilicate layer. Microcracks in the ytterbium disilicate layers usually had a random angular distribution indicative of equiaxed cracking. However, the two ytterbium disilicate layers subjected to the hottest plasma deposition conditions (4C and 5C) had ~3-4 times the density of high angle orientation ( $70^{\circ}$  from horizontal) cracks, but with no change in low angle microcrack population, Figure 5.13(d). Microstructural analysis indicated this crack distribution to be an additional population of micro-mud cracks within precipitated  $\text{Yb}_2\text{SiO}_5$  particles. The presence of such cracking in only the ytterbium disilicate 4C and 5C coatings resulted from the increased  $\text{Yb}_2\text{SiO}_5$  volume fraction in these layers. Microcracking of such precipitates resulted from a local state of tension upon cooling due to the difference in CTE between  $\text{Yb}_2\text{Si}_2\text{O}_7$  ( $4.1 \times 10^{-6} \text{ }^{\circ}\text{C}^{-1}$ ) and  $\text{Yb}_2\text{SiO}_5$  ( $7.5 \times 10^{-6} \text{ }^{\circ}\text{C}^{-1}$ )<sup>77,97</sup>. The vertical nature of this cracking resulted from the high l/t ratio and in-plane orientation of the large precipitates combined with the biaxial nature of the stress field in the relatively thin ytterbium disilicate layer.

The high silicon loss during plasma deposition of the rare earth silicates such as the ytterbium silicate system studied here makes it challenging to apply low porosity (dense)

ytterbium silicate microstructures via APS processing and will require careful selection and control of spray parameters. The challenges to the deposition of coatings for EBC applications are compounded by the formation of extensive mud cracking (providing high permeability oxygen and water vapor pathways to the underlying layers) in the ytterbium monosilicate system. While mud cracks are not formed in the disilicate material, loss of silicon leads to the formation of ytterbium monosilicate regions that are susceptible to microcracking upon cooling. If such cracks are retained on reheating, they are likely to reduce the effectiveness of the topcoat resistance to oxygen and steam permeation. However, if the volatility could be controlled, it may permit fabrication of coatings containing layers of varying phase fraction from a single stoichiometric powder composition. This might provide an ability to tailor the thermophysical properties of ytterbium silicate coatings or develop graded coatings by modification of APS deposition parameters.

## **5.5 Conclusions**

Low porosity (<2 %) ytterbium monosilicate and ytterbium disilicate coatings have been deposited using an air plasma spray approach. The dependence of the microstructure, composition and microcracking of these coatings was examined for a variety of spray parameters that resulted in close to fully dense coatings. It has been found that:

- a) Air plasma spray deposition of low porosity ytterbium mono- and disilicate layers on silicon and mullite coated SiC substrates has been shown to be possible over a wide range of plasma spray conditions using powders with a particle diameter of 20 to 50  $\mu\text{m}$ .
- b) The deposition of ytterbium monosilicate layers on silicon and mullite coated silicon carbide substrates resulted in substantial mud (channel) cracking perpendicular to the coating surface and randomly oriented microcracking. The mud cracks penetrated the entire thickness of the ytterbium monosilicate layer, and were formed because of the substantially higher CTE of the ytterbium monosilicate compared to that of the substrate. The equiaxed cracks appeared to result from local variations in splat composition and therefore elastic modulus and CTE.
- c) Low porosity ytterbium disilicate layers contained no mud cracks and exhibited less equiaxed microcracking than the monosilicate. Thermal dilatometry measurements indicated the bulk material had a CTE of approximately  $4 \times 10^{-6} \text{ }^\circ\text{C}^{-1}$ , very close to that of the SiC substrates. Due to the elimination of mud cracking and reduction of microcracking, short-circuit pathways for gas phase transport through this coating layer were greatly reduced.
- d) The high partial vapor pressure of SiO at elevated temperature resulted in substantial loss of silicon from the originally stoichiometric powder during air plasma spraying. The silicon depletion in deposited layers varied considerably within each coating due to the variation of temperature, particle trajectory and residence in the plasma plume. The average coating composition and compositional range of as-deposited splats were also strongly affected by the spray deposition parameters.

- e) The high volatility of Si led to precipitation of  $\text{Yb}_2\text{O}_3$  in the ytterbium monosilicate coatings and  $\text{Yb}_2\text{SiO}_5$  in the ytterbium disilicate layers. The crystal structures were verified as equilibrium phases and their lattice parameters measured using selected area electron diffraction (SAED) during TEM analysis. A metastable monoclinic  $\text{Yb}_2\text{SiO}_5$  was observed in both ytterbium monosilicate layers and ytterbium disilicate layers, but this phase transformed to the equilibrium monoclinic  $\text{Yb}_2\text{SiO}_5$  crystal structure during annealing.
- f) Variation of the deposition parameter had significant effects on phase fractions, splat aspect ratio, total length of micro-crack observed, and orientation of microcracking in both ytterbium silicates.

## 5.6 Appendix A: Dilatometry of $\text{Yb}_2\text{Si}_2\text{O}_7$

The thermal expansion coefficient (CTE,  $\alpha$ ) of  $\text{Yb}_2\text{Si}_2\text{O}_7$  has been measured for 95% dense spark plasma sintered (SPS) ytterbium disilicate, Figure 5.14. The SPS blank was machined to 25 mm x 5 mm x 5 mm in dimension and was lightly diamond polished to remove surface imperfections and to square edges. The resulting dilatometry specimen was annealed in lab air at 1400 °C for 100 hours prior to testing to establish oxygen stoichiometry in the material after sintering.

X-ray diffraction pole figures were produced for the dilatometry specimen to assess its crystallographic texture. The pole figures indicated no crystallographic texture in the dilatometry specimen. XRD patterns confirmed the specimen to be monoclinic ytterbium disilicate with no other phases discernible. Dilatometry was performed using a Netzsch

(Burlington, MA) 402-C dilatometer using high purity  $\alpha$ -alumina as a calibration standard. Heating and cooling ramp rates were 0.05 °C/s. Very slight hysteresis was observed in the heating and cooling curves of the specimen, Figure 5.14, but not to an extent to merit concern over the validity or accuracy of the CTE measurement.

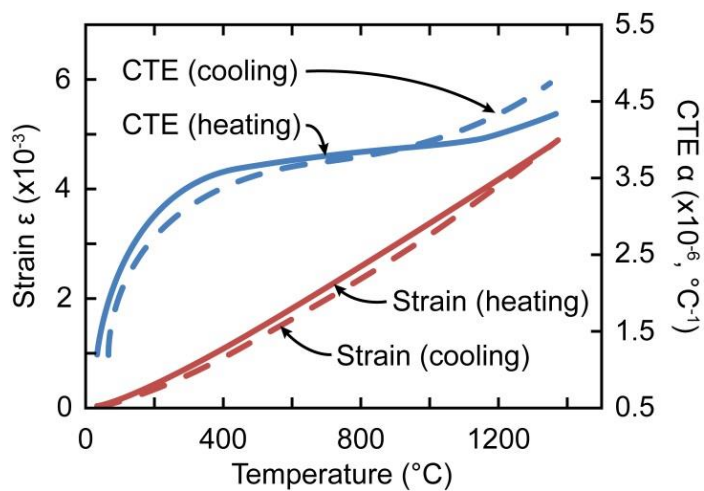


Figure 5.14: Thermal strain and expansion coefficient of 100 hour annealed 95% dense spark plasma sintered (SPS) ytterbium disilicate ( $\text{Yb}_2\text{Si}_2\text{O}_7$ ).

## **6 Delamination and Cracking of Yb<sub>2</sub>SiO<sub>5</sub>/Al<sub>6</sub>Si<sub>2</sub>O<sub>13</sub>/Si Coatings in Steam-cycling**<sup>5</sup>

**Synopsis:** An optimized air plasma spray process has been used to apply a model tri-layer Yb<sub>2</sub>SiO<sub>5</sub>/Al<sub>6</sub>Si<sub>2</sub>O<sub>13</sub>/Si environmental barrier coating (EBC) system  $\alpha$ -SiC substrates using low power deposition parameters to reduce silicon losses. During cooling, equibiaxial tensile stresses were developed in the ytterbium monosilicate layer (and to a lesser extent the Al<sub>6</sub>Si<sub>2</sub>O<sub>13</sub> layer) due to the mismatch of their coefficients of thermal expansion with those of the rest of the system. Vertical mud cracks then formed in the ytterbium monosilicate layer and bifurcated either in the Al<sub>6</sub>Si<sub>2</sub>O<sub>13</sub> layer or at one of its interfaces. Upon thermal cycling in a 90 % H<sub>2</sub>O + 10 % O<sub>2</sub> environment between 1316 °C and 110 °C, the bifurcated mud cracks propagated into the Si bond coat and grew laterally along the mid-plane of this layer. After extended cycling, these cracks linked to cause partial spallation of the coating. The faces of bifurcated cracks were accessible to the steam environment and found to have formed cristobalite, which was microfractured due to repeated  $\beta \leftrightarrow \alpha$  phase transformation upon thermal cycling. The crack bifurcation

---

<sup>5</sup> Based upon a technical article in preparation for the *Journal of the European Ceramic Society*.<sup>96</sup>

phenomenon was investigated by finite element analysis, and the terminal crack trajectory assessed in terms of energetic favorability and interface fracture mechanics concepts. The differences in failure mode between this system and an otherwise identical one deposited using high power deposition parameters is rationalized in terms of the differences in silicon layer microstructure and interface behavior.

Foucault de Francqueville, Stephen Sehr, and Matthew Begley (UCSB) performed the residual stress and ERR calculations presented in this chapter using LayerSlayer and LayerSlayer FEA. Bryan Harder and Dongming Zhu (NASA Glenn) also provided many helpful consultations regarding cracking behavior of EBCs.

## 6.1 Introduction

In Chapter 2  $\text{Yb}_2\text{SiO}_5/\text{Al}_6\text{Si}_2\text{O}_{13}/\text{Si}$  EBCs were deposited using a high power APS approach with large torch standoff distance. The combination of processing parameters resulted in porous silicon bond coats and mud cracked ytterbium monosilicate and mullite layers. These mud cracks were found to have an average spacing of  $280\ \mu\text{m}$ ,<sup>95</sup> and are highlighted in Figure 1(a) using white arrows. The mud cracks initiated at the surface of the coating and vertically penetrated both the  $\text{Yb}_2\text{SiO}_5$  and  $\text{Al}_6\text{Si}_2\text{O}_{13}$  layers before terminating at the  $\text{Al}_6\text{Si}_2\text{O}_{13} - \text{Si}$  interface, Figure 6.1(b) and (c). Chapter 3 found that the presence of these mud cracks led to rapid localized oxidation of the bond coat during steam-cycling, and early delamination failure.<sup>95</sup>

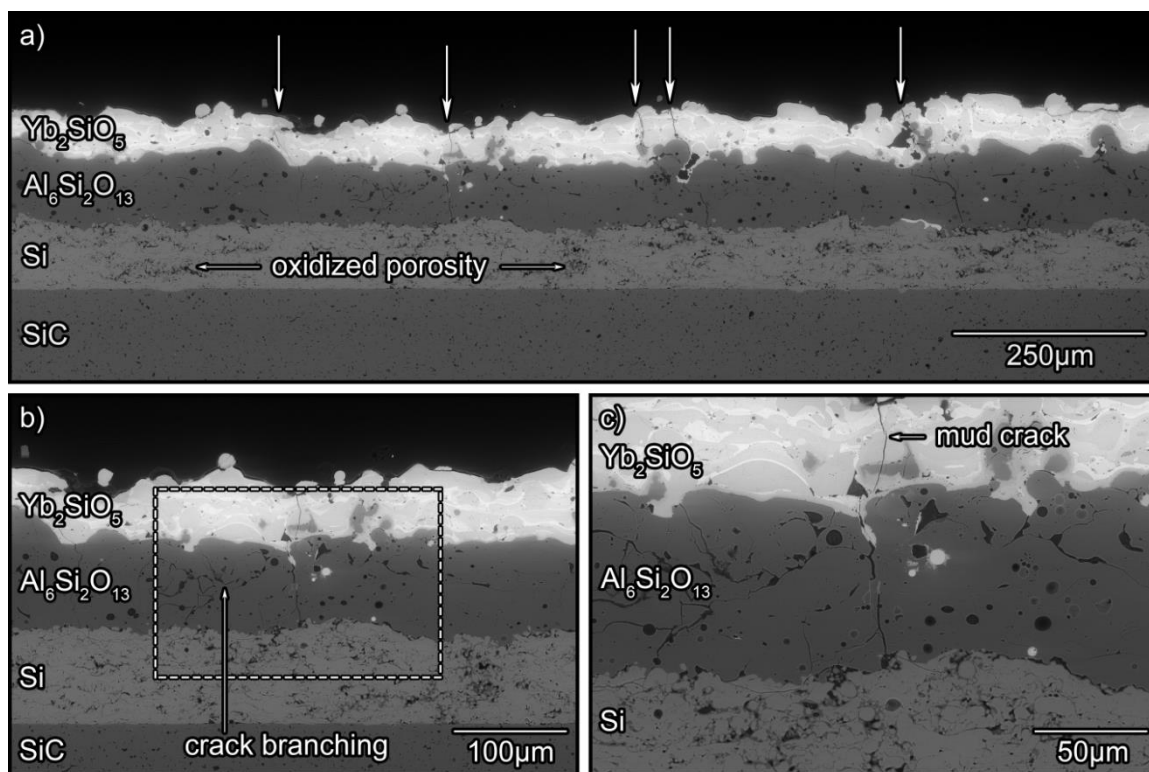


Figure 6.1: BSE images of an annealed tri-layer EBC deposited using high power plasma spray parameters from Chapter 2. (a) The three layers on a SiC substrate with mud cracks indicated. (b) Higher magnification view showing penetration of a mud crack, and (c) zoom of boxed region in (b) showing a higher magnification view of the mud crack within the EBC.

The failure mechanism of this  $\text{Yb}_2\text{SiO}_5/\text{Al}_6\text{Si}_2\text{O}_{13}/\text{Si}$  EBC involved water vapor and oxygen penetration through the mud cracked coating layers resulting in formation of a  $\beta$ -cristobalite ( $\text{SiO}_2$ ) thermally grown oxide (TGO) upon the surface of the Si bond coat, Figure 6.2(a). The cristobalite TGO underwent a reversible  $\beta \rightarrow \alpha$  phase transformation at  $\sim 220^\circ\text{C}$  that was accompanied by a 4.5 % decrease in volume during cooling.<sup>201,215,216</sup> The repetition of this reversible phase transformation during thermal cycling severely microfractured the TGO and resulted in loss of its protective ability, Figure 6.2(b). Rapid thickening of the TGO was then observed, and accompanied by development of high

stresses that were relieved by delamination fracture that initiated from the edge of the samples.<sup>95</sup> This process has been treated extensively in Chapter 3.

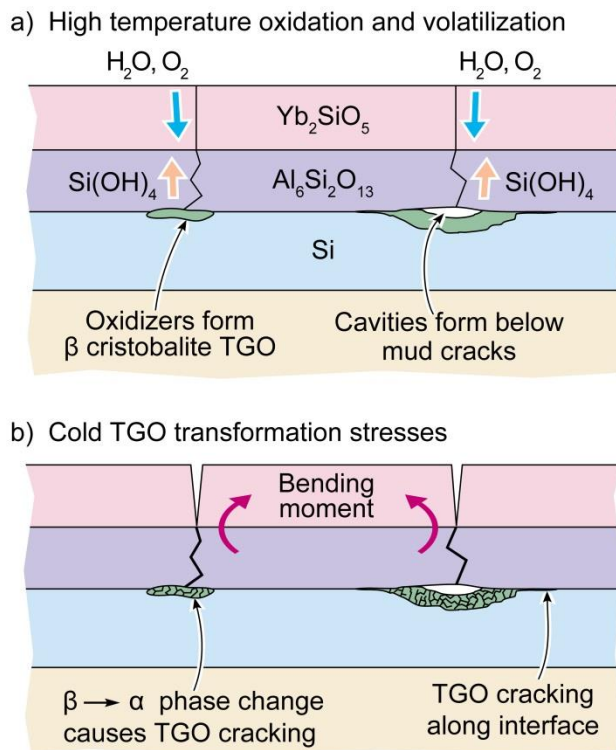


Figure 6.2: Schematic illustration of the failure mechanism of high power deposited tri-layer EBCs on a SiC substrate (see Chapter 3).

In Chapter 5, it was found that the plasma spray parameters used for application of the coating can significantly influence the composition and structure of the coating layers as well as the defects incorporated within them. This in turn is likely to influence the failure mechanisms of the coating. Here, the same  $\text{Yb}_2\text{SiO}_5/\text{Al}_6\text{Si}_2\text{O}_{13}/\text{Si}$  tri-layer EBC system studied in Chapters 2 and 3 was APS deposited onto SiC substrates using low power spray parameters optimized in Chapter 5 to reduce the loss of silicon during deposition, achieve high relative density in the three layers and to increase interfacial

adherence. The structure of the coatings and their failure mechanisms during steam-cycling are then explored and compared with those observed in Chapter 3.

## 6.2 Experimental

### 6.2.1 Coating Deposition

Six three-layer  $\text{Yb}_2\text{SiO}_5/\text{Al}_6\text{Si}_2\text{O}_{13}/\text{Si}$  coatings were deposited onto a grit blast roughened, 25.4 mm x 12.7 mm x 4.8 mm thick,  $\alpha$ -SiC Hexoloy™ (Saint Gobain Ceramics, Niagara Falls, NY) substrate surface. The APS deposition system used a Praxair SG-100 torch with a 02083-175 anode implementing internal powder injection and standard model 02083-120 cathode with a model 03083-112 gas injector. Deposition parameters for individual layers are given in Table 6.1. The structure of ytterbium monosilicate layers deposited using these spray parameters has been studied extensively.<sup>220</sup>

*Table 6.1: Deposition parameters for low power plasma spray parameter EBC layers.*

APS Layer	Torch Power (kW)	Arc Current (A)	Primary Ar (slm)	Secondary H <sub>2</sub> (slm)	Powder feed (g/min)	Carrier Ar (slm)
$\text{Yb}_2\text{SiO}_5$	11.2	275	84.95	0.94	41.5/lower	5.90
$\text{Al}_6\text{Si}_2\text{O}_{13}$	15.2	375	77.87	0.94	18.9/upper	5.43
Si	14.0	350	77.87	0.94	31.0/upper	5.90

Several aspects of the deposition process modified by Richards et al.<sup>220</sup> have been retained for the present study. Most importantly, an Ar/H<sub>2</sub> reducing gas was continuously flowed through the high temperature deposition furnace to minimize oxidation of the

substrate during preheating and the Si bond coat during deposition. After deposition of the Si layer the reducing gas flow was stopped. The deposition of all layers was performed at 1200 °C, and each layer took roughly 10 s to deposit. For a full description of other aspects of the tri-layer deposition process, the reader is referred to Richards et al.<sup>220</sup>. The target thickness of the ytterbium monosilicate layer was 125 μm (compared to 75 μm in the previously studied system) while that of the  $\text{Al}_6\text{Si}_2\text{O}_{13}$  layer and the Si bond coat was 75 μm, Figure 6.3.

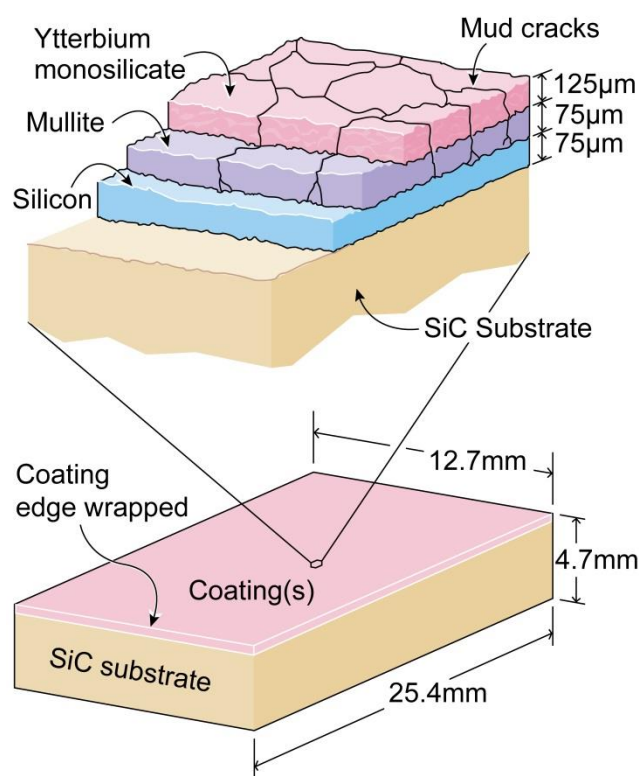


Figure 6.3: Schematic illustration of an as-deposited tri-layer coated  $\alpha$ -SiC substrate.

### 6.2.2 Coating Stabilization and Steam Furnace Cycling

The coated samples were annealed at 1300 °C in lab air for 20 hours to transform metastable phases in the ytterbium monosilicate and mullite layers. This annealing

treatment has previously been used in EBC studies.<sup>59,77-79,93,95,97,220</sup> Coated substrates were then thermally cycled in a steam-cycling furnace at 1316 °C in a flowing, atmospheric pressure, 90 % H<sub>2</sub>O/10 % O<sub>2</sub> gas environment with a flow velocity of 44 mm/s in the test gage corresponding to a volumetric flow of 4.1 slm. The furnace and flow conditions were identical to those used in a previous steam-cycling study of the Yb<sub>2</sub>SiO<sub>5</sub>/Al<sub>6</sub>Si<sub>2</sub>O<sub>13</sub>/Si system.<sup>95</sup> The minimum temperature experienced during cycling was 110 °C and the maximum temperature of 1316 °C was held for 1 h. These temperatures were periodically verified using a reference thermocouple inserted into the process tube. These testing conditions approximate the H<sub>2</sub>O partial pressure during lean hydrocarbon combustion at a pressure of ~10 atm. The samples were examined visually before testing and after every 25 steam cycles.

### **6.2.3 Coating Characterization**

The samples were sectioned, polished, and examined with a scanning electron microscope (Quanta 650 FE-SEM, FEI, Hillsboro, OR) operating in the back-scattered electron (BSE) mode. All images were collected under low-vacuum conditions. A gamma correction was applied to raw images to enable contrast of Yb and non-Yb containing materials to be simultaneously observed. The imaging conditions and image processing are consistent with prior work.<sup>95,220</sup> Elemental mapping by Energy Dispersive Spectroscopy (EDS: X-Max<sup>N</sup> SDD, Oxford Instruments, Concord, MA) was used to generate compositional maps. The EDS spectra were captured using a 20 kV accelerating voltage, which allowed for compositional identification of ytterbium by its L lines. The EDS spectra used for elemental mapping were not standardized.

Raman Spectroscopy was performed using an inVia (Renishaw, Hoffman Estates, IL) microscope and was used to identify bond coat oxidation phases in steam cycled coatings. The Raman analyses were performed using a 50x lens with a numerical aperture of 0.5. An argon-ion laser (wavelength of 488 nm) was used as the light source. Approximately 99 % of the Gaussian distributed incident light resided within a 1  $\mu\text{m}$  diameter spot, yielding a spatial resolution for this technique of approximately 1  $\mu\text{m}$ . This technique has previously been used to identify bond coat oxidation phases in EBCs.<sup>95</sup>

#### **6.2.4 Thermomechanical Analysis**

Thermomechanical analyses of coating stresses and strain energy release rates (ERR) for interfacial debonding of the elastic coating system were calculated using the LayerSlayer<sup>199</sup> software package. All calculations were performed using similar assumptions to prior work.<sup>95</sup> Briefly: (i) oxidation grows a stress free  $\beta$  cristobalite scale at 1316 °C, (ii) upon cooling, strain is generated by differential thermal contraction of layers (plastic flow/creep is neglected), (iii) at 220 °C an inversion-type phase transformation occurs in  $\beta$  (high) cristobalite to form the  $\alpha$  phase with a volume reduction of 4.5 %, (iv) cristobalite is assumed to be constrained in the plane of the coating by surrounding layers, and (v) stresses (and ERRs) are calculated based upon the thermal and transformation elastic strain mismatch. The thermophysical properties and residual stresses calculated using the LayerSlayer code for this elastic coating – substrate system after cooling to 20 °C from the (stress free) steam-cycling temperature of 1316 °C are listed in Table 2, and are similar to those calculated previously.<sup>95</sup>

Table 6.2: Thermomechanical properties and residual stress of the EBC system components.

Material	CTE ( $\times 10^6$ $^{\circ}\text{C}^{-1}$ )	Young's Modulus (GPa)	Poisson Ratio $\nu$	Thermal Stress (MPa) <sup>a</sup>	Low Power Layer Thickness	High Power Layer Thickness
Yb <sub>2</sub> SiO <sub>5</sub> $E_{APS}$ <sup>b</sup>	7.5 <sup>97</sup>	172 <sup>97</sup> 86	0.27 <sup>c</sup>	840 425	125 $\mu\text{m}$	75 $\mu\text{m}$
Mullite $E_{APS}$ <sup>b</sup>	5.3 <sup>70</sup>	220 <sup>186</sup> 110	0.28 <sup>187</sup>	215 110	75 $\mu\text{m}$	75 $\mu\text{m}$
Cristobalite- $\alpha$ Cristobalite- $\beta$	30 <sup>d</sup> 3.1 <sup>200</sup>	65 <sup>201</sup> 70 <sup>e</sup>	-0.164 <sup>202</sup> -0.042 <sup>203</sup>	4,350	0-15 $\mu\text{m}$	0-150 $\mu\text{m}$
Si $E_{APS}$ <sup>b</sup>	4.1 <sup>88</sup>	163 <sup>88</sup> 82/16 <sup>f</sup>	0.223 <sup>88</sup>	-180 -17	75 $\mu\text{m}$	100 $\mu\text{m}$
SiC ( $\alpha$ )	4.67	430	0.14	-55 -34	3.2mm	3.2mm

<sup>a</sup>Calculated at 20 $^{\circ}\text{C}$  after cooling from stress free condition at 1300 $^{\circ}\text{C}$  with LayerSlayer.

<sup>b</sup>Assumed 50% reduction in elastic modulus for APS material/cracking.

<sup>c</sup>Based on Y<sub>2</sub>Si<sub>2</sub>O<sub>7</sub>.<sup>204</sup>

<sup>d</sup>Average of values reported on the 20-200 $^{\circ}\text{C}$  interval.<sup>201,205</sup>

<sup>e</sup>Based on Young's modulus ratio of  $\alpha$  and  $\beta$  quartz<sup>206</sup> and  $\alpha$  cristobalite.

<sup>f</sup>86 GPa for low power layer and 16 GPa for high power layer based on microstructure.

The conditions promoting crack bifurcation were also assessed using Finite Element Analysis (FEA) combined with a J-integral solution of strain energy release rate<sup>234</sup>. The scenario simulated is shown in Figure 6.4(a), where a mud crack in the Yb<sub>2</sub>SiO<sub>5</sub> layer of the EBC penetrates into the mullite layer before bifurcating at some position within either the Al<sub>6</sub>Si<sub>2</sub>O<sub>13</sub> or Si layer. The bifurcation position was indexed by the normalized position scale defined in Figure 6.4(a). The angle of the crack propagation direction,  $\theta$ , was defined from the coating normal plane and was iterated over the range  $0^{\circ} \leq \theta \leq 85^{\circ}$  (from horizontal to near vertical) using a trial crack length  $a = 1 \mu\text{m}$ . The layer thicknesses were those given in Figure 6.3, and the interfaces of the system were assumed to be flat and pore free to simplify the computation. An automatic mesh generator was

used to permute the normalized bifurcation position and putative crack angle  $\theta$  to generate simulation grids for FEA and J-integral analyses.

Eight-node quadrilateral elements were used to model the problem except near the crack tip where six-node triangular elements were used. Meshes were created with varying parent crack depths starting at the  $\text{Yb}_2\text{SiO}_5 - \text{Al}_6\text{Si}_2\text{O}_{13}$  interface and stepping down into the Si bond coat. The putative crack angle was varied over the range of  $\theta$  previously given. FEA was performed using boundary conditions determined by the thermal residual stresses imposed by cooling from 1300 °C. The results of the FEA analysis were post-processed to calculate the energy release rate via the J-integral through the Virtual Crack Extension Method (VCEM)<sup>234</sup>. A representative simulation grid prepared by the automatic mesh generator is shown in Figure 6.4(b) while a high magnification view of the deformed mesh (using 5x displacement magnification to better illustrate the deformation) around a putative crack is shown in Figure 6.4(c). The absolute magnitude of J was tabulated for all simulation grids and also normalized by the strain energy release rate for pure channel cracking ( $J_{90^\circ}$ ). The above simulations were performed for the two different sets of elastic moduli listed in Table 6.2 as well as for low power EBC configurations<sup>95</sup>.

### 6.3 Results

Six substrates had coatings deposited upon them. No delaminations were observed along any of the edges or at any corners of the coatings after deposition or after a 20 hr, 1300 °C stabilization anneal in air. The edges of the coatings looked similar and the

direction of APS passes was not discernible in optical examination. All four edges of the samples appeared to be slightly over-sprayed, as indicated in Figure 3. Of the six coatings, one was used for investigation of as-deposited and annealed microstructures. The remaining five coated samples were thermally cycled in the steam-cycling apparatus.

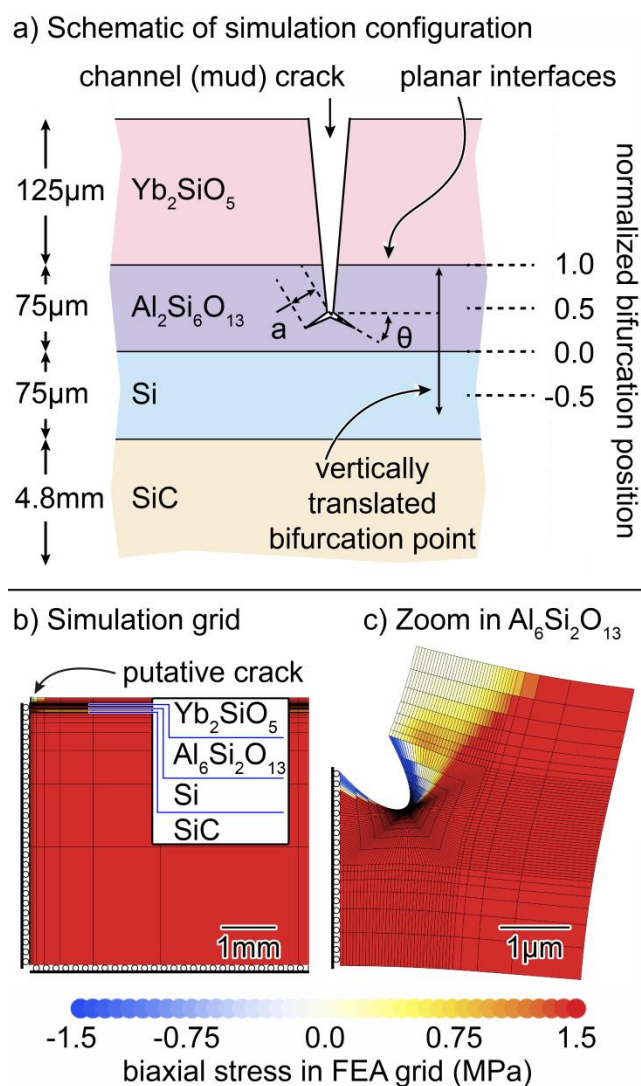


Figure 6.4: (a) Shows a schematic of the cracking configuration simulated with the relevant dimensions and scaling features indicated. (b) Part of the actual mesh simulated with (c) a higher magnification view of the putative crack in the  $\text{Al}_6\text{Si}_2\text{O}_{13}$  layer using 5x displacement magnification to show mesh behavior. (b) and (c) are for a normalized bifurcation position of 0.8 (parent crack length of  $140\mu\text{m}$ ) with  $\theta = 45^\circ$  and  $a = 1\mu\text{m}$ .

### 6.3.1 Coating Structure

BSE mode SEM micrographs of the coating – substrate system after stabilization annealing highlight the presence of periodically spaced mud cracks in the coating, Figure 6.5. In Figure 6.5(a), white arrows along the top of the coating indicate these mud cracks. By analyzing the number of mud cracks in a 25 mm span of the coating cross-section, the average mud crack spacing was determined to be 239  $\mu\text{m}$  with a standard deviation of 94  $\mu\text{m}$ . As with high power coatings, the large variance of mud crack spacing is reflective of the 2D measurement of the 3D cracking pattern. The  $\sim 240$   $\mu\text{m}$  average spacing corresponds to a 15 % reduction compared to the high power deposited tri-layer  $\text{Yb}_2\text{SiO}_5/\text{Al}_6\text{Si}_2\text{O}_{13}/\text{Si}$  EBC<sup>95</sup>. All three coating layers were fairly uniform and relatively dense. When measured by image analysis, the porosity was found to be  $\sim 1$  % in the ytterbium monosilicate layer and  $\sim 5$  % in the  $\text{Al}_6\text{Si}_2\text{O}_{13}$  and Si layers.

Mud cracks were observed to have penetrated the  $\text{Yb}_2\text{SiO}_5$  and  $\text{Al}_6\text{Si}_2\text{O}_{13}$  layers, Figure 6.5(b) and (c). Mud crack penetration of the oxide layers is consistent with mud cracking in several rare earth silicate based tri-layer systems.<sup>77,78</sup> The light and dark contrast features evident in the  $\text{Yb}_2\text{SiO}_5$  layer, Figure 6.5, are a manifestation of Si volatilization from the originally stoichiometric powder particles during APS processing.<sup>97,220</sup> The lighter contrast regions correspond to solidified particles that are depleted in Si. During their solidification, this resulted in the formation of a two-phase  $\text{Yb}_2\text{SiO}_5 + \text{Yb}_2\text{O}_3$  microstructure solidified droplet. The volume fraction of precipitated  $\text{Yb}_2\text{O}_3$  was  $\sim 15$  % for this topcoat.<sup>220</sup> This is in contrast to  $\sim 40$  vol% precipitated  $\text{Yb}_2\text{O}_3$  previously measured in coatings deposited with high power conditions.<sup>97</sup> The precipitated

$\text{Yb}_2\text{O}_3$  volume fraction, however, has only a small effect on the mechanical behavior of the system due to the similarity of CTE and elastic modulus of  $\text{Yb}_2\text{SiO}_5$  and  $\text{Yb}_2\text{O}_3$ .<sup>97</sup>

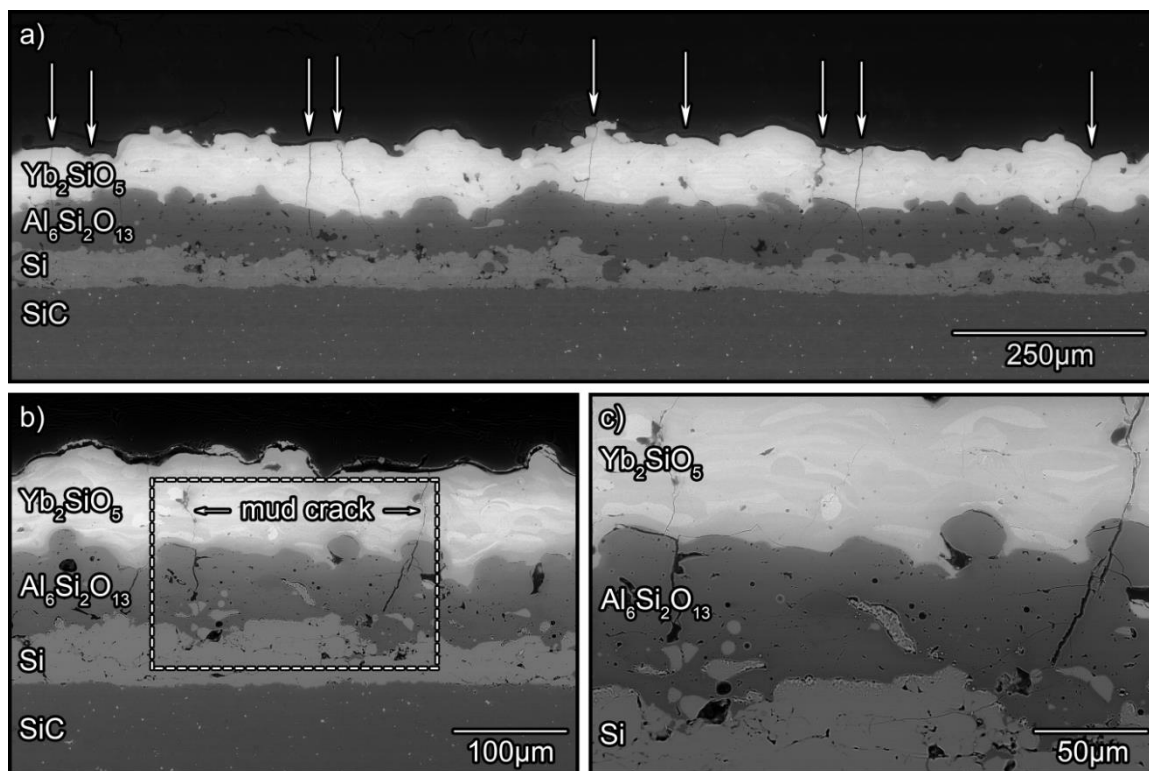
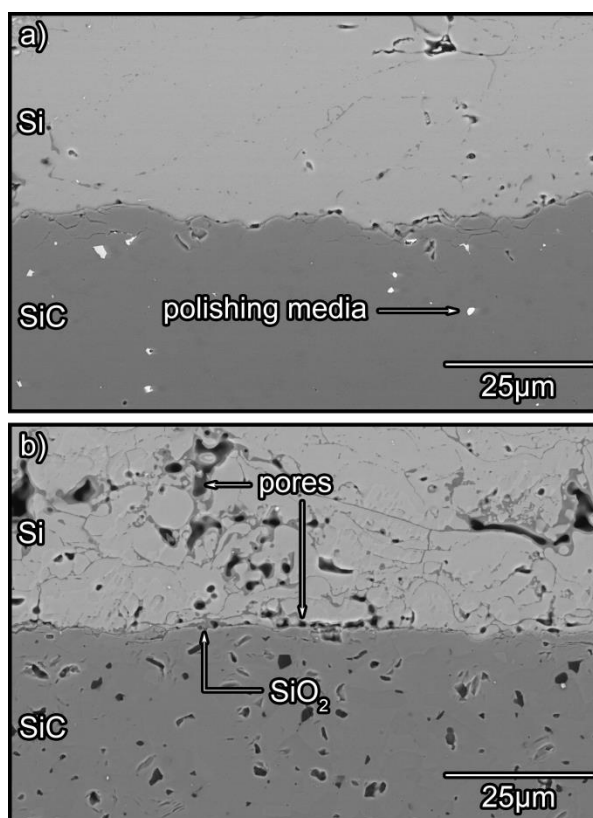


Figure 6.5: BSE images of an annealed tri-layer EBC deposited using optimized low power plasma spray parameters. (a) The three layers on a SiC substrate with mud cracks indicated. (b) Higher magnification view showing two mud cracks and (c) zoom of boxed region in (b) showing the penetration of the two mud cracks into the  $\text{Al}_6\text{Si}_2\text{O}_{13}$  layer.

The adherence of interfaces in the tri-layer coating is of particular interest due to the prevalence of interface delamination, particularly at the Si – SiC and  $\text{Al}_6\text{Si}_2\text{O}_{13}$  – Si interfaces.<sup>95</sup> When examined using BSE imaging, adhesion of the low power Si – SiC interface appeared excellent in comparison to that of the high power interface, Figure 6.6. The low power deposited Si – SiC interface had minimal interface porosity with no  $\text{SiO}_2$  formation, Figure 6.6(a). No delamination was observed at the Si – SiC interface in any

of the low power EBCs and intra-splat oxidation and porosity were minimal. In high power coatings, insufficient and inconsistent adhesion of the EBC has been attributed to porosity and oxidation at the Si – SiC interface, Figure 6.6(b), which resulted in delamination from coating edges or corners upon cooling from elevated temperature.<sup>95</sup>



*Figure 6.6: (a) Shows a typical Si – SiC interface of the low power deposited EBC with a well-bonded interface and limited porosity. (b) The Si – SiC interface formed when using high power plasma spray deposition parameters and no reducing gas flow.*

Adhesion at the  $\text{Al}_6\text{Si}_2\text{O}_{13}$  – Si interface was also improved in low power deposited tri-layers when compared to their high power counterparts, Figure 6.7. Considerable porosity was observed at the  $\text{Al}_6\text{Si}_2\text{O}_{13}$  – Si interface in high power EBCs; this interface was found to suffer oxidation damage during annealing, Figure 6.7(a) and (b). In

juxtaposition, the same interface in low power tri-layers had limited porosity and was not oxidized after annealing, Figure 6.7(c) and (d). The differences in processing of the two layers were the tighter Si powder size distribution, the revised APS deposition parameters and use of a reducing environment during elevated temperature deposition of silicon. These differences resulted in superior bonding at the  $\text{Al}_6\text{Si}_2\text{O}_{13}$  – Si interface in low power EBCs.

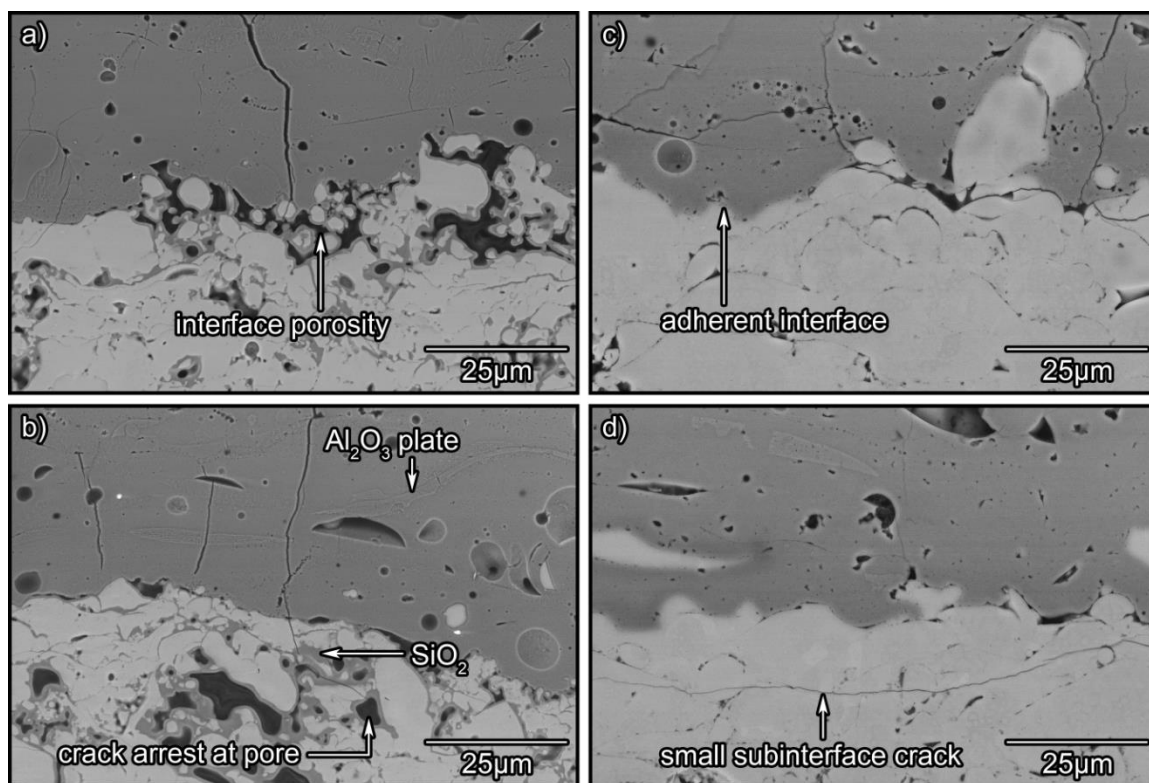


Figure 6.7: BSE images of  $\text{Al}_6\text{Si}_2\text{O}_{13}$  – Si interfaces in the annealed tri-layer EBC system. High power deposited interfaces are shown in (a) and (b) whereas (c) and (d) show the same interface in low power EBCs where the Si layer was deposited using a reducing gas flow.

Mud cracks in the tri-layer system frequently branched in the  $\text{Al}_6\text{Si}_2\text{O}_{13}$  layer or at one of its two interfaces, Figure 6.8. Crack branching was observed in the majority of

mud cracks, and in many cases took the form of a bifurcation into two cracks. The crack pair either terminated at the  $\text{Al}_6\text{Si}_2\text{O}_{13}$  – Si interface or penetrated several micrometers into the Si bond coat before arrest. Thermal residual stress calculations for the  $\text{Yb}_2\text{SiO}_5/\text{Al}_6\text{Si}_2\text{O}_{13}/\text{Si}$  EBC system, Table 6.1, indicate that the high CTEs of the  $\text{Yb}_2\text{SiO}_5$  and  $\text{Al}_6\text{Si}_2\text{O}_{13}$  layers result in substantial tensile residual stresses, even when significantly reduced moduli (consistent with APS processing) are used. A compressive stress in the Si layer is also predicted. The observed cracking is consistent with these stress calculations.

Bifurcation of mud cracks occurred at either the  $\text{Yb}_2\text{SiO}_5$  –  $\text{Al}_6\text{Si}_2\text{O}_{13}$  interface, Figure 6.8(a), within the  $\text{Al}_6\text{Si}_2\text{O}_{13}$  layer, Figure 6.8(b), or at the  $\text{Al}_6\text{Si}_2\text{O}_{13}$  – Si interface, Figure 6.8(c). Bifurcation at these three locations was observed with equal frequency, and all bifurcation locations resulted in crack ligaments that propagated along a trajectory towards or within the Si bond coat. The tendency for bifurcation in this system differed from previous observations of EBCs in the  $\text{Yb}_2\text{SiO}_5/\text{Al}_6\text{Si}_2\text{O}_{13}/\text{Si}$  system where mud cracks were found to terminate at the  $\text{Al}_6\text{Si}_2\text{O}_{13}$  – Si interface, as shown in Figure 6.7(a) and (b). It is noted that the low power EBCs of the present study have a higher density (particularly in the Si bond coat) and a thicker  $\text{Yb}_2\text{SiO}_5$  layer than for those previously studied.<sup>77,78,97</sup>

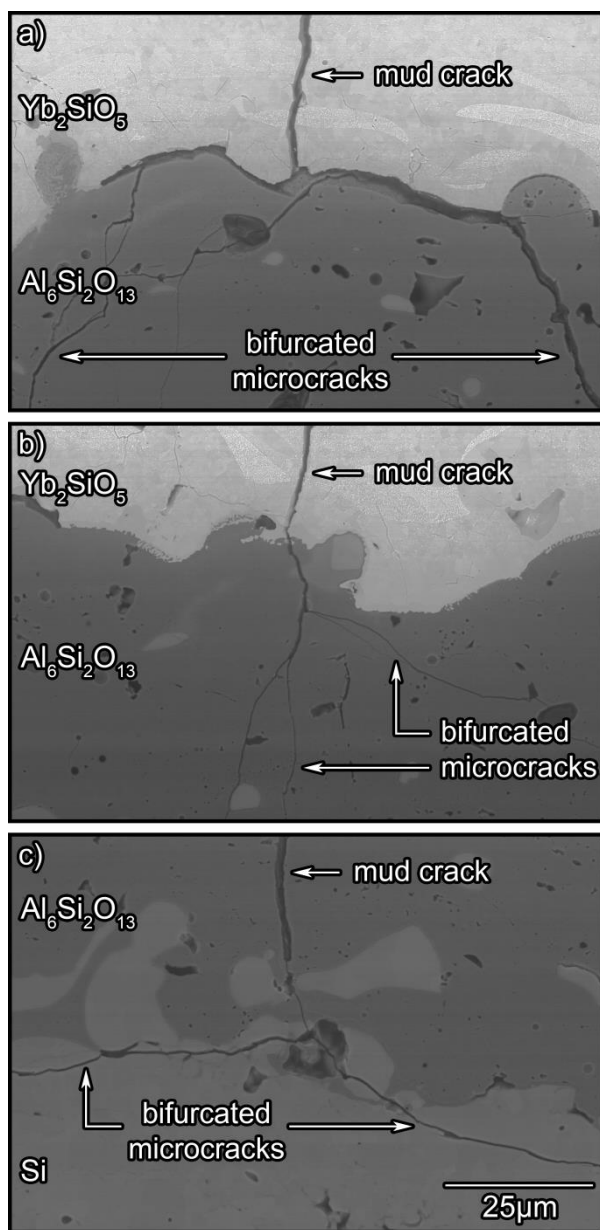


Figure 6.8: BSE micrographs of mud crack bifurcation in stabilization annealed low power  $Yb_2SiO_5/Al_6Si_2O_{13}/Si$  EBCs plasma sprayed onto  $\alpha$ -SiC. (a) Shows a bifurcation at the  $Yb_2SiO_5 - Al_6Si_2O_{13}$  interface, (b) bifurcation within the  $Al_6Si_2O_{13}$  layer, and (c) bifurcation at the  $Al_6Si_2O_{13} - Si$  interface. In all three cases the resultant trajectory of the bifurcated crack ligaments was directed toward the silicon bond coat.

### 6.3.2 Steam-cycling Response

Five samples were thermally cycled in the  $\text{H}_2\text{O}/\text{O}_2$  environment between  $1316\text{ }^\circ\text{C}$  and  $110\text{ }^\circ\text{C}$ . One coating partially spalled after 250 steam cycles while the other four survived much longer, with one sample visibly beginning to spall after 725 steam cycles. The cumulative spallation probability is plotted against the number of steam cycles for low and high power  $\text{Yb}_2\text{SiO}_5/\text{Al}_6\text{Si}_2\text{O}_{13}/\text{Si}$  EBCs<sup>95</sup> in Figure 6.9. A paired t-test was performed on the mean and an f-test on the variance of the lifetime data with the result that  $P = 0.2821$  for the mean and  $P = 0.3168$  for the variance, respectively. Therefore, insufficient statistical evidence exists, even at an  $\alpha = 0.25$  significance level, to indicate that either the average sample life or the variability in sample life differed between the two sets of samples. No volatilization was observed from the surface of the  $\text{Yb}_2\text{SiO}_5$  layer throughout steam-cycling.

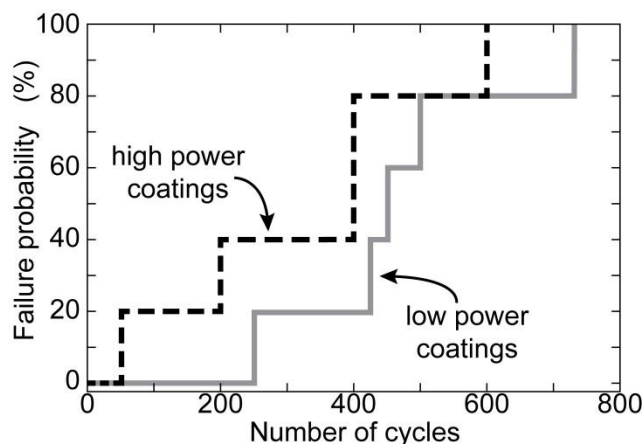


Figure 6.9: Spallation failure probability of low power and high power<sup>95</sup> tri-layer coatings as a function of number of 60 min steam cycles at  $1316\text{ }^\circ\text{C}$ .

No optically visible damage was evident in the annealed coatings, Figure 6.10(a). Spallation of the coating during cycling, however, was readily observed optically, Figure

6.10(b). Though some spallation was observed at the coating's corners after 250 steam cycles, spallation also occurred from the middle of the specimens. This behavior was typical of all steam cycled low power EBCs, and markedly different to that observed for high power EBCs. There, spallation initiated at coating edges where oxidation damage was most severe, and the delamination propagated towards the center of the sample.<sup>95</sup> In contrast, edge spallation of low power EBCs resulted from propagation of a delamination crack that had initiated internally at the nearest mud crack to the coating edge and then grown outward to the edge, Figure 6.10(c).

A previously unobserved failure mode found in all five low power steam cycled samples was the propagation of delamination cracks within the bond coat, Figure 6.11. This failure mechanism was particularly evident in the coating that failed at 250 steam cycles and was observed across the entire specimen. Though this was the first of the five steam cycled samples to fail, it most clearly exhibits this new failure mode due to the reduced crack face oxidation damage associated with its short life. Examination of the serial cross-sections, Figure 6.11, shows that propagation of the delamination cracks occurred through the mid-plane of the Si bond coat, and originated from bifurcated mud cracks. In the case of Figure 6.11, these mud cracks bifurcated within the  $\text{Al}_6\text{Si}_2\text{O}_{13}$  layer (a) and at the  $\text{Yb}_2\text{SiO}_5 - \text{Al}_6\text{Si}_2\text{O}_{13}$  interface (b), corresponding to the bifurcation locations indicated in Figure 6.8(b) and (a), respectively.

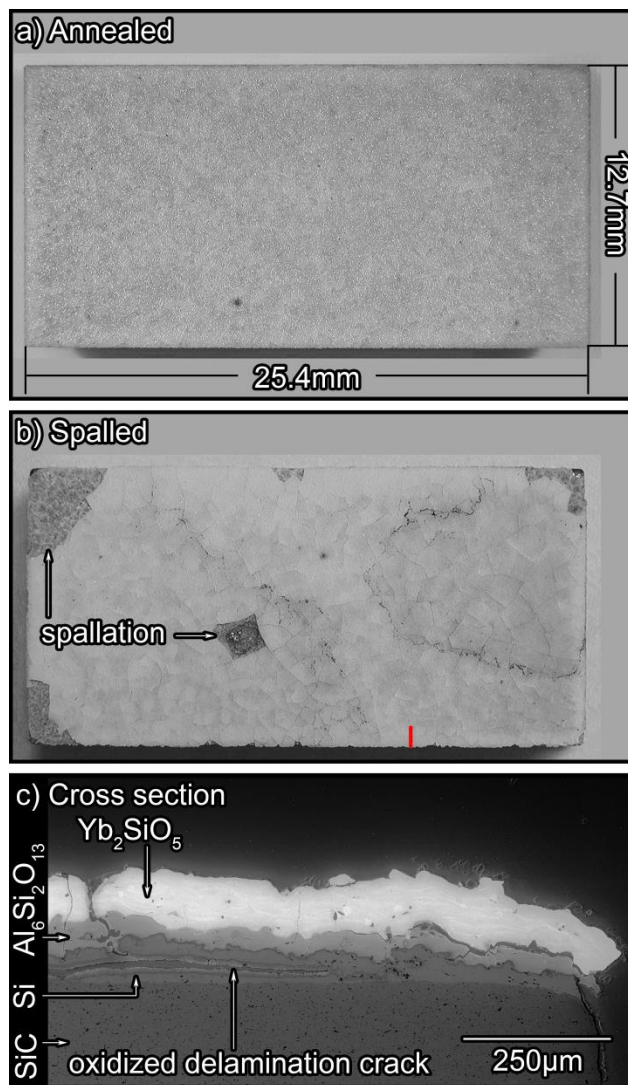


Figure 6.10: (a) Shows an annealed tri-layer EBC deposited using low power plasma spray parameters. The same sample after 250 steam cycles at 1316°C is imaged optically in (b) and its cross section near an edge in (c) using BSE mode SEM imaging. The red bar in (b) indicates the location of the section shown in (c).

A darker gray (lower atomic number) layer can be seen to have formed on the bifurcated crack faces within the Si bond coat, Figure 6.11. An EDS analysis of this layer indicated it was composed of only Si and O, and was therefore a thermally grown oxide (TGO). Further analysis using Raman spectroscopy identified the ambient temperature phase to be  $\alpha$  (low) cristobalite ( $\text{SiO}_2$ ) based on the presence of only two spectral peaks

not belonging to Si with wavenumbers of  $230\text{ cm}^{-1}$  and  $416\text{ cm}^{-1}$  that are typical of  $\alpha$ -cristobalite.<sup>212-214</sup> Cristobalite has previously been identified to be the dominant TGO phase grown in the  $\text{Yb}_2\text{SiO}_5/\text{Al}_6\text{Si}_2\text{O}_{13}/\text{Si}$  system using this Raman technique<sup>95</sup> and has also been identified as a dominant reaction product with either oxidizer at comparable temperature.<sup>51,235</sup>

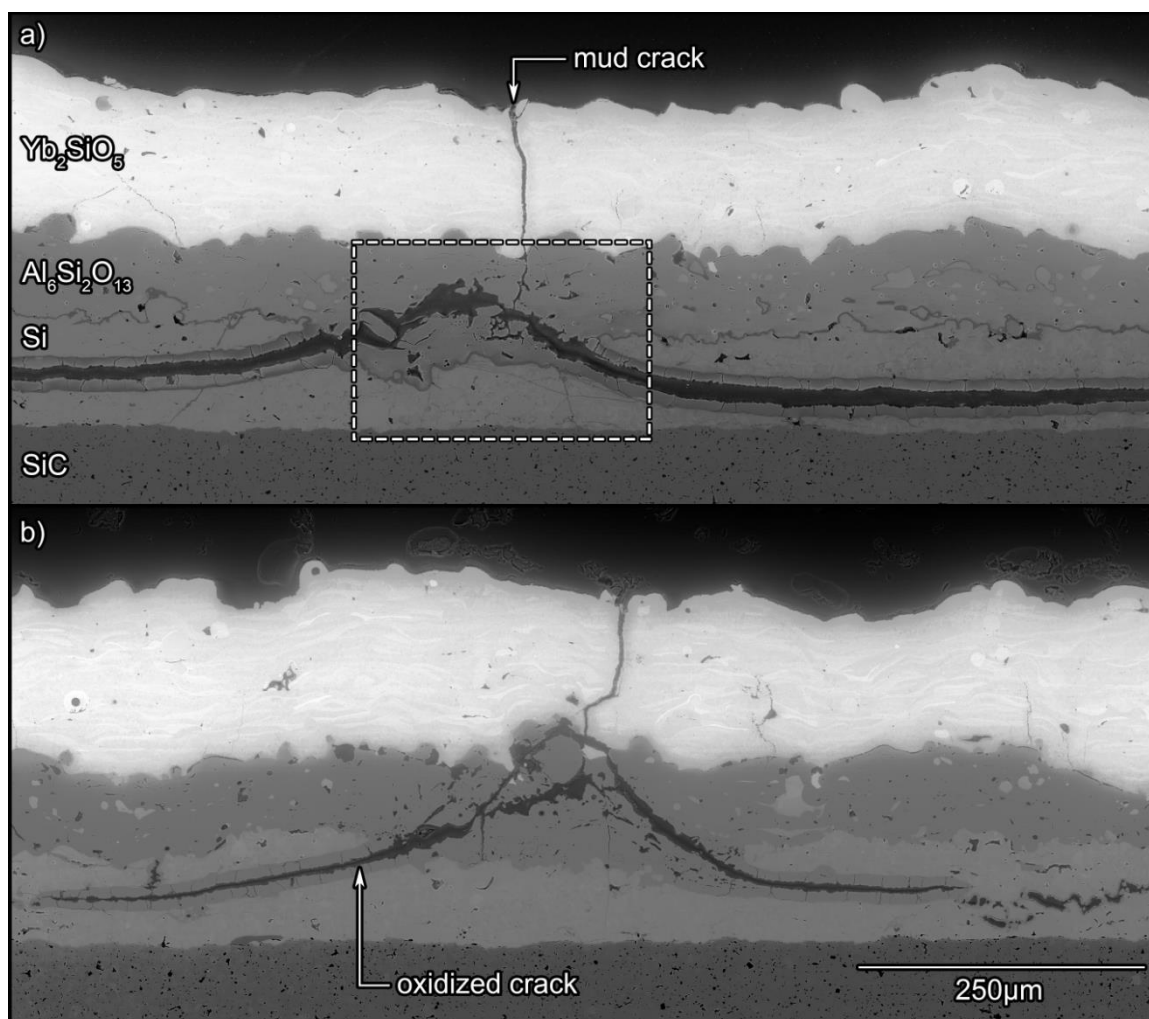


Figure 6.11: Cross sectional BSE micrographs of the same failed coating presented in Figure 8 after 250 1-hour steam cycles at  $1316^\circ\text{C}$  with cross-sections at (a) 1mm and (b) 3mm from the coating edge. Note the oxide layer that has formed on the bifurcated crack faces in the silicon bond coat.

The thickness of this TGO was measured to be less than 15  $\mu\text{m}$  on each single crack face in all bifurcated ligaments of the specimen that failed at 250 steam cycles. The TGO layer on bifurcated crack faces was thickest where the crack first entered the Si layer at 10-15  $\mu\text{m}$  and thinnest at the crack tip at 5  $\mu\text{m}$  or less. Close examination revealed it had micro-mud cracked with the microcracks running normal to crack face and arresting at the interface with silicon, Figure 6.12(a). Interlinked, oxidized pore chains were also observed ahead of delamination crack tips, indicating that damage was occurring ahead of the crack tip prior to crack propagation. Some oxidation of the Si bond coat at the  $\text{Al}_6\text{Si}_2\text{O}_{13}$  – Si interface was observed, but its thickness was less than 3  $\mu\text{m}$  in all specimens (except very near to surface connected mud cracks). This again contrasted with the oxidation behavior of high power deposited tri-layers where severe oxidation was observed across the entirety of the  $\text{Al}_6\text{Si}_2\text{O}_{13}$  – Si interface in all samples as a consequence of the significant porosity in the coating layers.<sup>95</sup>

EDS mapping of the mud crack bifurcation within the dashed box in Figure 6.11(a) was performed to analyze the extent of oxidation, Figure 6.12. This mapping indicates that bifurcation began within the  $\text{Al}_6\text{Si}_2\text{O}_{13}$  layer, consistent BSE imaging, and not within the thermally grown oxide located at the original  $\text{Al}_6\text{Si}_2\text{O}_{13}$  – Si interface. The micro-mud cracking of the TGO formed on the bifurcated crack faces, Figure 6.12(a), also did not penetrate the Si upon which it had grown, consistent with previous observations of the cristobalite TGO formed upon Si in this EBC system.<sup>95</sup> However, it was clear that these micro-mud cracks created diffusive short circuits for oxidizing species to reach the bond coat. The EDS mapping of Figure 6.12 also indicated that only minimal internal

oxidation had occurred within the Si bond coat, which is commensurate with the low porosity and improved interfacial bonding of the low power Si bond coat, Figure 6.6(b).

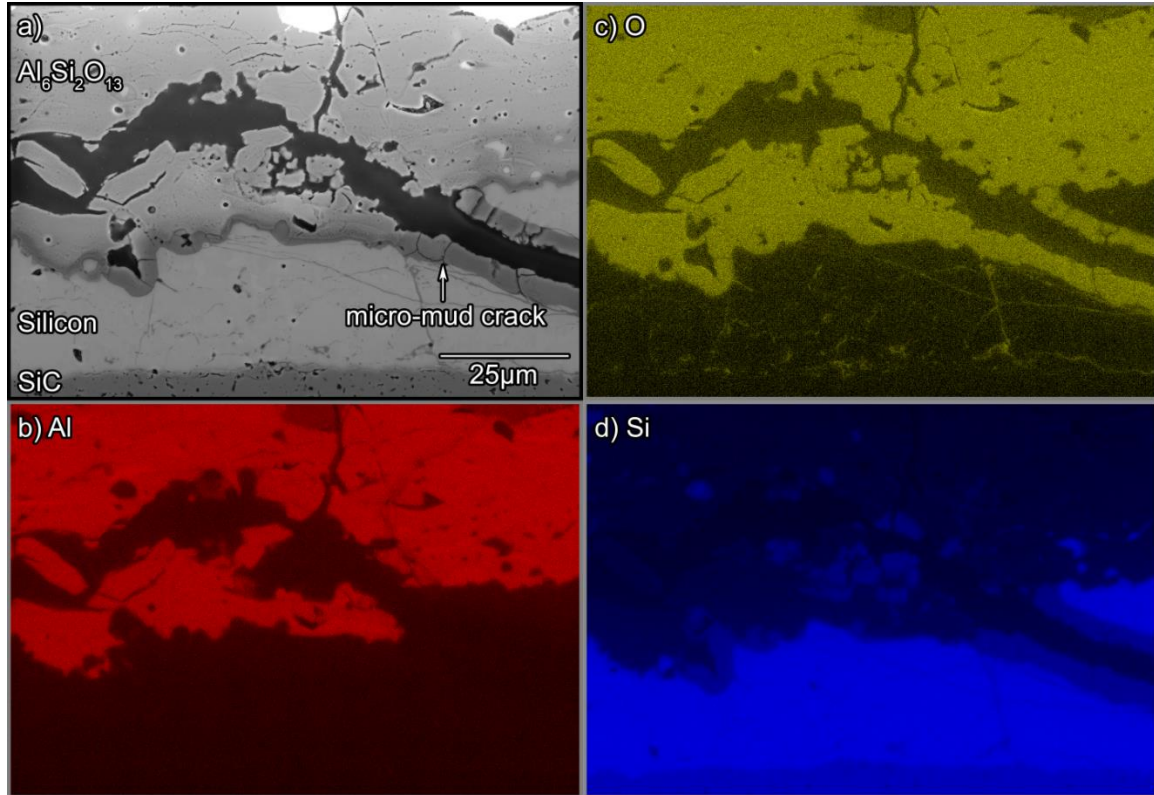


Figure 6.12: (a) BSE mode image of mud-crack and bifurcated delamination cracks for the dashed box region in Figure 9. EDS dot maps are shown for (b) aluminum, (c) oxygen and (d) silicon signals for the same region.

#### 6.4 Calculated Stress States, Strain Energy Release Rates and FEA of Cracking

The mechanical properties and calculated thermal residual stresses for the EBC system of Figure 6.3 are presented in Table 6.2. The thermal residual stresses have been calculated for full elastic moduli appropriate for dense material and reduced elastic moduli ( $E_{APS}$  values in Table 6.2) that are more appropriate for low porosity APS

deposited materials.<sup>122-124,207-209</sup> The similar values assumed for ceramic layers in the low power and high power system are due to the similarity of microstructure and density for the two layers. The calculated residual stresses values were tensile in the ytterbium monosilicate and mullite layers and compressive in the silicon bond coat, and similar to those of the high power EBC system.<sup>95</sup> The high CTE of the TGO layer, combined with significant volume change during the  $\alpha \rightarrow \beta$  phase change resulted in an unrelaxed  $\alpha$ -cristobalite tensile thermal residual stress (at 20 °C) that exceed 4 GPa. As indicated previously,<sup>95</sup> the stored elastic strain energy of cristobalite in this system provides a potent driving force for its mud cracking, and delamination from the silicon to which it is attached.

The energy release rates for delamination crack extension at the various interfaces in the system before TGO formation have been calculated assuming plane-strain constraint and plotted as a function of topcoat thickness, Figure 6.13. The ERR values have been calculated assuming bulk material elastic moduli for dense coating materials and for the 50% reduced ( $E_{APS}$ ) elastic moduli as indicated in Table 6.2; the trends are similar with the magnitude of ERR reduced by a factor of  $\sim 1/2$  for the lower moduli system. The high thermal residual stress in the  $\text{Yb}_2\text{SiO}_5$  layer and significant ERR for its delamination dominates the ERR of the entire system: debonding at any interface that also releases the  $\text{Yb}_2\text{SiO}_5$  topcoat from the SiC substrate has a similar ERR. The ERR was also found to scale linearly with topcoat thickness. Since the low power EBC had a 125  $\mu\text{m}$  thick topcoat, while that of the high power deposited EBC used a 75  $\mu\text{m}$  thick topcoat, the ERR was higher in the low power coating system studied here.

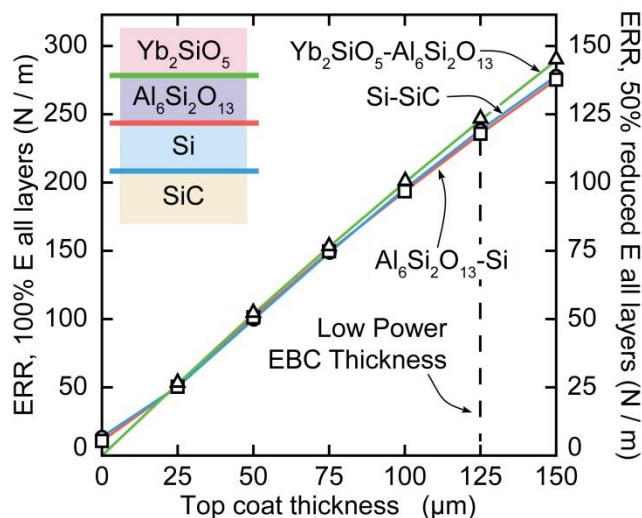


Figure 6.13: The ERR for delamination at the various interfaces in the tri-layer EBC as a function of topcoat thickness prior to TGO growth. Results using bulk (left) and APS (right) estimated elastic moduli are shown.

The ERR for bifurcation cracking has been investigated using FEA simulations combined with J-integral calculations<sup>234</sup>. In this approach the ERR for extension of a putative bifurcated crack is computed as a function of putative bifurcation crack angle from horizontal (coating plane) at various depths in the coating system, Figure 6.4. The calculations have been performed for full elastic moduli of all layers, Figure 6.14(a) and (b), and for 50% reduced ( $E_{APS}$ ) elastic moduli, Figure 6.14(c) and (d). The results show that the absolute ERR for bifurcation reaches a maximum just above the  $Al_6Si_2O_{13}$  – Si interface (normalized depth of zero) at high bifurcation angles; Figure 6.14(a) and (c). Normalization of the ERR by that for channel cracking ( $J_{90^\circ}$ ) indicates that crack bifurcation yields approximately 55 % of the ERR for pure channel cracking at bifurcation angles between  $50^\circ$  and  $80^\circ$  from the horizontal plane at all penetration depths, Figure 6.14(b) and (d).

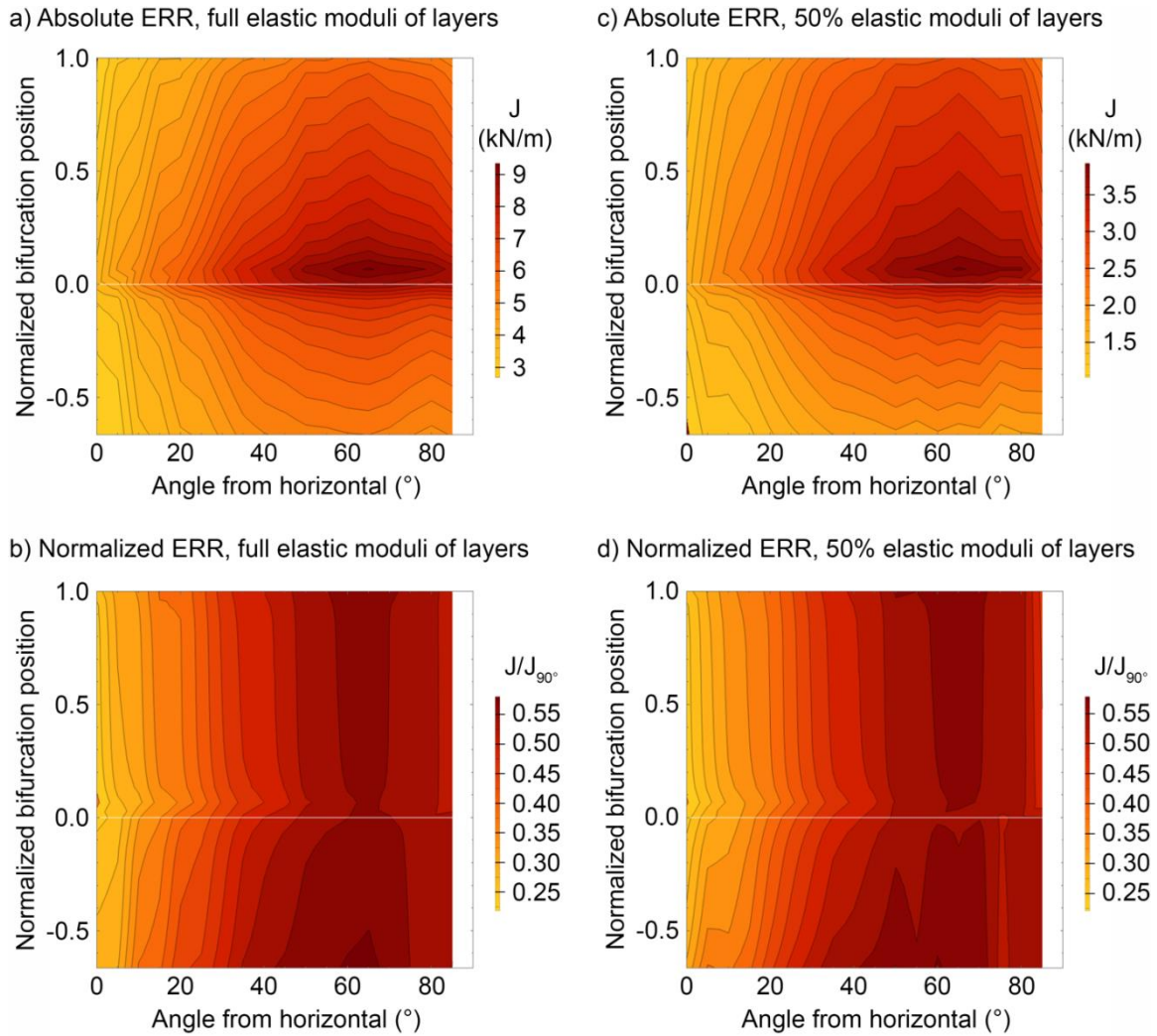


Figure 6.14: FEA computed ERR maps for bifurcation cracking as a function of putative crack angle and bifurcation depth in low power deposited EBCs. Subplots (a) and (b) show the absolute and normalized ERR using the bulk material elastic moduli for coating layers given in Table 6.2. Subplots (c) and (d) show analogous ERR results for coating layers with 50% of the bulk elastic moduli, summarized in Table 6.2. The normalized ERR results were obtained by dividing the ERR for bifurcated crack extension by that for a vertically penetrating single crack.

Preliminary simulations comparable to those of Figure 6.14 have been performed for the high power EBC and resulted in a similar ERR distribution and low energy release for bifurcation relative to channel cracking. Preliminary simulations were also performed for longer putative cracks as a surrogate for investigating the energy release achieved by

encountering a large, symmetrical defect. 5  $\mu\text{m}$  and 10  $\mu\text{m}$  putative cracks were investigated in the low power EBC system using the reduced elastic moduli in Table 6.2, Figure 6.15(a) and (b), and the ERR behavior was nearly identical to that presented in Figure 6.14(c) for 1  $\mu\text{m}$  putative cracks. Figure 6.15 also shows the behavior for long putative cracks in the high power EBC system with properties given in Table 6.2; the peak ERR experienced at near channel cracking conditions is a factor of 2 higher than for the low power system, but the minimum ERR in delamination cracking orientation is comparable. The similarity of these maps indicates that the ERR is relatively insensitive to the length over which a crack propagates on a local (micro) scale in both systems. If a crack propagates 10  $\mu\text{m}$  it will form an area of cracked surface that is 10 times greater than the same crack propagating over 1  $\mu\text{m}$ . If the ERR is constant, the 10  $\mu\text{m}$  crack will release 10 times the energy of the 1  $\mu\text{m}$  crack. The implications of these various cracking behaviors will be addressed in the discussion, Section 6.5.

The mechanics that drive failure during steam-cycling have also been investigated. Figure 6.16 compares the failure modes of the high and low power deposited coatings during steam-cycling. In the low power deposited system, failure of the coating system resulted from the horizontal penetration of a bifurcated crack through the silicon bond coat. Since such cracks are exposed to the external oxidizing environment, TGO formation occurs on the freshly exposed crack faces, Figure 6.9 and Figure 6.10. The strain energy resulting from crack face TGO thermal contraction and phase transformation therefore acts only upon already debonded sections of the coating and *does not contribute to the ERR for adherent sections*. In addition, since very little TGO growth was observed at the  $\text{Al}_6\text{Si}_2\text{O}_{13}$  – Si interface above the region of delamination

crack propagation, the ERR is governed by that of the thicknesses and thermomechanical properties of the layered system.

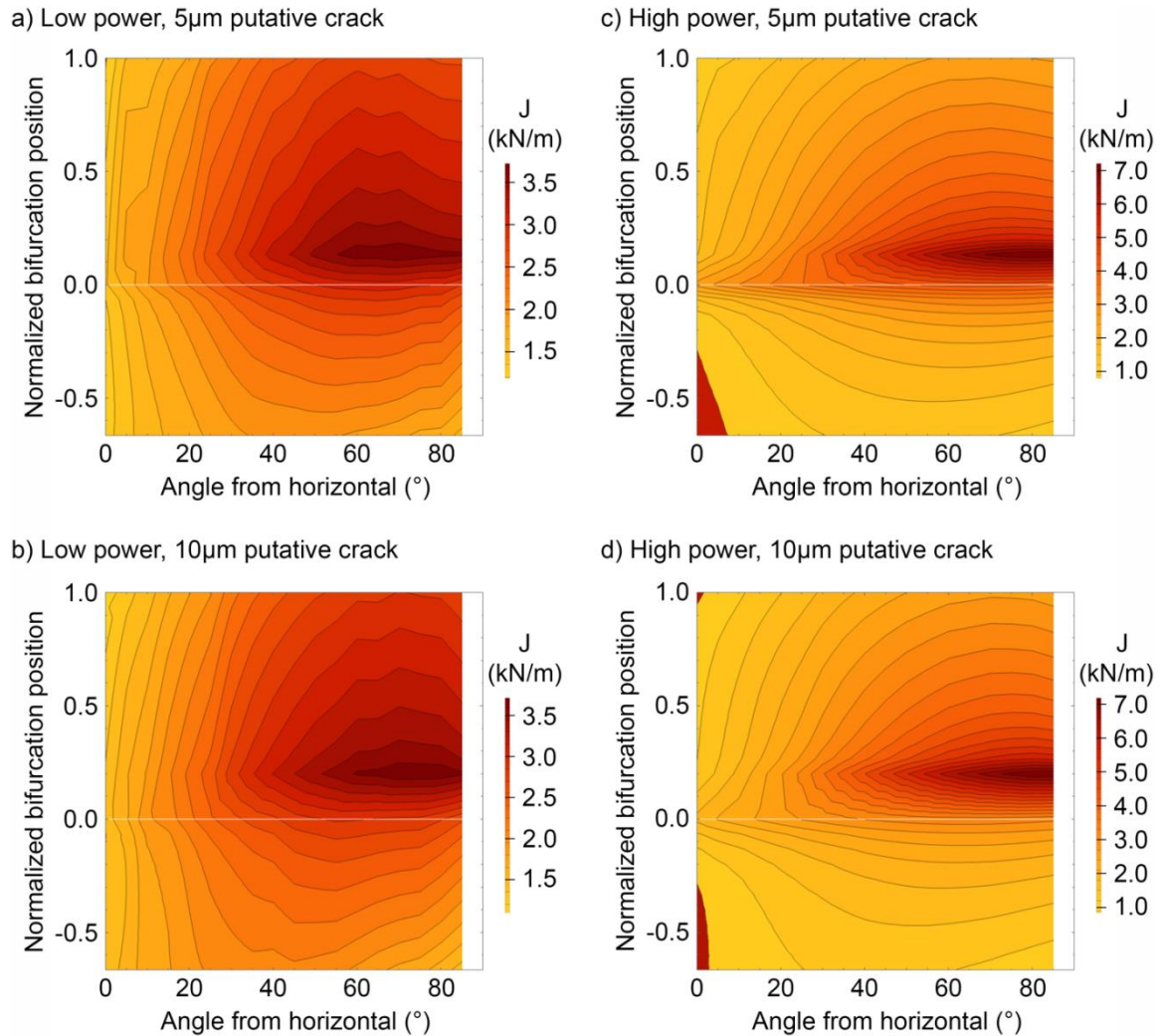


*Figure 6.15: FEA computed ERR maps for bifurcation cracking as a function of putative crack angle and bifurcation depth. Subplots (a) and (b) show the absolute ERR for 5 $\mu\text{m}$  and 10 $\mu\text{m}$  putative cracks in the low power EBC using the 50% reduced elastic moduli for coating layers given in Table 6.2. Subplots (c) and (d) show analogous ERR results for high power layers using the reduced elastic moduli given in Table 6.2.*

It is also clear that the bifurcated cracks tended to propagate on a plane that was approximately midway through the silicon bond coat. The ERR for extension of the bond

coat bifurcation crack (with no surface TGO) has been computed as a function of the crack depth within the Si bond coat to identify the most favored fracture plane in adherent sections of the coating, Figure 6.17. The analysis indicates that for both full and 50% reduced elastic moduli, the variation of ERR varies by only ~1 % with depth in the bon coat, indicating that crack path selection is not energetically based. Instead, it is likely that other aspects of the mechanics of crack growth near interfaces contributed to crack path selection.<sup>236</sup> The crack tip stress intensity experienced by cracks near interfaces have a significant  $K_{II}$  component if elastic modulus mismatch exists across the interface.<sup>219,237-241</sup> Therefore, cracks that intrinsically seek a minimum  $K_{II}$  criterion for propagation will be repelled by interfaces if the toughness of the interface and layer through which the crack propagates are comparable. This scenario is precisely that experienced for the Si bond coat, where the toughness of the layer is similar to its surrounding interfaces due to the intrinsically low toughness of Si.<sup>209</sup> A minimum  $K_{II}$  propagation criterion then draws the propagating crack to the mid-plane of the Si bond coat to avoid the  $K_{II}$  “toughening” effect of its two interfaces.

## 6.5 Discussion

The use of optimized low power APS conditions for the deposition of a model tri-layer EBC applied to a SiC substrate has resulted in a change in failure mode during steam-cycling compared to a similar coating system deposited using higher power conditions.<sup>95</sup> The study has therefore exposed a significant dependency of the failure mechanism upon the parameters that differed between the two coating systems. The thicknesses, pore fractions, elastic moduli and residual stresses of the two coating

systems are summarized in Table 6.3 together with a qualitative indication of adherence of each layer to the one below.

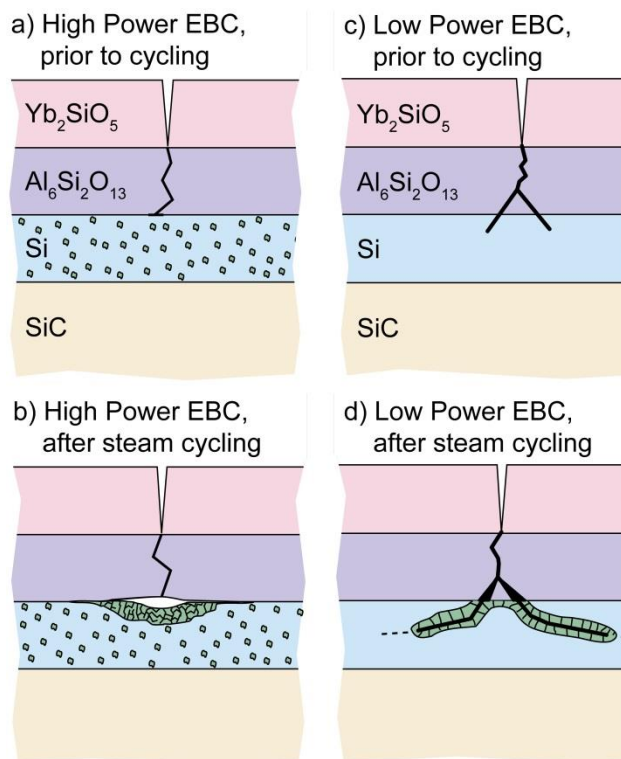


*Figure 6.16: Schematic illustration of the differences in failure mode for (a) high and (c) low power deposited tri-layer EBCs in the annealed condition. The fracture mechanisms that develop during steam-cycling are shown in (b) and (c) for high and low power deposition respectively.*

Low power APS deposition of the Yb<sub>2</sub>SiO<sub>5</sub>/Al<sub>6</sub>Si<sub>2</sub>O<sub>13</sub>/Si tri-layer EBC on SiC substrates resulted in the development of a substantial tensile residual stress in the coating system after cooling from 1316 °C, Table 6.2. The stresses are sufficient to provide ERR considerably in excess of the toughness of oxide ceramics, which lie in the range of 1-50 N/m (loosely equivalent to 0.1-10 Mpa\*m<sup>1/2</sup>)<sup>218</sup>. In both low power and high power tri-layer EBCs, the stored elastic strain energy was high enough to cause mud

cracking. Mud crack spacing was 240  $\mu\text{m}$  in low power EBCs as opposed to the 280  $\mu\text{m}$  previously observed for high power EBCs<sup>95</sup>. The alteration of mud crack spacing originates from the difference in ERR<sup>219</sup> associated with the varying structure.

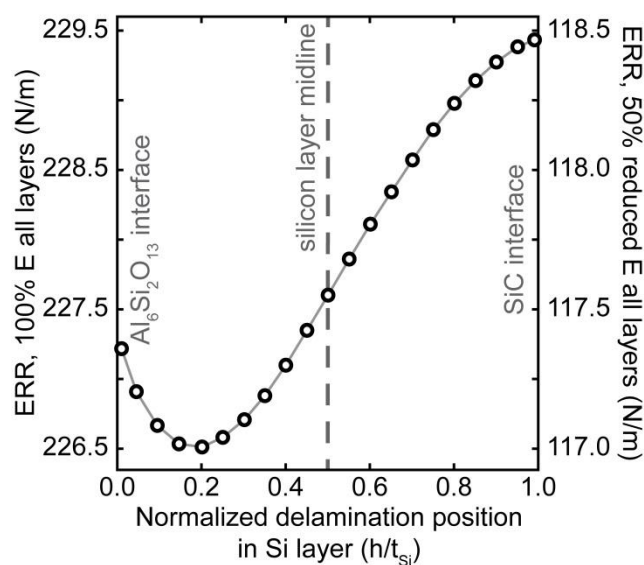


Figure 6.17: The ERR for delamination as a function of normalized penetration depth into the Si layer of the tri-layer EBC.

Table 6.3: Properties of tri-layer  $\text{Yb}_2\text{SiO}_5/\text{Al}_6\text{Si}_2\text{O}_{13}/\text{Si}$  EBCs.

Coating system	Layer	Thickness	Porosity (%)	Elastic modulus (GPa)	Residual Stress (MPa)	Adherence to layer below
Low Power	$\text{Yb}_2\text{SiO}_5$	125 $\mu\text{m}$	1	86	420	Moderate
	$\text{Al}_6\text{Si}_2\text{O}_{13}$	75 $\mu\text{m}$	5	110	109	Excellent
	Si	75 $\mu\text{m}$	5	82	-88	Excellent
	SiC	4.8mm	N/A	430	-48	N/A
High Power	$\text{Yb}_2\text{SiO}_5$	75 $\mu\text{m}$	2	86	425	Good
	$\text{Al}_6\text{Si}_2\text{O}_{13}$	75 $\mu\text{m}$	8	110	110	Moderate
	Si	100 $\mu\text{m}$	20	16	-17	Poor
	SiC	3.2mm	N/A	430	-34	N/A

Bifurcation of mud cracks was observed in low power EBCs. Consequently, assessing the scenario that contributes to bifurcation in the low power EBC but not in the high power EBC<sup>95</sup> is of interest. In high power EBCs, Figure 6.16(a), mud cracks penetrated the  $\text{Yb}_2\text{Si}_2\text{O}_5$  and  $\text{Al}_6\text{Si}_2\text{O}_{13}$  layers but terminated at the porous Si bond coat. In low power EBCs, Figure 6.16(c), mud cracks penetrated the  $\text{Yb}_2\text{Si}_2\text{O}_5$  and  $\text{Al}_6\text{Si}_2\text{O}_{13}$  layers but also bifurcated. The bifurcation occurred at several positions within the coating, Figure 6.8, but for simplicity of analysis it will be assumed that this bifurcation occurs at the median position in Figure 6.16(c). Bifurcation behavior has been reviewed by several authors in the context of crack bifurcation in layered ceramics<sup>242-246</sup> and also extensively in the context of coating delamination at or below interfaces<sup>73,236,238-241,247-256</sup>. However, no literature was identified that reasonably applied to the complex bifurcation scenario observed here. Additionally, no studies have attempted to assess such behaviors in structures with the heterogeneity of APS coatings.

The initiation of bifurcation events was studied using a combined FEA and J-integral approach, and bifurcation was found to be unfavorable in both the low power and high power EBC systems, i.e. propagation of two bifurcated crack ligaments along an incremental distance (1  $\mu\text{m}$ ) released less energy than propagation of a single channel crack along that same distance. When combined with the observation of bifurcation at interfaces and defects within the coating, as in Figure 6.8, it is clear that the phenomenon is related to defect populations. Large defects are plentiful, and have been previously identified in this system.<sup>95,97,220</sup> Preliminary simulations were used to address the energy release by encountering a defect, Figure 6.15: the ERR was calculated for the scenario in

which a channel crack encounters a large 10-20  $\mu\text{m}$  symmetrical defect in the coating. As mentioned in Section 6.4, the ERRs were all very similar, indicating the relative insensitivity of ERR to crack propagation length on a micro-scale.

From these calculations, it can be determined that the energy released by following a 20  $\mu\text{m}$  defect (10  $\mu\text{m}$  putative crack) is roughly 10 times that for following a 2  $\mu\text{m}$  defect (1  $\mu\text{m}$  putative crack). This indicates that crack path selection is extremely sensitive to microstructure in these systems. However, without simulating *the exact microstructure observed*, the FEA results may only be used as a reference, not as a direct representation of the actual system. Also, it is stressed that the high energy release for following a defect of a particular size and angle does not necessarily suggest continued propagation along that path. The continued propagation will be dependent on the microstructure ahead of the advancing and energetic favorability of crack paths.

The higher energy release rates calculated for the high power EBC system than for the low power EBC system appear contradictory to the behavior observed. However, it is strongly emphasized that these simulations reflect the mechanical properties and physical dimensions given in Table 6.2. These properties have been inferred for these systems, and simulations have been performed on defect-free microstructures: considerable uncertainty exists in the correlation of simulated conditions and the actual fracture processes that occurred. The stresses used in FEA simulation are the thermal residual stresses developed for uncracked material, which again is not likely to accurately reflect the true stress states of the materials due to the severe microcracking observed, particularly in high power EBCs which experienced severe microfracture in the  $\text{Al}_6\text{Si}_2\text{O}_{13}$  layer<sup>97</sup>. Extensive simulations appear necessary to resolve this issue, and knowledge of the exact

mechanical properties of the coating layers (elastic moduli, stress states, toughnesses, interface toughnesses, defect structure and populations) will be necessary to accurately simulate behavior for any given coating system.

The ending crack trajectory running through the Si bond coat has also been assessed in low power EBCs. The terminal crack trajectory through the mid-plane of the Si bond coat appears to be energetically neutral when compared to delamination at other planes within the layer, Figure 6.17. However, when  $K_{II}$  effects of neighboring interfaces are considered the ultimate propagation path through the mid-plane of the Si layer appears to be mechanically favored. The cracking behavior between the initiation of bifurcation and the end bifurcated ligament trajectory (as well as the bifurcation depth itself) appears to be a mechanical phenomenon that depends heavily upon the local structure of the coating, Figure 6.8.

In low power EBCs, mud crack bifurcation resulted in a newly observed damage mechanism upon cycling, wherein coating spallation occurred by a combination of thermomechanical and environmental effects. This damage mechanism is schematically illustrated in Figure 6.18. After the stabilization annealing treatment, the CTE mismatch between the coating layers and the substrate resulted in a large tensile residual stress in the ytterbium monosilicate layer. A smaller tensile stress was also formed in the  $Al_6Si_2O_{13}$  layer, Table 6.2 and Figure 6.18(a). Such stresses resulted in the formation of mud cracks, which bifurcated in the  $Al_6Si_2O_{13}$  layer or at one of its interfaces. The result of the crack bifurcation was to redirect the crack path in such a way as to maximize strain energy release, which is consistent with coating mechanics predictions.<sup>248,256</sup>

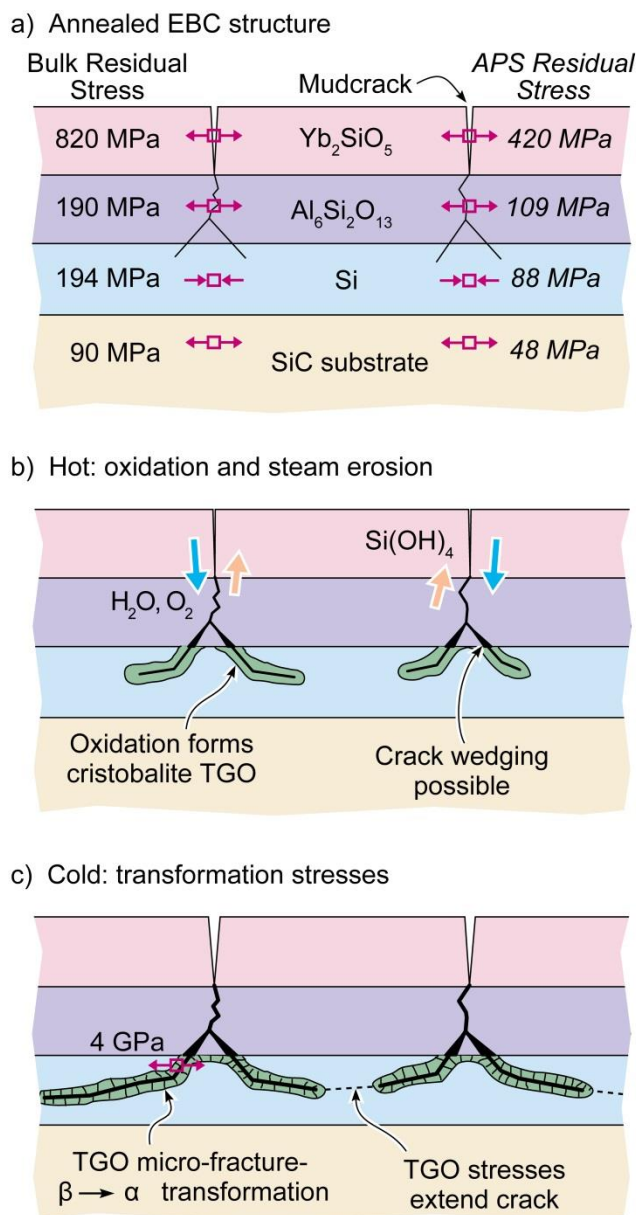


*Figure 6.18: Damage mechanisms contributing to failure of the tri-layer EBC. (a) Shows the stresses in the post annealed coating system. (b) Illustrates the damage mechanisms active during high temperature exposure and (c) shows the mechanical damage that develops during cooling of the sample.*

At 1316 °C the active damage mechanism in low power EBCs was environmental: though mud cracks were mechanically closed,  $\text{O}_2$  and  $\text{H}_2\text{O}$  permeated through the bifurcated mud crack network and began to oxidize the Si bond coat. The small scale

processes and mechanics of TGO growth upon Si in this system have already been examined in high power EBCs by Richards et. al.,<sup>95</sup> and the reaction products and growth of cristobalite are found to be similar in the present low power EBC system: a  $\beta$ -cristobalite TGO grew along the bifurcated crack ligaments, Figure 6.18(b). The volumetric increase upon oxidation may have provided a wedging mechanism that propped mud cracks open even at high temperature. Upon cooling, Figure 6.18(c), the CTE mismatch-derived residual stresses began to develop and the bifurcated mud cracks began to re-open. The thermally grown  $\beta$  cristobalite transformed to the  $\alpha$ -phase at  $\sim 220$  °C with a volume reduction of  $\sim 4.5$  %, <sup>95</sup> resulting in severe microcracking of the TGO in an orientation normal to that of the primary crack ligament (micro-mud cracking).

At the crack tip, the volumetric contraction had the effect of advancing the crack (at the minimum) through the oxide grown in front of the crack during the hot cycle. Repeated thermal cycling resulted in incremental growth of the delaminations through the mid-plane of the Si bond coat with eventual linkage between the bifurcated ligaments of neighboring mud cracks, as suggested by the dashed line in Figure 6.18(c). This linkage resulted in the spallation of a section of the EBC. The incremental growth and linkage of these delamination cracks is supported by the varying thickness of TGO across individual cracks (thinnest TGO near the crack tip and thickest near the crack root) and the presence of interlinked oxidized pores immediately ahead of the crack tip, Figure 6.11. These pores would have oxidized when the crack advanced either behind or in front of the cross-section imaged, allowing oxidizer access through the fractured TGO during the hot cycle. Unfortunately, the highly heterogeneous nature of the APS coatings studies prohibits analysis of this crack advance rate with current data.

## 6.6 Conclusions

Tri-layer  $\text{Yb}_2\text{SiO}_5/\text{Al}_6\text{Si}_2\text{O}_{13}/\text{Si}$  EBCs have been deposited onto  $\alpha$ -SiC substrates using a low power APS approach.<sup>220</sup> These coatings have been steam cycled to failure (defined as any observed spallation) in an atmospheric pressure, slowly flowing 90 %  $\text{H}_2\text{O}/10$  %  $\text{O}_2$  environment using 60 min hot (1316 °C) and 10 min cool (110 °C) cycles. The coating lifetime was controlled by interactions between mechanical damage resulting from thermal residual stresses and phase transformation with environmental damage and growth of oxide scales experienced during the hot cycle of testing. Specifically, it was found that:

- a) Mud crack bifurcation is a phenomenon that depends heavily upon defects within the coating. Mud cracks penetrating the upper layers of the low power EBC bifurcated upon encountering flaws as opposed to continuing to propagate in the form of a single mud crack. Exact determination of the conditions that lead to bifurcation within highly heterogeneous APS materials will require further simulation.
- b) The difference in mud crack structure (bifurcation) when compared to other coatings using comparable macrostructure and materials<sup>95</sup> led to the occurrence of an additional, as yet unreported failure mechanism wherein bifurcated cracks propagated through the mid-plane of the bond coat in the form of delamination cracks upon steam-cycling. This terminal crack trajectory has been determined to be mechanically favored.

- c) Oxidizers penetrated the bifurcated crack structure and oxidized the Si bond coat. A high density bond coat and improved coating layer adhesion resulted in a singular oxidizer access route through the bifurcated mud crack network. Cristobalite was again confirmed to be the primary oxidation product in this system.
- d) The mean steam-cycling lifetime of low power  $\text{Yb}_2\text{SiO}_5/\text{Al}_6\text{Si}_2\text{O}_{13}/\text{Si}$  EBCs and variance in steam-cycling lifetime did not differ considerably from those reported for high power EBCs of the same materials system but different macrostructure.<sup>95</sup>
- e) Altering the deposition process to achieve higher density and increased layer adherence did not circumvent the fundamental thermomechanical limitations of the  $\text{Yb}_2\text{SiO}_5/\text{Al}_6\text{Si}_2\text{O}_{13}/\text{Si}$  EBC system. The *intrinsically high strain energy release rates (ERRs) of this materials system* that result from mismatched CTEs were not overcome by attempts to inhibit oxidation by increasing coating layer density and interface adhesion.

Ultimate failure in the tri-layer  $\text{Yb}_2\text{SiO}_5/\text{Al}_6\text{Si}_2\text{O}_{13}/\text{Si}$  system was controlled by the high stored elastic strain energy in this system at low temperature, which resulted in the formation of gas diffusion pathways via mud cracking. The avoidance of coating structures that result in damage upon cooling from deposition (either in the form of mud cracking or bifurcated mud cracking) will be critical for improved durability. Elimination of such high diffusivity paths would most readily be achieved by some combination of closer CTE matching constraint and reduced elastic modulus, both of which lower the ERR of the system. Guided simulation of environmental and mechanical damage appears

to be a very promising avenue for establishment and examination of critical materials system design criteria for EBCs.

## **7 Ytterbium Disilicate-Silicon Coating Performance in Steam-cycling**<sup>6</sup>

**Synopsis:** Environmental barrier coatings (EBCs) must be used to protect SiC components exposed to high temperatures in water vapor and oxygen rich environments. An EBC system utilizing a silicon bond layer attached to the SiC and a dense ytterbium disilicate ( $\text{Yb}_2\text{Si}_2\text{O}_7$ ) topcoat has been proposed for this purpose. Both layers of the coating system have well matched coefficients of thermal expansion with the substrate, and the topcoat has been reported to have a relatively low susceptibility to erosion in water rich environments. An air plasma spray method has been used to deposit this bi-layer EBC on  $\alpha$ -SiC substrates and the coating system's thermo-cyclic behavior in a flowing 90 %  $\text{H}_2\text{O}$ /10 %  $\text{O}_2$  environment investigated. Using thermal cycles consisting of a 60 min hold at 1316 °C and 10 min at 110 °C, it has been found that a thermally grown (silica) oxide (TGO) is formed at the silicon-ytterbium disilicate interface. The TGOs thickness exhibits linear oxidation kinetics consistent with diffusion through the ytterbium silicate controlling the growth rate. Edge delamination of the coating system

---

<sup>6</sup> Based upon a technical article in preparation for *Advanced Materials*.<sup>257</sup>

was observed after 2,000 cycles consistent with steam erosion of the TGO directly exposed to the environment.

This research was performed at UVA with the assistance of Kelly Young, who was an outstanding undergraduate research assistant. Foucault de Francqueville, Stephen Sehr, and Matthew Begley (UCSB) also performed mechanical analyses of the system. Elizabeth Opila and Robert Golden (UVA) were a party to many helpful discussions regarding various environmental aspects of the work.

## 7.1 Introduction

At this stage in the dissertation, a brief recapitulation of EBC philosophy and findings of the previous chapters is necessary. For applications up to 1316 °C (2400 °F), research (including that performed in this dissertation) has focused on EBC systems consisting of a Si “bond coat” applied to the SiC, which is then covered by materials that impede the diffusion of oxygen and water vapor and that are highly resistant to steam volatilization.<sup>59,63,64,66,77-79,93-98</sup> The design objective for the bond coat is similar to that of the aluminum-rich metallic layer used in TBC systems: it provides a reservoir of metal to capture oxidizers before they can react with the underlying component. The objective of the upper EBC layers is then to reduce the Si layer’s outer surface exposure to oxidizers, while also itself being resistant to steam volatilization.<sup>77,78</sup>

These design objectives must be achieved without violating numerous constraints. For example, the various layers must have a coefficient of thermal expansion (CTE) similar to SiC to avoid cracking or delamination during heating and cooling over the wide

temperature range experienced during gas turbine engine operation, as demonstrated in Chapters 2, 3, 5 and 6. The EBC materials must also be thermochemically compatible so that deleterious reaction products are not formed between them. In addition, they must meet the other demands of the engine environment which include resistance to foreign object damage (FOD)<sup>18,21,22</sup> and reactions with molten calcium-magnesium-aluminum-silicates<sup>16-18,61,62</sup> (CMAS).

The ytterbium monosilicate ( $\text{Yb}_2\text{SiO}_5$ )/mullite ( $\text{Al}_6\text{Si}_2\text{O}_{13}$ )/Si tri-layer system has received significant attention in this dissertation due to the reported thermochemical compatibility between its component materials and the very low steam volatility of  $\text{Yb}_2\text{SiO}_5$  (YbMS).<sup>196</sup> However, the high CTE results in the development of a high (biaxial) tension and significant stored elastic strain energy in the YbMS layer during cooling. This was relieved by various forms of macrofracture including pure mud cracking and bifurcated cracking, as described in Chapters 2, 3, 5, and 6.<sup>95-97</sup> The presence of cracks through the YbMS layer then provides oxidizing species a short circuit to the Si bond coat, resulting in rapid growth of a cristobalite ( $\text{SiO}_2$ ) phase on the outer silicon surface. The thermally grown oxide (TGO) experiences a large reduction in volume (~4.5 %) during its cubic to tetragonal (inversion type)  $\beta \rightarrow \alpha$  phase transformation upon cooling through ~220 °C, which causes severe microcracking, loss of oxidation protection and premature spallation of the EBC (Chapters 3 and 6). These behaviors indicate that high CTE topcoat candidates such as YbMS, other rare earth silicates with high CTE and aluminum-silicates such as mullite are undesirable materials for environmental barrier (diffusion impeding) applications.

Ytterbium disilicate (YbDS), a line compound in the  $\text{Yb}_2\text{O}_3\text{-SiO}_2$  binary phase diagram<sup>81</sup> with composition  $\text{Yb}_2\text{Si}_2\text{O}_7$ , is a promising alternate material for the environmental barrier layer application since it has a CTE much more closely matched to that of SiC ( $4.1 \times 10^{-6} \text{ }^\circ\text{C}^{-1}$  for  $\text{Yb}_2\text{Si}_2\text{O}_7$ <sup>220</sup> versus  $4.7 \times 10^{-6} \text{ }^\circ\text{C}^{-1}$  for SiC, see Chapter 5). YbDS therefore satisfies one of the primary design constraints for EBC applications. However, its resistance to volatilization by reactions with water vapor is less than that of its monosilicate counterpart.<sup>196</sup> Indeed, YbDS surfaces exposed to high velocity, high temperature steam have been observed to volatilize silica leaving a YbMS surface layer.<sup>258</sup> The oxygen and water vapor diffusivities of YbDS at the relevant temperatures have not been characterized, and its thermochemical stability in contact with Si has not been reported.

Chapter 5 has already optimized the process of applying YbDS coatings to Si bond coat protected SiC substrates.<sup>220</sup> The primary goal of the present chapter is therefore to investigate the evolution of an APS deposited YbDS/Si coating system on a SiC substrate as it is subjected to thermal cycling between  $110 \text{ }^\circ\text{C}$  and  $1316 \text{ }^\circ\text{C}$  in a slowly flowing steam/oxygen environment. The study characterizes the growth of the TGO layer on the silicon bond coat, investigates the process by which the topcoat is partially volatilized during cycling, and explores the mechanism by which coating failure is most likely to occur during thermal cycling in water vapor rich environments.

## 7.2 Experimental

### 7.2.1 Coating Deposition

Bi-layer YbDS/Si coatings were deposited onto surface roughened 25.4 mm x 12.7 mm x 4.8 mm thick  $\alpha$ -SiC Hexoloy™ substrates (Saint Gobain Ceramics, Niagara Falls, NY), Figure 7.1. The substrate edges were ground forming a 45 ° chamfer to facilitate over-coating the edges of the sample where delamination most often initiates.<sup>95</sup> The target thickness of the silicon layer was 50  $\mu$ m while that of YbDS layer was 125  $\mu$ m. The plasma spray deposition parameters used for each layer are summarized in Table 7.1. The structure of as deposited and stabilization annealed YbDS layers deposited using this spray parameter condition has been recently reported by Richards et al.<sup>220</sup> The spray conditions were chosen to ensure deposition of low void content coatings while limiting the loss of SiO from the liquid droplets during transit through the plasma plume. This SiO loss is a result of its higher vapor pressure (compared to ytterbium species) at the droplet temperatures encountered in plasma spray deposition. It results in the formation of a two phase YbDS + YbMS coating observable by a difference in gray scale contrast when imaged in the scanning electron microscope using backscattered electrons (BSE mode imaging), Figure 7.2(a). In the coatings studied here, the YbMS volume fraction was ~15 %, and can be seen in Figure 7.2(a) as elongated regions of lighter contrast oriented in the plane of the coating. YbMS precipitates can also be seen in the YbDS topcoat, Figure 7.2(b), consistent with prior studies of this system.<sup>220</sup> Though the topcoat is a mixture of YbDS and YbMS, it will be referenced as the “YbDS layer” for convenience.

The APS powders used for deposition were the same as those used in prior EBC research,<sup>220</sup> and consisted of a specially produced stoichiometric YbDS powder

(Treibacher Industrie Inc., Toronto, ON) and APS grade SL-111 Si powder (Micron Metals, Bergenfield, NJ). The YbDS powder size distribution was the same as that previously reported<sup>220</sup> and varied between 20 and 50  $\mu\text{m}$ . The Si powder was sieved before use to remove fine and coarse particles so that its powder diameter ranged between 70 and 110  $\mu\text{m}$ . The spray parameters for Si deposition were adjusted to result in a low porosity Si bond coat similar to that previously reported,<sup>96,220</sup> Table 7.1. Its rough surface, Figure 7.2(a) and (b) was intended to improve the adhesion between the two coatings.

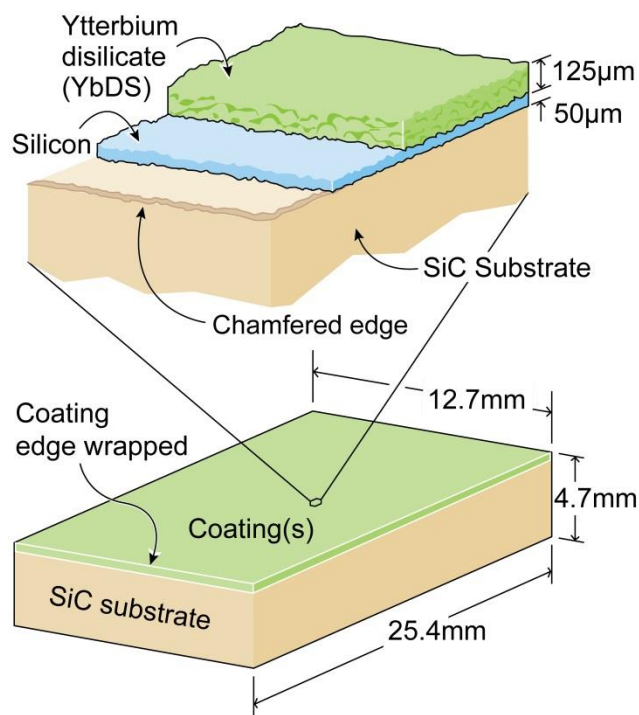


Figure 7.1: Schematic illustration of a bi-layer  $\text{Yb}_2\text{Si}_2\text{O}_7/\text{Si}$  (YbDS/Si) coated  $\alpha$ -SiC substrate.

Both the Si and YbDS layers were deposited onto substrates placed in a box furnace held at a temperature of 1200  $^\circ\text{C}$ . To reduce oxidation of the SiC and Si bond coat surfaces during deposition, an Ar/H<sub>2</sub> reducing gas mixture was continuously flowed the

furnace at a rate of 20 slm. After deposition of the Si layer, the reducing gas flow was terminated and the YbDS layer was deposited into the furnace. The coated samples were finally stabilization annealed at a temperature of 1300 °C in air for 20 hours.<sup>59,77-79,93,95-</sup>

<sup>97,220</sup> This process has previously been determined to result in excellent adhesion of interfaces in EBC systems.<sup>220</sup>

*Table 7.1: Deposition parameters for air plasma sprayed YbDS/Si layers.*

APS Layer	Torch Power (kW)	Arc Current (A)	Primary Ar (slm)	Secondary H <sub>2</sub> (slm)	Powder feed (g/min)	Carrier Ar (slm)
Yb <sub>2</sub> Si <sub>2</sub> O <sub>7</sub>	11.2	275	84.95	0.94	41.5/lower	5.90
Si	22.7	500	77.87	0.94	31.0/upper	5.90

### 7.2.2 Steam-cycling

Coated substrates were thermally cycled in a steam-cycling furnace using a 60 min hot (1316 °C) and a 10 min cold (110 °C) cycle at atmospheric pressure with a 90 % H<sub>2</sub>O/10 % O<sub>2</sub> environment flowing through the hot section of the furnace at flow speed of 44 mm/s (a volumetric flow of 4.1slm). The environment local to these substrates during steam-cycling is shown in Figure 7.3. For the testing configuration used here, 4 samples were initially cycled simultaneously, with one being removed after 250, 500, 750 and 1,000 cycles. This was followed by the testing of a single sample for 2,000 cycles (1,500 cycles individually). The flow conditions were similar to those previously used for steam-cycling studies,<sup>95</sup> and approximate the H<sub>2</sub>O partial pressure during lean hydrocarbon combustion at a pressure of 10 atm. Saturation of Si-bearing vapors (Si(OH)<sub>4</sub> species) can occur in this furnace due to the low velocity and large number of samples simultaneously tested. Its primary purpose was to investigate the thermo-cyclic

damage mechanisms. During steam-cycling, all the samples were therefore examined optically every 100 cycles to assess damage visually.

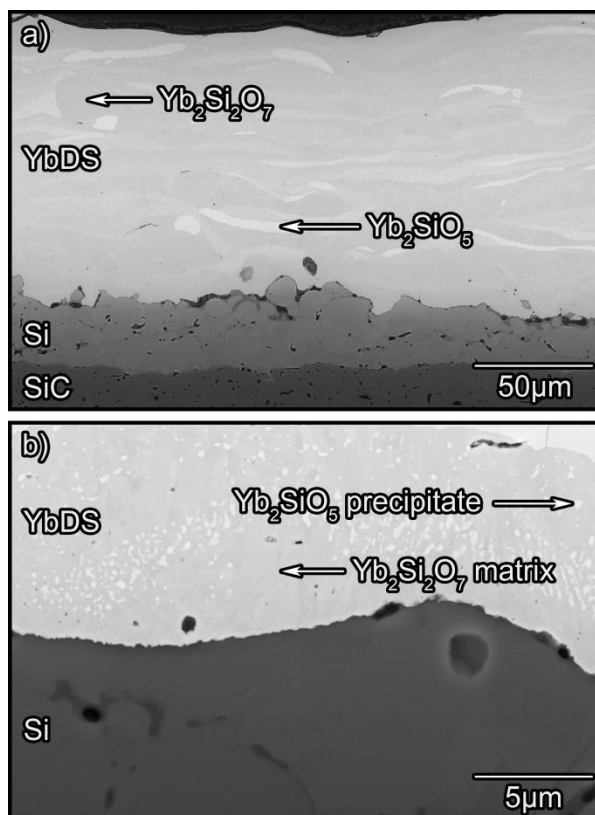
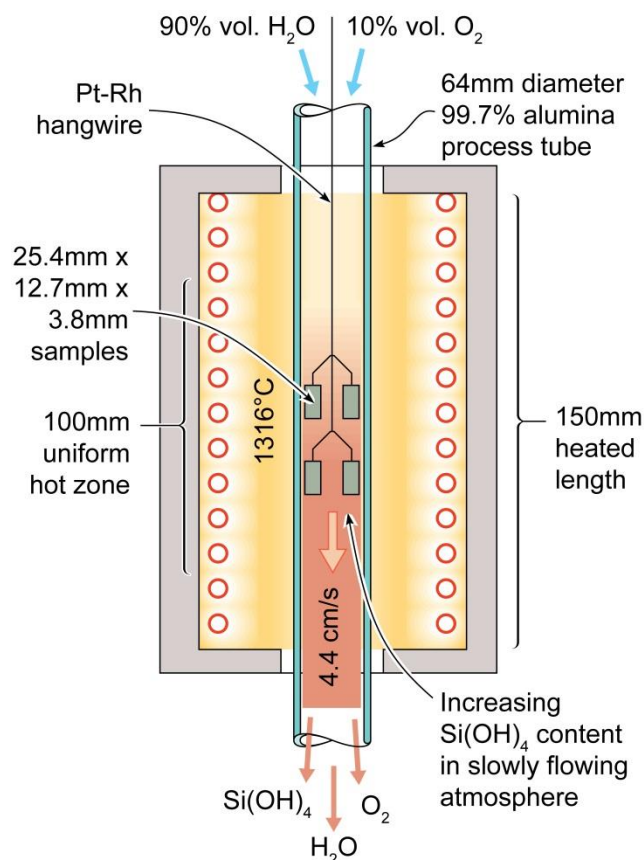


Figure 7.2: BSE images of an annealed YbDS/Si bi-layer coating deposited onto  $\alpha$ -SiC. (a) Low magnification image showing two phases in the YbDS topcoat. (b) High magnification view of the YbDS – Si interface showing interface structure and small  $\text{Yb}_2\text{SiO}_5$  (YbMS) precipitates in the YbDS topcoat.

### 7.2.3 Coating Characterization

X-ray diffraction (XRD) measurements of the YbDS topcoat (X'Pert Pro MPD, PANalytical, Westborough, MA) were performed on some samples. Samples were then sectioned, polished, and examined with a Quanta 650 field emission scanning electron microscope (FEI, Hillsboro, OR) operating in the back-scattered electron (BSE) mode. All images were collected under low-vacuum conditions. A gamma correction was

applied to the images to enhance relative contrast between high and low-Z materials.<sup>95,220</sup> Energy dispersive spectroscopy (EDS) was used for elemental microanalysis (X-Max<sup>N</sup> SDD, Oxford Instruments, Concord, MA). EDS spectra were captured using a 10 kV accelerating voltage and small spot size to minimize fluorescence interactions.<sup>220</sup>



*Figure 7.3: Schematic illustration of the testing configuration and environment local to the samples during the 1316°C hot cycle of steam-cycling.*

Layer thicknesses were calculated by averaging measurements from 50 different equally spaced areas across the coating cross-section. The thickness of oxide scales was measured in several hundred evenly spaced locations across the coating cross-section and averaged. Standard deviations of thickness for the oxide scale were less than 100 nm.

Raman Spectroscopy using an inVia microscope (Renishaw, Hoffman Estates, IL) was used to identify the TGO phase.<sup>18,19</sup> Raman analyses were performed using a 50x lens with a numerical aperture of 0.5. An argon laser (488 nm) was used as the light source. Approximately 99 % of the Gaussian distributed incident light of the source resided within a 1  $\mu\text{m}$  diameter circle on the sample, yielding a spatial resolution for this technique of  $\sim 1 \mu\text{m}$ .

#### ***7.2.4 Energy Release Rates and Residual Stresses***

Thermomechanical analyses of coating stresses and strain energy release rates (ERR) for debonding of the elastic coating system were calculated using the LayerSlayer<sup>199</sup> software package. All ERR calculations assume that coating layers remained elastic during cooling and ignored stress relief by mechanisms such as cracking or creep. The ERR analysis was similar to those previously conducted on tri-layer EBC systems.<sup>95,96</sup> The thermophysical properties and the small residual stresses calculated for this elastic coating – substrate bi-layer after cooling from the stabilization (stress free) annealing temperature of 1300 °C (before TGO growth had commenced) are listed in Table 7.2.

### **7.3 Results**

Six low porosity YbDS on Si bi-layer coatings were deposited on SiC substrates using the APS approach. The average thickness of the YbDS layer in the cross-section examined for each sample is reported in Table 7.3. Slight variations in thickness of the YbDS layer were observed in between individual coatings and over the cross-section

within the same coating. In general, the maximum and minimum thicknesses varied within  $\pm 10 \mu\text{m}$  of the reported average. These variations are typical of the stochastic APS process.<sup>220</sup> One of the samples was used to characterize the coating composition and structure while the remaining samples were steam cycled between 110 °C and 1316 °C with a hold time of 60 min at the maximum temperature. One of the samples was removed from the steam-cycling furnace after 250, 500, 750, 1,000, and 2,000 steam-cycles. The last (2,000 cycle) sample resided for 1,500 steam cycles alone in the steam furnace.

Table 7.2: Thermophysical properties of EBC system components.

Material	CTE ( $\times 10^6$ °C <sup>-1</sup> )	Young's Modulus (GPa)	Poisson Ratio $\nu$	Thermal Stress (MPa) <sup>a</sup>	Low Power Layer Thickness	Application
YbDS $E_{APS}$ <sup>b</sup>	4.1 <sup>220</sup>	180 <sup>220</sup> 86	0.27 <sup>c</sup>	-170 -88	125 $\mu\text{m}$	Topcoat
Cristobalite- $\alpha$ Cristobalite- $\beta$	30 <sup>d</sup> 3.1 <sup>200</sup>	65 <sup>201</sup> 70 <sup>c</sup>	-0.164 <sup>202</sup> -0.042 <sup>203</sup>	>4,350	0-5 $\mu\text{m}$	Oxidation product
Si $E_{APS}$	4.1 <sup>88</sup>	163 <sup>88</sup> 70 <sup>209</sup>	0.223 <sup>88</sup>	-145 -65	50 $\mu\text{m}$	Bondcoat
SiC ( $\alpha$ )	4.67	430	0.14	24 12	4.8mm	Substrate

<sup>a</sup>Calculated at 20°C after cooling from stress free condition at 1300°C with LayerSlayer.

<sup>b</sup>Assumed 50% reduction in elastic modulus for APS material/cracking.

<sup>c</sup>Based on  $\text{Y}_2\text{Si}_2\text{O}_7$ .<sup>204</sup>

<sup>d</sup>Average of values reported on the 20-200°C interval.<sup>201,205</sup>

<sup>e</sup>Based on Young's modulus ratio of  $\alpha$  and  $\beta$  quartz<sup>206</sup> and  $\alpha$  cristobalite.

While edge damage was evident upon optical inspection, Figure 7.4, the damage did not appear to have affected the sample center even after 2,000 cycles, and none of the coatings had spalled in locations other than the coating edges. Figure 7.5 shows BSE mode SEM images of the as-deposited and annealed coating cross sections and a

selection of those that had been steam cycled. Minimal changes in layer thicknesses and coating structure were apparent in these low magnification images at the coating center. Examination of these images indicated the gradual (and very minor) formation of a new phase at the YbDS – Si interface, Figure 7.5, and the appearance of a layer of porous and microcracked material at the outer surface of the YbDS layer in the sample removed from the furnace after 2,000 steam cycles, Figure 7.5(f).

*Table 7.3: YbDS layer thicknesses of samples. Thicknesses range is  $\pm 10\mu\text{m}$ .*

Coating Condition	As-Deposited	Annealed	250 Cycles	500 Cycles	750 Cycles	1,000 Cycles	2,000 Cycles
Thickness ( $\mu\text{m}$ )	125	135	125	155	130	135	125

### **7.3.1 Thermally Grown Oxide (TGO)**

When examined by SEM in the BSE imaging mode at high magnification, all of the steam cycled coatings were found to have a darker grey phase present at the YbDS – Si interface, Figure 7.6. This dark grey phase was observed to be dense and of consistent thickness for each sample. EDS analysis of the layer revealed that it contained only Si and O. There are 11 crystalline polymorphs of silica and two others non-crystalline phases;<sup>259</sup> to identify the phase formed here a Raman analysis of the layer was performed. The only spectral peaks present not belonging to Si had wavenumbers of  $230\text{ cm}^{-1}$  and  $416\text{ cm}^{-1}$ , indicating the layer to be  $\alpha$ -cristobalite with  $\text{SiO}_2$  stoichiometry.<sup>212-214</sup> This  $\alpha$ -cristobalite had presumably formed as  $\beta$ -cristobalite at  $1316\text{ }^\circ\text{C}$  and transformed on cooling through  $220\text{ }^\circ\text{C}$  to the  $\alpha$  phase. Cristobalite has previously been identified as the TGO phase formed upon a Si bond coat during thermal cycling at this temperature<sup>95,96</sup>

and on SiC oxidized at comparable temperature,<sup>51,235</sup> even though it is not the equilibrium phase at this temperature. The  $\text{Yb}_2\text{O}_3 - \text{SiO}_2$  phase diagram relevant to this EBC system has only four stoichiometric phases at temperatures up to the YbDS melting point (1650 °C): YbDS, YbMS, and the two terminal oxides.<sup>81</sup> This indicates that there is no mixing of  $\text{Yb}_2\text{Si}_2\text{O}_7$  and  $\text{SiO}_2$  at temperatures up to ~1650 °C, and it is therefore concluded that the  $\text{Yb}_2\text{Si}_2\text{O}_7 - \text{SiO}_2$  interface is thermochemically stable.<sup>260</sup>

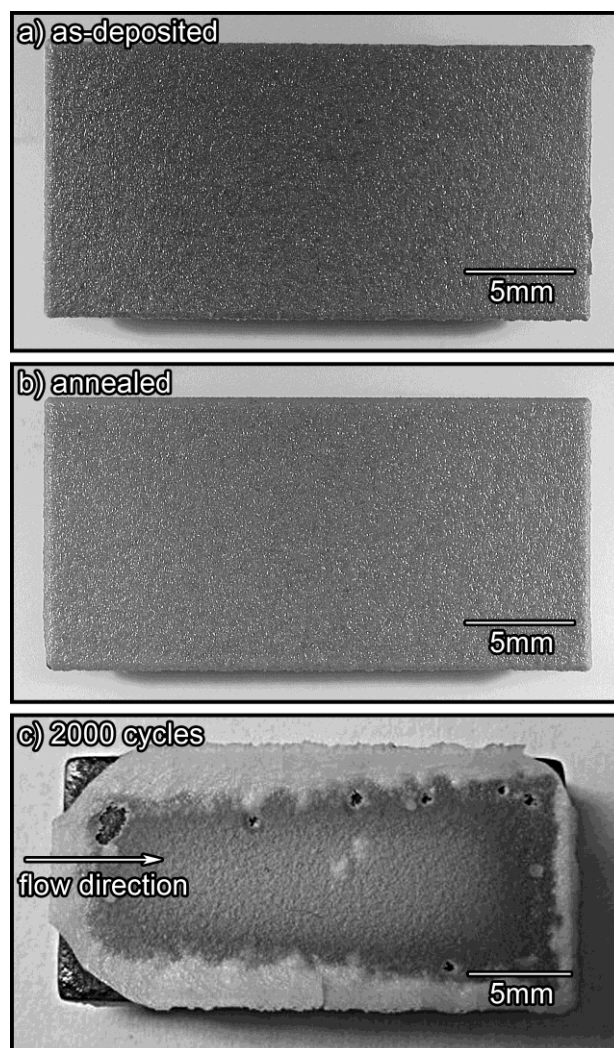


*Figure 7.4: Optical images of YbDS/Si coated SiC substrates. (a) As-deposited, (b) annealed, and (c) after 2,000 steam cycles at 1316°C with the gas flow direction indicated.*

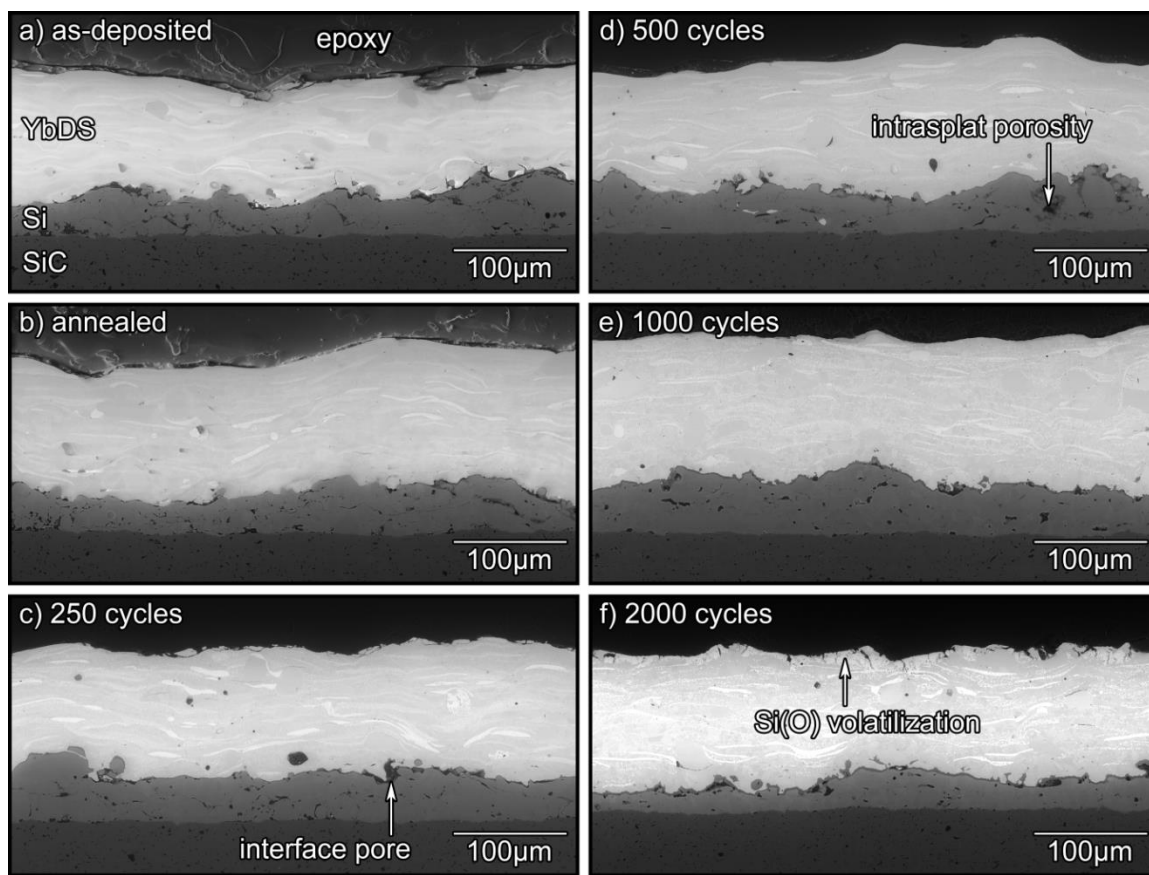


Figure 7.5: BSE mode SEM micrographs of YbDS/Si coated system before and after steam-cycling. (a) As-deposited, (b) annealed, (c) after 250 steam cycles, (d) 500 cycles, (e) 1,000 cycles, and (f) 2,000 cycles.

Examination of Figure 7.6 indicates that the thickness of the thermally grown oxide (TGO) increased with high temperature exposure time, reaching a thickness of a few micrometers after 2,000 steam cycles. The TGO was dense and adherent in all samples. The average measured thickness of the TGO for the steam-cycled samples has been plotted as a function of hot cycle exposure time in Figure 7.7(a). The measured change in oxide thickness with accumulated time,  $h'(t)$  at 1316 °C could be well fitted to a linear relation:  $h'(t) = h_0 + k_l t$  where the linear rate constant  $k_l = 1.18$  nm/h and  $h_0 = 139$  nm.

This  $h_o$  value agrees with observations of annealed coatings that had a TGO thickness (before steam-cycling) of 100-200 nm.

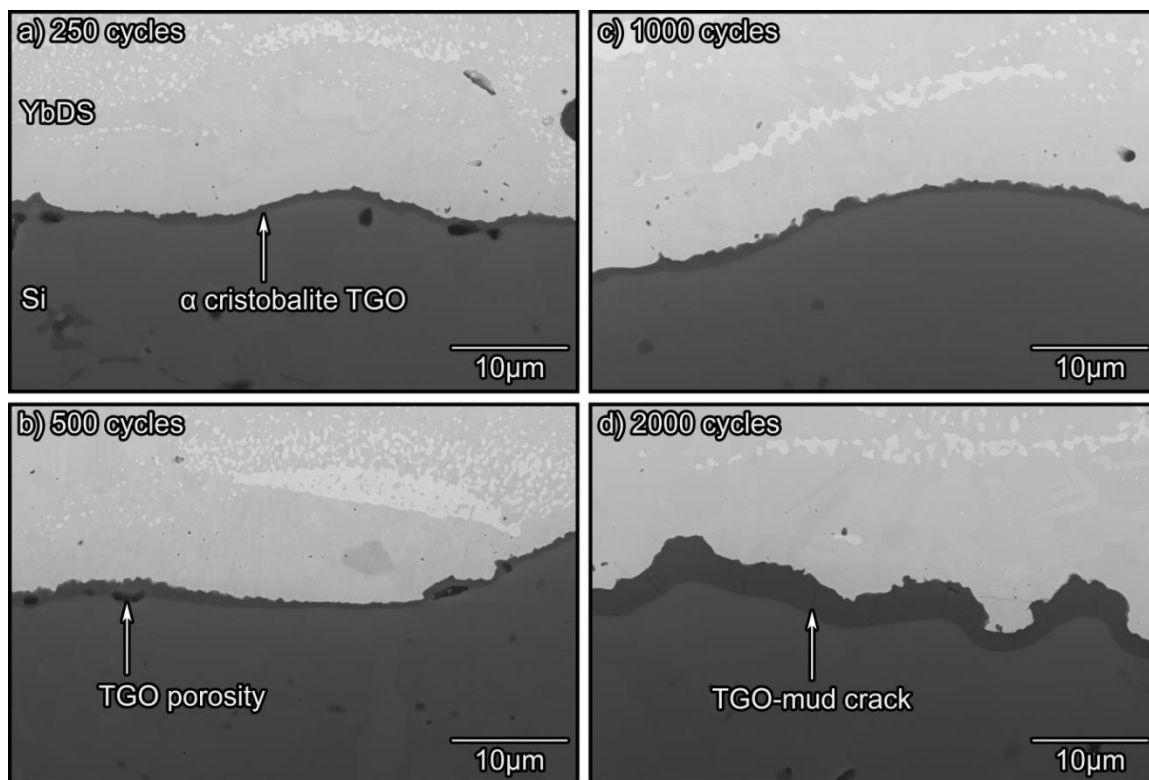


Figure 7.6: BSE micrographs of the YbDS – Si interface after steam-cycling showing the development of a thermally grown oxide (TGO). (a) After 250, (b) 500, (c) 1,000, and (d) 2,000 cycles at 1316°C with 90% $H_2O$ /10% $O_2$  flowing at 44mm/s.

Careful examination of the TGO layer of the sample exposed to 2,000 steam cycles, Figure 7.6(d) and Figure 7.8(a), showed that it contained closely spaced vertical cracks that fully penetrated the oxide layer. Some of these cracked segments had additionally delaminated from the underlying Si layer. Vertical cracking of the TGO was also observed in the sample exposed to 1,000 steam cycles, Figure 7.8(b), but to a much lesser extent than the 2,000 cycle sample. This appeared to be a form of mud cracking, and was

only observed in the samples exposed to 1,000 or 2,000 steam-cycles. The opening dimension of these cracks was measured to be in the range of 3-10 nm.

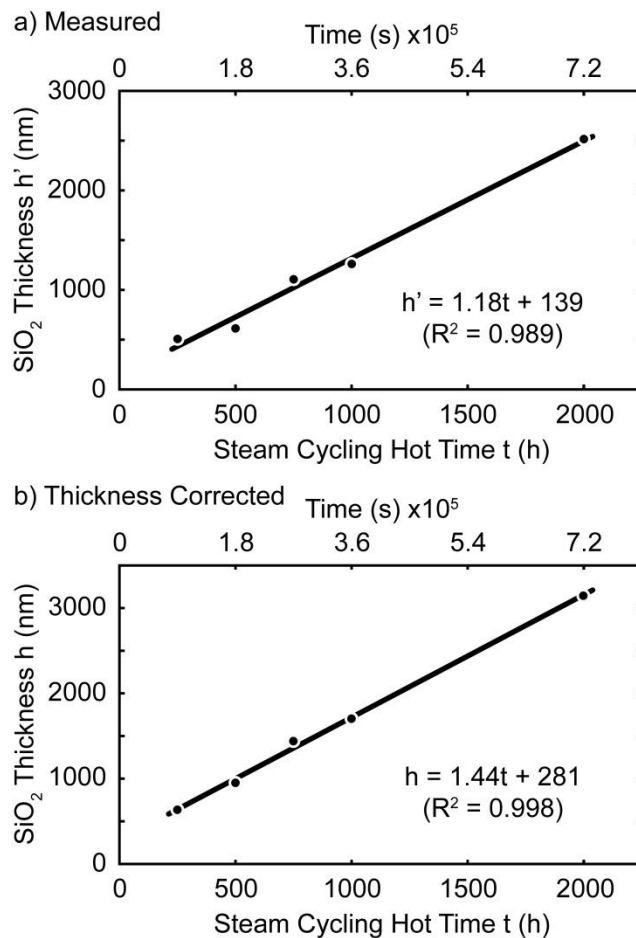


Figure 7.7: Plots of SiO<sub>2</sub> TGO thickness as a function of accumulated exposure time at 1316°C for a bi-layer EBC. (a) Average thicknesses measured from multiple samples with varying YbDS layer thickness. (b) Average thicknesses normalized for thermally grown silica beneath a 100µm thick YbDS layer.

### 7.3.2 YbDS Volatilization

The 2,000 steam-cycle topcoat was the only topcoat observed to have suffered significant surface reaction with the steam environment, Figure 7.5(f). It was tested individually in the steam-cycling furnace for 1,500 cycles, whereas the other four

samples were all tested together. Because the steam environment flow speed was low and the area of (uncoated) SiC exposed to the environment was large when 4 samples were present (at least 2,800 mm<sup>2</sup>), a significant Si(OH)<sub>4</sub> concentration is expected from the reaction between the SiO<sub>2</sub> scale grown on the exposed SiC. The recession rate of SiO<sub>2</sub> was calculated for the conditions used here by the method of Golden and Opila,<sup>257</sup> and found to be 44.65 nm/h.

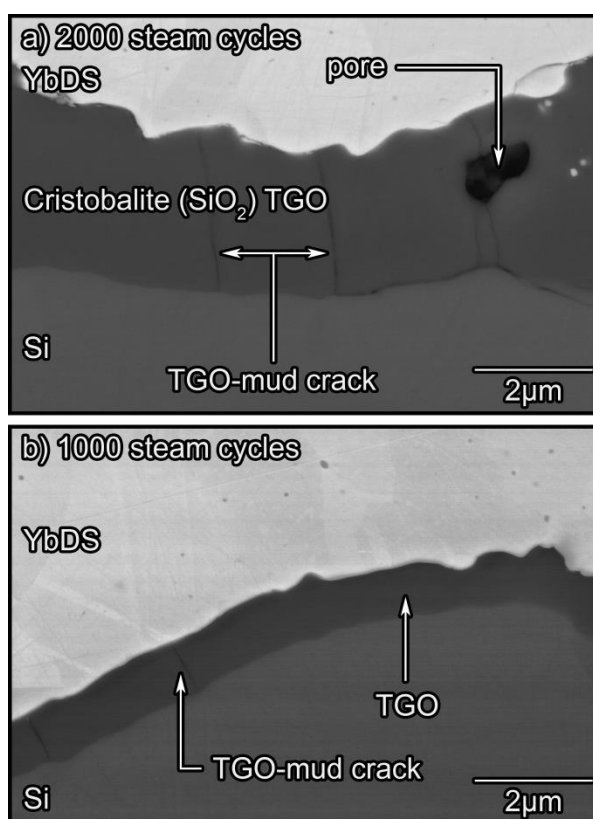


Figure 7.8: BSE micrograph of the thermally grown cristobalite (SiO<sub>2</sub>) oxide at the YbDS – Si interface during steam-cycling. (a) TGO at the YbDS – Si interface after 2,000 steam cycles, (b) after 1,000 steam cycles.

Assuming the surface area of SiO<sub>2</sub> to be 700 mm<sup>2</sup> per sample, 1.35 x 10<sup>-9</sup> moles of Si(OH)<sub>4</sub> were therefore formed every second while four samples were in the furnace.

However, only  $3.38 \times 10^{-10}$  moles of  $\text{Si(OH)}_4$  would be formed every second with one sample in the furnace. The equilibrium partial pressure of  $\text{Si(OH)}_4$ , using experimental thermochemical data for the similar Y-Si-O system,<sup>181</sup> was found to be  $4.97 \times 10^{-6}$ . Since the gas flow rate through the steam-cycling furnace was 4.1 slm, the  $\text{Si(OH)}_4$  concentration was 40 % of the saturation limit with four samples in the furnace but only 10 % of the saturation limit with 1 sample in the furnace. When the 2,000 cycle sample was tested individually, the exposed surface area of SiC was small enough to avoid  $\text{Si(OH)}_4$  saturation, and surface volatilization of the YbDS layer was observed.

The environmentally attacked YbDS layer was 5-15  $\mu\text{m}$  thick, Figure 7.5(f). Using handbook X-ray Mass Attenuation Coefficients,<sup>234</sup> the maximum depth of penetration of 45 kV X-rays was calculated to be  $\sim 75 \mu\text{m}$  for YbDS and  $\sim 56 \mu\text{m}$  for YbMS, with the majority of the diffracted signal in an XRD experiment coming from a region within 20  $\mu\text{m}$  of the surface. Therefore, XRD is a suitable technique for a phase analysis of the surface volatilized region. Figure 7.9 shows an XRD pattern of the surface of the sample subjected to 2,000 cycles and compares it to that of a sample after only the annealing treatment. All indexed peaks could be attributed to one of three phases, which have all previously been observed in this system.<sup>220</sup> The XRD patterns indicate significant volume fractions of the I2/a structure YbMS and C2/m YbDS were present after cycling. Only a trace amount of the metastable P21/c YbMS phase was identified. The significantly higher ratio of YbMS to YbDS reflection peaks in the diffraction pattern of the 2,000 cycle sample indicates a considerably elevated fraction of YbMS at the sample surface, compared to the starting material which consisted of 85 vol% YbDS and 15 vol% YbMS.

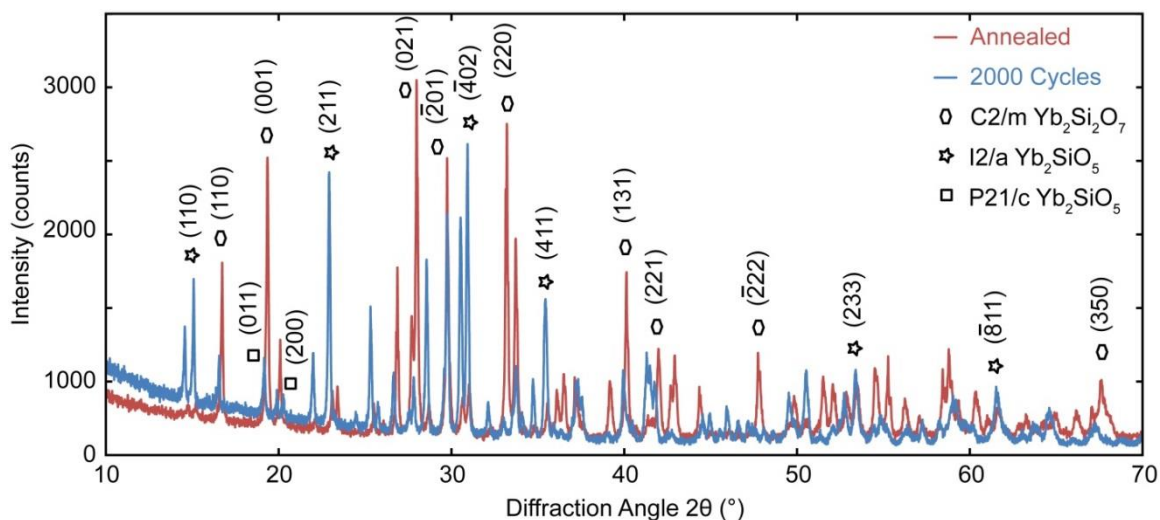


Figure 7.9: X-ray diffraction patterns of the annealed and 2,000 steam-cycle sample surfaces. All peaks of the patterns have been indexed using equilibrium YbDS (C2/m) and equilibrium I2/a and metastable P21/c YbMS peaks. The slightly raised background of the 2,000 cycle pattern results from a very thin layer of epoxy on the surface that was used to prevent spallation during handling.

Figure 7.10(a) shows a higher magnification BSE image of the surface volatilized region with Yb and Si EDS dot maps presented in Figure 7.10(b) and (c). These dot maps indicate increased Yb and reduced Si content in the surface volatilized layer when compared to the unaffected material below. Based upon the crystallographic identification of only YbMS and YbDS by XRD and the differences in Yb and Si content indicated by EDS, this surface volatilized layer was identified as predominantly YbMS. YbMS has previously been observed on the surface of YbDS samples exposed to a steam jet, and was attributed to volatilization of  $\text{SiO}_2$ .<sup>258</sup> Figure 7.11 shows three higher magnification BSE mode SEM images of the 2,000 cycle sample surface. They indicate that the surface layer had also become porous. The pores had roughly circular cross sections but were long in length and appeared interconnected with the surface of the coating. The porosity of this surface layer and reduced  $\text{SiO}_2$  content when compared to

the deposited topcoat are consistent with loss of  $\text{SiO}_2$  from the YbDS layer during steam-cycling. On the other hand, the YbMS that was then formed exhibited greater resistance to volatilization,<sup>78,258</sup> indicating that the YbDS topcoat can provide better than anticipated environmental protection under these conditions.

The origin of the porosity in the environmentally affected surface layer is consistent with  $\text{SiO}_2$  loss from the YbDS layer by formation gaseous  $\text{Si}(\text{OH})_4$  leaving behind a region of YbMS. If Yb is assumed to exhibit no volatility, the resulting volume reduction during conversion of YbDS to YbMS is 26 %. Since the coating is laterally constrained, this volume reduction results in a hydrostatic tension that may have been partially relaxed by forming pores. The initial stage of this creep-enabled pore formation mechanism is schematically illustrated in Figure 7.12(a). As exposure continues, the pores resulting from  $\text{SiO}_2$  volatilization grow into the coating extending the open porous structure. Volatilization then occurs by a gas path diffusional route with simultaneous transport of oxidizer into and  $\text{Si}(\text{OH})_4$  out of the coating. The close spacing of the tunneling pores is such that little solid state diffusion of  $\text{SiO}_2$  is required to convert the YbDS to YbMS, Figure 7.12(b).

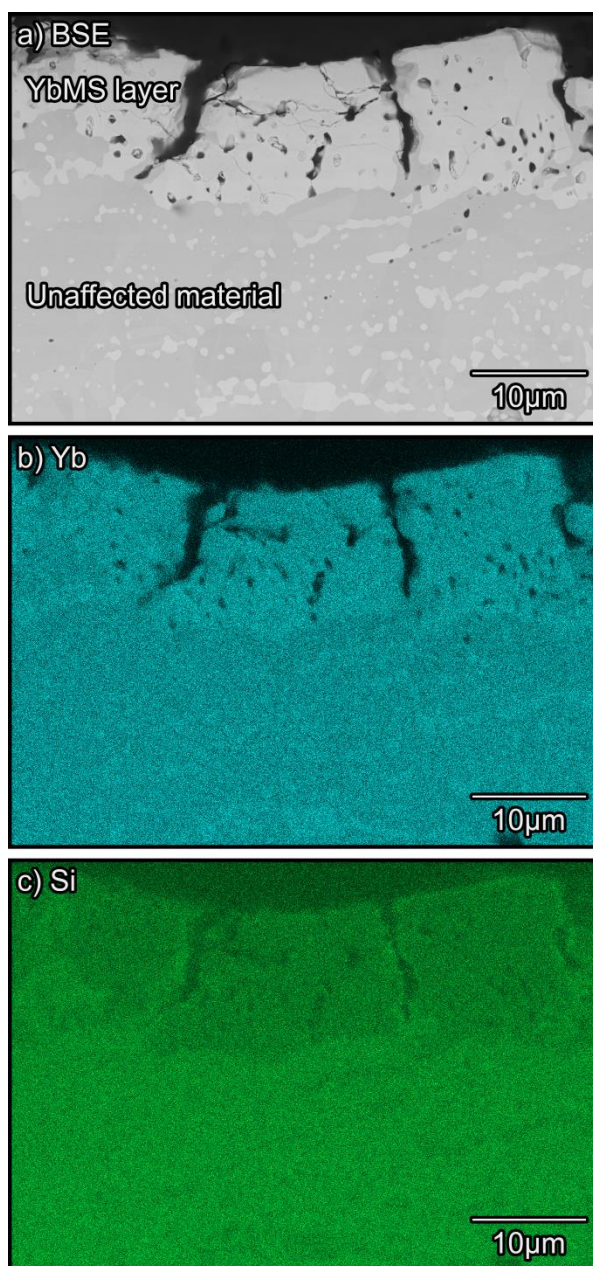


Figure 7.10: (a) BSE micrograph of a surface volatilized region of the topcoat. Dot map of (b) Yb and (c) Si from EDS analysis.

Several forms of mechanical damage were observed in the sample surface exposed to 2,000 hours of flowing steam and oxygen at 1316 °C, Figure 7.11. Some areas experienced vertical cracking of the adherent, but porous YbMS surface layer, Figure

7.11(a). In other areas, Figure 7.11(b), delamination cracks had resulted in spalling of the compositionally modified surface region. In yet other areas, propagation of a delamination crack through the underlying unaffected YbDS resulted in partial spallation, Figure 7.11(c). The damage appeared to result from residual stresses that arise upon cooling from steam-cycling due to the CTE mismatch between YbMS ( $7.5 \times 10^{-6} \text{ }^\circ\text{C}^{-1}$ ) and the YbDS or substrate ( $4.1 \times 10^{-6} \text{ }^\circ\text{C}^{-1}$  and  $4.67 \times 10^{-6} \text{ }^\circ\text{C}^{-1}$ , respectively), which are in the range of 400-900 MPa depending upon the elastic moduli assumed for the layers.<sup>96</sup>

### **7.3.3 Edge Delamination**

The edges of the coatings were observed to undergo delamination which increased in severity with the number of steam cycles, Figure 7.13. It was manifested as lifting-off of the coating edge. This edge delamination occurred despite attempts to extend the coating over the sides of the substrate during deposition by chamfering the corners, Figure 7.13(a). The progression of the edge failure mode with number of cycles can be seen in Figure 7.13(a) through (d). It began with the oxidation of the thin Si bond coat at the side of the substrates forming the darker gray TGO phase seen with BSE imaging. EDS and Raman analyses of this dark gray phase indicate it to be  $\alpha$ -cristobalite ( $\text{SiO}_2$ ). This  $\text{SiO}_2$  layer underwent rapid volatilization and mechanical spallation at the coating edge, rapidly consuming the Si bond coat, and allowed the YbDS layer to bend away from the substrate surface. The distance of both TGO growth and delamination from the edge of the coating increased with accumulation of steam cycles.

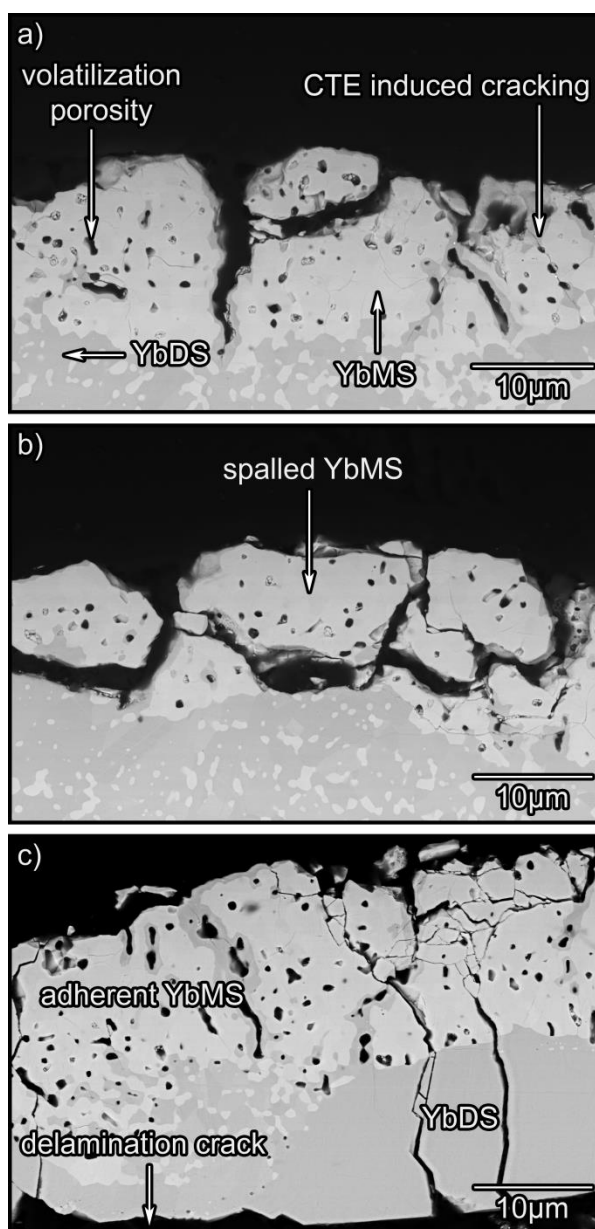


Figure 7.11: BSE cross-section micrographs showing SiO<sub>2</sub> volatilization from the YbDS surface after 2,000 steam cycles at 1316°C. (a) Adherent area of YbMS with porosity and microcracking. (b) Spalled region of surface volatilized layer. (c) Delaminated region of coating containing steam-reduced YbMS and region of unaffected YbDS.

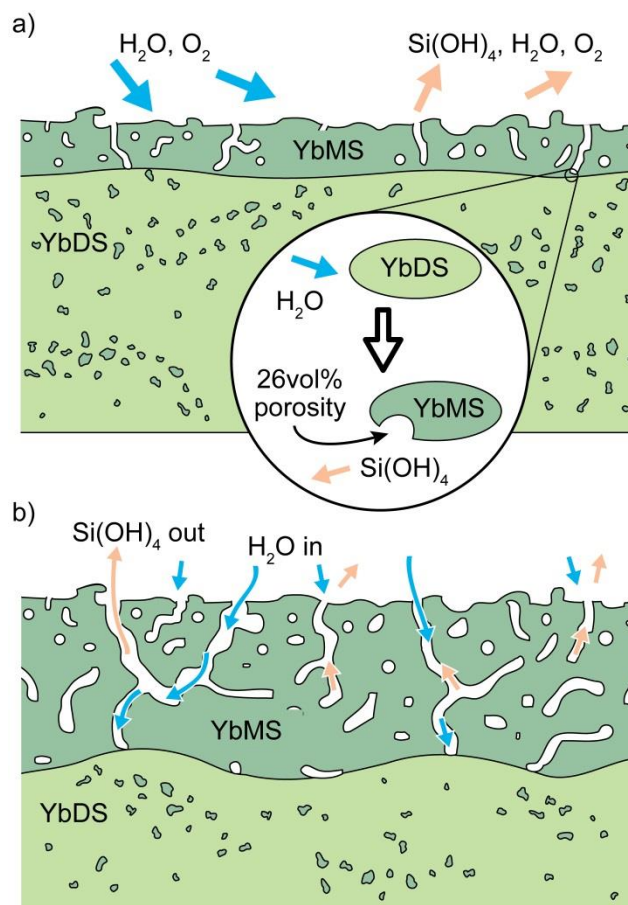


Figure 7.12: Schematic illustration of the volatility mechanism that results in a porous surface layer of YbMS on the surface of exposed YbDS after steam-cycling. (a) Initial phases of volatilization and (b) late in exposure.

The upward bending of the coating is consistent with oxidation of silicon to form  $\alpha$ -cristobalite which incurs a large ( $\sim 100\%$ ) volume increase,<sup>95,96</sup> during silicon layer oxidation. This region of oxide that grows inwards from the coating edge can then be envisioned as a wedge inserted at the edge of the coating, Figure 7.14(a). As this wedge extends laterally through the Si bond coat, the YbDS topcoat above will be subjected to a bending load and creep deform since YbDS has negligible creep flow stress at the upper testing temperature of  $1316\text{ }^{\circ}\text{C}$ .<sup>209</sup> The  $\alpha \rightarrow \beta$  cristobalite phase change on cooling results

in microfracture during cooling, enabling the  $\text{SiO}_2$  at the exposed edge to mechanically spall and be more rapidly volatilized by the steam environment. The removal of material at the exposed back of the wedge also allows oxidation to continue at the un-oxidized front, thereby permitting the wedge to more grow inwards towards the coating center. The combination of these processes results in effective translation of the cristobalite wedge from the coating edge towards the coating center with increasing cyclic exposure, Figure 7.14(b).

#### **7.4 Oxide Growth at the Silicon Surface**

Thermal cycling between 110 °C and 1316 °C of low porosity YbDS-protected silicon coated SiC substrates in an atmospheric pressure, 90 %  $\text{H}_2\text{O}$ /10 %  $\text{O}_2$  environment has resulted in the slow growth of a cristobalite TGO layer on the silicon surface at the YbDS – Si interface. After 2,000 hours of exposure at 1316 °C, the thickness of this oxide layer reached 2.5  $\mu\text{m}$ . This contrasted sharply with similar studies of YbMS protected silicon layers on the same substrate where TGO thicknesses of 15-150  $\mu\text{m}$  (porous layer observed at sample edge in high power coating) were observed after less than 400 hours of exposure.<sup>95,96</sup> In the YbMS coated system, very rapid oxidation occurred because mud cracks fully penetrated the YbMS and provided a rapid transport path for the oxidizing species to reach the silicon surface. The slow TGO growth rate observed in the mud crack free YbDS layer indicates that diffusional transport of the oxidizing species through the YbDS layer has limited the transport of oxygen and therefore rate of oxidation of the Si bond coat surface.

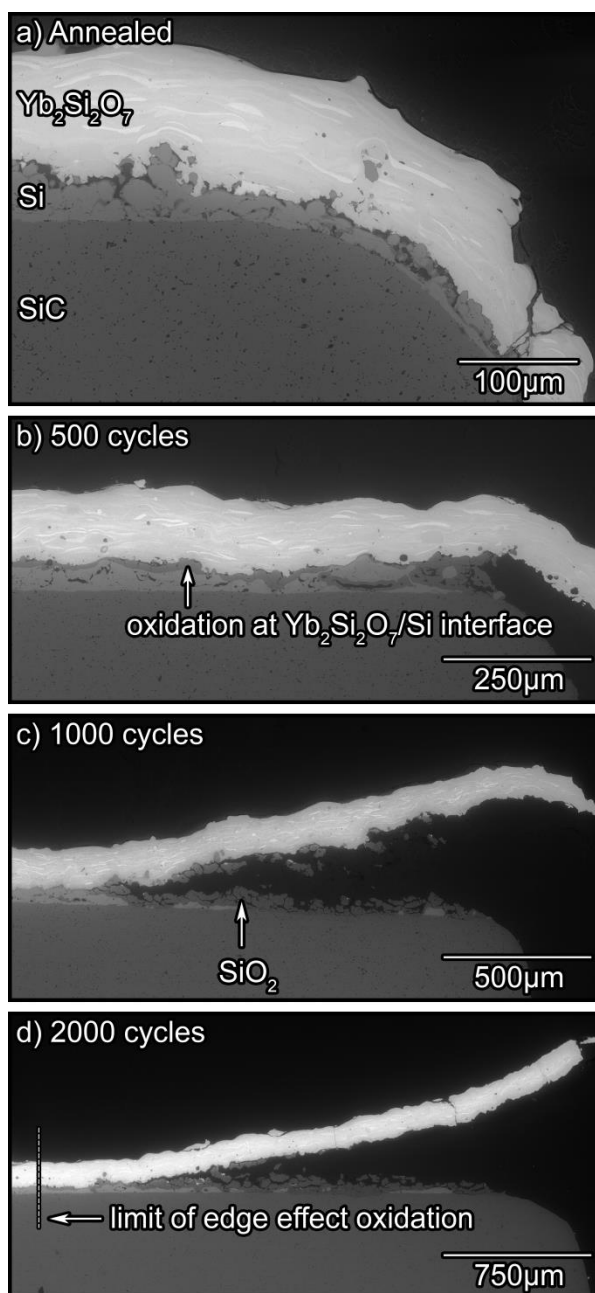


Figure 7.13: BSE micrographs of coating edges showing edge attack during steam-cycling of the bi-layer EBCs. (a) Annealed coating with edge over-sprayed, (b) edge TGO growth after 500 steam cycles, (c) significant edge lifting after 1,000 steam cycles, and (d) example of edge delamination after 2,000 steam cycles.

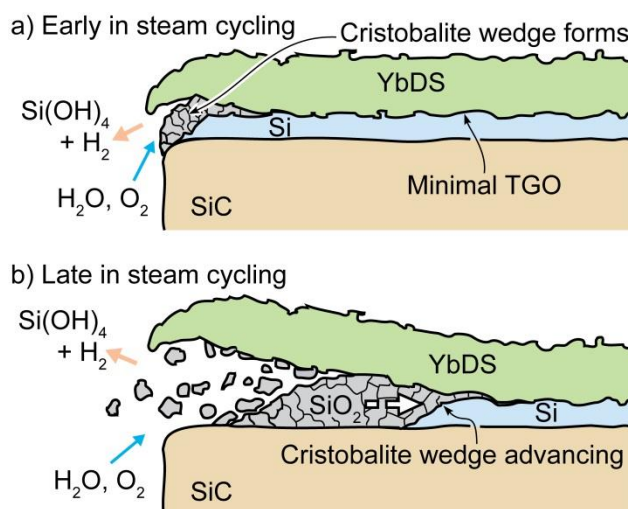


Figure 7.14: Schematic illustration of the SiO<sub>2</sub> wedging mechanism that lead to edge lifting during steam-cycling of YbDS/Si EBCs deposited on SiC.

The silica TGO thicknesses measured in experiment, Figure 7.7(a), were obtained from samples of slightly differing YbDS thicknesses, Table 7.3. To compensate for this, the data has been corrected to that for a constant YbDS layer thickness of 100  $\mu\text{m}$ . Since there exists constant oxygen partial pressure at the environment – YbDS and YbDS – SiO<sub>2</sub> interfaces, diffusion can be modelled by a one-dimensional representation of Fick's First Law. The flux of the oxidizing species,  $J(x)$ , that passes through a plane in the YbDS layer at distance  $x$  below the surface of the layer depends upon the YbDS diffusion coefficient,  $D$ , and the gradient in partial pressure of the oxidant through the YbDS layer:

$$J(x) = -D \frac{dp}{dx} \quad 7.1$$

where  $p$  is the partial pressure of the oxidizer presumed here to be monatomic oxygen. Assuming a constant diffusivity coefficient within the YbDS layer, the oxidizing species partial pressure at the Si-YbDS interface is established by thermochemical equilibrium

and was calculated by FactSage software using Y-Si-O experimental thermochemical data<sup>231</sup> to be  $4.29 \times 10^{-10}$  at 1316 °C, while on the exterior it was taken to be unity. The oxidizing flux reaching a growing SiO<sub>2</sub> layer is directly proportional to the thickness of the YbDS layer through which it diffused. If all this flux is assumed in silica formation, the TGO thickness will also be directly proportional to the thickness of the diffusion barrier. The thickness of the TGO layer as a function of time,  $h'(t)$  for samples with variable thickness diffusion barriers is then related to that for a constant thickness diffusion barrier,  $h(t)$  by:

$$h(t) = h'(t) * x_{meas} / x_{tar} \quad 7.2$$

where  $x_{meas}$  is the measured YbDS thickness paired with  $h'(t)$  and  $x_{tar}$  is the scaled (desired) YbDS thickness paired with  $h(t)$ . Each measured TGO thickness ( $h'(t)$ ) was adjusted using Equation 7.2 to that for a 100 μm YbDS layer thickness ( $x_{tar} = 100 \mu\text{m}$ ), and these values have been plotted as a function of oxidation time in Figure 7.8(b). The silica layer thickness remained linearly related to the oxidation time, but with a slightly altered linear rate constant due to the thinner diffusion barrier assumed:  $k_l = 1.44 \text{ nm/h}$ .

It is also of great interest to determine the value of the previously mentioned oxygen diffusion coefficient. This may be calculated from Equation 7.1 if the oxygen flux  $J_O$  and the partial pressure gradient across the diffusion layer  $\frac{dp}{dx}$  are known. The diffusion distance has already been assumed to be 100 μm in Figure 7.8(b), so that the previously stated interface pressures may be used to calculate the partial pressure gradient

of O across the YbDS diffusion layer:  $\frac{dp}{dx} = 10^7 \text{ m}^{-1}$ . The monatomic oxygen flux  $J_O$  is then the only remaining value needed to calculate  $D_O$ .

The molar flux of monatomic oxygen through the topcoat may be expressed by identity as:

$$J_O \equiv \dot{m}_O / M_O \quad 7.3$$

Where  $\dot{m}_O$  is the mass flow of oxygen through the topcoat and  $M_O$  is the molar mass of O. The assumption that all mass flux through the YbDS layer is consumed in cristobalite growth will again be invoked such that  $\dot{m}_O$  is equivalent to the rate at which oxygen is consumed to form the TGO,  $\dot{m}_c$  (in mass accumulated per unit time per unit area). This rate is by definition equal to the mass fraction of oxygen in  $\text{SiO}_2$  multiplied by the rate at which  $\text{SiO}_2$  is grown:

$$\dot{m}_O = \dot{m}_c \equiv \dot{I}_{\text{SiO}_2} * M_{\text{SiO}_2} / M_O \quad 7.4$$

Where  $\dot{I}_{\text{SiO}_2}$  is the TGO growth rate (in mass accumulated per unit time per unit area) and  $M_{\text{SiO}_2} / M_O$  is the mass fraction of oxygen in  $\text{SiO}_2$ .  $\dot{I}_{\text{SiO}_2}$ , the mass growth rate of the TGO, is simply the linear growth rate of the TGO ( $k_l$ ) multiplied by the density of cristobalite,  $\rho_c$ . The oxygen flux may then be readily calculated by combining Equations 7.3 and 7.4:

$$J_O = (k_l * \rho_c * M_{\text{SiO}_2} / M_O^2) \quad 7.5$$

If Equation 7.5 is solved using  $k_l = 1.44 \text{ nm/h}$  as determined in Figure 7.7(b), a density of thermally grown cristobalite of  $2.340 \text{ g/cm}^3$ , a molar mass of  $\text{SiO}_2$  of  $60.083 \text{ g/mol}$  and a molar mass of O of  $15.999 \text{ g/mol}$ , the flux of oxygen through the YbDS layer is

calculated to be  $J_O = 3.11 \times 10^{-8} \text{ mol s}^{-1}\text{m}^{-2}$ . This value may then be plugged into Equation 7.1 along with the oxygen pressure gradient:  $D_O = 3 \times 10^{-15} \text{ m}^2\text{s}^{-1}$  at 1316 °C.

$D_O$  may also be used to calculate the TGO thickness at which the oxidation rate would transition from linear kinetics dominated by diffusion through the YbDS layer to parabolic kinetics dominated by diffusion through cristobalite. The calculation is performed using a simple ratio of mean-square diffusion distances of the form  $t = x^2 / D$ . Assuming an oxidizer diffusion coefficient for cristobalite of  $2 \times 10^{-17} \text{ m}^2\text{s}^{-1}$  at 1316 °C,<sup>261</sup> the critical scale thickness at which the oxidation rate dependence changes from linear to parabolic growth with a 125 μm YbDS topcoat is 2.24μm.

It is immediately noted that though the cristobalite scale thicknesses for 1,000 steam-cycles or less fall significantly below this threshold, the scale thickness at 2,000 steam cycles falls marginally above this rate transition point, Figure 7.7(a). However, cristobalite scales in the 1,000 and 2,000 steam-cycle samples experienced TGO-mud cracking, Figure 7.8, such that fast diffusion paths through the scale existed. These paths would have greatly increased the effective  $D_O$  in cristobalite scales thicker than ~1.5 μm where the TGO-mud cracking was observed. As a consequence, the oxidation behavior remained rate-limited by diffusion of oxygen through the YbDS layer. It is expected that this linear oxidation trend would continue indefinitely so long as the YbDS layer remained crack-free and of constant thickness.

## 7.5 Fracture Mechanisms

The various fracture processes observed in the YbDS/Si system are at first surprising since there is a small difference in the CTE of the substrate, silicon and YbDS layers in this system, Table 7.2. However, the formation of a  $\beta$ -phase cristobalite  $\text{SiO}_2$  layer at the YbDS/Si interface can result in large residual stresses being formed upon cooling, especially after the  $\beta$  to  $\alpha$  transformation upon cooling through  $220\text{ }^\circ\text{C}$ .<sup>95,96</sup> This results in the accumulation of stored elastic energy in the system that is then available to drive fracture. The strain energy release rates (ERRs) available to drive the growth of delamination cracks have been calculated for the various interfaces of the system in LayerSlayer using the thermophysical data in Table 7.2, and are plotted as a function of TGO thickness in Figure 7.15.

The ERR calculations were performed using both the Young's elastic modulus of fully dense ( $E_{\text{Bulk}}$ ) YbDS and a modulus reduced to 50 % of this value ( $E_{\text{APS}}$ ) typical of low porosity APS materials.<sup>122-124,207-209</sup> For Si, the calculations used the polycrystalline bulk elastic modulus and an elastic modulus experimentally determined for a comparable Si bond coat.<sup>209</sup> These calculations have been presented in Figure 7.15(a) for YbDS with bulk material elastic modulus and in Figure 7.15(b) for YbDS with an APS elastic modulus. In both Figure 7.15(a) and (b) ERR curves for delamination at the Si – SiC interface have been included for bulk and APS elastic moduli of Si. However, this change of properties had little effect on the ERRs for delamination at other interfaces.

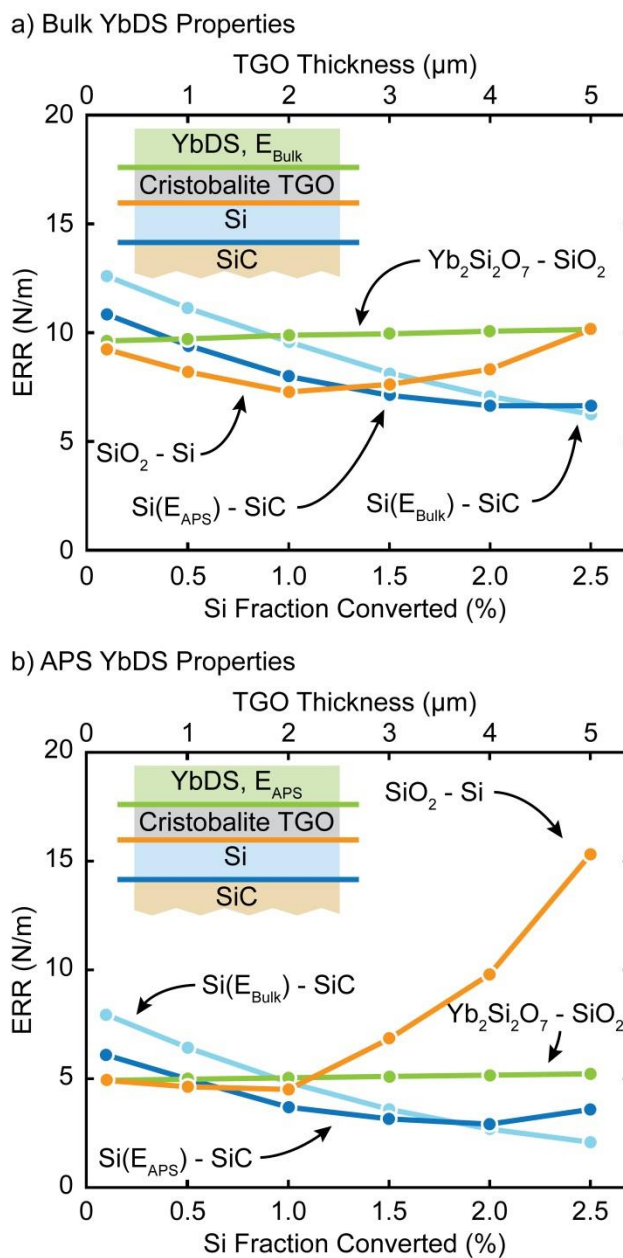


Figure 7.15: Predicted strain energy release rates of the interfaces in the YbDS – Si EBC system after cooling from 1316°C to 20°C. The calculations used (a) bulk elastic properties of YbDS with APS and bulk elastic modulus for Si layer and (b) APS modified elastic modulus for YbDS with APS and bulk elastic modulus for Si. All mechanical properties are listed in Table 7.2.

With no cristobalite layer, the ERR calculated for all interfaces in the system was found to be below 13 N/m for bulk elastic modulus of YbDS and below 8 N/m for APS

elastic modulus, Figure 7.15. As the system was steam cycled and a cristobalite TGO layer grew at the original YbDS – Si interface, the ERR for delamination of the YbDS – SiO<sub>2</sub> interface remained relatively constant due to the static nature of the YbDS layer. The ERR was roughly 2x higher in the bulk elastic modulus case than for the APS elastic modulus case. The ERR for delamination of the Si – SiC interface assuming bulk elastic modulus of Si decreased by about a factor of 2 in all cases when ~5 μm of cristobalite TGO thickness was achieved. The ERR for delamination of this interface assuming APS elastic modulus of Si decreased gradually to roughly 70% of its initial value. These trends were independent of the elastic modulus used for YbDS in calculation of the ERR.

The ERR for debonding at the SiO<sub>2</sub> – Si interface was strongly affected by the elastic modulus selected for the YbDS layer. When the bulk elastic modulus of YbDS was used in calculations, the ERR for this interface was ~10 N/m with no cristobalite scale, decreased to ~8 N/m at a cristobalite scale thickness of 2 μm, and then increased back to ~10 N/m at a cristobalite scale thickness of 5 μm. On the other hand, when the APS elastic modulus for YbDS was used in calculations the ERR for the interface was ~5 N/m with no cristobalite growth, dipped slightly with 1 μm of cristobalite growth, and then increased with loosely parabolic dependence to ~16 N/m with 5 μm of cristobalite growth. Regardless of the elastic moduli chosen for the YbDS and silicon layers, the ERR at all interfaces remained below 20 N/m for cristobalite scale thicknesses up to 5 μm. These energy release rates are 1-2 orders of magnitude lower than those calculated for the YbMS/Al<sub>6</sub>Si<sub>2</sub>O<sub>13</sub>/Si tri-layer EBC system.<sup>95,96</sup>

Assessment of the driving force for TGO-mud cracking (channel cracking of the TGO) is also of interest due to the observation of this phenomenon in Figure 7.6 and

Figure 7.7. The strain energy release rate (ERR) achieved by steady state channel cracking of a thin coating layer has been assessed by Vlassak.<sup>262</sup> The equation  $G_{SS} = \frac{\pi \sigma^2 t (1 - \nu^2)}{2 E} g(\alpha, \beta, \eta)$  was given for the steady state energy release rate via channel cracking, where  $\sigma$  is the stress,  $t$  is the thickness,  $\nu$  is the Poisson's ratio, and  $E$  is the elastic modulus, all of the TGO.  $g$  is a calculated function presented in that work based upon the crack opening dimension. This form of the equation inherently ignores layers above and below, such that some error may be assumed due to interface constraint.

The requisite mechanical properties for this calculation have been presented in Table 7.2, and the crack-opening dimension has been measured for TGO-mud cracking to be in the range of 3-10 nm (Section 7.3.1). The calculated ERR ranges between 6.8 N/m for 3 nm crack opening dimension and 22.5 N/m for 10 nm crack opening dimension at a TGO thickness of 1.5  $\mu\text{m}$ . By comparison,  $G_{IC}$  for  $\alpha$ -cristobalite has been calculated to be in the range of 7.1-7.7 N/m depending upon the fracture mechanism experienced.<sup>263</sup> Therefore, channel cracking of the TGO was energetically favorable and is expected for TGO thicknesses exceeding  $\sim 1.5 \mu\text{m}$ . This is in reasonable agreement with the relationship between TGO thickness (exposure time) and TGO-mud cracking observed in Section 7.3.1.

## 7.6 Conclusions

YbDS/Si bi-layer EBCs were deposited onto SiC substrates using a previously optimized APS approach. Five samples were isothermally steam cycled in a slowly

flowing 90 % H<sub>2</sub>O/10 % O<sub>2</sub> environment using 60 min hot (1316 °C) and 10 min cold (110 °C) cycle. It was found that:

- a) Dense APS deposited bi-layers consisting of 125 μm thick YbDS on a 50 μm thick Si bond coat have been found to environmentally protect the underlying silicon carbide during isothermal steam-cycling to 1316°C for 2,000 cycles.
- b) The Si bond coat exhibited linear oxidation kinetics with a linear rate constant of 1.44 nm/h for up to 2,000-hour exposures to H<sub>2</sub>O/O<sub>2</sub> at 1316 °C in a bi-layer system whose topcoat diffusion barrier layer was 100 μm thick.
- c) The oxygen diffusion coefficient for the YbDS layer at 1316°C was calculated from TGO thickening kinetics to be  $D_O = 3 \times 10^{-15} \text{ m}^2\text{s}^{-1}$ , and agreed well with the oxygen diffusion coefficients for other complex oxides at this temperature.
- d) Linear bond coat oxidation to form microcrack-free cristobalite has been estimated to terminate at a TGO thickness of ~2.24 μm whereupon the growth rate would transition to parabolic behavior controlled by diffusion through the uncracked TGO. However, at TGO thicknesses of ~1.5 μm and above, TGO-mud cracking was observed providing diffusive short-circuits through the scale and extending the linear oxidation regime indefinitely.
- e) The estimated ERR for delamination in the system were predicted to remain below 20 N/m for cristobalite scales up to 5 μm in thickness (twice that after 2,000 cycles of oxidation), consistent with good adherence of the bi-layer coating far from its edges.
- f) Oxidation of the bond coat at the edge of the samples initiated delamination cracking at the bond coat- YbDS interface. This damage progressed towards the interior of the

- samples as the number of cycles increased due to a combination of TGO microfracture and steam volatilization of the surface connected TGO layer.
- g) Loss of  $\text{SiO}_2$  from an approximately 15  $\mu\text{m}$  thick surface layer of the YbDS layer was observed after prolonged steam-cycling at 1316 °C in lower  $\text{Si}(\text{OH})_4$  partial pressure test environments. This was accompanied by the formation of creep-enabled voids that, in combination with mud cracks and delamination cracks, relieved the significant shrinkage stress associated with  $\text{SiO}_2$  loss.

The dense YbDS/Si bi-layer EBCs deposited in this study had excellent steam-cycling durability while providing total aerial coverage. This combination of attributes indicates that the system may be a viable option for some isothermal applications up to 1316 °C. Further analysis of mechanical properties and the effect of thermal gradients would be necessary to assess the viability of the system for use in rotating and internally cooled applications. Further assessment of surface volatilization of YbDS under high velocity flows in a thermal cycling will also be necessary.

## 8 Mechanical Properties of APS EBC Materials<sup>7</sup>

**Synopsis:** Development work in Environmental Barrier Coatings (EBCs) for Ceramic Matrix Composites (CMCs) has focused considerably on the identification of materials systems and coating architectures to meet application needs. Logically, these development efforts have focused heavily on thermochemistry, but thermomechanical properties remain largely untreated. The evolution of EBC systems has occurred rapidly so that the minimal accumulation of published thermomechanical data for comprehension of failure modes and modeling lags considerably behind cutting edge and concept systems. Materials property data exists for some simple systems in the bulk form, but the effects of air plasma spray (APS) deposition on the critical properties of strength and fracture behavior are not well studied. To address the lack of thermomechanical data, stand-alone plasma sprayed panels of baseline EBC materials (silicon, ytterbium disilicate) have been fabricated via APS and their resultant quasi-static and time dependent mechanical properties have been assessed. These properties include elastic modulus, toughness, low and high temperature flexure strength, and creep. The mixed-

---

<sup>7</sup> A peer reviewed conference proceeding published by the American Ceramic Society.<sup>209</sup>

mode fracture resistance of Si/MI-CMC interfaces has also been explored via 4-point bend interface toughness testing. The accumulated results are compared to properties of bulk material.

Deposition of the APS materials studied in this Chapter and characterization of those materials was performed at the University with the assistance of Jeroen Djeikers and Hengbei Zhao (UVA). The remainder of the work including mechanical testing and analyses was performed at the NASA Glenn Research center under the guidance of Dongming Zhu with modeling support by Louis Ghosn, both of whom are co-authors in the publication upon which this chapter is based. The contributions of Ralph Pawlik (NASA Glenn) were also significant: Ralph ran all of the physical materials tests aside from the laser thermal gradient creep tests. All NASA work was supported under NASA's Fundamental Aeronautics Program.

## **8.1 Introduction**

Thermochemical concerns are an important – even dominant – design driver in the development of robust EBCs due to the necessity of prime reliance. However, as potential candidate EBC coating concepts begin to be identified for turbine engine applications, a more comprehensive understanding of their thermomechanical properties is needed to assess their response during implementation in future gas turbines, in particular for utilizing ceramic rotating components that are internally cooled. The properties of interest and their testing in comparable TBC applications have already been reviewed in Section 1.6.

Chapter 7 has described one bi-layer EBC ( $\text{Yb}_2\text{Si}_2\text{O}_7/\text{Si}$ ) that has excellent steam-cycling durability, but the response to mechanical and thermal gradient loading is unreported. It is therefore of interest to measure the mechanical properties that will control failure of such a coating system in engine-like conditions. The purpose of this chapter of the dissertation is to perform preliminary measurements of the quasi-static and time-dependent response of the two materials in the  $\text{Yb}_2\text{Si}_2\text{O}_7/\text{Si}$  EBC system in their as-deposited (APS) conditions. The properties of interest include elastic modulus, fracture toughness, low and high temperature strength, and creep properties.

## 8.2 Experimental

Stand-alone plates for test specimen manufacture were deposited at the University using the Praxair-TAFA air plasma spray system described in Chapter 4. Both  $\text{Yb}_2\text{Si}_2\text{O}_7$  and Si materials were deposited using a 75 mm torch standoff with 610 mm/s torch traverse rate and 3 mm step size. The plasma torch used was a Praxiar SG-100 torch with internal hardware configuration comprising a 02083-175 anode, 02083-120 cathode, and 03083-112 gas injector. Deposition of both stand-alone panels required more than 500 passes to achieve target thickness (greater than 12 mm). The spray parameters used for deposition of Si were: 77.87 slm primary Ar gas flow, 1.18 slm secondary  $\text{H}_2$  gas flow, 550 A direct arc current, and 4.72 slm Ar powder carrier gas flow.  $\text{Yb}_2\text{Si}_2\text{O}_7$  spray parameters were: 103.83 slm primary Ar flow, 0.94 slm secondary  $\text{H}_2$  flow, 235 A direct arc current, and Ar powder carrier gas flow of 4.72 slm.

The  $\text{Yb}_2\text{Si}_2\text{O}_7$  powder used had particle diameter ranging 30-90  $\mu\text{m}$ ; the powder was a hollow spherical powder (HOSP) developed for NASA by Sulzer/Oerlikon Metco (Westbury, NY) for improved coating processing, performance, and stability. The Si was an electronics grade powder supplied by Micron Metals (Bergenfield, NJ), and was sieved to retain particles with a diameter of 80-130  $\mu\text{m}$ . The deposited stand-alone panels measured approximately 130 mm x 65 mm x 13 mm, and were subsequently diamond precision ground to multiple 50 mm x 5 mm x (4 or 3) mm specimens, Figure 8.1. Some of the Si specimens subsequently had the 50 mm x 5 mm face APS coated with  $\text{Yb}_2\text{Si}_2\text{O}_7$  for oxidation protection during laser thermal gradient creep testing. After fine grinding, the sample bevels were lightly sanded and the density of specimens was measured using the Archimedes method. Some specimens were sectioned for microstructural analysis.

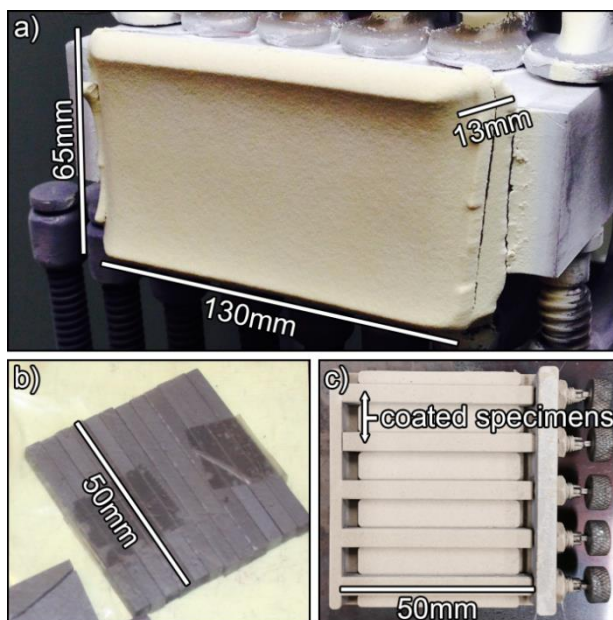


Figure 8.1: Photographs of (a) the 13 mm thick air plasma sprayed  $\text{Yb}_2\text{Si}_2\text{O}_7$  stand-alone plate in the deposition fixture, (b) Si test bars after machining from a stand-alone APS silicon plate, and (c) APS  $\text{Yb}_2\text{Si}_2\text{O}_7$  coated Si test bars.

Tests of the elastic modulus, fracture toughness, low temperature flexure strength, high temperature flexure strength, isothermal creep, and laser thermal gradient creep were subsequently performed. Mechanical testing techniques were implemented according to ASTM standards when applicable.<sup>8</sup> Fracture toughness was determined using the single edge V-notched beam (SEVNB) method.<sup>264,265</sup> The orientation of crack tested with respect to microstructure in the SEVNB toughness testing was comparable to that which would be observed in mud cracking or channel cracking, with crack oriented through splat thickness. The 4-point flexure testing arrangement used for isothermal and laser thermal gradient testing is schematically illustrated in Figure 8.2 with relevant dimensions indicated. For a more detailed description of the testing methodologies implemented, the reader is referred to Choi et. al.,<sup>120</sup> where the mechanical testing procedures used in this study have been extensively documented.

Interface toughness testing was performed upon specimens fabricated on SiC/SiC melt infiltrated ceramic matrix composite (MI-CMC) substrates. These tests were conducted using a stiffener-modified 4-point flexure interface toughness test that has been used for several coating applications including TBCs.<sup>119,266-271</sup> A schematic illustration of the test specimen and testing configuration is given in Figure 8.3. The stiffener (Haynes 230 alloy) was adhered using a thin layer of high strength epoxy. It is also important to note that some curvature was observed in stiffener beams prior to adhering them to test specimens, such that residual stresses are expected in the as-prepared composite beams. The effect of residual stresses in this testing method will be

---

<sup>8</sup> For further description of those testing methodologies, the reader is referred to the relevant ASTM standard: ASTM C 1259 for elastic modulus determination by impulse excitation of vibration, ASTM C 1161 for low temperature flexure strength testing, and ASTM C 1211 for high temperature flexure strength testing.

addressed further in discussion. Testing was run with constant actuator displacement at a rate of 0.02117 mm/s with load continuously monitored. Solutions for  $K_I$ ,  $K_{II}$ , and phase load angle  $\varphi$  were determined using a finite element analysis (FEA) approach.

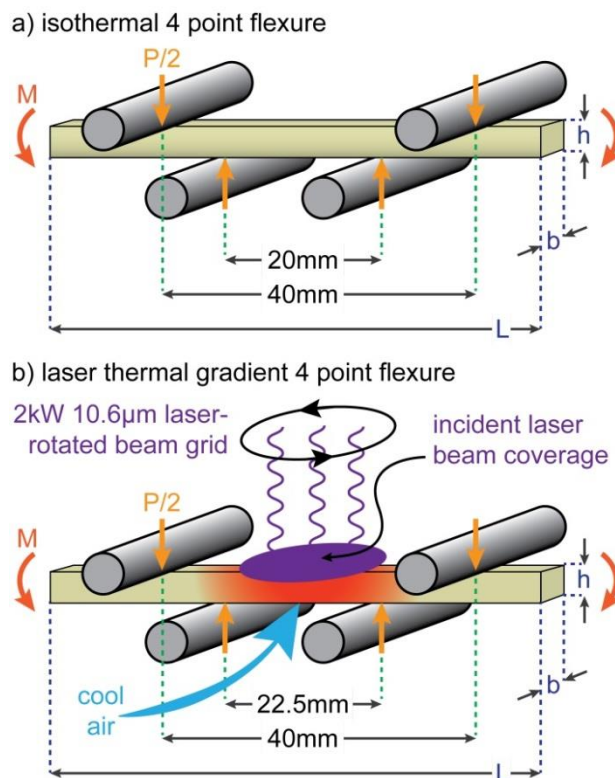


Figure 8.2: Schematic illustrations of (a) the 4-point bending apparatus used for isothermal flexure tests (toughness, strength, and creep), and (b) the 4-point bending apparatus used for laser thermal gradient creep flexure testing. The incident laser beam had a  $\sim 25$  mm diameter uniform profile. To create the uniform incident heat flux, a rotated integrator lens was used to distribute the beam. Both fixtures are operated in lab air.

All creep tests were performed in air using 4-point flexure. Interpretation of creep data and stresses in 4-point flexure creep has been conducted according to the analysis of Hollenberg, Terwilliger, and Gordon.<sup>162</sup> As mentioned in Section 8.1, this method is useful for quantitative initial analyses, such as those of interest in this work. As no a-

priori knowledge of creep stress exponent  $n$  may be assumed for these APS materials, creep displacement data has been interpreted for the elastic beam case (identical to  $n = 1$ ). The validity of this assumption is subsequently discussed. This method assumes that tensile and compressive creep behaviors of the material are identical. For laser thermal gradient creep testing, the incident radiation was supplied by a continuous operation 2kW 10.6  $\mu\text{m}$  CO<sub>2</sub> laser. Zhu et. al.<sup>272</sup> have described the laser thermal gradient testing method thoroughly. Though creep in such a scenario occurs at different temperatures and stresses throughout the sample, for convenience a single weighted inverse temperature ( $1/T$ ) average denoted  $T_w$  between the front and back face temperatures is used.

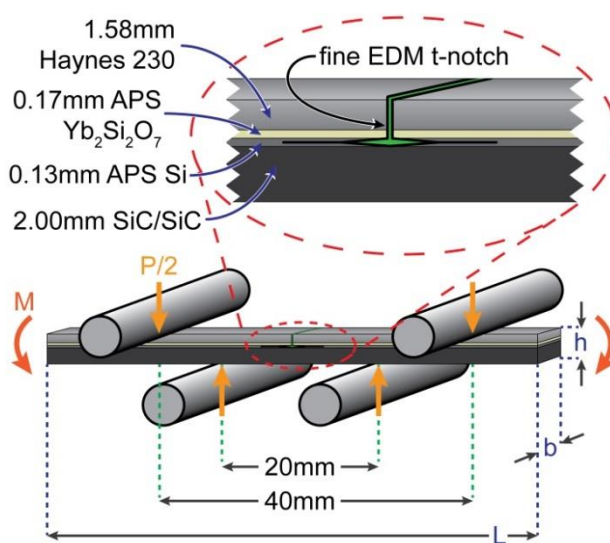


Figure 8.3: Schematic illustration of the 4-point bending test configuration used for mixed-mode fracture testing. The inset shows the EDM notch used to establish a “T”-shaped pre-crack in the stiffener and APS coating.

## 8.3 Results

### 8.3.1 APS $\text{Yb}_2\text{Si}_2\text{O}_7$

The as-deposited microstructure of the  $\text{Yb}_2\text{Si}_2\text{O}_7$  coating is shown in Figure 8.4 at several different magnifications. Again, the authors comment that the processed coating is not necessarily fully optimized for EBC applications. The primary source of porosity in the APS  $\text{Yb}_2\text{Si}_2\text{O}_7$  material is a population of uniformly distributed, relatively spherical isolated (not interconnected) pores, Figure 8.4(a). The porosity has been measured by both Archimedes method and image analysis to be ~10 %, to which the spherical intersplat pores contribute 8-9 % of total porosity. The light and dark contrast areas are a manifestation of Si loss from the near-stoichiometric powder during plasma spray deposition.<sup>97</sup> Light contrast regions correspond to those areas that are Si depleted whereas the darker grey regions correspond to areas with minimal or no Si loss, Figure 8.4(b). At this point, the extent of Si volatilization and resulting phase distribution has not been characterized. No cracking is evident in the coating at any magnification. One other feature of importance is the retention of segments of unmelted HOSP  $\text{Yb}_2\text{Si}_2\text{O}_7$  that are bound within the matrix, Figure 8.4(c). The porosity in these features contributes the remaining 1-2 % of total porosity of the coating. Finally, at the smallest scale, strings of connected nano-porosity and minor intersplat decohesion are observed, Figure 8.4(d).

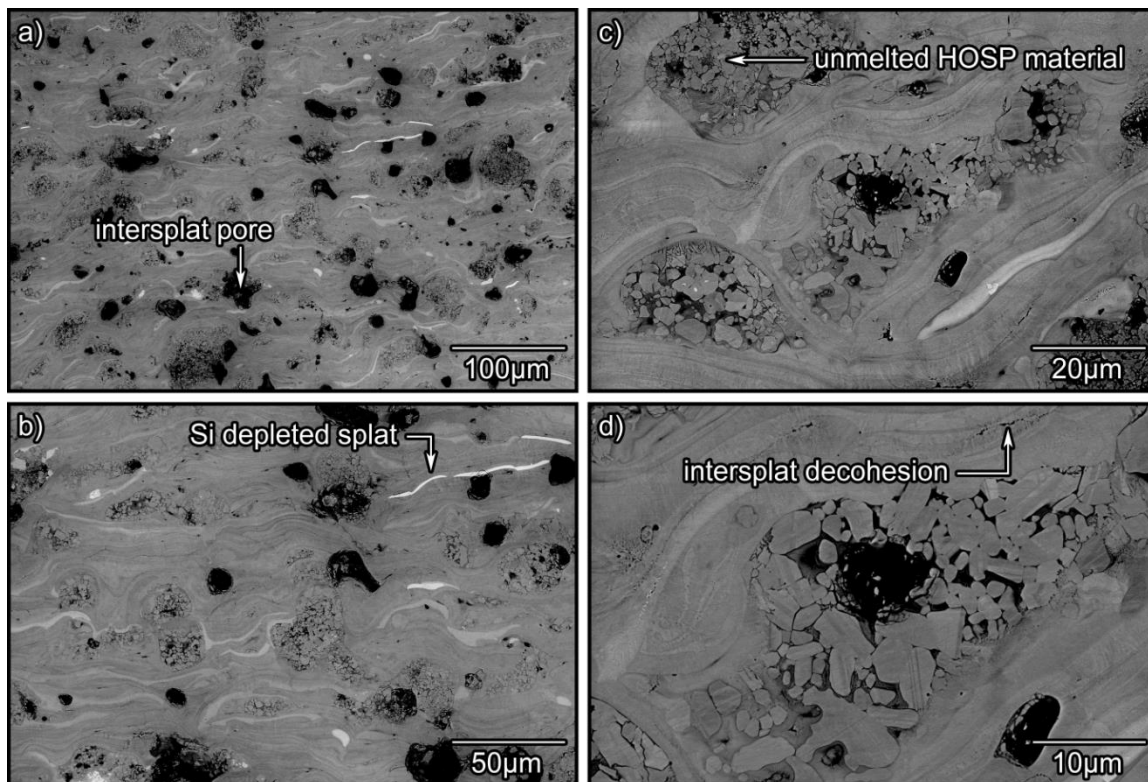


Figure 8.4: BSE mode SEM images of the as-deposited  $\text{Yb}_2\text{Si}_2\text{O}_7$  stand-alone plate at a series of magnifications illustrating features relevant to the mechanical response showing (a) low magnification image with intersplat porosity, (b) the presence of (lighter contrast) Si depleted splats, (c) partially melted HOSP particles bound in the matrix, and (d) isolated intersplat pores and poorly adhered splat boundaries.

Mechanical tests have been performed according to ASTM standards when applicable as described in Section 8.2, and the results are shown with standard deviations in Table 8.1. The scatter of data in elastic modulus, low temperature flexure strength, high temperature flexure strength, and  $K_{IC}$  is low. Isothermal creep tests have been performed over a 25 h test interval at a maximum outer ligament tension of 15.8 MPa and at several temperatures, Figure 8.5(a). The creep behavior exhibits a considerable primary creep regime that is typical to ceramic materials.<sup>154</sup> The primary creep portion of the curves may be used to determine the primary creep parameter  $s$  by maximizing the linear fit of

the data on an  $\epsilon/t^{-s}$  vs.  $t$  plot, as in Figure 8.5(b). Using this method, the value of  $s$  determined is 0.79. This is within the range of creep parameters expected for APS ceramic materials.<sup>120</sup> The secondary creep rates in isothermal testing were  $d\epsilon/dt = 3.39 \times 10^{-9} \text{ s}^{-1}$  at 800 °C,  $5.63 \times 10^{-9} \text{ s}^{-1}$  at 850 °C, and  $1.23 \times 10^{-8} \text{ s}^{-1}$  at 900 °C at the calculated maximum outer ligament tension of 15.8 MPa. The activation energy calculated using isothermal primary creep data was 127 kJ/mol whereas the activation energy calculated using isothermal secondary creep data was 135 kJ/mol.

*Table 8.1: Physical and mechanical properties of air plasma sprayed Yb<sub>2</sub>Si<sub>2</sub>O<sub>7</sub>.*

Physical/Mechanical Property	Value, $\sigma$ - st. dev.
Relative Density- Archimedes and image analysis	90-91 %
Elastic Modulus- impulse excitation	34 GPa, 2.53
25 °C 4-point Flexure Strength	19.7 MPa, 0.62
900 °C 4-point Flexure Strength	24.3 MPa, 0.42
25 °C K <sub>IC</sub> 4-point Flexure	0.925 MPa*m <sup>0.5</sup> , 0.05
800 °C -900 °C isothermal primary creep E <sub>a</sub>	137.2 kJ/mol
800 °C -900 °C isothermal secondary creep E <sub>a</sub>	134.7 kJ/mol
1067 °C & 1207 °C laser thermal gradient secondary creep E <sub>a</sub>	187.1 kJ/mol
800 °C-1207 °C secondary creep E <sub>a</sub>	154.6 kJ/mol
800 °C -900 °C isothermal primary creep $s$ parameter	0.78
Creep stress exponent $n$	~1

Laser thermal gradient 4-point flexure creep testing has also been performed on the APS Yb<sub>2</sub>Si<sub>2</sub>O<sub>7</sub> material. The test performed was a two-temperature test wherein the testing temperature was altered mid test by increasing the laser power. This has allowed for measurement of the creep rate at two different temperatures during a single test where very minimal creep deformation occurred during testing at the (lower) first temperature, Figure 8.6. The front side, back side, and weighted average temperature are also given along with the calculated outer ligament tension of 7.4 MPa. The calculated secondary creep strain rates are presented in Figure 8.6(b) and were measured as  $d\epsilon/dt = 1.05 \times 10^{-8}$

$s^{-1}$  at 981 °C and  $6.96 \times 10^{-8} s^{-1}$  at 1152 °C. The activation energy determined using these two laser thermal gradient data points was 165 kJ/mol.

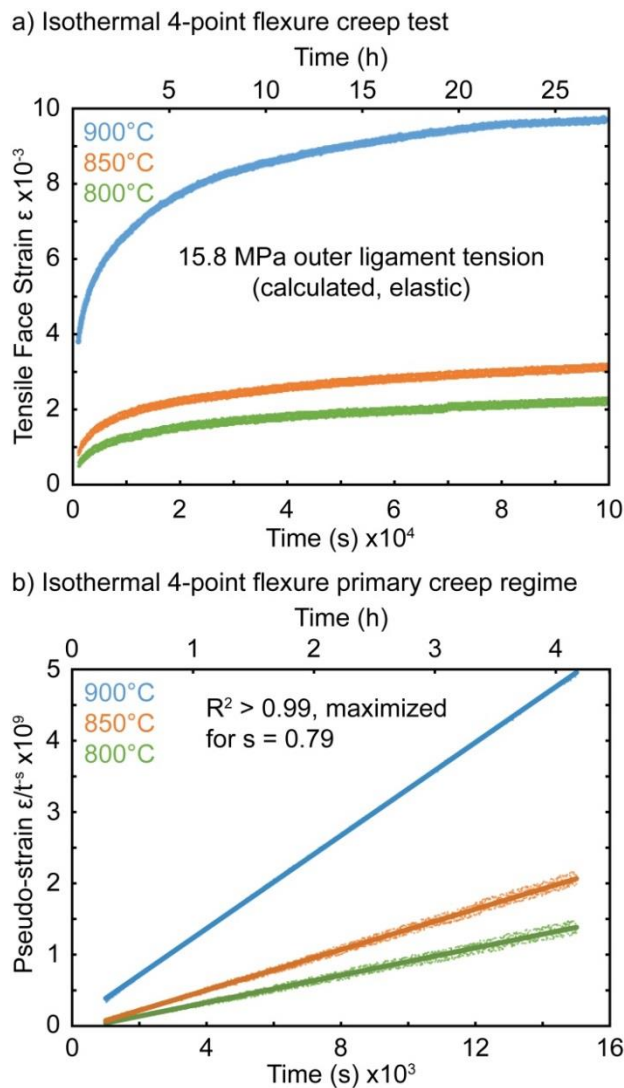
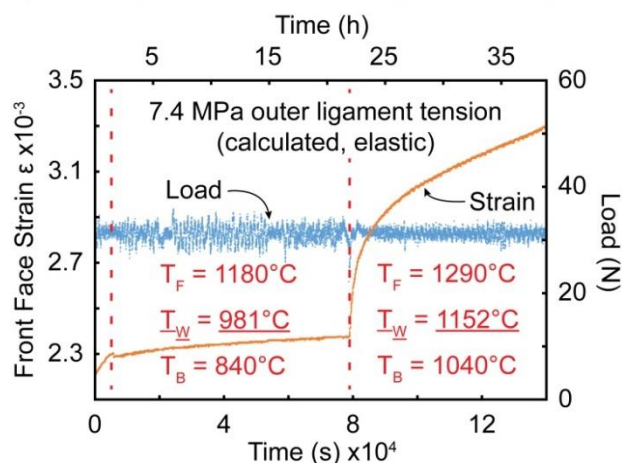


Figure 8.5: Isothermal 4-point flexure creep data of air plasma sprayed  $Yb_2Si_2O_7$ . (a) Shows the effect of temperature on the surface strain versus time behavior for a calculated surface stress of 15.8 MPa. (b) The pseudo-strain versus time response during the primary creep regime of the tests shown in (a).

a) Two-temperature laser thermal gradient creep test



b) Two-temperature secondary creep regimes

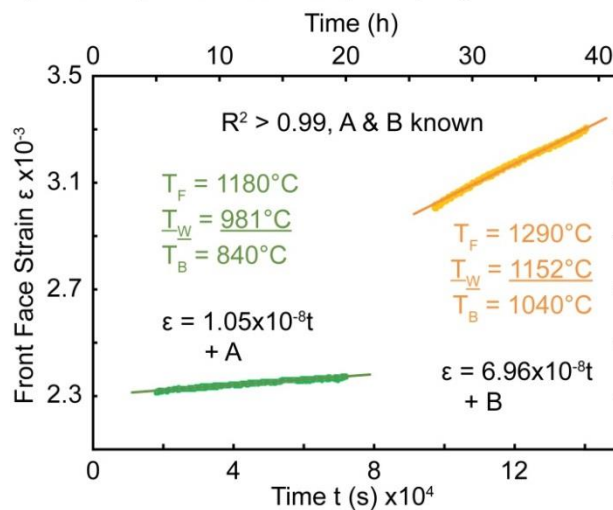


Figure 8.6: Laser thermal gradient creep curves for APS  $\text{Yb}_2\text{Si}_2\text{O}_7$ . (a) Strain and load curves for the two-temperature test with front face, back face, and inverse  $T$  average (weighted) test temperatures. (b) Linear fit strain equations for the two different temperature regimes of the thermal gradient creep test.

If it is assumed that the creep deformation mechanism is similar between isothermal and laser thermal gradient tests, the data from the two tests may be compared on a  $\ln(d\epsilon/dt)$  vs.  $1/T$  plot and used to determine both a refined activation energy and to estimate the creep stress exponent  $n$ , Figure 8.6. Depending on the true stress assumed in the creep-rate determining ligament, values of  $n$  calculated range between 0.8 and 1.9.

Assuming the true stress experienced in the creep-rate determining ligament of the beam is half of that calculated in the elastic case for the outer ligament (3.7 MPa) due to rapid stress relaxation in the outer ligament at high temperatures and inherent lower load at sub-surface ligaments, the creep stress exponent  $n$  is determined to be approximately 1. The mechanical properties data for APS  $\text{Yb}_2\text{Si}_2\text{O}_7$  can be found in Table 8.1.

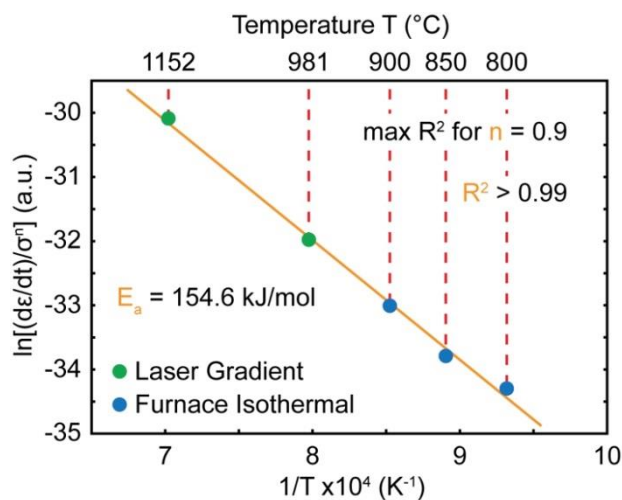


Figure 8.7: Determination of creep stress parameter “ $n$ ” for APS  $\text{Yb}_2\text{Si}_2\text{O}_7$  through optimization of  $R^2$  in an Arrhenius-type creep activation energy ( $E_a$ ) determination plot.

### 8.3.2 APS Si

The as-deposited microstructure of the APS Si stand-alone coating is shown in Figure 8.8 both with and without the protective  $\text{Yb}_2\text{Si}_2\text{O}_7$  layer. Porosity in the APS Si layer was low, with measurements by both the Archimedes method and image analysis yielding porosities of ~6 %. The observed porosity is all of the isolated (not interconnected) intersplat variety and has a relatively uniform distribution throughout the stand-alone specimens, Figure 8.8(a). When viewed at high magnification, Figure 8.8(b), intersplat boundaries are evident. The boundaries appear a darker shade of grey in BSE mode

imaging, and therefore may have a very fine layer of secondary phase. Due to the scale of these boundaries, proper identification of composition and phase would require TEM analysis, which has not been endeavored. Figure 8.8(c) and (d) show sections of the stand-alone APS Si that have been protectively coated with  $\text{Yb}_2\text{Si}_2\text{O}_7$  for laser thermal gradient testing and illustrate good adherence and consistency of the coating layer.

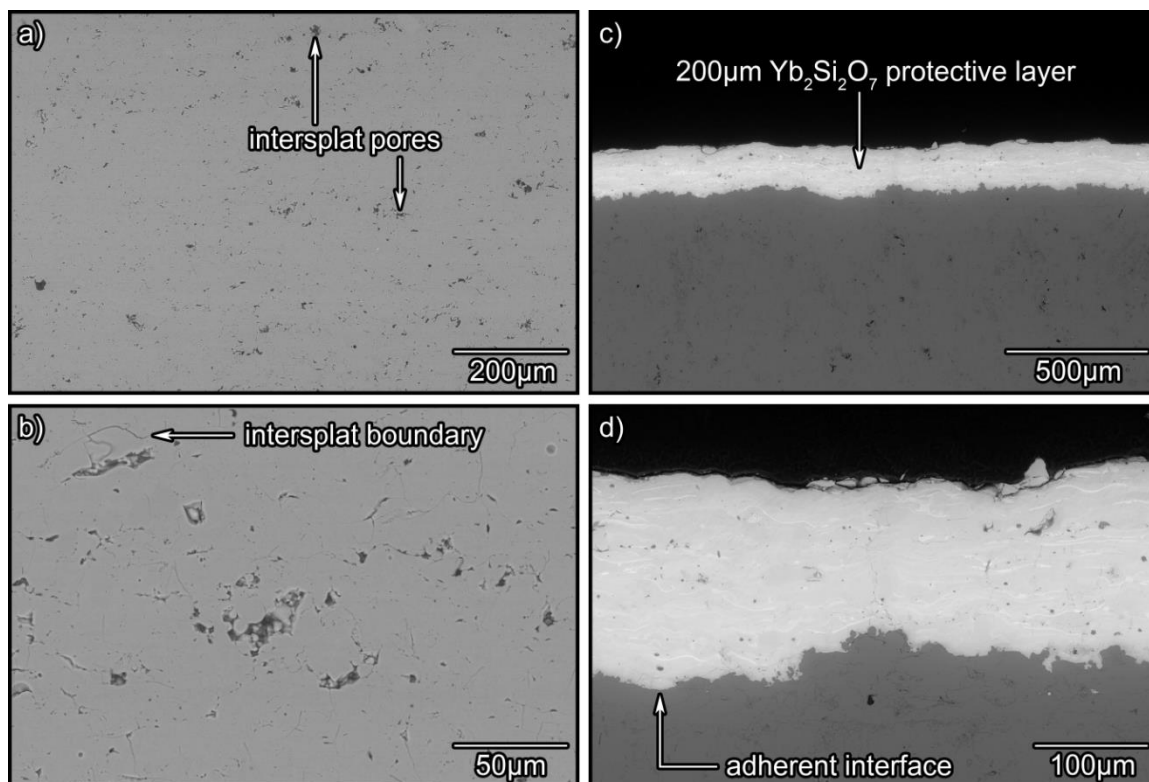


Figure 8.8: BSE SEM images of (a) the as-deposited stand-alone Si plate showing the uniform distribution of pores. (b) Higher magnification image showing intersplat boundary and pore structures. (c) Low magnification image of an APS  $\text{Yb}_2\text{Si}_2\text{O}_7$  coated silicon test specimen used to protect the sample from oxidation during laser thermal gradient testing. (d) Higher magnification image of the  $\text{Yb}_2\text{Si}_2\text{O}_7$  – Si coating interface showing good interface adherence.

The results of mechanical testing on stand-alone APS Si are presented in Table 8.2. Scatter in elastic modulus, low temperature flexure strength, and fracture toughness is

low. Only two samples were tested for high temperature flexure strength due to the limited number of specimens available, but these specimens had significantly disparate strengths of 171.7 MPa and 201.9 MPa. Creep of the APS Si material has been measured exclusively using the laser thermal gradient approach. However, the laser thermal gradient specimens include a 200  $\mu\text{m}$  protective  $\text{Yb}_2\text{Si}_2\text{O}_7$  layer that may be anticipated to handle a considerable portion of the thermal load. The temperature distribution throughout the sample may be readily calculated using conventional heat transfer equations assuming a 1-D equal heat flux scenario, which is reasonable given the scale of the sample.

*Table 8.2: Physical and mechanical properties of air plasma sprayed Si.*

Physical/Mechanical Property	Value, $\sigma$ - st. dev.
Relative Density- Archimedes and image analysis	94-95 %
Elastic Modulus- impulse excitation	73 GPa, 2.12
25 °C 4-point Flexure Strength	76.6 MPa, 1.32
900 °C 4-point Flexure Strength	186.8 MPa
25 °C $K_{IC}$ 4-point Flexure	1.540 $\text{MPa}\cdot\text{m}^{0.5}$ , 0.05
1050 °C -1180 °C laser thermal gradient secondary creep $E_a$	283.5 kJ/mol

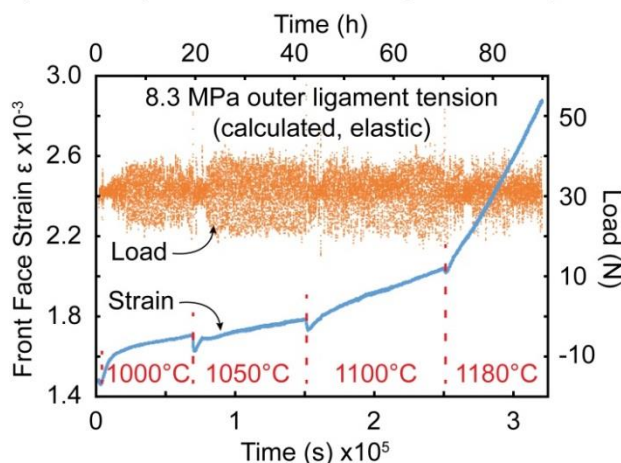
The estimated thermal conductivity of  $\text{Yb}_2\text{Si}_2\text{O}_7$  is  $\sim 2.0$  W/mK while that of Si is 20 W/mK<sup>273,274</sup> at 1300 °C. The thermal gradient across a Si test coupon for test temperatures between 1,000 °C and 1250 °C is then estimated to be  $< 8$  °C. For coated Si coupons, the majority of the thermal gradient is observed within the  $\text{Yb}_2\text{Si}_2\text{O}_7$  layer with the Si specimen being approximately isothermal. Therefore, creep testing of coated APS Si specimens in the laser thermal gradient 4-point flexure rig can be approximated to be isothermal creep testing. The load and calculated creep strain data for the creep test are presented in Figure 8.9(a) along with the appropriate creep temperatures for Si. The

secondary creep equations corresponding to the creep test are plotted in Figure 8.9(b) and yield secondary creep strain rates  $d\varepsilon/dt = 1.22 \times 10^{-8} \text{ s}^{-1}$  at 1,000 °C,  $1.30 \times 10^{-8} \text{ s}^{-1}$  at 1050 °C,  $2.47 \times 10^{-8} \text{ s}^{-1}$  at 1100 °C, and  $1.25 \times 10^{-7} \text{ s}^{-1}$  at 1180 °C. The creep strain rate data can be plotted as  $\ln(d\varepsilon/dt)$  vs.  $1/T$  for determination of creep activation energy, Figure 8.10. It is noted that the 1,000 °C data point (Figure 8.10) is slightly suspect and possibly part of either another creep regime or due to errant thermal data from pyrometers. As such, activation energy has been determined using the 1050 °C, 1100 °C, and 1180 °C data points. The calculated creep activation energy for this set of data points is 283 kJ/mol.

### 8.3.3 *Mixed-Mode Interface Toughness*

FEA analysis has been used to determine stress intensity factor solutions for the stiffener-modified 4-point flexure interface toughness problem. The solutions can be expressed in the common form of  $K_I = \frac{F_I(a)P(S_o-S_i)}{BW^{1.5}}$ ,  $K_{II} = \frac{F_{II}(a)P(S_o-S_i)}{BW^{1.5}}$ , and  $\phi = \text{atan}\left(\frac{K_{II}}{K_I}\right)$ . In the steady state energy release regime (crack length  $a > 0.1$  \* inner load support span), FEA calculations for the present configuration yield  $K_{I,\text{normalized}} = 1.07$ ,  $K_{II,\text{normalized}} = 0.59$ , and phase angle  $\phi = 29.10^\circ$ . Three specimens have been tested, and five distinct crack propagation incidents have been identified. An example of one of these tests is shown in Figure 8.11, and the results of all three tests are given in Table 8.3 for the five distinct crack propagation events with average, standard deviation, maximum, and minimum values listed.

a) Four-temperature laser thermal gradient creep test



b) Four-temperature secondary creep regimes

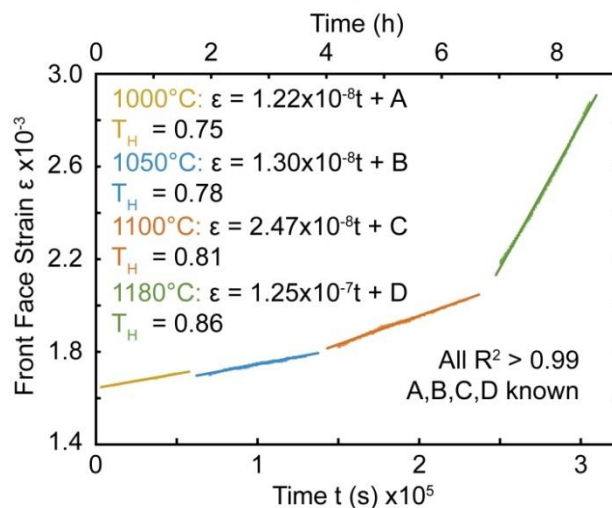


Figure 8.9: Laser thermal gradient creep curves for APS Si. (a) Strain and load curves for the four-temperature test with front face, back face, and Si test temperatures. (b) Linear fit strain equations for the four different temperature regimes of the thermal gradient creep test.

## 8.4 Discussion

### 8.4.1 APS $\text{Yb}_2\text{Si}_2\text{O}_7$

The microstructure of Figure 8.4 indicates deposition of mixed  $\text{Yb}_2\text{Si}_2\text{O}_7 + \text{Yb}_2\text{SiO}_5$  material. Deposition of mixed microstructures has previously been observed in the  $\text{Yb}_2\text{O}_3\text{-SiO}_2$  system and has been attributed to volatilization of Si from the originally

stoichiometric powder during APS processing.<sup>97</sup> Further analysis of Figure 8.4 indicates that no cracking is present in the as-deposited material, even when viewed at very high magnifications. This is in part due to deposition parameter selection to avoid cracking even during the deposition of very thick coatings where the thermal load delivered to the stand-alone plate was very high. The development of this set of coating parameters was inherently coupled with reduced density in the deposited coatings, thereby yielding the ~10 % porosity observed and unmelted HOSP clusters. The material parameters are therefore representative of a 10 % porous APS  $\text{Yb}_2\text{Si}_2\text{O}_7$  coating structure.

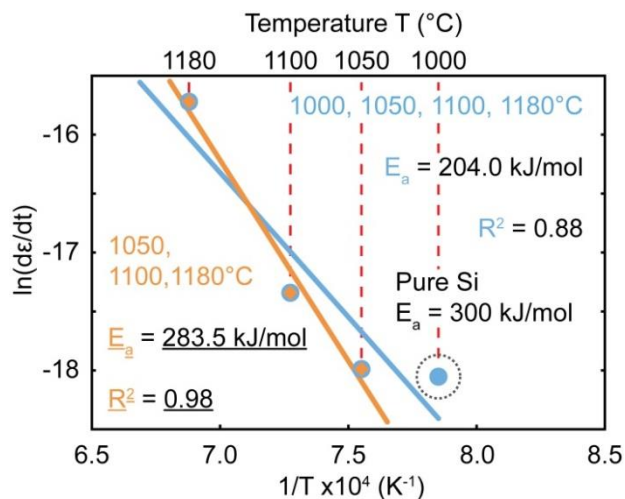


Figure 8.10: Creep activation energy ( $E_a$ ) determination for APS Si in an Arrhenius-type plot.

The elastic modulus determined by impulse excitation of vibration in this study is low in comparison to the elastic modulus of bulk  $\text{Yb}_2\text{Si}_2\text{O}_7$  that has been measured by various techniques (and for various compositions spanning silica lean to silica rich in hot pressed samples from NASA development programs) to be in the range of 150-180 GPa. This modulus reduction may be a result of the very large quantity of intersplat boundary that

results from the deposition of the fine spherical particulates bound within the HOSP precursor material. Retained HOSP clusters may also contribute to the low observed elastic modulus. As previously mentioned, no fine scale cracking is observed in the APS structure. Accordingly, the reduced modulus cannot be attributed to distributed micro- or nano-scale cracking. Elastic moduli of comparable value have previously been observed in APS TBC materials.<sup>118,122,123</sup>

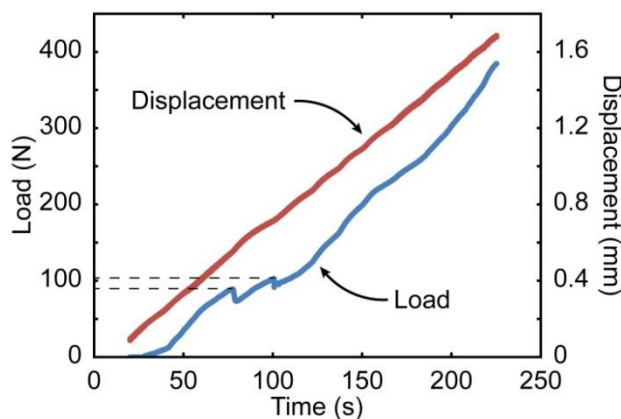


Figure 8.11: Load and displacement curves for a 4-point bending interfacial toughness test.

Table 8.3: Interface toughness  $K_c$  of Si – MI-CMC interface at  $G_c$  calculated from finite element analysis solutions with phase load angle  $\phi = 29.1^\circ$ .

Interface Toughness	$K_I @ G_c$ (MPa*m <sup>1/2</sup> )	$K_{II} @ G_c$ (MPa*m <sup>1/2</sup> )
Mean	1.92	1.06
Standard Deviation	0.34	0.188
Maximum	2.36	1.30
Minimum	1.58	0.87

The fracture toughness of the as-deposited APS Yb<sub>2</sub>Si<sub>2</sub>O<sub>7</sub> has been measured to be 0.925 MPa\*m<sup>1/2</sup>, which represents a ~50 % reduction from the value measured for dense, bulk processed material (~2 MPa\*m<sup>1/2</sup>, previous NASA unpublished data). This reduction

in toughness is likely due to some combination of the microstructural features discussed above. Though fracture toughness is an intrinsic material property, the scale of the SEVNB test when compared to the microstructure is such that porosity and boundaries in the structure will have an effect upon the observed value. Therefore, the toughness value reported should not be considered as the intrinsic toughness of the material, but instead that of the APS  $\text{Yb}_2\text{Si}_2\text{O}_7$  structure.

The 25 °C flexure strength of the as-deposited material is also low in comparison to equi-biaxial data for bulk densified  $\text{Yb}_2\text{Si}_2\text{O}_7$  materials which have been tested at NASA. These hot pressed materials span the compositional space from silica lean to silica rich compositions and have 25 °C flexure strengths in the range of ~100 MPa to ~120 MPa, with silica lean or rich compositions at the lower end of this spectrum. The equi-biaxial flexure strength of stoichiometric  $\text{Yb}_2\text{SiO}_5$ , however, has been measured to be only ~15 MPa, so it is reasonable to expect that with the presence of both  $\text{Yb}_2\text{SiO}_5$  and 10 % porosity in the stand-alone material the flexure strength would be reduced to the observed value of 19.7 MPa. This trend also applies to the 900 °C flexure strength, which experienced a marginal increase to 24.3 MPa.

Stresses are expected to arise in rotating hardware during service from two primary sources. First, the physical rotation of turbine blades leads to the generation of a centrifugal stress. The magnitude of this stress depends upon a large number of variables including the rotation rate of the turbine, the distance of the blade from the central axis, the density of coating layers, and the thickness of coating layers. On top of this, additional stresses are imposed by thermal gradients that are established by internal cooling. These thermal gradients may exceed 100 °C across thermal barrier layers,

thereby imposing a significant thermal stress. At operation temperatures of 1316 °C and above, even small stresses may be expected to result in creep over the thousands of hours of lifetime expected for turbine materials. Creep performance of coatings is therefore an important consideration for rotating hardware.

Creep behavior of rare earth silicates remains unpublished. As such, there is no available data to which the present creep experiments for APS  $\text{Yb}_2\text{Si}_2\text{O}_7$  may be compared, even in the isothermal case. Efforts are presently underway to fabricate hot pressed specimens from the same HOSP material used for APS processing, but this data is as of yet unavailable. As such, circumstantial interpretation of the APS  $\text{Yb}_2\text{Si}_2\text{O}_7$  creep performance is difficult, and one must instead view the data in an absolute context. In isothermal testing at 900 °C with a maximum tensile face load of 15.8 MPa, 1 % strain is observed in 25 h, Figure 8.5. This temperature is far below the intended service temperature of the material, and the stress level is low when compared with possible thermally or mechanically induced stresses. If such creep data is extrapolated to higher temperatures, extremely high creep rates are predicted. In addition, the material exhibits severe primary creep behavior, which may in part be an artifact resulting from 4-point flexure creep testing.<sup>165,169</sup> This primary creep may result in rapid deformation of as-deposited components upon entering service.

One method of testing such a high creep rate material at elevated temperature is to use a thermal gradient-based modification of isothermal 4-point flexure. This setup adds geometric constraint to the creep of the test specimen by keeping one face of the sample (and the 4-point bending fixture) comparably cool, thereby allowing higher testing temperatures on the sample surface without mechanically compromising the entire

specimen. The test also bears the added benefit of realistically replicating the thermal gradient exposure experienced in gas turbine engines. The drawback of this technique, however, is that comprehensive analytical solutions for creep have not been determined. Simple corrections may be implemented to account for shifts in the neutral axis of the beam, stress relaxation at high temperatures, and for the true creep temperature, but to some extent the interpretation of the creep data will be confounded by the complexity of the test. Therefore, it should be interpreted as an application/engineering oriented test. In this work, an inverse T average between the front face and back face is used as the assessing metric for the creep temperature.

Having established the creep temperature and creep rates (Section 8.3.1), a reasonable range for the secondary creep parameter  $n$  may be determined by comparing the isothermal data at 15.8 MPa to the laser thermal gradient data at 7.4 MPa (assuming no surface relaxation or neutral axis shifts). If shifts in neutral axis and surface stress relaxation are assumed such that the true creep-restraining ligament stress is a factor of 2 lower than that calculated by pure elastic techniques for the outer ligament, a range of possible  $n$  values can be established using these two testing methodologies. The value calculated for  $n$  ranges from 1.9 with a creep-restraining ligament stress of 7.4 MPa in laser thermal gradient testing to 0.8 with a creep-restraining ligament stress of 3.7 MPa in laser thermal gradient testing. It is therefore reasonable to assume that the true value of  $n$  is on the order of 1 for this APS  $\text{Yb}_2\text{Si}_2\text{O}_7$ . For comparison, an  $n$  value of 1 indicates pure diffusional creep whereas dislocation and stress activated creep mechanisms have  $n$  in the range of 2-7. True isothermal determination of  $n$  using additional APS specimens is ongoing.

The activation energies for creep calculated from the isothermal data, laser thermal gradient data, and isothermal + laser thermal gradient data range from ~135 to ~165 kJ/mol, Table 3 and Figure 8.7. For comparison, the activation energy for surface diffusion in APS YSZ has been determined to be ~105 kJ/mol.<sup>68</sup> The activation energy is then commensurate with a primarily diffusion-based creep mechanism that is additionally supported by the determination of the creep stress exponent  $n$ . Based on this combination of data, it appears that creep of the 10 % porous APS  $\text{Yb}_2\text{Si}_2\text{O}_7$  is surface-diffusional and therefore sensitive to the microstructure (porosity, splat boundaries, retained HOSP clusters) of the specimens.

The creep performance of the APS  $\text{Yb}_2\text{Si}_2\text{O}_7$  material bears two important consequences. First, if these coatings are applied to rotating hardware where significant centrifugal stresses exist, significant flow of the material is expected due to the extremely high creep rates observed. This could severely limit coating life or prohibit use of the material in rotating hardware. Second, considerable creep of the material at very low stresses indicates that total stress relaxation will occur at high temperatures. In (uncooled) isothermal hardware this is not problematic, but in cooled hardware where thermal gradients through the coating layer may be 100 °C or greater this can have important mechanical effects. Presuming the coating layer stress relieves in the thermal gradient at operating temperature, upon cooling the outer ligament will develop an additional gradient-induced thermal residual stress. Depending on the mismatch of CTE between coating and substrate, this may have either beneficial or disadvantageous effects.

#### 8.4.2 APS Si

The elastic modulus determined by impulse excitation for 94 % dense APS Si was 73 GPa, roughly half of the 163 GPa elastic modulus reported for bulk, isotropic polycrystal.<sup>88</sup> It is therefore evident that the reduction in elastic modulus is determined by the physical structure of the APS layer, which is shown in Figure 8.8 and has been described in Section 8.3.2. The visible intersplat boundaries in the structures of Figure 8.8 may result from partial boundary oxidation of the Si during APS processing, and contribute to the heterogeneous nature of splat boundaries in the stand-alone specimens. This oxidation results from mixing of the surrounding atmosphere into the plume from flow boundary turbulence. No cracking is observed in this structure, so that the difference in elastic modulus must be tied predominantly to the intersplat boundaries, porosity, and very limited oxidation observed.

The fracture toughness ( $K_{IC}$ ) of the APS Si structure has been determined to be 1.54  $\text{MPa}\cdot\text{m}^{1/2}$ , which corresponds to a significant increase over the 0.8-0.9  $\text{MPa}\cdot\text{m}^{1/2}$  catalogued for dense polycrystalline samples.<sup>88</sup> Again, due to the difference in scale between testing and the microstructure, the  $K_{IC}$  test is probing the toughness of the APS Si structure, not the intrinsic toughness of Si. It appears that the presence of intersplat boundary, a secondary phase (silica) on some boundaries, and 6 % porosity contribute to a slight toughening effect of the structure. Due to the nature of the defects, it is likely that the toughening results from some combination of crack arrest at intersplat boundaries and effective crack blunting by spherical pores.

Flexure strength of the APS Si is also considerably reduced when compared to dense polycrystal. The 25 °C flexure strength of the APS material was 76.6 MPa, whereas

dense polycrystal flexure strength is ~260 MPa.<sup>88</sup> It is worthwhile to note, however, that the scatter in 25 °C flexure strength for APS Si is extremely low, whereas the scatter in flexure strength for dense polycrystal is extremely high. The low scatter (and comparably low flexure strength) for the APS material is likely a result of a consistent flaw population within the APS material. Assuming all samples had a critical flaw of the same size (reasonable due to the high density of flaws in the APS structure), then all specimens should fail at the same stress level, as observed. The 900 °C flexure strength averaged 186.8 MPa for APS Si vs. ~500 MPa for dense polycrystal.<sup>88</sup> In the 900 °C flexure tests the scatter in strength was high for both the APS material and the dense polycrystal. As 900 °C is over the ductile to brittle transition temperature in Si, it is likely that failure results from the linkage of many flaws, and is therefore variable in both the APS Si and dense polycrystal.

All creep tests performed on Si were executed in the 4-point flexure laser thermal gradient rig. As detailed in Section 8.3.2, however, the thermal gradient across the thickness of the Si sample has been calculated to be <8 °C, such that the test may be considered as an isothermal creep flexure test. The creep rates agree reasonably (same orders of magnitude) with those published for glide of dislocations on the <111> planes in dense Si polycrystal.<sup>88</sup> A direct quantitative comparison of creep rates, however, is complicated due to the (unanalyzed) mechanical effects of the protective Yb<sub>2</sub>Si<sub>2</sub>O<sub>7</sub> layer. The activation energy of 284 kJ/mol for creep of the APS material is also in good agreement with the activation energy for dislocation glide on the <111> planes of bulk, polycrystalline Si at 300 kJ/mol.<sup>88</sup> It appears, therefore, that the creep of the APS Si

structure can be reasonably predicted by bulk polycrystalline Si data for temperatures in excess of 1,000 °C, provided the pore structure is accounted for.

### ***8.4.3 Mixed-Mode Interface Toughness***

Preliminary mixed-mode interface toughness has been determined for the as-deposited model  $\text{Yb}_2\text{Si}_2\text{O}_7/\text{Si}/\text{MI-CMC}$  system. Application of this technique and interpretation of the data, however, bears several additional considerations that merit discussion. In general, the 4-point flexure interface toughness test and stiffener-modified 4-point flexure interface toughness test have considerable documentation and verification in public literature,<sup>119,266-271</sup> and the interpretation of data used in the present study is much the same.

It is worthwhile to note that the FEA solutions calculated apply specifically to steady state propagation of a pure delamination-type crack. Crack kinking and interface roughness will have local effects on  $K_I$ ,  $K_{II}$ , and  $\phi$  that are not considered in the present analysis. The tests were not performed in a fixture that uses a floating-platen type load arrangement, such that asymmetry in crack propagation will have a minor effect on the data. Again, the authors stress that this work is exploratory, and used primarily to determine the viability of this testing technique and provide initial figures for APS EBC structures applied to SiC/SiC composites.

All three tests (and all 5 propagation events) occurred in a “saw-tooth” load pattern, i.e. load spikes and then drops. This loading pattern is typical of interfaces that have inconsistent toughness<sup>275</sup> and is therefore expected for the highly heterogeneous

interfaces in APS coatings. The small number of load spikes per sample is reflective of the low toughness of this interface (and baseline EBC materials), and may be affected by residual stresses in both the coating and the stiffener. As previously mentioned, the stiffeners used in this study had some curvature before bonding to the EBC specimens. This pre-curvature would result in considerable variations in the applied  $K$  with flexure because the stored elastic energy of the stiffener would have differed slightly between samples. This is important as the stored energy of the stiffener dominates the strain energy release rate of the composite beam.<sup>268</sup> As such, the residual stress in the stiffener may have contributed significantly to scatter in the data and have had some effect upon the measured toughness. Contributions of the residual stresses in the coating would be small in comparison to residual stress in the bonded stiffener.

Despite the above limitations, the data recorded from this test method appears consistent, Table 8.3. The  $K_I$  and  $K_{II}$  values are of appropriate magnitude considering the mechanical properties reported in Section 8.3.2 for the APS Si layer. As a very broad generality, the mixed-mode critical energy release rate at a phase load angle of  $30^\circ$  is roughly  $1/3$  greater than at phase load angle  $0^\circ$  (pure  $K_I$ ),<sup>236</sup> such that  $K_I = 1.92 \text{ MPa}\cdot\text{m}^{1/2}$  and  $K_{II} = 1.06 \text{ MPa}\cdot\text{m}^{1/2}$  are plausible  $K$  values for the Si-CMC interface when  $G_C$  is attained based upon the properties determined for the Si layer. The test appears very promising for quantitatively determining mixed-mode interface toughness in EBC systems in as-fabricated and aged conditions.

## 8.5 Conclusions

Stand-alone APS  $\text{Yb}_2\text{Si}_2\text{O}_7$  and Si panels have been deposited with approximate dimensions of 130 mm x 65 mm x 13 mm. These stand-alone panels were diamond ground into mechanical properties testing specimens measuring approximately 50 mm x 5 mm x (4 or 3) mm. The specimens were sectioned and their microstructure analyzed. Archimedes density, porosity image analysis measurement, and elastic modulus measurement via impulse excitation of vibration were performed. Low temperature (25 °C) flexure strength, high temperature (900 °C) flexure strength, and fracture toughness of the APS structure have all been measured. Creep behavior of the APS  $\text{Yb}_2\text{Si}_2\text{O}_7$  material has been determined using isothermal and laser thermal gradient 4-point flexure. Creep behavior of the APS Si has been measured using laser thermal gradient 4-point flexure, but heat transfer calculations have indicated that the Si is effectively isothermal. Finite element analysis modeling has been coupled with experimental 4-point flexure stiffener-assisted interphase toughness testing to determine the mixed-mode fracture resistance of an APS Si – MI-CMC interface. The above measurements led to the following conclusions:

- a) Elastic moduli and flexure strengths of APS materials are low when compared to their bulk densified counterparts. The ~90 % dense APS  $\text{Yb}_2\text{Si}_2\text{O}_7$  elastic modulus and flexure strength was reduced by 4-5 times when compared to equi-biaxial data for similar systems. The ~94 % dense APS Si elastic modulus and flexure strength was reduced by 2-3 times when compared to published data for Si of comparable (electronics grade) purity.

- b) Fracture toughness ( $K_{IC}$ ) of the APS structures has been measured for cracks that propagated normal to the coating surface, i.e. in an orientation reflective of coating mud (or channel) cracking. The measured toughness of the APS  $Yb_2Si_2O_7$  was  $0.93 \text{ MPa}\cdot\text{m}^{1/2}$  for a structure that is both porous and contained significant fractions of  $Yb_2SiO_5$ . The measured toughness of the APS Si was  $1.54 \text{ MPa}\cdot\text{m}^{1/2}$  indicating some minor toughening from the APS structure.
- c) Creep rates of the APS  $Yb_2Si_2O_7$  at temperatures above  $900 \text{ }^\circ\text{C}$  are very high. The creep activation energy determined for APS  $Yb_2Si_2O_7$  was  $\sim 155 \text{ kJ/mol}$  with  $n$  determined to be  $\sim 1$ , indicating that steady state creep was a diffusion controlled process in this material.
- d) The high  $Yb_2Si_2O_7$  creep rates suggest that this material may suffer from rapid creep in coating applications for rotating hardware with high centrifugal stresses. The low flow stress also may lead to stress relaxation in thermal gradients, which could have significant effects upon the stress states and strain energy release rates of the coating upon cooling.
- e) The creep activation energy for APS Si was  $\sim 284 \text{ kJ/mol}$ , which is comparable to the activation energy for bulk dislocation creep by glide on the Si  $\langle 111 \rangle$  planes. Creep rates are also comparable to those observed for creep by Si  $\langle 111 \rangle$  dislocation glide.
- f) Interfacial toughness measurements in EBC systems applied to CMCs are possible using a stiffener-modified 4-point flexure testing approach. Testing yields toughnesses that are reasonable for the Si – MI-CMC interface based on the other mechanical properties measured for this system. This testing method will allow for the mixed-mode toughness of aged structures to be assessed in the future.

## 9 Discussion

Through the course of this dissertation, two separate EBC systems with different ytterbium silicate topcoats have been investigated. The first was a tri-layer  $\text{Yb}_2\text{SiO}_5/\text{Al}_6\text{Si}_2\text{O}_{13}/\text{Si}$  system that was identified as a candidate EBC in the mid 2,000's based on preliminary testing.<sup>77,94</sup> A version of this system was deposited by APS using high power deposition parameters at the NASA Glenn Research Center where the initial investigations on the system had been previously performed. Chapters 2 and 3 of this dissertation focus on the analysis of that coating system, which was found to be deficient because of poor adhesion between the silicon bond coat and substrate, interconnected bond coat porosity, and uncontrolled loss of SiO from the ytterbium monosilicate and mullite layers.

In Chapter 5, this same  $\text{Yb}_2\text{SiO}_5$ -based tri-layer system was deposited using an APS process designed to enable deposition using optimized low power spray parameters with the intent of remedying the issues identified in Chapters 2 and 3. Chapter 6 then discussed the performance of this system in steam-cycling, which was found comparable to that of the high power tri-layer EBC despite resolution of the adherence issues identified in that system. The work presented in these chapters are the first reports of

failure mechanisms of the  $\text{Yb}_2\text{SiO}_5/\text{Al}_6\text{Si}_2\text{O}_{13}/\text{Si}$  system in steam-cycling and the first documentations of EBC failure resulting from cristobalite TGO formation.

Due to the relatively short lifetime of the tri-layer ytterbium monosilicate based systems, investigations were redirected to focus on a bi-layer  $\text{Yb}_2\text{Si}_2\text{O}_7/\text{Si}$  system deposited using low power plasma spray parameters at UVA. Deposition of the ytterbium disilicate layer was also detailed in Chapter 5, and the steam-cycling performance of this system was documented in Chapter 7. The  $\text{Al}_6\text{Si}_2\text{O}_{13}$  layer was eliminated due to its propensity for cracking, its high CTE and elastic modulus, its reactivity with  $\text{Yb}_2\text{Si}_2\text{O}_7$  (which penetrates  $\text{Al}_6\text{Si}_2\text{O}_{13}$  grain boundaries), difficulty depositing the desirable high relative density EBC microstructures and no observed interfacial reactions between the ytterbium silicates and silicon in preliminary testing. The resulting system was a bi-layer with total thickness of  $\sim 175 \mu\text{m}$  reduced from  $\sim 275 \mu\text{m}$  for tri-layers. No failures were obtained in steam-cycling of the bi-layer  $\text{Yb}_2\text{Si}_2\text{O}_7/\text{Si}$  EBC with test durations up to 2,000 cycles at  $1316^\circ\text{C}$ , indicating greatly improved durability of this system.

The demonstration of this system's viability through thermocyclic steam testing prompted investigations of the mechanical properties of the component APS layers as a method of assessing their performance when mechanically loaded. Chapter 8 presents this analysis where stand-alone panels of  $\text{Yb}_2\text{Si}_2\text{O}_7$  and Si were plasma sprayed at UVA, machined into mechanical properties specimens, and tested for quasi-static and time-dependent mechanical properties at NASA. The implications of the measured mechanical properties were then interpreted in the context of various EBC applications. This work is the first to report publically the steam erosion resistance of the  $\text{Yb}_2\text{Si}_2\text{O}_7/\text{Si}$  bi-layer system and is the first report of mechanical properties of APS EBC materials.

To this point, the dissertation has been presented in the chronological sequence in which it was performed. This method conveys the evolution of knowledge acquired regarding EBC systems and processing throughout the dissertation, but belies the knowledge gained regarding EBCs as a whole. Therefore, the dissertation will now be reviewed topically in the context of APS processing, the  $\text{Yb}_2\text{SiO}_5/\text{Al}_6\text{Si}_2\text{O}_{13}/\text{Si}$  system and the  $\text{Yb}_2\text{Si}_2\text{O}_7/\text{Si}$  system.

## 9.1 Air Plasma Spray of EBC Materials

Extensive trials were performed to analyze the effects of spray parameter selection upon microstructure throughout this dissertation. Over 200 coatings with individual combinations of spray parameters were deposited and the resulting samples sectioned and analyzed. The fine details of this work have been presented in Chapter 5, but the result was the realization of high relative density layers of Si,  $\text{Al}_6\text{Si}_2\text{O}_{13}$ ,  $\text{Yb}_2\text{SiO}_5$ , and  $\text{Yb}_2\text{Si}_2\text{O}_7$  deposited by the APS process using low power deposition with internal powder injection. The layers of high relative density described in that chapter were attained by iteratively adjusting spray parameters.

Relative densities as high as 95 % were measured for low power deposited Si bond coats, which sharply contrasted the ~80 % relative density of Si layers deposited using high power parameters. Chapter 6 subsequently demonstrated that a high-density bond coat is vital in reducing the rate at which silica forms upon thermocyclic exposure to oxidizing species. High temperature deposition of Si under a reducing environment in the low power APS technique also considerably improved adhesion at both the  $\text{Al}_6\text{Si}_2\text{O}_{13}$  –

Si and Si – SiC interfaces, Figure 6.6 and Figure 6.7. No delamination was observed upon cooling, whereas partial delamination was prolific in high power APS coatings where the Si bond coat was deposited onto ambient temperature SiC substrates, Chapter 3. The difference in interfacial adhesion was related to the less severe quench of deposited splats and the absence of silica and porosity at the interfaces in low power EBCs. Comparable adhesion was not, however, observed at the  $\text{Yb}_2\text{Si}_2\text{O}_7$  – Si interface in the low power depositions of Chapters 7 and 8, suggesting surface wetting issues or chemical incompatibility between  $\text{Yb}_2\text{Si}_2\text{O}_7$  and Si.

$\text{Al}_6\text{Si}_2\text{O}_{13}$  layer relative densities as high as 95 % and ytterbium silicate layer relative densities greater than 98 % were also achieved by low power deposition. Again, the structure of these layers and method of their deposition was presented in Chapter 5. The target application of these ceramic layers is as an environmental barrier, so consistently dense layers are desirable to act as diffusion barriers. High relative density in the  $\text{Yb}_2\text{SiO}_5$  and  $\text{Al}_6\text{Si}_2\text{O}_{13}$  layers, however, comes with the penalty of severe cracking when deposited onto SiC. High relative density  $\text{Yb}_2\text{Si}_2\text{O}_7$  layers, on the other hand, were found to be crack free.

In Chapters 2 and 5, it was demonstrated that non-stoichiometry of these layers resulted from volatilization of Si from the pseudo-binary ytterbium silicate and aluminum silicate layers during APS deposition. This volatilization was shown to occur whether the plasma forming gas was noble (Ar/He mixture, Chapter 2) or reducing (Ar/ $\text{H}_2$  mixture, Chapter 5). The extent of this volatilization was also found to vary considerably in the  $\text{Yb}_2\text{O}_3$  –  $\text{SiO}_2$  system based upon deposition parameters used. Specifically, it was demonstrated in Chapter 5 that the relationships between total volatility and deposition

parameters are not straightforward, i.e. the effect of changing deposition arc current was not the same as for changing secondary H<sub>2</sub> fraction in the plasma forming gas.

From a materials perspective, the relative Si volatilization during processing was controlled by two primary factors. First, the absolute magnitude of Si-bearing species was considered as a measure of the driving force for volatilization. This vapor pressure is controlled by the temperature experienced by particles entrained in the plasma (Chapters 2 and 5). The second factor is the vapor pressure ratio between the dominant Si-bearing and dominant Yb-bearing vapor pressure species. Much like Si, the vapor pressure of Yb-bearing species will dictate their evaporation rate. It was thereby concluded that the relative vapor pressure ratio between the Si-bearing and Yb-bearing species was a critical factor in determining the deviation from stoichiometry experienced during APS deposition. This ratio, however, was found to be constant over the temperature range expected for APS deposition, Figure 5.12. As a result, relative volatility was dominated by changes in the partial pressure of Si-bearing species with temperature.

From an APS processing perspective, the variation of volatility with spray parameter was determined by the thermal history of particles entrained in the plasma plume. This is typically referred to as the temperature – time (T-t) history or the temperature – time – velocity (T-t-v) history. Variation of spray parameters would have directly altered the temperature – time histories of injected particles as discussed in Chapters 1 and 5 and therefore the stoichiometry of the deposits as well. This also explains the variations of stoichiometry between individual splats: particles that spent the greatest duration at high temperature would have experienced the greatest Si volatilization.

Variations of microfracture within the ytterbium silicate layers as a function of deposition parameter were also studied in Chapter 5. The extent of microfracture varied considerably in  $\text{Yb}_2\text{SiO}_5$  layers as a function of spray parameter but not in  $\text{Yb}_2\text{Si}_2\text{O}_7$  layers (except in vertical orientation at the highest powers). However, the angular distribution of microcracking in both was uniform, indicating that the experienced microfracture was equiaxed. At this point, the origins of this variation are not precisely understood. Modeling and diagnostic analyses of the APS process have yet to achieve an understanding of substrate-particle interactions in even the most fundamental metal systems, much less in complicated pseudo-binary oxides that experience complex volatility issues. As such, a plethora of fundamental APS processing and modeling opportunities exist in this complex realm.

Deposition power is frequently used as a measure of the processing conditions in the thermal spray industry, but Chapter 5 has demonstrated the use of deposition power alone to be an insufficient metric of the APS process for the pseudo-binary oxides deposited in this dissertation. Still, broad trends in microstructure were observed with deposition power, Figure 5.7 and Figure 5.11. This was true not only within the low power studies performed at the University (Chapter 5), but also when high power depositions are considered (Chapter 2). At about 3x the deposition power, high power deposited  $\text{Yb}_2\text{SiO}_5$  experienced roughly 3x the Si volatilization, matching the trend line of Figure 5.7.

## 9.2 Performance of the $\text{Yb}_2\text{SiO}_5/\text{Al}_6\text{Si}_2\text{O}_{13}/\text{Si}$ System

Micro and macrofracture were pervasive within as-deposited  $\text{Yb}_2\text{SiO}_5$  layers whether deposited using high power or low power combinations of spray parameters. In high power tri-layer coatings considerable microfracture of the ceramic layers was observed. This microcracking, however, was overshadowed by the extent of partial delamination and channel (mud) cracking. In Chapter 3, partial delaminations were observed to have occurred at the Si – SiC interface of high power EBCs and were found to have originated at coating edges and corners. The delaminations were attributed to insufficient bonding of the interface due to interface porosity and oxidation. Severe edge delamination had resulted in spallation of coatings upon cooling from deposition or the stabilization annealing treatment.

The strain energy release rate (ERR) during delamination at various interfaces within the high power tri-layer coating was also determined in Chapter 3. Among the requisite data for this calculation, the CTE of  $\text{Yb}_2\text{SiO}_5$  was verified by dilatometry to be  $7.5 \times 10^{-6} \text{ }^\circ\text{C}^{-1}$  and the elastic modulus was tested by nano-indentation and found to be 172 GPa. Large tensile thermal residual stresses and accompanying stored elastic strain energy release rate (ERR) of up to 150 N/m were identified as the driving force for mud cracking and partial edge delamination. Mud cracks initiated at the surface, penetrated the  $\text{Yb}_2\text{SiO}_5$  and  $\text{Al}_6\text{Si}_2\text{O}_{13}$  layers, and then terminated at the  $\text{Al}_6\text{Si}_2\text{O}_{13}$  – Si interface in these coatings. That interface was found to have considerable porosity originating from an abundance of very small radius particles that comprised the Si bond coat. The bond coat was also identified to have 20 % porosity, which would have considerably altered the mechanical

properties of this layer when compared to bulk Si, as suggested by the 10 % elastic modulus used in calculations for the APS structure in Chapters 3 and 6.

In Chapter 5, low power depositions eliminated the edge delaminations observed in high power coatings by processing the Si bond coat at elevated temperature (nominally 1200 °C) in a reducing environment (Ar/H<sub>2</sub>). No delaminations were observed despite the tri-layer system having a calculated ERR 60 % higher than the comparable high power deposited system (Chapter 6). Therefore, interfacial adhesion was significantly improved by the refined low power processing of the Si bond coat at high temperature and under a reducing environment. The altered spray parameters, layer thicknesses, and as-deposited defects also resulted in a change of the mud crack spacing: high power tri-layer EBCs had an average mud crack spacing of 280 μm whereas low power EBCs had an average mud crack spacing of 240 μm.

The microstructural analyses of Chapter 6 focused on differences in mud cracking that resulted in a new failure mode in low power tri-layers. The previously mentioned 60 % increase in ERR combined with the different coating configuration resulted in cracks bifurcating at interfaces and large defects within the Al<sub>6</sub>Si<sub>2</sub>O<sub>13</sub> layer, as shown in Figure 6.8. The bifurcation behavior was assessed using Finite Element Analysis (FEA) and J-integral calculation of ERR, and was found to be unfavorable in both the low power and high power systems. However, the energy release for following large (10-20 μm) defects was assessed and suggests a large energy release for following defects in both systems. The origins of bifurcation have not been conclusively identified, but are clearly linked to the plethora of defects in the APS structure. Further modeling efforts are needed to fully understand the factors that control bifurcation behavior.

The divergent mud cracking behavior detailed in Chapters 3 and 6 illustrates the difference that small microstructural changes may have upon APS EBC behavior. This slight difference in initial cracking resulted in significant consequences for the long-term behavior in steam-cycling. In Chapter 3, it was demonstrated that the high power EBC microstructure leads to penetration of oxidizers down mud cracks and the subsequent formation of a cristobalite thermally grown oxide (TGO) at the  $\text{Al}_6\text{Si}_2\text{O}_{13}$  – Si interface during cycling in flowing 90 %  $\text{H}_2\text{O}$ /10 %  $\text{O}_2$ . This TGO grew rapidly and was severely microcracked. The microcracking was attributed to the  $\beta \rightarrow \alpha$  inversion-type phase transformation in cristobalite upon cooling through  $\sim 220$  °C, which is accompanied by a  $\sim 4.5$  vol% contraction. The microfracture compromises the protective abilities of normally dense, vitreous  $\text{SiO}_2$  scales.

Growth of the TGO and the extent of its cracking was most severe at coating edges in high power deposited tri-layers. Ultimate failure occurred by spallation of the upper layers of the coating by interlinked TGO microfracture, which always initiated at the sample edge and propagated towards the sample center. Oxidizer penetration appears to have occurred through the poorly bonded  $\text{Al}_6\text{Si}_2\text{O}_{13}$  – Si interface. Based on cross-sectional imaging of the failed coatings such as Figure 3.6, it was hypothesized that a three-dimensional network of void space was developed below mud cracks that allowed for gas path diffusional access from the coating edges.

On the other hand, high temperature thermocyclic exposure of low power deposited tri-layers (described in Chapter 6) found that bifurcated mud crack ligaments propagated through the mid-plane of the Si layer in the form of delamination cracks, the faces of which were covered by a cristobalite TGO. The cristobalite thickness observed on crack

faces at 250 cycles was  $\sim 15 \mu\text{m}$ , representing a significant decrease in oxidation from the high power EBC. A cyclic crack growth mechanism was proposed wherein oxidation occurred at the tip of the crack in the Si layer during the hot cycle and then was subsequently microfractured during the cold cycle by the cristobalite  $\beta \rightarrow \alpha$  phase transformation. This process cyclically advanced the delamination crack. Eventual linkage of these delamination cracks resulted in spallation.

Unlike the high power deposited system, failure in the low power deposited  $\text{Yb}_2\text{SiO}_5/\text{Al}_6\text{Si}_2\text{O}_{13}/\text{Si}$  EBCs occurred uniformly across the coating. Microstructural examination also revealed the extent of oxidation to be consistent across specimens: no selective edge attack was observed. This was verified by examination of the coating edges, where no delaminations initiated at the coating edge were identified. Therefore, the revised low power processing contributed to significantly enhanced interface bonding that effectively eliminated environmental attack of interfaces, removing both quasi-static and time-dependent edge damage mechanisms.

Both high power and low power EBCs failed before 800 steam cycles. Statistical analyses of the lifetime data indicated neither a difference in mean lifetime nor a difference in the variance of the lifetime between the two tri-layer EBC systems. Despite the delayed onset of failure in low power EBCs, it is clear that no significant improvement in coating lifetime was achieved through the revised low power deposition. The properties of this system appear to be such that the upper limit of durability is below 1,000 steam cycles at  $1316^\circ\text{C}$ .

### 9.3 Environmental and Mechanical Behavior of the $\text{Yb}_2\text{Si}_2\text{O}_7/\text{Si}$ System

Bi-layer  $\text{Yb}_2\text{Si}_2\text{O}_7/\text{Si}$  coatings were found to be free of both mud cracks and delamination cracks. Microfracture was also greatly reduced in comparison to  $\text{Yb}_2\text{SiO}_5$ -based tri-layers. At a fundamental level, the difference in CTE between the two ytterbium silicates was the property responsible for the differences in cracking: in this dissertation  $\text{Yb}_2\text{Si}_2\text{O}_7$  was measured to have a CTE of  $\sim 4.1 \times 10^{-6} \text{ }^\circ\text{C}^{-1}$  compared to the  $\alpha$ -SiC reported value of  $\sim 4.67 \times 10^{-6} \text{ }^\circ\text{C}^{-1}$ . The elastic modulus measured by nano-indentation for  $\text{Yb}_2\text{Si}_2\text{O}_7$  was 180 GPa. One other important difference was the elimination of the  $\text{Al}_6\text{Si}_2\text{O}_{13}$  layer. From a coating design standpoint, minimization of both thickness and the number of coating layers is desirable. With the removal of the  $\text{Al}_6\text{Si}_2\text{O}_{13}$  layer, the entire coating was predicted to develop a small, compressive residual stress upon cooling, as detailed in Chapter 7. The revised system also had extremely low ERRs ( $\sim 10 \text{ N/m}$ ) in its pre-exposed state.

A thin, porous  $\text{Yb}_2\text{SiO}_5$  layer was found on the outer surface of the  $\text{Yb}_2\text{Si}_2\text{O}_7$  layer after 2,000 cycles of testing. This layer was observed only when the steam-cycling apparatus was not near saturation in  $\text{Si}(\text{OH})_4$  volatilized from exposed  $\text{SiO}_2$  grown on SiC (only the 2,000 cycle sample). The  $\text{Yb}_2\text{SiO}_5$  layer was determined to result from  $\text{SiO}_2$  volatilization from  $\text{Yb}_2\text{Si}_2\text{O}_7$ , which was accompanied by a 26 vol% reduction. This produced a porous  $\text{Yb}_2\text{SiO}_5$  surface layer that was found to be severely cracked or partially spalled, presumably due to its high CTE and the thermo-cyclic nature of testing. The volatilization is consistent with prior weight loss and steam jet characterization of  $\text{Yb}_2\text{Si}_2\text{O}_7$  in flowing steam environments.<sup>78,258</sup> Further controlled cyclic volatility

investigations are necessary to determine the performance of  $\text{Yb}_2\text{Si}_2\text{O}_7$  in high flow thermocyclic conditions typical of gas turbine applications.

Edge attack was also observed during steam-cycling of the  $\text{Yb}_2\text{Si}_2\text{O}_7/\text{Si}$  bi-layers. This occurred through oxidation of the Si bond coat to cristobalite with a 100 % volume increase. Oxidizers penetrated the  $\text{Yb}_2\text{Si}_2\text{O}_7 - \text{Si}$  interface and caused continuing oxidation inwards along the interface. The cristobalite formed by oxidation of the bond coat was subsequently volatilized or mechanically spalled at coating edges, allowing further oxidizer penetration. The volumetric expansion of the Si bond coat upon oxidation led to the coating edge lifting phenomenon pictured in Figure 7.13, the severity of which increased with greater exposure.

In Chapter 7, high temperature thermocyclic exposure in the slowly flowing 90 %  $\text{H}_2\text{O}/10\%$   $\text{O}_2$  environment led to the formation of a cristobalite TGO at the  $\text{Yb}_2\text{Si}_2\text{O}_7 - \text{Si}$  interface. Neither mud cracking nor spallation of the coatings was observed in exposures of up to 2,000 cycles. The mechanical driving forces were assessed for the system with cristobalite scales grown at the  $\text{Yb}_2\text{Si}_2\text{O}_7 - \text{Si}$  interface and the calculated ERR was less than 20 N/m for all interfaces at a cristobalite TGO thickness of 5  $\mu\text{m}$ , twice that observed at 2,000 steam cycles of exposure. The low ERR supports the absence of cracking in this system even after significant cristobalite formation.

The thickness of the TGO was measured after various exposure times and found to follow linear growth kinetics. The linear oxidation rate constant  $k_l$  was measured to be 1.44 nm/h when normalized to a 100  $\mu\text{m}$   $\text{Yb}_2\text{Si}_2\text{O}_7$  diffusion barrier thickness, Figure 7.7(b). As mentioned in Chapter 7, this TGO growth rate represents a 1-2 order of

magnitude reduction when compared to that found in the  $\text{Yb}_2\text{SiO}_5/\text{Al}_6\text{Si}_2\text{O}_{13}/\text{Si}$  system. The linear oxidation behavior is also in contradiction to the typically established parabolic growth of protective oxides such as  $\text{SiO}_2$ , and indicates that the rate-limiting diffusion step was not transport through the growing scale. Rather, the growth rate of the TGO was limited by diffusion of the oxidizing species through the  $\text{Yb}_2\text{Si}_2\text{O}_7$  environmental barrier layer.  $k_t$  was used to calculate an oxygen flux ( $J_O$ ) through this layer, which was subsequently used to solve Fick's First Law for an effective monatomic oxygen diffusion coefficient.  $D_O = 3 \times 10^{-15} \text{ m}^2\text{s}^{-1}$  for  $\text{Yb}_2\text{Si}_2\text{O}_7$  at 1316 °C.

The thickness at which the oxidation behavior would transition from linear growth controlled by diffusion through the  $\text{Yb}_2\text{Si}_2\text{O}_7$  layer to parabolic growth controlled by diffusion through a growing, dense cristobalite scale was calculated using the diffusion coefficient found for  $\text{Yb}_2\text{Si}_2\text{O}_7$  and published data for monatomic oxygen diffusion through cristobalite<sup>261</sup>. The transition scale thickness was determined to be  $\sim 2.24 \mu\text{m}$  for the coating configuration tested, which is below the TGO thickness observed in the 2,000 cycle test. However, the TGO was found to be channel (mud) cracked, such that short circuit oxidizer diffusion would have been the dominant transport mechanism. Accordingly, it was determined in Chapter 7 that oxidation of the Si bond coat would continue at a linear rate indefinitely.

Based on the steam-cycling testing and observed oxidation behavior, the  $\text{Yb}_2\text{Si}_2\text{O}_7/\text{Si}$  system was concluded to be a potential candidate for 1316 °C isothermal applications. Volatility of the topcoat may be a concern, but the volatilization and spallation behavior of the surface layer have yet to be addressed. One method to avoid the volatilization would be to deposit a more environmentally stable layer above the bi-layer. Such a

configuration would be necessary for (rotating) applications where total thickness is a concern, but for stationary hardware it may be possible to simply use very thick coatings such that repeated surface spallation is tolerable.

In Chapter 8, mechanical properties investigations were performed upon APS  $\text{Yb}_2\text{Si}_2\text{O}_7$  and APS Si materials as a proxy for assessment of stressed environmental exposure. As such, the testing is anticipated to be considerably less severe than the true environment experienced by rotating hardware. Fracture toughness, low temperature flexure strength, high temperature flexure strength, and creep were all examined to the extent possible based on the limited number of specimens. Elastic modulus, low temperature flexure strength, and high temperature flexure strength were all tested according to ASTM standards. Fracture toughness was determined by a single edge V-notched bending (SEVNB) technique.<sup>264,265</sup> Creep behavior was tested in 4-point flexure both with and without thermal gradients imposed upon the specimen.

The mechanical properties of as deposited, ~10 % porous APS  $\text{Yb}_2\text{Si}_2\text{O}_7$  were significantly altered when compared to those of similar bulk material (hot pressed or spark plasma sintered). Quasi-static properties were all reduced by roughly a factor of 5 when compared to bulk properties. This trend is well established for APS ceramic materials which can have reductions in elastic modulus in the as-deposited condition in the range of 2-10x.<sup>120,122,124</sup> Reductions in the flexure strength were also considerable, but these were explained by porosity and the presence of  $\text{Yb}_2\text{SiO}_5$  in Chapter 8. The toughness of the APS  $\text{Yb}_2\text{Si}_2\text{O}_7$  structure was measured to be roughly half that of bulk material. Creep rates of APS  $\text{Yb}_2\text{Si}_2\text{O}_7$  were extremely high: 1 % creep strain was observed in testing after 25 h at only 900 °C with a load of only 15.8 MPa. Creep

activation energy was in the realm of 150 kJ/mol. The extremely high creep rates and low activation energy signify that this material is incapable of bearing the stresses seen in rotating hardware.

The mechanical properties of as-deposited ~6 % porous APS Si were also altered. Elastic modulus, low temperature flexure strength, and high temperature flexure strength were all reduced by a factor of 2-3 when compared to bulk material. Unlike all other properties, the fracture toughness ( $K_{IC}$ ) of the APS Si was slightly increased when compared to bulk polycrystalline Si. The increase in toughness was attributed to the presence of porosity, intrasplat boundaries, and minor intrasplat oxidation functioning as crack arresting or blunting mechanisms in Chapter 8. Reductions in both low and high temperature flexure strength were reasonable based on the porosity of the material. Creep rates and creep activation energy of the APS Si were comparable to dislocation glide on the  $\langle 111 \rangle$  planes of bulk Si polycrystal. The similarity in creep rate and activation energy to bulk material indicates that bulk Si properties may be used to approximate the creep behavior of the APS material.

The altered mechanical behavior of the APS  $Yb_2Si_2O_7$  and Si materials indicates that the use of bulk properties is inappropriate for APS materials systems. Materials property data will need to be determined for individual coating microstructures to accurately model EBC system behavior. Perhaps most importantly, the mechanical properties of the presently considered bi-layer  $Yb_2Si_2O_7$ /Si system are insufficient for mechanically loaded (rotating) systems. Fracture toughness, low temperature flexure strength, and high temperature flexure strength are all low. For the prime-reliant EBC application, these properties are concerning. However, the most important issue identified in Chapter 8 was

the extremely poor creep performance of  $\text{Yb}_2\text{Si}_2\text{O}_7$ . In isothermal applications, this poor creep performance is likely acceptable. For rotating components, however, the very high creep rates are grossly inadequate and would literally lead to the coating creeping off of the component.

## **10 Conclusions**

This dissertation has broadly addressed the four goals initially stated: (i) APS capabilities have been developed at UVA and the relationships between deposition parameters and the microstructure of deposited coating layers studied. (ii) The steam-cycling behavior of the tri-layer  $\text{Yb}_2\text{SiO}_5/\text{Al}_6\text{Si}_2\text{O}_{13}/\text{Si}$  EBC system has been examined. Both high power and low power APS deposited versions were critically analyzed and compared. (iii) Insights from processing studies were combined with lessons learned from the two  $\text{Yb}_2\text{SiO}_5/\text{Al}_6\text{Si}_2\text{O}_{13}/\text{Si}$  systems to select, deposit and test a revised bi-layer  $\text{Yb}_2\text{Si}_2\text{O}_7/\text{Si}$  EBC with greatly improved performance in steam-cycling. (iv) Mechanical properties tests of APS  $\text{Yb}_2\text{Si}_2\text{O}_7$  and Si materials have been used as a metric to assess the viability of this system for mechanically loaded (rotating) hardware.

The primary results from this work have been addressed topically in the discussion, and following that format will now be presented based upon their relevance to APS Deposition, the  $\text{Yb}_2\text{SiO}_5/\text{Al}_6\text{Si}_2\text{O}_{13}/\text{Si}$  EBC system, and the  $\text{Yb}_2\text{Si}_2\text{O}_7/\text{Si}$  EBC system. Finally, the entire dissertation will be closed with suggested avenues for future research.

## 10.1 APS Deposition

- Very dense layers of Si,  $\text{Al}_6\text{Si}_2\text{O}_{13}$ ,  $\text{Yb}_2\text{SiO}_5$ , and  $\text{Yb}_2\text{Si}_2\text{O}_7$  can be deposited by the Air Plasma Spray (APS) process using low power deposition with internal powder injection. Relative densities as high as 95 % were measured for Si bond coats, which contrasts the ~80 % density of Si layers deposited using high power parameters.  $\text{Al}_6\text{Si}_2\text{O}_{13}$  relative densities as high as 95 % and ytterbium silicate relative densities as high as 99 % were achieved. High relative density is important in the bond coat to reduce the rate at which thermally grown silica forms upon thermocyclic exposure to oxidizers, and important for ceramic layers of the EBC to reduce oxidizer diffusion to the surface of the underlying bond coat. Careful spray parameter selection and well controlled deposition are imperative in achieving target microstructures.
- Volatilization of Si occurred from the pseudo-binary  $\text{Yb}_2\text{O}_3 - \text{SiO}_2$  system during APS deposition. The volatilization occurred whether the plasma forming gas was an Ar/He mixture or a reducing Ar/ $\text{H}_2$  mixture. Vapor pressure curves for relevant species were calculated as a function of temperature and indicate that the relative Si volatilization during plasma spraying was controlled by the absolute magnitude of Si-bearing species vapor pressure and the vapor pressure ratio between Si-bearing and Yb-bearing species. The magnitude of Si-bearing species vapor pressure increased considerably with temperature while the vapor pressure ratio remained constant. This indicates that the temperature – time history of a particle during the deposition process directly controlled its chemistry.

- Low power deposition of the Si bond coat at elevated temperature in a reducing environment (Ar/H<sub>2</sub>) considerably improved adhesion at both the Al<sub>6</sub>Si<sub>2</sub>O<sub>13</sub> – Si and Si – SiC interfaces. No partial delamination or spallation of coatings deposited under these conditions was observed, while partial delamination and spallation were prolific in those high power coatings where the Si was sprayed onto an ambient temperature SiC substrate in air. The difference in interfacial adherence is related to both the slower cooling rate of deposited splats and the absence of silica and pores at these interfaces. Comparable adhesion was not, however, observed at the Yb<sub>2</sub>Si<sub>2</sub>O<sub>7</sub> – Si interface, suggesting surface wetting issues or chemical incompatibility.

## 10.2 Yb<sub>2</sub>SiO<sub>5</sub>/Al<sub>6</sub>Si<sub>2</sub>O<sub>13</sub>/Si Tri-layer EBC

- Extensive macrofracture (mud cracking) and microfracture of as-deposited and annealed Yb<sub>2</sub>SiO<sub>5</sub> layers was consistent with the development of high tensile stresses and stored elastic strain energy release rate (ERR) upon cooling from elevated temperature. Channel (mud) cracking was observed with an average crack spacing of 280 μm in high power coatings and 240 μm in low power coatings (high scatter due to 3D structure with standard deviation of approximately 100 μm in both cases). Severe microcracking of Yb<sub>2</sub>SiO<sub>5</sub> layers occurred despite the large energy release by mud cracking. The ERR calculated for this system (75-150 N/m depending upon elastic moduli assumed) and the extent of cracking reflect the coefficient of thermal expansion mismatch: Yb<sub>2</sub>SiO<sub>5</sub> was found to have a CTE of 7.5 x10<sup>-6</sup> °C<sup>-1</sup> versus only

$4.67 \times 10^{-6} \text{ }^\circ\text{C}^{-1}$  for SiC. This indicates the paramount importance of CTE as a design criterion for environmental barrier layers.

- Small differences in the deposited structure of  $\text{Yb}_2\text{SiO}_5/\text{Al}_6\text{Si}_2\text{O}_{13}$  tri-layers affect fracture behavior. High power EBCs had a  $\sim 75 \text{ } \mu\text{m}$   $\text{Yb}_2\text{SiO}_5$  topcoat and a  $\sim 20 \%$  porous Si bond coat. Low power EBCs had a  $\sim 125 \text{ } \mu\text{m}$   $\text{Yb}_2\text{SiO}_5$  topcoat and  $\sim 5 \%$  porous Si bond coat. The difference in topcoat thickness led to  $\sim 60 \%$  higher ERR in the low power EBC while the disparity in bond coat density led to greatly varying compliance. This resulted in mud crack termination at the  $\text{Al}_6\text{Si}_2\text{O}_{13} - \text{Si}$  interface in the high power system whereas bifurcation occurred in the low power system. The bifurcation behavior was assessed using Finite Element Analysis (FEA) and J-integral calculation of ERR, and was found to be unfavorable in both systems. It was also identified that the energy release by following defects (cracks or poorly bonded boundaries) in the coating is very large, so that microstructure plays a dominant role in crack path selection. Further modeling is needed to determine the exact circumstances that result in bifurcation, but modeling is clearly a powerful tool for investigation of mechanical phenomena and design criteria in EBCs.
- In high power EBCs where mud cracks terminated at the  $\text{Al}_6\text{Si}_2\text{O}_{13} - \text{Si}$  interface, high temperature thermocyclic exposure in  $90 \%$   $\text{H}_2\text{O}/10 \%$   $\text{O}_2$  led to the formation of a cristobalite  $\text{SiO}_2$  scale at the  $\text{Al}_6\text{Si}_2\text{O}_{13} - \text{Si}$  interface. This thermally grown oxide (TGO) microcracked severely at thicknesses greater than a few micrometers. The

microcracking is attributed to the reversible  $\beta \rightarrow \alpha$  transformation in cristobalite at  $\sim 220$  °C, which is accompanied by a  $\sim 4.5$  vol% reduction. The large volume change causes the severe microfracture observed, and creates high diffusivity pathways that compromise the protective ability of the TGO. TGO thicknesses as great as  $100 \mu\text{m}$  were grown in 400 cycles (400 hot hours). Severe preferential attack was observed at coating corners and edges with the greatest TGO thicknesses found in these locations. There, the cristobalite scale grew rapidly at the  $\text{Al}_6\text{Si}_2\text{O}_3 - \text{Si}$  interface and eventually led to delamination crack propagation to the nearest mud crack. This led to progressive spallation of the upper layers of the coating starting from the sample edge and progressing towards the center.

- In low power EBCs where mud cracks bifurcated, high temperature thermocyclic exposure in 90 %  $\text{H}_2\text{O}/10$  %  $\text{O}_2$  led to propagation of the bifurcated mud crack ligaments through the mid-plane of the Si layer. The faces of these delamination cracks were covered by a cristobalite TGO. Microfracture of the TGO was found to be oriented exclusively in the surface normal direction to the delamination crack. Minimal oxidation was observed at the  $\text{Al}_6\text{Si}_2\text{O}_{13} - \text{Si}$  interface with this bifurcation mechanism, indicating that the upper layers of the EBC had successfully protected the Si bond coat in these areas. The delamination cracks grew through the Si bond coat by cyclic extension, with eventual spallation resulting from linkage of delamination cracks. Unlike high power deposited tri-layers, failure was not localized to edges of the sample and damage appeared uniform in cross-section. This indicates that interfacial adhesion plays a significant role in the oxidation damage.

- The premature failure of this coating system is reflective of both the thermomechanical incompatibility of the coating layers with the substrate and the formation of cristobalite: all  $\text{Yb}_2\text{SiO}_5/\text{Al}_6\text{Si}_2\text{O}_{13}/\text{Si}$  tri-layer EBCs failed before 800 steam cycles of exposure. The mean lifetime and variance in lifetime were not statistically different between high power EBCs and low power EBCs despite the considerable difference in failure mechanism observed between these two coatings. The massive ERRs resulting from cristobalite formation necessitate mitigation strategies. If acceptable durability is to be achieved, either: (i) the formation of cristobalite must be entirely eliminated, (ii) the  $\beta$  phase only must be stabilized to avoid phase transformation and the high CTE  $\alpha$  phase, or (iii) the formation rate of cristobalite must be drastically reduced. The first two options will require alternate bond coats or intermediate layers, whereas the third option may be implemented by greatly reducing oxidizer access to the bond coat.

### 10.3 $\text{Yb}_2\text{Si}_2\text{O}_7/\text{Si}$ Bi-layer EBC

- Channel (mud) cracking was not observed in the  $\text{Yb}_2\text{Si}_2\text{O}_7$  system and microfracture was greatly reduced in comparison to the  $\text{Yb}_2\text{SiO}_5$  systems. The differences in macrofracture and microfracture resulted from the greatly improved CTE match between  $\text{Yb}_2\text{Si}_2\text{O}_7$  and SiC:  $4.1 \times 10^{-6} \text{ }^\circ\text{C}^{-1}$  for  $\text{Yb}_2\text{Si}_2\text{O}_7$  versus  $4.67 \times 10^{-6} \text{ }^\circ\text{C}^{-1}$  for SiC. No delamination or spallation of  $\text{Yb}_2\text{Si}_2\text{O}_7/\text{Si}$  bi-layer EBCs occurred during the deposition process or the subsequent stabilization annealing treatment. The absence

of mud cracking, delamination, and spallation has been further rationalized by the calculation of low, compressive thermal residual stresses and very small ERRs (<10 N/m). In the sense of coating mechanics, materials such as  $\text{Yb}_2\text{Si}_2\text{O}_7$  with slightly lower CTE than the substrate are excellent candidates for environmental barrier layers since the elimination of cracking also eliminates short circuit oxidizer diffusion paths to the bond coat.

- Minimal damage was observed in  $\text{Yb}_2\text{Si}_2\text{O}_7/\text{Si}$  bi-layer exposures up to 2,000 cycles. However, edge attack occurred during cycling wherein the Si bond coat was oxidized to cristobalite (with a ~100 % volume expansion) and subsequently volatilized and mechanically spalled at coating edges. The volumetric expansion led to the observed coating edge lifting phenomenon. Volatilization of  $\text{SiO}_2$  from the surface of the  $\text{Yb}_2\text{Si}_2\text{O}_7$  layer was also identified.  $\text{SiO}_2$  volatilization from  $\text{Yb}_2\text{Si}_2\text{O}_7$  was accompanied by a 26 vol% reduction resulting in a porous  $\text{Yb}_2\text{SiO}_5$  surface layer that was found to be severely cracked or partially spalled. Volatilization appears to have occurred via a gas path diffusion route through the open porous network formed in the  $\text{Yb}_2\text{SiO}_5$ . Adhesion of the  $\text{Yb}_2\text{Si}_2\text{O}_7 - \text{Si}$  interface and volatilization of  $\text{SiO}_2$  from  $\text{Yb}_2\text{Si}_2\text{O}_7$  are both concerns for the long term durability of this system.
- High temperature thermocyclic exposure in 90 %  $\text{H}_2\text{O}/10$  %  $\text{O}_2$  still led to the formation of a cristobalite TGO at the  $\text{Yb}_2\text{Si}_2\text{O}_7 - \text{Si}$  interface. The thickness of the cristobalite TGO was measured after various exposure times and found to follow linear growth kinetics. The linear growth rate ( $k_l$ ) was 1.44nm/h when normalized to a

100  $\mu\text{m}$   $\text{Yb}_2\text{Si}_2\text{O}_7$  layer thickness, which represents a two order of magnitude reduction when compared to cristobalite growth rates in the  $\text{Yb}_2\text{SiO}_5/\text{Al}_6\text{Si}_2\text{O}_{13}/\text{Si}$  system. An effective monatomic oxygen diffusion coefficient ( $D_O$ ) through the APS  $\text{Yb}_2\text{Si}_2\text{O}_7$  layer was calculated based on  $k_l$  and found to be  $D_O = 3.11 \times 10^{-15} \text{ m}^2\text{s}^{-1}$ . The relatively low oxygen diffusivity of this layer and its lack of cracking indicate that it has great merit as an environmental (diffusion) barrier layer for SiC.

- The mechanical properties of as-deposited  $\sim 10\%$  porous APS  $\text{Yb}_2\text{Si}_2\text{O}_7$  were significantly altered compared to those of bulk material. Neither quasi-static nor time-dependent bulk material properties were applicable to APS  $\text{Yb}_2\text{Si}_2\text{O}_7$ .
- Elastic modulus, low temperature flexure strength, and high temperature flexure strength were all reduced  $\sim 5\text{x}$  when compared to bulk material properties (some variation based on stoichiometry of the reference silicate).
- The toughness of the APS structure was reduced by a factor of 2 when compared to dense, bulk material.
- Creep rates of APS  $\text{Yb}_2\text{Si}_2\text{O}_7$  were extremely high: 1 % creep strain was observed in testing after 25 h at only 900 °C and with a load of only 15.8 MPa.
- Creep activation energy was in the realm of 150 kJ/mol, which is within the activation energy regime for surface diffusion processes.

The low toughness and flexure strength of  $\text{Yb}_2\text{Si}_2\text{O}_7$  are undesirable for loaded applications, but could be tolerated due to the layer's excellent functionality as a diffusion barrier. However, when the very poor creep performance of the material is taken into account, it is clear that  $\text{Yb}_2\text{Si}_2\text{O}_7$  cannot be used in loaded applications.

- The mechanical properties of as-deposited ~6 % porous APS Si were generally altered when compared to those of bulk material. Quasi-static bulk material properties were found to be inappropriate for APS Si, but time-dependent properties were similar in the range of temperatures and stresses examined.
- Elastic modulus, low temperature flexure strength, and high temperature flexure strength were all reduced by a factor of 2-3 when compared to bulk material.
- Fracture toughness ( $K_{IC}$ ) was slightly increased when compared to bulk Si, presumably due to toughening mechanisms active at splat boundaries.
- Creep rates and creep activation energy were comparable to dislocation glide on the  $\langle 111 \rangle$  planes of bulk Si polycrystal.

The low toughness and flexure strength of Si combined with relatively high creep rates indicate that the material would be undesirable in loaded applications.

## 10.4 Future Work

This dissertation has exposed severe mechanical weaknesses in both the Si bond coat and the ytterbium disilicate topcoat of baseline EBC systems. For rotated applications, these issues will need to be addressed. Si bond coats also suffer from formation and long term stability cristobalite, which *must* be avoided in future bond coats. Potential research directions that address the shortcomings of the  $\text{Yb}_2\text{Si}_2\text{O}_7/\text{Si}$  baseline EBC system will now be addressed. Development areas include bond coats, environmental barrier layers, topcoats, modeling efforts, and more advanced EBC systems.

### ***10.4.1 Bond Coat***

One method for improving the properties of the bond coat is to form a composite between Si and another material. So long as a relatively uniform distribution of Si exists in the bond coat, diffusing oxidizers will still react with Si before reaching the substrate. Hafnia is a particularly appealing material to use for composite applications because it has a relatively low CTE ( $\sim 6 \times 10^{-6} \text{ }^\circ\text{C}^{-1}$ )<sup>276</sup> and the highest environmental stability of known oxides in water vapor containing environments.<sup>196</sup> Hafnia-silicon bond coat systems have been explored at the NASA Glenn research center,<sup>277</sup> but much work is still needed to fully understand their behavior due to the great number of compounds that can form in the system at various temperatures<sup>278</sup>. The system is also particularly appealing because thermally grown silica reacts with hafnia to form hafnium silicate ( $\text{HfSiO}_4$ - CTE in  $3.6\text{-}5.5 \times 10^{-6} \text{ }^\circ\text{C}^{-1}$  range<sup>277,279</sup>),<sup>280</sup> which should eliminate problems associated with cristobalite transformation provided that oxidation rates are lower than the hafnia-silicon reaction rate.

### ***10.4.2 Environmental Barrier Layer***

The extremely high creep rates of ytterbium disilicate are a primary concern. The creep of this material is likely to be best addressed by one of two methods. First, the diffusion coefficient of this material could be significantly altered by doping. Many of the rare earth silicates are isomorphous, so a multi-RE disilicate could have significantly reduced diffusion coefficient and thereby reduced diffusional creep (assuming creep is

bulk diffusion based). This would also have the dual benefit of reducing oxidizer diffusion, improving the layers functionality as an environmental barrier. Second, Eshelby strengthening could be used to enhance the creep performance. This is akin to dispersoid strengthening, and has considerable potential if an acceptable strengthening particle/material could be identified. Again, hafnia is a possibility for this application, though it will react with ytterbium disilicate<sup>260</sup>.

#### ***10.4.3 Thermal Barrier Layer***

A thermal barrier layer has been suggested for use above the environmental barrier layer to serve both a TBC-type function and help mitigate CMAS attack. Hafnia and stabilized hafnia layers are particularly appealing for a number of reasons, including stability of reaction products with ytterbium silicates.<sup>64,260</sup> Investigating the properties of systems implementing hafnia TBCs as the outermost layer will be highly desirable. Both vapor deposited and plasma sprayed forms of this system are appealing. The University has the requisite equipment and experience to study both approaches.

#### ***10.4.4 Modeling***

Modeling of EBCs will be extremely useful in identifying practical materials design spaces. Since the design constraints of EBCs are so unique for a protective coating system, some guidance on the property space of mechanically viable coatings is extremely important. Evaluation of the demands of CTE, elastic modulus, strength,

toughness and creep are particularly interesting for EBCs targeted at both isothermal and thermal gradient applications.

#### *10.4.5 Advanced Systems*

As indicated in Chapter 1, the drive to increase operating temperature is enormous. Future developments are targeted at 1482 °C (2700 °F) surface temperature of bond coats with topcoats at 1649 °C (3000 °F).<sup>277</sup> This is above the melting point of silicon, so no free silicon will be permissible in such systems. These systems will require new classes of materials, and are not likely to be championed by universities due to the demands of testing large numbers of materials and the associated personnel and raw materials costs. Experimentation with such systems has already been conducted at NASA and turbine engine OEMs over the last several years. However, there may be opportunities for university involvement through fundamental scientific investigations of the performance of simple systems such as the rare earth silicides.

## 11 References

1. M. P. Boyce, "Gas turbine engineering handbook." Butterworth-Heinemann, (2011).
2. T. Giampaolo, "The gas turbine handbook: Principles and practices." Marcel Dekker Incorporated, (2003).
3. P. P. Walsh and P. Fletcher, "Gas turbine performance." Blackwell Science, Limited, (2004).
4. J. H. Perepezko, "The hotter the engine, the better," *Science*, 326[5956] 1068-69 (2009).
5. J. T. DeMasi-Marcin and D. K. Gupta, "Protective coatings in the gas turbine engine," *Surface and Coatings Technology*, 68–69[0] 1-9 (1994).
6. J. C. Williams and E. A. Starke Jr, "Progress in structural materials for aerospace systems," *Acta Materialia*, 51[19] 5775-99 (2003).
7. B. J. McBride and S. Gordon, "Computer program for calculation of complex chemical equilibrium compositions and applications, II. Users manual and program description," *NASA reference publication*, 1311 84-85 (1996).
8. A. G. Evans, D. Mumm, J. Hutchinson, G. Meier, and F. Pettit, "Mechanisms controlling the durability of thermal barrier coatings," *Progress in materials science*, 46[5] 505-53 (2001).
9. A. Evans and J. Hutchinson, "The mechanics of coating delamination in thermal gradients," *Surface and Coatings Technology*, 201[18] 7905-16 (2007).
10. H. Zhao, Z. Yu, and H. N. Wadley, "The influence of coating compliance on the delamination of thermal barrier coatings," *Surface and Coatings Technology*, 204[15] 2432-41 (2010).
11. M. R. Begley and H. N. Wadley, "Delamination of Ceramic Coatings with Embedded Metal Layers," *Journal of the American Ceramic Society*, 94[s1] s96-s103 (2011).
12. M. R. Begley and H. N. Wadley, "Delamination resistance of thermal barrier coatings containing embedded ductile layers," *Acta Materialia*, 60[6] 2497-508 (2012).
13. A. Davis and A. Evans, "Some effects of imperfection geometry on the cyclic distortion of thermally grown oxides," *Oxidation of metals*, 65[1-2] 1-14 (2006).
14. A. Davis and A. Evans, "Effects of bond coat misfit strains on the rumpling of thermally grown oxides," *Metallurgical and Materials Transactions A*, 37[7] 2085-95 (2006).

15. Z. Yu, H. Zhao, and H. N. Wadley, "The Vapor Deposition and Oxidation of Platinum-and Ytria-Stabilized Zirconia Multilayers," *Journal of the American Ceramic Society*, 94[8] 2671-79 (2011).
16. S. Krämer, J. Yang, C. G. Levi, and C. A. Johnson, "Thermochemical Interaction of Thermal Barrier Coatings with Molten CaO–MgO–Al<sub>2</sub>O<sub>3</sub>–SiO<sub>2</sub> (CMAS) Deposits," *Journal of the American Ceramic Society*, 89[10] 3167-75 (2006).
17. S. Krämer, J. Yang, and C. G. Levi, "Infiltration-Inhibiting Reaction of Gadolinium Zirconate Thermal Barrier Coatings with CMAS Melts," *Journal of the American Ceramic Society*, 91[2] 576-83 (2008).
18. R. Wellman and J. Nicholls, "Erosion, corrosion and erosion–corrosion of EB PVD thermal barrier coatings," *Tribology International*, 41[7] 657-62 (2008).
19. J. Nicholls, M. Deakin, and D. Rickerby, "A comparison between the erosion behaviour of thermal spray and electron beam physical vapour deposition thermal barrier coatings," *Wear*, 233 352-61 (1999).
20. X. Chen, M. Y. He, I. Spitsberg, N. A. Fleck, J. W. Hutchinson, and A. G. Evans, "Mechanisms governing the high temperature erosion of thermal barrier coatings," *Wear*, 256[7] 735-46 (2004).
21. N. Fleck and T. Zisis, "The erosion of EB-PVD thermal barrier coatings: The competition between mechanisms," *Wear*, 268[11] 1214-24 (2010).
22. X. Chen, R. Wang, N. Yao, A. Evans, J. Hutchinson, and R. Bruce, "Foreign object damage in a thermal barrier system: mechanisms and simulations," *Materials Science and Engineering: A*, 352[1] 221-31 (2003).
23. R. Schafrik, "Personal Communication." in., 2008.
24. H. Ohnabe, S. Masaki, M. Onozuka, K. Miyahara, and T. Sasa, "Potential application of ceramic matrix composites to aero-engine components," *Composites Part A: Applied Science and Manufacturing*, 30[4] 489-96 (1999).
25. M. Takeda, J. Sakamoto, A. Saeki, Y. Imai, and H. Ichikawa, "High performance silicon carbide fiber Hi-Nicalon for ceramic matrix composites," pp. 37-44 in *Ceram. Eng. Sci. Proc. Vol. 16*.
26. R. E. Tressler, "Recent developments in fibers and interphases for high temperature ceramic matrix composites," *Composites Part A: Applied Science and Manufacturing*, 30[4] 429-37 (1999).
27. F. Christin, "Design, fabrication, and application of thermostructural composites (TSC) like C/C, C/SiC, and SiC/SiC composites," *Advanced Engineering Materials*, 4[12] 903-12 (2002).
28. R. Naslain and F. Christin, "SiC-matrix composite materials for advanced jet engines," *MRS Bull.*, 28[9] 654-58 (2003).
29. N. Igawa, T. Taguchi, T. Nozawa, L. L. Snead, T. Hinoki, J. C. McLaughlin, Y. Katoh, S. Jitsukawa, and A. Kohyama, "Fabrication of SiC fiber reinforced SiC composite by chemical vapor infiltration for excellent mechanical properties," *J Phys Chem Solids*, 66[2-4] 551-54 (2005).
30. J. Y. Park, "Fabrication of SiC Fiber-SiC Matrix Composites by Reaction Sintering," *Journal of the Korean Ceramic Society*, 45[4] 204-07 (2008).
31. A. G. Evans and D. B. Marshall, "Overview no. 85 The mechanical behavior of ceramic matrix composites," *Acta Metallurgica*, 37[10] 2567-83 (1989).

32. D. B. Marshall and A. G. Evans, "Failure Mechanisms in Ceramic-Fiber/Ceramic-Matrix Composites," *Journal of the American Ceramic Society*, 68[5] 225-31 (1985).
33. A. G. Evans, F. W. Zok, and J. Davis, "The role of interfaces in fiber-reinforced brittle matrix composites," *Composites Science and Technology*, 42[1-3] 3-24 (1991).
34. M. Rühle and A. G. Evans, "High toughness ceramics and ceramic composites," *Progress in Materials Science*, 33[2] 85-167 (1989).
35. J. DiCarlo, H.-M. Yun, G. Morscher, and R. Bhatt, "SiC/SiC composites for 1200 C and above," pp. 77-98. in *Handbook of Ceramic Composites*. Springer, 2005.
36. G. N. Morscher, G. Ojard, R. Miller, Y. Gowayed, U. Santhosh, J. Ahmad, and R. John, "Tensile creep and fatigue of Sylramic-iBN melt-infiltrated SiC matrix composites: Retained properties, damage development, and failure mechanisms," *Composites Science and Technology*, 68[15-16] 3305-13 (2008).
37. H. M. Yun and J. A. DiCarlo, "Comparison of the tensile, creep, and rupture strength properties of stoichiometric SiC fibers," pp. 259-72 in *Proceedings of the 23rd annual conference on composites, materials and structures*. Vol. 20.
38. S. Zhu, M. Mizuno, Y. Nagano, J. Cao, Y. Kagawa, and H. Kaya, "Creep and Fatigue Behavior in an Enhanced SiC/SiC Composite at High Temperature," *Journal of the American Ceramic Society*, 81[9] 2269-77 (1998).
39. B. N. Cox and F. W. Zok, "Advances in ceramic composites reinforced by continuous fibers," *Current Opinion in Solid State and Materials Science*, 1[5] 666-73 (1996).
40. F. E. Heredia, J. C. McNulty, F. W. Zok, and A. G. Evans, "Oxidation Embrittlement Probe for Ceramic-Matrix Composites," *Journal of the American Ceramic Society*, 78[8] 2097-100 (1995).
41. T. E. Steyer, F. W. Zok, and D. P. Walls, "Stress rupture of an enhanced nicalon/silicon carbide composite at intermediate temperatures," *Journal of the American Ceramic Society*, 81[8] 2140-46 (1998).
42. L. U. Ogbuji, "Pest-resistance in SiC/BN/SiC composites," *Journal of the European Ceramic Society*, 23[4] 613-17 (2003).
43. L. U. J. T. Ogbuji, "Oxidative pest degradation of Hi-Nicalon/BN/SiC composite as a function of temperature and time in the burner rig," pp. 105 in *23rd Annual Conference on Composites, Advanced Ceramics, Materials, and Structures-B: Ceramic Engineering and Science Proceedings*. Vol. 230. (2009).
44. K. J. LaRochelle and G. Morscher, "Tensile Stress Rupture Behavior of a Woven Ceramic Matrix Composite in Humid Environments at Intermediate Temperature—Part I," *Applied Composite Materials*, 13[3] 147-72 (2006).
45. W. Xu, F. W. Zok, and R. M. McMeeking, "Model of Oxidation-Induced Fiber Fracture in SiC/SiC Composites," *Journal of the American Ceramic Society*, 97[11] 3676-83 (2014).
46. E. J. Opila, "Oxidation and Volatilization of Silica Formers in Water Vapor," *Journal of the American Ceramic Society*, 86 1238-48 (2003).
47. E. J. Opila, D. S. Fox, and N. S. Jacobson, "Mass Spectrometric Identification of Si-O-H(g) Species from the Reaction of Silica with Water Vapor at Atmospheric Pressure," *Journal of the American Ceramic Society*, 80 1009-12 (1997).

48. E. J. Opila and R. E. Hann Jr., "Paralinear Oxidation of CVD SiC in Water Vapor," *Journal of the American Ceramic Society*, 80 197-205 (1997).
49. E. J. Opila, J. L. Smialek, R. C. Robinson, D. S. Fox, and N. S. Jacobson, "SiC Recession Caused by SiO<sub>2</sub> Scale Volatility under Combustion Conditions: II, Thermodynamics and Gaseous-Diffusion Model," *Journal of the American Ceramic Society*, 82 1826-34 (1999).
50. J. A. Costello and R. E. Tressler, "Oxidation Kinetics of Silicon Carbide Crystals and Ceramics: I, In Dry Oxygen," *Journal of the American Ceramic Society*, 69[9] 674-81 (1986).
51. E. J. Opila, "Variation of the Oxidation Rate of Silicon Carbide with Water-Vapor Pressure," *Journal of the American Ceramic Society*, 82 625-36 (1999).
52. R. A. Miller, "Current status of thermal barrier coatings -- An overview," *Surface and Coatings Technology*, 30[1] 1-11 (1987).
53. M. Yoshiba, K. Abe, T. Aranami, and Y. Harada, "High-temperature oxidation and hot corrosion behavior of two kinds of thermal barrier coating systems for advanced gas turbines," *J Therm Spray Tech*, 5[3] 259-68 (1996).
54. D. R. Clarke, M. Oechsner, and N. P. Padture, "Thermal-barrier coatings for more efficient gas-turbine engines," *MRS Bulletin*, 37[10] 891-98 (2012).
55. R. Darolia, "Thermal barrier coatings technology: critical review, progress update, remaining challenges and prospects," *International materials reviews*, 58[6] 315-48 (2013).
56. N. P. Padture, M. Gell, and E. H. Jordan, "Thermal Barrier Coatings for Gas-Turbine Engine Applications," *Science*, 296[5566] 280-84 (2002).
57. A. G. Evans, D. R. Mumm, J. W. Hutchinson, G. H. Meier, and F. S. Pettit, "Mechanisms controlling the durability of thermal barrier coatings," *Progress in Materials Science*, 46[5] 505-53 (2001).
58. J. Kimmel, N. Miriyala, J. Price, K. More, P. Tortorelli, H. Eaton, G. Linsey, and E. Sun, "Evaluation of CFCC liners with EBC after field testing in a gas turbine," *Journal of the European Ceramic Society*, 22 2769-75 (2002).
59. K. N. Lee, "Current status of environmental barrier coatings for Si-Based ceramics," *Surface and Coatings Technology*, 133-134 1-7 (2000).
60. K. N. Lee, "Key Durability Issues With Mullite-Based Environmental Barrier Coatings for Si-Based Ceramics," *Journal of Engineering for Gas Turbines and Power*, 122 632-36 (2000).
61. N. L. Ahlborg and D. Zhu, "Calcium–magnesium aluminosilicate (CMAS) reactions and degradation mechanisms of advanced environmental barrier coatings," *Surface and Coatings Technology*, 237 79-87 (2013).
62. K. M. Grant, S. Krämer, J. Löfvander, and C. G. Levi, "CMAS degradation of environmental barrier coatings," *Surface and Coatings Technology*, 202[4] 653-57 (2007).
63. D. Zhu, S. R. Choi, J. I. Eldridge, K. N. Lee, and R. A. Miller, "Surface cracking and interface reaction associated delamination failure of thermal and environmental barrier coatings," (2003).
64. D. Zhu, D. S. Fox, L. J. Ghosn, and B. Harder, "Creep Behavior of Hafnia and Ytterbium Silicate Environmental Barrier Coating Systems on SiC/SiC Ceramic Matrix Composites," (2011).

65. D. Zhu, K. N. Lee, and R. A. Miller, "Thermal Conductivity and Thermal Gradient Cyclic Behavior of Refractory Silicate Coatings on SiC/SiC Ceramic Matrix Composites," pp. 443-52 in 25th Annual Conference on Composites, Advanced Ceramics, Materials, and Structures: B: Ceramic Engineering and Science Proceedings, Volume 22, Issue 4.
66. D. Zhu, K. N. Lee, and R. A. Miller, "Thermal gradient cyclic behavior of a thermal/environmental barrier coating system on SiC/SiC ceramic matrix composites," pp. 171-78 in ASME Turbo Expo 2002: Power for Land, Sea, and Air.
67. D. Zhu, K. N. Lee, and R. A. Miller, "Cyclic Failure Mechanisms of Thermal and Environmental Barrier Coating Systems Under Thermal Gradient Test Conditions," (2002).
68. D. Zhu and R. A. Miller, "Determination of creep behavior of thermal barrier coatings under laser imposed high thermal and stress gradient conditions," *Journal of materials research*, 14[1] 146-61 (1999).
69. S. M. Meier, Gupta, DK, "Evolution of thermal barrier coatings in gas turbine engine applications," *Trans. ASME, J. Eng. Gas Turbines Power*, 116 250-57 (1994).
70. K. N. Lee, R. A. Miller, and N. S. Jacobson, "New Generation of Plasma-Sprayed Mullite Coatings on Silicon Carbide," *Journal of the American Ceramic Society*, 78 705-10 (1995).
71. K. N. Lee and R. A. Miller, "Development and environmental durability of mullite and mullite/YSZ dual layer coatings for SiC and Si<sub>3</sub>N<sub>4</sub> ceramics," *Surface and Coatings Technology*, 86-87 142-48 (1996).
72. M. Y. He, J. W. Hutchinson, and A. G. Evans, "Simulation of stresses and delamination in a plasma-sprayed thermal barrier system upon thermal cycling," *Materials Science and Engineering: A*, 345[1-2] 172-78 (2003).
73. A. G. Evans and J. W. Hutchinson, "The mechanics of coating delamination in thermal gradients," *Surface and Coatings Technology*, 201[18] 7905-16 (2007).
74. J. M. Ambrico, M. R. Begley, and E. H. Jordan, "Stress and shape evolution of irregularities in oxide films on elastic-plastic substrates due to thermal cycling and film growth," *Acta Materialia*, 49[9] 1577-88 (2001).
75. C. H. Hsueh, "Thermal stresses in elastic multilayer systems," *Thin Solid Films*, 418[2] 182-88 (2002).
76. K. N. Lee, "Contamination Effects on Interfacial Porosity during Cyclic Oxidation of Mullite-Coated Silicon Carbide," *Journal of the American Ceramic Society*, 81 3329-32 (1998).
77. K. N. Lee, "Protective Coatings for Gas Turbines." in *The Gas Turbine Handbook*. Edited by R. Dennis. United States Department of Energy (DOE), 2006.
78. K. N. Lee, D. S. Fox, and N. P. Bansal, "Rare earth silicate environmental barrier coatings for SiC/SiC composites and Si<sub>3</sub>N<sub>4</sub> ceramics," *Corrosion of Ceramic Matrix Composites*, 25 1705-15 (2005).
79. K. N. Lee, D. S. Fox, J. I. Eldridge, D. Zhu, R. C. Robinson, N. P. Bansal, and R. A. Miller, "Upper Temperature Limit of Environmental Barrier Coatings Based on Mullite and BSAS," *Journal of the American Ceramic Society*, 86 1299-306 (2003).

80. H. E. Eaton, W. P. Allen, N. S. Jacobson, N. P. Bansal, E. J. Opila, J. L. Smialek, K. N. Lee, I. T. Spitsberg, H. Wang, and P. J. Meschter, "Barium strontium aluminosilicate barrier layer." in. Google Patents, 2002.
81. I. A. Bondar, "Rare-earth silicates," *Ceramics International*, 8 83-89 (1982).
82. T. Fukudome, S. Tsuruzono, W. Karasawa, and Y. Ichikawa, "Development and evaluation of ceramic components for gas turbine," *ASME Paper GT-2002-30627* (2002).
83. H. Chen, Y. Gao, Y. Liu, and H. Luo, "Hydrothermal Synthesis of Ytterbium Silicate Nanoparticles," *Inorganic Chemistry*, 49[4] 1942-46 (2010).
84. S. Stecura and W. J. Campbell, "Thermal expansion and phase inversion of rare-earth oxides." in. Bureau of Mines. College Park Metallurgy Research Center, Md., 1960.
85. I. A. Aksaf and J. A. Pask, "Stable and Metastable Equilibria in the System SiO<sub>2</sub>-Al<sub>2</sub>O<sub>3</sub>," *Journal of the American Ceramic Society*, 58[11-12] 507-12 (1975).
86. R. G. Munro, "Evaluated Material Properties for a Sintered alpha-Alumina," *Journal of the American Ceramic Society*, 80[8] 1919-28 (1997).
87. P. Patnaik, "Handbook of Inorganic Chemistry." in. ISBN 0-07-049439-8), the McGraw-Hill Companies, 344, 2002.
88. R. Hull, "Properties of crystalline silicon." IET, (1999).
89. R. W. Olesinski and G. J. Abbaschian, "The C-Si (Carbon-Silicon) system," *Bulletin of Alloy Phase Diagrams*, 5[5] 486-89 (1984).
90. X. Ma, C. Li, and W. Zhang, "The thermodynamic assessment of the Ti-Si-N system and the interfacial reaction analysis," *Journal of Alloys and Compounds*, 394[1-2] 138-47 (2005).
91. N. Toropov and V. Vasil'eva, "Phase diagram of the scandia-silica binary system," *Zh. Neorg. Khim*, 7 1938-45 (1962).
92. M. Zinkevich, "Thermodynamics of rare earth sesquioxides," *Progress in Materials Science*, 52[4] 597-647 (2007).
93. B. J. Harder, J. D. Almer, C. M. Weyant, K. N. Lee, and K. T. Faber, "Residual Stress Analysis of Multilayer Environmental Barrier Coatings," *Journal of the American Ceramic Society*, 92 452-59 (2009).
94. K. N. Lee, J. I. Eldridge, and R. C. Robinson, "Residual Stresses and Their Effects on the Durability of Environmental Barrier Coatings for SiC Ceramics," *Journal of the American Ceramic Society*, 88 3483-88 (2005).
95. B. T. Richards, M. R. Begley, and H. N. G. Wadley, "Mechanisms of Ytterbium Monosilicate/Mullite/Silicon Coating Failure during Thermal Cycling in Water Vapor," *Submitted Article* (2015).
96. B. T. Richards, F. de Francqueville, S. Sehr, M. R. Begley, and H. N. Wadley, "Delamination of Ytterbium Monosilicate/Mullite Bi-layers on Silicon Coated SiC During Thermal Cycling in Water Vapor," *Submitted Article* (2015).
97. B. T. Richards and H. N. G. Wadley, "Plasma spray deposition of tri-layer environmental barrier coatings," *Journal of the European Ceramic Society*, 34[12] 3069-83 (2014).
98. D. Zhu and R. A. Miller, "Sintering and creep behavior of plasma-sprayed zirconia- and hafnia-based thermal barrier coatings," *Surface and Coatings Technology*, 108-109[0] 114-20 (1998).

99. E. Pfender, "Fundamental studies associated with the plasma spray process," *Surface and Coatings Technology*, 34 1-14 (1988).
100. H. Singh, B. S. Sidhu, D. Puri, and S. Prakash, "Use of plasma spray technology for deposition of high temperature oxidation/corrosion resistant coatings – a review," *Materials and Corrosion*, 58[2] 92-102 (2007).
101. J. H. Zaat, "A Quarter of a Century of Plasma Spraying," *Annual Review of Materials Science*, 13 9-42 (1983).
102. R. McPherson, "The relationship between the mechanism of formation, microstructure and properties of plasma-sprayed coatings," *Thin Solid Films*, 83[3] 297-310 (1981).
103. K. T. Faber, C. M. Weyant, B. Harder, J. Almer, and K. Lee, "Internal stresses and phase stability in multiphase environmental barrier coatings," *International Journal of Materials Research*, 98 1188-95 (2007).
104. B. J. Harder, J. Almer, K. N. Lee, and K. T. Faber, "In situ stress analysis of multilayer environmental barrier coatings," *Powder Diffraction*, 24 94-98 (2009).
105. B. J. Harder and K. T. Faber, "Transformation kinetics in plasma-sprayed barium- and strontium-doped aluminosilicate (BSAS)," *Scripta Materialia*, 62 282-85 (2010).
106. B. J. Harder, J. Ramirez-Rico, J. D. Almer, K. N. Lee, and K. T. Faber, "Chemical and Mechanical Consequences of Environmental Barrier Coating Exposure to Calcium-Magnesium-Aluminosilicate," *Journal of the American Ceramic Society*, 94 s178-s85 (2011).
107. K. N. Lee, R. A. Miller, N. S. Jacobson, and E. J. Opila, "Environmental Durability of Mullite Coating/SiC and Mullite-YSZ Coating/SiC Systems," pp. 1037-44 in Proceedings of the 19th Annual Conference on Composites, Advanced Ceramics, Materials, and Structures—B: Ceramic Engineering and Science Proceedings.
108. K. N. Lee, N. S. Jacobson, and R. A. Miller, "Refractory oxide coatings on SiC ceramics," *MRS bulletin*, 19 35-38 (1994).
109. K. N. Lee and R. A. Miller, "Oxidation Behavior of Mullite-Coated SiC and SiC/SiC Composites under Thermal Cycling between Room Temperature and 1200-1400C," *Journal of the American Ceramic Society*, 79 620-26 (1996).
110. J.-y. J. Kwon, "Microstructural Evolution and Residual Stresses of Air-Plasma Sprayed Thermal Barriers Coatings Under Thermal Eexposure," *Surface review and letters*, 17 337-43 (2010).
111. A. Nusair Khan, J. Lu, and H. Liao, "Effect of residual stresses on air plasma sprayed thermal barrier coatings," *Surface and Coatings Technology*, 168 291-99 (2003).
112. P. Scardi, M. Leoni, and L. Bertamini, "Residual stresses in plasma sprayed partially stabilised zirconia TBCs: influence of the deposition temperature," *Thin Solid Films*, 278 96-103 (1996).
113. A. Rabiei and A. G. Evans, "Failure mechanisms associated with the thermally grown oxide in plasma-sprayed thermal barrier coatings," *Acta Materialia*, 48[15] 3963-76 (2000).
114. R. A. Miller, "Thermal barrier coatings for aircraft engines: history and directions," *J Therm Spray Tech*, 6[1] 35-42 (1997).

115. C. H. Lee, H. K. Kim, H. S. Choi, and H. S. Ahn, "Phase transformation and bond coat oxidation behavior of plasma-sprayed zirconia thermal barrier coating," *Surface and Coatings Technology*, 124[1] 1-12 (2000).
116. K. W. Schlichting, N. P. Padture, E. H. Jordan, and M. Gell, "Failure modes in plasma-sprayed thermal barrier coatings," *Materials Science and Engineering: A*, 342[1-2] 120-30 (2003).
117. R. Vaßen, G. Kerkhoff, and D. Stöver, "Development of a micromechanical life prediction model for plasma sprayed thermal barrier coatings," *Materials Science and Engineering: A*, 303[1-2] 100-09 (2001).
118. D. Zhu and R. A. Miller, "Thermal conductivity and elastic modulus evolution of thermal barrier coatings under high heat flux conditions," *J Therm Spray Tech*, 9[2] 175-80 (2000).
119. P. F. Zhao, C. A. Sun, X. Y. Zhu, F. L. Shang, and C. J. Li, "Fracture toughness measurements of plasma-sprayed thermal barrier coatings using a modified four-point bending method," *Surface and Coatings Technology*, 204[24] 4066-74 (2010).
120. S. R. Choi, D. Zhu, and R. A. Miller, "Mechanical Properties/Database of Plasma-Sprayed ZrO<sub>2</sub>-8wt% Y<sub>2</sub>O<sub>3</sub> Thermal Barrier Coatings," *International Journal of Applied Ceramic Technology*, 1[4] 330-42 (2004).
121. S. R. Choi, D. Zhu, and R. A. Miller, "Effect of Sintering on Mechanical Properties of Plasma-Sprayed Zirconia-Based Thermal Barrier Coatings," *Journal of the American Ceramic Society*, 88[10] 2859-67 (2005).
122. T. A. Cruse, B. Johnsen, and A. Nagy, "Mechanical properties testing and results for thermal barrier coatings," *J Therm Spray Tech*, 6[1] 57-66 (1997).
123. J. T. Demasi and M. Ortiz, "Thermal barrier coating life prediction model development, phase 1," (1989).
124. S. M. Meier, D. M. Nissley, K. D. Sheffler, and T. A. Cruse, "Thermal barrier coating life prediction model development," *Journal of Engineering for gas turbines and power*, 114[2] 258-63 (1992).
125. R. Soltani, T. W. Coyle, and J. Mostaghimi, "Creep Behavior of Plasma-Sprayed Zirconia Thermal Barrier Coatings," *Journal of the American Ceramic Society*, 90[9] 2873-78 (2007).
126. E. Lugscheider, R. Nickel, and N. Papenfuß-Janzen, "A model of the interface between plasma jet simulation and the simulation of coating formation during atmospheric plasma spraying (APS)," pp. 373-80 in *Journal de Physique IV (Proceedings)*. Vol. 120.
127. E. Meillot and G. Balmigere, "Plasma spraying modeling: Particle injection in a time-fluctuating plasma jet," *Surface and Coatings Technology*, 202[18] 4465-69 (2008).
128. K. Remesh, S. C. M. Yu, H. W. Ng, and C. C. Berndt, "Computational study and experimental comparison of the in-flight particle behavior for an external injection plasma spray process," *J Therm Spray Tech*, 12[4] 508-22 (2003).
129. T. Streibl, A. Vaidya, M. Friis, V. Srinivasan, and S. Sampath, "A Critical Assessment of Particle Temperature Distributions During Plasma Spraying: Experimental Results for YSZ," *Plasma Chem Plasma Process*, 26[1] 73-102 (2006).

130. J. P. Trelles and J. V. R. Heberlein, "Simulation results of arc behavior in different plasma spray torches," *J Therm Spray Tech*, 15[4] 563-69 (2006).
131. M. Vardelle, P. Fauchais, A. Vardelle, K. I. Li, B. Dussoubs, and N. J. Themelis, "Controlling particle injection in plasma spraying," *J Therm Spray Tech*, 10[2] 267-84 (2001).
132. M. Vardelle, A. Vardelle, P. Fauchais, and C. Moreau, "Pyrometer system for monitoring the particle impact on a substrate during a plasma spray process," *Measurement Science and Technology*, 5[3] 205 (1994).
133. P. Wang, S. C. M. Yu, and H. W. Ng, "Particle velocities, sizes and flux distribution in plasma spray with two powder injection ports," *Materials Science and Engineering: A*, 383[1] 122-36 (2004).
134. R. L. Williamson, J. R. Fincke, and C. H. Chang, "A Computational Examination of the Sources of Statistical Variance in Particle Parameters During Thermal Plasma Spraying," *Plasma Chem Plasma Process*, 20[3] 299-324 (2000).
135. R. L. Williamson, J. R. Fincke, and C. H. Chang, "Numerical study of the relative importance of turbulence, particle size and density, and injection parameters on particle behavior during thermal plasma spraying," *J Therm Spray Tech*, 11[1] 107-18 (2002).
136. H.-B. Xiong, L.-L. Zheng, S. Sampath, R. L. Williamson, and J. R. Fincke, "Three-dimensional simulation of plasma spray: effects of carrier gas flow and particle injection on plasma jet and entrained particle behavior," *International Journal of Heat and Mass Transfer*, 47[24] 5189-200 (2004).
137. T. Zhang, D. T. Gawne, and B. Liu, "Computer modelling of the influence of process parameters on the heating and acceleration of particles during plasma spraying," *Surface and Coatings Technology*, 132[2-3] 233-43 (2000).
138. C. Chang, "Numerical simulation of alumina spraying in argon-helium plasma jet," pp. 1-5 in Presented at the 1992 International Thermal Spray Conference, Orlando, FL, 1-5 Jun. 1992. Vol. 1.
139. H.-P. Li and X. Chen, "Three-dimensional simulation of a plasma jet with transverse particle and carrier gas injection," *Thin Solid Films*, 390[1-2] 175-80 (2001).
140. K. Ramachandran, N. Kikukawa, and H. Nishiyama, "3D modeling of plasma-particle interactions in a plasma jet under dense loading conditions," *Thin Solid Films*, 435[1-2] 298-306 (2003).
141. K. Ramachandran and H. Nishiyama, "Fully coupled 3D modeling of plasma-particle interactions in a plasma jet," *Thin Solid Films*, 457[1] 158-67 (2004).
142. J. P. Trelles, C. Chazelas, A. Vardelle, and J. V. R. Heberlein, "Arc Plasma Torch Modeling," *J Therm Spray Tech*, 18[5-6] 728-52 (2009).
143. M. Vardelle, A. Vardelle, P. Fauchais, and M. I. Boulos, "Plasma-particle momentum and heat transfer: Modelling and measurements," *AIChE Journal*, 29[2] 236-43 (1983).
144. C. Moreau, P. Cielo, M. Lamontagne, S. Dallaire, and M. Vardelle, "Impacting particle temperature monitoring during plasma spray deposition," *Measurement Science and Technology*, 1[8] 807 (1990).
145. H. Liu, E. J. Lavernia, and R. H. Rangel, "Numerical simulation of substrate impact and freezing of droplets in plasma spray processes," *Journal of Physics D: Applied Physics*, 26[11] 1900 (1993).

146. J. Mostaghimi, M. Pasandideh-Fard, and S. Chandra, "Dynamics of Splat Formation in Plasma Spray Coating Process," *Plasma Chem Plasma Process*, 22[1] 59-84 (2002).
147. H.-P. Li and E. Pfender, "Three Dimensional Modeling of the Plasma Spray Process," *J Therm Spray Tech*, 16[2] 245-60 (2007).
148. M. Friis, C. Persson, and J. Wigren, "Influence of particle in-flight characteristics on the microstructure of atmospheric plasma sprayed yttria stabilized ZrO<sub>2</sub>," *Surface and Coatings Technology*, 141[2-3] 115-27 (2001).
149. V. Srinivasan, M. Friis, A. Vaidya, T. Streibl, and S. Sampath, "Particle Injection in Direct Current Air Plasma Spray: Salient Observations and Optimization Strategies," *Plasma Chem Plasma Process*, 27[5] 609-23 (2007).
150. C. A. Johnson, J. A. Ruud, R. Bruce, and D. Wortman, "Relationships between residual stress, microstructure and mechanical properties of electron beam-physical vapor deposition thermal barrier coatings," *Surface and Coatings Technology*, 108-109[0] 80-85 (1998).
151. R. Taylor, J. R. Brandon, and P. Morrell, "Microstructure, composition and property relationships of plasma-sprayed thermal barrier coatings," *Surface and Coatings Technology*, 50[2] 141-49 (1992).
152. E. Lugscheider, K. Bobzin, S. Bärwulf, and A. Etzkorn, "Mechanical properties of EB-PVD-thermal barrier coatings by nanoindentation," *Surface and Coatings Technology*, 138[1] 9-13 (2001).
153. A. Kucuk, C. C. Berndt, U. Senturk, R. S. Lima, and C. R. C. Lima, "Influence of plasma spray parameters on mechanical properties of yttria stabilized zirconia coatings. I: Four point bend test," *Materials Science and Engineering: A*, 284[1-2] 29-40 (2000).
154. W. D. Kingery, H. K. Bowen, and D. R. Uhlmann, "Introduction to Ceramics," pp. 1032 2 ed. Wiley: New York, (1976).
155. G. D. Quinn and R. Morrell, "Design data for engineering ceramics: a review of the flexure test," *Journal of the American Ceramic Society*, 74[9] 2037-66 (1991).
156. M. G. Jenkins, S. M. Wiederhorn, and R. K. Shiffer, "Creep Testing of Advanced Ceramics," *Mechanical Testing Methodology for Ceramic Design and Reliability* 171 (1998).
157. J. A. Salem and S. R. Choi, "Creep behavior of silicon nitride determined from curvature and neutral axis shift measurements in flexure tests," *Life prediction methodologies and data for ceramic materials* 84-97 (1994).
158. B. Dyson and T. Gibbons, "Use of reference stress to correlate creep fracture lifetimes of monolithic ceramics in uniaxial tension and flexure," *Materials science and technology*, 9[2] 151-54 (1993).
159. R. F. Krause, "Observed and theoretical creep rates for an alumina ceramic and a silicon nitride ceramic in flexure," *Journal of the American Ceramic Society*, 75[5] 1307-10 (1992).
160. C. F. Chen and T. j. Chuang, "Improved analysis for flexural creep with application to sialon ceramics," *Journal of the American Ceramic Society*, 73[8] 2366-73 (1990).

161. G. Grathwohl, "Regimes of creep and slow crack growth in high-temperature rupture of hot-pressed silicon nitride," pp. 573-86. in *Deformation of Ceramic Materials II*. Springer, 1984.
162. G. Hollenberg, G. Terwilliger, and R. S. Gordon, "Calculation of Stresses and Strains in Four-Point Bending Creep Tests," *Journal of the American Ceramic Society*, 54[4] 196-99 (1971).
163. T. Fett and D. Munz, "Measurement of transient and stationary creep of HPSN in bending," *International Journal of High Technology Ceramics*, 4[2] 281-88 (1988).
164. T. Fett, K. Keller, and D. Munz, "An analysis of the creep of hot pressed silicon nitride in bending," *J Mater Sci*, 23[2] 467-74 (1988).
165. T. J. Chuang and S. M. Wiederhorn, "Damage-Enhanced Creep in a Siliconized Silicon Carbide: Mechanics of Deformation," *Journal of the American Ceramic Society*, 71[7] 595-601 (1988).
166. T.-J. Chuang, "Estimation of power-law creep parameters from bend test data," *J Mater Sci*, 21[1] 165-75 (1986).
167. R. Morrell and K. Ashbee, "High temperature creep of lithium zinc silicate glass-ceramics," *J Mater Sci*, 8[9] 1253-70 (1973).
168. A. Venkateswaran, K. Y. Donaldson, and D. Hasselman, "Role of Intergranular Damage-Induced Decrease in Young's Modulus in the Nonlinear Deformation and Fracture of an Alumina at Elevated Temperatures," *Journal of the American Ceramic Society*, 71[7] 565-76 (1988).
169. K. Jakus and S. M. Wiederhorn, "Creep Deformation of Ceramics in Four-Point Bending," *Journal of the American Ceramic Society*, 71[10] 832-36 (1988).
170. A. Rosenfield, W. Duckworth, and D. Shetty, "Damage analysis of creep in bending," *Journal of the American Ceramic Society*, 68[9] 483-85 (1985).
171. M. Ferber, M. Jenkins, and V. Tennery, "Comparison of tension, compression, and flexure creep for alumina and silicon nitride ceramics," *Ceram. Eng. Sci. Proc. I*, 1 1028-45 (1989).
172. P. K. Talty and R. A. Dirks, "Determination of tensile and compressive creep behaviour of ceramic materials from bend tests," *J Mater Sci*, 13[3] 580-86 (1978).
173. H. Cohrt, G. Grathwohl, and F. Thümmeler, "Non-stationary stress distribution in a ceramic bending beam during constant load creep," *Res Mechanica*, 10[1] 55-71 (1984).
174. M. Fitzpatrick, A. Fry, P. Holdway, F. Kandil, J. Shackleton, and L. Suominen, "Determination of residual stresses by X-ray diffraction," (2005).
175. K. F. J. Heinrich, pp. 1509. in *X-Ray Optics and Microanalysis*, 4th International Congress on X-Ray Optics and Microanalysis. Edited by R. Castaing, Deschamps, P., Philibert, J. Hermann, Paris, 1966.
176. W. Reuter, "The ionization function and its application to the electron probe analysis of thin films," pp. 121-30 in *Proceedings 6th International Congress on X-ray Optics and Microanalysis*.
177. S. Sumithra and A. M. Umarji, "Role of crystal structure on the thermal expansion of  $\text{Ln}_2\text{W}_3\text{O}_{12}$  ( $\text{Ln} = \text{La}, \text{Nd}, \text{Dy}, \text{Y}, \text{Er}$  and  $\text{Yb}$ )," *Solid State Sciences*, 6[12] 1313-19 (2004).

178. K. Remesh, H. W. Ng, and S. C. M. Yu, "Influence of process parameters on the deposition footprint in plasma-spray coating," *J Therm Spray Tech*, 12[3] 377-92 (2003).
179. T. Zhang, Y. Bao, D. T. Gawne, B. Liu, and J. Karwatzki, "Computer model to simulate the random behaviour of particles in a thermal-spray jet," *Surface and Coatings Technology*, 201[6] 3552-63 (2006).
180. S. Dru, E. Meillot, K. Wittmann-Teneze, R. Benoit, and M. L. Saboungi, "Plasma spraying of lanthanum silicate electrolytes for intermediate temperature solid oxide fuel cells (ITSOFCs)," *Surface and Coatings Technology*, 205[4] 1060-64 (2010).
181. C. W. Bale, P. Chartrand, S. A. Degterov, G. Eriksson, K. Hack, R. Ben Mahfoud, J. Melançon, A. D. Pelton, and S. Petersen, "FactSage thermochemical software and databases," *Calphad*, 26[2] 189-228 (2002).
182. V. Pecharsky and P. Zavalij, "Fundamentals of powder diffraction and structural characterization of materials," Vol. 69. Springer, (2008).
183. P. Townsend, D. Barnett, and T. Brunner, "Elastic relationships in layered composite media with approximation for the case of thin films on a thick substrate," *Journal of Applied Physics*, 62[11] 4438-44 (1987).
184. C.-H. Hsueh, "Modeling of elastic deformation of multilayers due to residual stresses and external bending," *Journal of Applied Physics*, 91 9652 (2002).
185. K. K. Phani and S. K. Niyogi, "Elastic Modulus-Porosity Relation in Polycrystalline Rare-Earth Oxides," *Journal of the American Ceramic Society*, 70[12] C-362-C-66 (1987).
186. H. Ledbetter, S. Kim, D. Balzar, S. Crudele, and W. Kriven, "Elastic Properties of Mullite," *Journal of the American Ceramic Society*, 81 1025-28 (1998).
187. T.-I. Mah and K. S. Mazdiyasn, "Mechanical Properties of Mullite," *Journal of the American Ceramic Society*, 66 699-703 (1983).
188. Saint-Gobain, "Hexoloy Data Sheets." in., 2010.
189. H. M. O'Bryan, P. K. Gallagher, and G. Berkstresser, "Thermal Expansion of Y<sub>2</sub>SiO<sub>5</sub> Single Crystals," *Journal of the American Ceramic Society*, 71 C-42-C-43 (1988).
190. G. Di Girolamo, C. Blasi, L. Piloni, and M. Schioppa, "Microstructural and thermal properties of plasma sprayed mullite coatings," *Ceramics International*, 36 1389-95 (2010).
191. W. M. Kriven and J. A. Pask, "Solid Solution Range and Microstructures of Melt-Grown Mullite," *Journal of the American Ceramic Society*, 66 649-54 (1983).
192. I. T. Spitsberg, H. Wang, and R. W. Heidorn, "Method for thermally spraying crack-free mullite coatings on ceramic-based substrates." in. Google Patents, 2001.
193. J. F. Shackelford and R. H. Doremus, "Ceramic and glass materials: structure, properties and processing." Springer, (2008).
194. H. Schneider, K. Okada, and J. A. Pask, "Mullite and mullite ceramics." J. Wiley, (1994).
195. B. E. Deal and A. S. Grove, "General Relationship for the Thermal Oxidation of Silicon," *Journal of Applied Physics*, 36 3770-78 (1965).

196. N. S. Jacobson, D. S. Fox, J. L. Smialek, C. Deliacorte, and K. N. Lee, "Performance of ceramics in severe environments." in. Edited by GRC. NASA Glenn Research Center, Cleveland, OH, USA, 2005.
197. K. M. Grant, S. Krämer, G. G. E. Seward, and C. G. Levi, "Calcium Magnesium Alumino-Silicate Interaction with Yttrium Monosilicate Environmental Barrier Coatings," *Journal of the American Ceramic Society* no-no (2010).
198. J. Liu, L. Zhang, Q. Liu, L. Cheng, and Y. Wang, "Calcium–magnesium–aluminosilicate corrosion behaviors of rare-earth disilicates at 1400°C," *Journal of the European Ceramic Society*, 33[15–16] 3419-28 (2013).
199. R. W. Jackson and M. R. Begley, "Critical cooling rates to avoid transient-driven cracking in thermal barrier coating (TBC) systems," *International Journal of Solids and Structures*, 51[6] 1364-74 (2014).
200. E. Bourova and P. Richet, "Quartz and Cristobalite: high-temperature cell parameters and volumes of fusion," *Geophysical Research Letters*, 25[13] 2333-36 (1998).
201. D. R. Peacor, "High-temperature single-crystal study of the cristobalite inversion," *Z Kristallogr*, 138 274-98 (1973).
202. H. Gercek, "Poisson's ratio values for rocks," *International Journal of Rock Mechanics and Mining Sciences*, 44[1] 1-13 (2007).
203. A. Ballato, "Poisson's ratios of auxetic and other technological materials," *Ultrasonics, Ferroelectrics and Frequency Control, IEEE Transactions on*, 57[1] 7-15 (2010).
204. Z. Sun, Y. Zhou, J. Wang, and M. Li, " $\gamma$ -Y<sub>2</sub>Si<sub>2</sub>O<sub>7</sub>, a Machinable Silicate Ceramic: Mechanical Properties and Machinability," *Journal of the American Ceramic Society*, 90[8] 2535-41 (2007).
205. K. Yamahara, K. Okazaki, and K. Kawamura, "Molecular dynamics study of the thermal behaviour of silica glass/melt and cristobalite," *Journal of Non-Crystalline Solids*, 291[1–2] 32-42 (2001).
206. D. Lakshtanov, S. Sinogeikin, and J. Bass, "High-temperature phase transitions and elasticity of silica polymorphs," *Phys Chem Minerals*, 34[1] 11-22 (2007).
207. S.-H. Leigh, C.-K. Lin, and C. C. Berndt, "Elastic Response of Thermal Spray Deposits under Indentation Tests," *Journal of the American Ceramic Society*, 80[8] 2093-99 (1997).
208. C. J. Li and A. Ohmori, "Relationships between the microstructure and properties of thermally sprayed deposits," *J Therm Spray Tech*, 11[3] 365-74 (2002).
209. B. T. Richards, L. J. Ghosn, D. Zhu, and H. Wadley, "Mechanical Properties of Air Plasma Sprayed Environmental Barrier Coating (EBC) Systems: Preliminary Assessments," *Proceedings of the 39th International Conference and Exposition on Advanced Ceramics and Composites* (2015).
210. J. S. Wallace and J. Ilavsky, "Elastic modulus measurements in plasma sprayed deposits," *J Therm Spray Tech*, 7[4] 521-26 (1998).
211. C. Li, A. Ohmori, and R. McPherson, "The relationship between microstructure and Young's modulus of thermally sprayed ceramic coatings," *J Mater Sci*, 32[4] 997-1004 (1997).
212. J. B. Bates, "Raman Spectra of  $\alpha$  and  $\beta$  Cristobalite," *The Journal of Chemical Physics*, 57[9] 4042-47 (1972).

213. F. L. Galeener, "Raman and ESR studies of the thermal history of amorphous SiO<sub>2</sub>," *Journal of Non-Crystalline Solids*, 71[1–3] 373-86 (1985).
214. I. P. Swainson, M. T. Dove, and D. C. Palmer, "Infrared and Raman spectroscopy studies of the  $\alpha$ - $\beta$  phase transition in cristobalite," *Phys Chem Minerals*, 30[6] 353-65 (2003).
215. D. Hatch and S. Ghose, "The  $\alpha$ - $\beta$  phase transition in cristobalite, SiO<sub>2</sub>," *Phys Chem Minerals*, 17[6] 554-62 (1991).
216. A. J. Leadbetter and A. F. Wright, "The  $\alpha$ - $\beta$  transition in the cristobalite phases of SiO<sub>2</sub> and AlPO<sub>4</sub> I. X-ray studies," *Philosophical Magazine*, 33[1] 105-12 (1976).
217. G. H. A. M. van der Steen and H. van den Boom, "Raman spectroscopic study of hydrogen-containing vitreous silica," *Journal of Non-Crystalline Solids*, 23[2] 279-86 (1977).
218. D. Tromans and J. A. Meech, "Fracture toughness and surface energies of minerals: theoretical estimates for oxides, sulphides, silicates and halides," *Minerals Engineering*, 15[12] 1027-41 (2002).
219. L. B. Freund and S. Suresh, "Thin film materials : stress, defect formation, and surface evolution," pp. 750. Cambridge University Press: Cambridge, UK, (2003).
220. B. T. Richards, H. Zhao, and H. N. G. Wadley, "Structure, Composition and Defect Control of Plasma Spray Deposited Ytterbium Silicate Coatings " *Submitted Article* (2015).
221. S. Carlson, J. Hölsä, T. Laamanen, M. Lastusaari, M. Malkamäki, J. Niittykoski, and R. Valtonen, "X-ray absorption study of rare earth ions in Sr<sub>2</sub>MgSi<sub>2</sub>O<sub>7</sub>:Eu<sup>2+</sup>,R<sup>3+</sup> persistent luminescence materials," *Optical Materials*, 31[12] 1877-79 (2009).
222. M. A. Małecka and L. Kępiński, "Solid state reactions in highly dispersed single and mixed lanthanide oxide–SiO<sub>2</sub> systems," *Catalysis Today*, 180[1] 117-23 (2012).
223. T. Yamamoto, T. Matsuyama, T. Tanaka, T. Funabiki, and S. Yoshida, "Generation of acid sites on silica-supported rare earth oxide catalysts: Structural characterization and catalysis for [small alpha]-pinene isomerization," *Physical Chemistry Chemical Physics*, 1[11] 2841-49 (1999).
224. T. Yamamoto, T. Tanaka, T. Matsuyama, T. Funabiki, and S. Yoshida, "XAFS study of the structure of the silica-supported ytterbium oxide catalyst," *Solid State Communications*, 111[3] 137-42 (1999).
225. G. Calas, G. Brown, Jr., G. Waychunas, and J. Petiau, "X-ray absorption spectroscopic studies of silicate glasses and minerals," *Phys Chem Minerals*, 15[1] 19-29 (1987).
226. J. C. Van Loon, J. H. Galbraith, and H. M. Aarden, "The determination of yttrium, europium, terbium, dysprosium, holmium, erbium, thulium, ytterbium and lutetium in minerals by atomic-absorption spectrophotometry," *Analyst*, 96[1138] 47-50 (1971).
227. P. D. Dragic, C. G. Carlson, and A. Croteau, "Characterization of defect luminescence in Yb doped silica fibers: part I NBOHC," *Opt. Express*, 16[7] 4688-97 (2008).
228. B. J. Harder, "Phase transformations and residual stresses in environmental barrier coatings," pp. 261. in *Materials Science*, Vol. Ph.D. Northwestern University, Chicago, IL, 2009.

229. J. Felsche, "The crystal chemistry of the rare-earth silicates," pp. 99-197. in *Rare Earths*, Vol. 13. Springer Berlin / Heidelberg, 1973.
230. G. Costa and N. Jacobson, "Thermochemistry of Rare Earth Silicates for Environmental Barrier Coatings."
231. O. Fabrichnaya, H. Jürgen Seifert, R. Weiland, T. Ludwig, F. Aldinger, and A. Navrotsky, "Phase equilibria and thermodynamics in the  $Y_2O_3-Al_2O_3-SiO_2$  system," *Zeitschrift für Metallkunde*, 92[9] 1083-97 (2001).
232. S. Dyshlovenko, L. Pawlowski, P. Roussel, D. Murano, and A. Le Maguer, "Relationship between plasma spray operational parameters and microstructure of hydroxyapatite coatings and powder particles sprayed into water," *Surface and Coatings Technology*, 200[12-13] 3845-55 (2006).
233. S. Janisson, E. Meillot, A. Vardelle, J. F. Coudert, B. Pateyron, and P. Fauchais, "Plasma spraying using Ar-He-H<sub>2</sub> gas mixtures," *J Therm Spray Tech*, 8[4] 545-52 (1999).
234. J. H. Hubbell and S. M. Seltzer, "Tables of X-ray mass attenuation coefficients and mass energy-absorption coefficients 1 keV to 20 MeV for elements Z= 1 to 92 and 48 additional substances of dosimetric interest." in. National Inst. of Standards and Technology-PL, Gaithersburg, MD (United States). Ionizing Radiation Div., 1995.
235. M. J. Guinel and M. G. Norton, "Oxidation of silicon carbide and the formation of silica polymorphs," *Journal of materials research*, 21[10] 2550-63 (2006).
236. J. W. Hutchinson and Z. Suo, "Mixed mode cracking in layered materials," *Advances in applied mechanics*, 29 63-191 (1991).
237. H. Cao and A. Evans, "An experimental study of the fracture resistance of bimaterial interfaces," *Mechanics of Materials*, 7[4] 295-304 (1989).
238. J. W. Hutchinson, M. Mear, and J. R. Rice, "Crack paralleling an interface between dissimilar materials," *Journal of Applied Mechanics*, 54[4] 828-32 (1987).
239. H. Lu and T. J. Lardner, "Mechanics of subinterface cracks in layered material," *International Journal of Solids and Structures*, 29[6] 669-88 (1992).
240. K. S. Venkatesha, T. S. Ramamurthy, and B. Dattaguru, "A study of the behaviour of subinterface cracks in bimaterial plates," *Engineering Fracture Mechanics*, 59[2] 241-52 (1998).
241. T. Ye, Z. Suo, and A. G. Evans, "Thin film cracking and the roles of substrate and interface," *International Journal of Solids and Structures*, 29[21] 2639-48 (1992).
242. R. Bermejo and R. Danzer, "High failure resistance layered ceramics using crack bifurcation and interface delamination as reinforcement mechanisms," *Engineering Fracture Mechanics*, 77[11] 2126-35 (2010).
243. K. Hbaieb, R. M. McMeeking, and F. F. Lange, "Crack bifurcation in laminar ceramics having large compressive stress," *International Journal of Solids and Structures*, 44[10] 3328-43 (2007).
244. M. Lugovy, N. Orlovskaya, V. Slyunyayev, G. Gogotsi, J. Kübler, and A. J. Sanchez-Herencia, "Crack bifurcation features in laminar specimens with fixed total thickness," *Composites Science and Technology*, 62[6] 819-30 (2002).
245. M. Oechsner, C. Hillman, and F. F. Lange, "Crack Bifurcation in Laminar Ceramic Composites," *Journal of the American Ceramic Society*, 79[7] 1834-38 (1996).

246. A. J. Phillipps, W. J. Clegg, and T. W. Clyne, "Fracture behaviour of ceramic laminates in bending—I. Modelling of crack propagation," *Acta Metallurgica et Materialia*, 41 805-17 (1993).
247. A. Evans, M. Drory, and M. Hu, "The cracking and decohesion of thin films," *Journal of Materials Research*, 3[05] 1043-49 (1988).
248. M. Y. He, F. E. Heredia, D. J. Wisnuchek, M. C. Shaw, and A. G. Evans, "The mechanics of crack growth in layered materials," *Acta Metallurgica et Materialia*, 41[4] 1223-28 (1993).
249. M. H. Meliani, Z. Azari, G. Pluvinage, and Y. G. Matvienko, "The effective T-stress estimation and crack paths emanating from U-notches," *Engineering Fracture Mechanics*, 77[11] 1682-92 (2010).
250. Z. Suo and J. W. Hutchinson, "Steady-state cracking in brittle substrates beneath adherent films," *International Journal of Solids and Structures*, 25[11] 1337-53 (1989).
251. M. D. Thouless, A. G. Evans, M. F. Ashby, and J. W. Hutchinson, "The edge cracking and spalling of brittle plates," *Acta Metallurgica*, 35[6] 1333-41 (1987).
252. X. Wang, "Elastic T-stress for cracks in test specimens subjected to non-uniform stress distributions," *Engineering Fracture Mechanics*, 69[12] 1339-52 (2002).
253. A. G. Evans and J. W. Hutchinson, "On the mechanics of delamination and spalling in compressed films," *International Journal of Solids and Structures*, 20[5] 455-66 (1984).
254. M. D. Drory and A. G. Evans, "Experimental Observations of Substrate Fracture Caused by Residually Stressed Films," *Journal of the American Ceramic Society*, 73[3] 634-38 (1990).
255. M. D. Drory, M. D. Thouless, and A. G. Evans, "On the decohesion of residually stressed thin films," *Acta Metallurgica*, 36[8] 2019-28 (1988).
256. A. G. Evans and J. W. Hutchinson, "The thermomechanical integrity of thin films and multilayers," *Acta Metallurgica et Materialia*, 43[7] 2507-30 (1995).
257. B. T. Richards, K. A. Young, F. de Francqueville, S. Sehr, M. R. Begley, and H. N. Wadley, "Thermal Cycling of Ytterbium Disilicate-Silicon Coated Silicon Carbide in a Water Vapor Environment," *Advanced Materials*, In Preparation (2015).
258. S. Ueno, T. Ohji, and H.-T. Lin, "Recession behavior of Yb<sub>2</sub>Si<sub>2</sub>O<sub>7</sub> phase under high speed steam jet at high temperatures," *Corrosion Science*, 50[1] 178-82 (2008).
259. N. Wiberg, "Holleman-Wiberg's inorganic chemistry," *Academic Press, New York* (2001).
260. D. L. Poerschke, J. S. Van Sluytman, K. B. Wong, and C. G. Levi, "Thermochemical compatibility of ytterbia-(hafnia/silica) multilayers for environmental barrier coatings," *Acta Materialia*, 61[18] 6743-55 (2013).
261. M. A. Lamkin, F. L. Riley, and R. J. Fordham, "Oxygen mobility in silicon dioxide and silicate glasses: a review," *Journal of the European Ceramic Society*, 10 347-67 (1992).
262. J. J. Vlassak, "Channel cracking in thin films on substrates of finite thickness," *International Journal of Fracture*, 119[4] 299-323 (2003).

263. D. Tromans and J. A. Meech, "Fracture toughness and surface energies of covalent minerals: theoretical estimates," *Minerals Engineering*, 17[1] 1-15 (2004).
264. J. Kübler, "Fracture toughness of ceramics using the SEVNB method: preliminary results," pp. 155-62 in Proceedings of the 21st Annual Conference on Composites, Advanced Ceramics, Materials, and Structures-B: Ceramic Engineering and Science Proceedings, Volume 18, Issue 4.
265. J. Kübler, "Fracture toughness of ceramics using the SEVNB method: first results of a joint VAMAS/ESIS round robin," pp. 494-502 in 23rd Annual Conference on Composites, Advanced Ceramics, Materials, and Structures: A: Ceramic Engineering and Science Proceedings, Volume 20, Issue 3.
266. P. Charalambides, H. Cao, J. Lund, and A. Evans, "Development of a test method for measuring the mixed mode fracture resistance of bimaterial interfaces," *Mechanics of Materials*, 8[4] 269-83 (1990).
267. P. Charalambides, J. Lund, A. Evans, and R. McMeeking, "A test specimen for determining the fracture resistance of bimaterial interfaces," *Journal of applied mechanics*, 56[1] 77-82 (1989).
268. I. Hofinger, M. Oechsner, H.-A. Bahr, and M. V. Swain, "Modified four-point bending specimen for determining the interface fracture energy for thin, brittle layers," *International Journal of Fracture*, 92[3] 213-20 (1998).
269. N. Klingbeil and J. Beuth, "Interfacial fracture testing of deposited metal layers under four-point bending," *Engineering fracture mechanics*, 56[1] 113-26 (1997).
270. Y. Yamazaki, A. Schmidt, and A. Scholz, "The determination of the delamination resistance in thermal barrier coating system by four-point bending tests," *Surface and Coatings Technology*, 201[3-4] 744-54 (2006).
271. P. Y. Théry, M. Poulain, M. Dupeux, and M. Braccini, "Spallation of two thermal barrier coating systems: experimental study of adhesion and energetic approach to lifetime during cyclic oxidation," *J Mater Sci*, 44[7] 1726-33 (2009).
272. D. Zhu, R. A. Miller, B. A. Nagaraj, and R. W. Bruce, "Thermal conductivity of EB-PVD thermal barrier coatings evaluated by a steady-state laser heat flux technique," *Surface and Coatings Technology*, 138[1] 1-8 (2001).
273. C. Glassbrenner and G. A. Slack, "Thermal conductivity of silicon and germanium from 3 K to the melting point," *Physical Review*, 134[4A] A1058 (1964).
274. H. Shanks, P. Maycock, P. Sidles, and G. Danielson, "Thermal conductivity of silicon from 300 to 1400 K," *Physical Review*, 130[5] 1743 (1963).
275. S. Howard, A. Phillipps, and T. Clyne, "The interpretation of data from the four-point bend delamination test to measure interfacial fracture toughness," *Composites*, 24[2] 103-12 (1993).
276. B. Ohnysty and F. Rose, "Thermal expansion measurements on thoria and hafnia to 4500 F," *Journal of the American Ceramic Society*, 47[8] 398-400 (1964).
277. D. Zhu, "Development and Performance Evaluations of HfO<sub>2</sub>-Si and Rare Earth-Si Based Environmental Barrier Bond Coat Systems for SiC/SiC Ceramic Matrix Composites," (2014).
278. D. Shin, R. Arróyave, and Z.-K. Liu, "Thermodynamic modeling of the Hf-Si-O system," *Calphad*, 30[4] 375-86 (2006).

279. K. Nakano, N. Fukatsu, and Y. Kanno, "Thermodynamics of Zr/Hf-mixed silicates as a potential for environmental barrier coatings for Tyranno-hex materials," *Surface and Coatings Technology*, 203 1997-2002 (2009).
280. T. Smirnova, V. Kaichev, L. Yakovkina, V. Kosyakov, S. Beloshapkin, F. Kuznetsov, M. Lebedev, and V. Gritsenko, "Composition and structure of hafnia films on silicon," *Inorganic Materials*, 44[9] 965-70 (2008).

## **12 Appendix A: Experimental Methods**

The experimental methods presented at the beginning of each chapter in this dissertation are sufficient to re-create the experiments performed. However, some additional information regarding the testing methods may be useful for the context of experimental continuity, and aid in comprehension of the rationalization behind certain experimental methods. The following sections present this additional information.

### **12.1 Scanning Electron Microscopy**

Scanning Electron Microscopy (SEM) was the primary characterization technique used in this dissertation. SEM analyses were performed on two different FEI (Hillsboro, OR) Microscopes: a Quanta 600 (VT ICTAS NCFL) and a Quanta 650 (UVA NMCF). The Quanta 600 instrument was equipped with a Bruker AXS Energy Dispersive Spectroscopy (EDS) system (Bruker Corporation, Ewing, NJ) and the Quanta 650 was equipped with an Oxford Instruments EDS system (X-Max<sup>N</sup> 150 SDD, Oxford Instruments, Concord, MA).

Imaging was consistently performed using an accelerating voltage of 10 kV. This accelerating voltage was selected to strike a balance between minimizing the electron beam interaction volume (low kV) and maximizing signal (high kV). All images in this dissertation were captured using Backscattered Electrons (BSEs). The backscattered signal is directly related to the electron density of the material imaged, so that higher atomic number (Z) elements emit stronger BSE signals. Therefore, the BSE imaging mode is very sensitive to the compositional differences in EBCs. This leads to significant benefits in the microstructural analyses performed in this dissertation. The spot size used for analyses on either Quanta system was in the range of 3-5 (physical dimension of the spot is instrument and working distance dependent, and not reported by FEI), depending on the magnification used in imaging. Very high magnification images were also occasionally captured at lower accelerating voltages down to 3 kV in order to achieve a reduced BSE interaction volume. Pixel dwell times for all images were greater than 30  $\mu$ s, and generally 60  $\mu$ s or longer in duration.

EDS spectra were generally collected using an accelerating voltage of 20 kV. This accelerating voltage was selected for multiple reasons. By handbook X-ray Mass Attenuation Coefficients,<sup>234</sup> X-ray attenuation is highest at low accelerating voltages. Therefore, higher kV electrons will have an increased interaction volume by reduced X-ray attenuation. The high kV also leads to a strong signal due to greater X-ray emission, but secondary fluorescence (through the 5 different M emission lines of Yb) is very high so that the true interaction volume may be very large (many 10's of micrometers possible). Using a lower accelerating voltage therefore appears desirable, but this greatly reduces the signal and does not appear to significantly affect the severity of the

fluorescence issues. Using a 20 kV accelerating voltage also allows spectral analysis of Yb by its L lines (7.414 keV), which helps with discrimination from Al (Al K at 1.486 keV overlaps Yb M at 1.521 keV), and the L spectra are slightly more accurate compositionally. The greatly improved signal at high kV is also highly desirable for mapping purposes.

## **12.2 Image Adjustments and Analyses**

All image adjustments in this dissertation were performed using Adobe Photoshop (Adobe Systems Inc., San Jose, CA) and analyses were performed using ImageJ (NIST, Gaithersburg, MD). Contrast adjustments were performed by multi-stage gamma corrections to normalize the contrast ranges of the disparate signals from high and low Z materials to a single visible range. Brightness was also linearly adjusted. No selective or area based contrast modifications were used to highlight individual features at any point throughout this dissertation. As previously indicated, image analysis has been performed on BSE SEM images. The overwhelming majority of this work was performed using simple contrast threshold operations. These operations are relatively insensitive to threshold settings in the high contrast images captured in this dissertation, but as with all subjective analysis techniques some bias may be assumed.

Porosity and phase fractions were the primary microstructural features measured by the threshold operation. Even with the subjectivity of the threshold operation, the high contrast differences between these features in the BSE imaging mode lead to minimal error using this technique. For phase fractions, the actual fraction calculated may

qualitatively be in the range of 1 % of the reported value: reported values are a best estimate using the mean threshold value identified to reasonably encompass the target image features. For porosity measurements, errors are minimal due to the extreme contrast differences between pores and the surrounding material. When compared with Archimedes density measurements of samples, the image analysis threshold operations for porosity agreed to within 1 %, confirming the accuracy of this measurement technique.

Crack distributions and aspect ratios of splats have also been calculated. These distributions were determined by individually measuring all linear crack segments and splats in a collection of BSE images that span a 1 mm length of the coating. In both cases, the number of features sampled was so great that numerical errors are effectively nil. However, this does not preclude subjective errors in the analyses. Particularly for the case of measuring splat aspect ratios, the definition of length and height of a particular splat is somewhat arbitrary. Best estimates were used based upon the longest dimensions observed horizontally and vertically in these cases. Likewise with crack lengths, discrimination of a linear crack segment is highly subjective, and best estimates were used throughout the extensive collections performed (greater than 10,000 individual crack segments were measured and tabulated in this dissertation).

### **12.3 X-ray Diffraction (XRD)**

As-deposited and annealed topcoats were subjected to X-ray diffraction (XRD) measurements (X'Pert Pro MPD, PANalytical, Westborough, MA) with patterns

analyzed by Rietveld refinement (HighScore Plus, PANalytical, Westborough, MA). These measurements were all performed using a flat bracket sample holder, which leads to some (minor) error in the height of the sample in the beam path. This error was deemed to be inconsequential in the context of phase identification, and was accordingly ignored. Fluorescence was evident in the diffraction patterns of all samples by the elevated background. Fluorescence was found to be far more severe when the incident X-ray source was Cr as opposed to Cu; this is supported by handbook X-ray Mass Attenuation Coefficients,<sup>234</sup> which indicate that Yb has higher Cr radiation absorption than Cu radiation absorption.

The high background resulting from fluorescence and the very large number of reflection peaks in the ytterbium silicate systems lead to considerable difficulties in volume fraction analyses by Rietveld refinement. Indeed, it appears likely that spike experiments are necessary for true quantitative verification by XRD methods. This technique has previously been used for the analysis of BSAS-based EBCs, and determined to be the only reliable method for true quantitative analysis of phase fractions using X-ray diffraction.<sup>228</sup>

Though crystallographic phases have been identified by XRD in both as-deposited and annealed topcoats, these phases have been verified in annealed coatings using electron diffraction in the transmission electron microscope (TEM). This additional verification solidifies the phase identifications performed by XRD. TEM based electron diffraction characterizations of as-deposited phases have not been performed. This work would be a requisite step in the analysis of phase evolution in these systems.

## 12.4 Mechanical Properties Testing

All mechanical properties tests were performed at the NASA Glenn Research Center. Test specimens were also fabricated in the NASA Glenn machine shop by fine diamond grinding of the sprayed stand-alone panels.

Elastic modulus was determined using the Impulse Excitation method for rectangular cross section beam specimens as defined in ASTM C 1259. The test setup records the natural frequency of the beam when excited mechanically in the desired mode (flexure on any axis or torsion about any axis). An Audio-Technica (Stow, OH) ATM350 condenser microphone amplified with an M-Audio (Cumberland, RI) DMP preamplifier was used to acoustically detect and amplify the natural frequency emitted by the mechanically excited beam. A computer system instrumented with National Instruments (Austin, TX) acoustic signal acquisition hardware and Sound & Vibration Toolset software was used to determine the natural frequency.

A Single Edge V-Notch Beam (SEVNB) technique was used to test fracture toughness. The test utilizes a 0.25 mm wide diamond saw notch that is sharpened with a razorblade coated in diamond slurry. The technique facilitates preparation of samples that cannot be micro-machined by electronic discharge and that are difficult to stably pre-crack by fatigue. The test has been extensively verified for the application of fracture toughness testing of technical ceramics by international round robin.<sup>265</sup> The physical toughness test was performed using a 4-point bend fixture with 20 mm support and 10 mm load spans. The load rate used for all tests was 0.008 mm/s.

Both flexure strength and isothermal creep tests were performed in a 4-point bend fixture with 40 mm support and 20 mm load spans. Again, the load rate used was 0.008 mm/s. Beam center point deflection was measured using a linear variable data transducer (LVDT) for creep displacement measurement. None of the flexure tests used a floating platen type load arrangement. Instead, all tests were performed using superalloy rollers that were mounted to the symmetric bending fixture. This method may result in some slight error in the values determined (a few percent maximum), but such errors are irrelevant in the present work as the context is not for engineering design curves. The greater simplicity of this experimental setup makes it far more valuable for the basic flexure strength and creep experiments performed.